UNIVERSIDAD POLITÉCNICA DE CARTAGENA

DEPARTAMENTO DE TECNOLOGÍAS DE LA INFORMACIÓN Y LAS COMUNICACIONES

UNIVERSIDAD POLITÉCNICA
DE CARTAGENA

E.T.S.I.T.

Techniques for Loss Reduction in Waveguide Filters

Tesis Doctoral

Autor: José Antonio Lorente Acosta
Directores: Alejandro Álvarez Melcón
Christoph Ernst

Cartagena, Octubre 2013

Imagen de portada / Cover photo: Artemis satellite. European Space Agency (ESA)

Universidad Politécnica de Cartagena

DT-16

CONFORMIDAD DE SOLICITUD DEAUTORIZACIÓN DE DEPÓSITO DE TESIS DOCTORAL POR EL/LA DIRECTOR/A DE LA TESIS

Dr. Christoph Ernst, y Dr. Alejandro Alvarez Melcón Directores de la Tesis doctoral "Techniques for Loss Reduction in Waveguide Filters".

INFORMA:

Que la referida Tesis Doctoral, ha sido realizada por D/Dª. José Antonio Lorente Acosta, dando mi conformidad para que sea presentada ante la Comisión de Doctorado, para ser autorizado su depósito.

La rama de conocimiento por la que esta tesis ha sido desarrollada es:

- ☐ Ciencias
- ☐ Ciencias Sociales y Jurídicas
- X Ingeniería y Arquitectura

En Cartagena, a 5 de Septiembre de 2013

LOS/LAS DIRECTORES/AS DE LA TESIS

[redacted]

Fdo.: Alejandro Alvarez Melcon

[redacted]

Fdo: Christoph Ernst

COMISIÓN DE DOCTORADO

Universidad Politécnica de Cartagena

DT-17

CONFORMIDAD DE DEPÓSITO DE TESIS DOCTORAL POR LA COMISIÓN ACADÉMICA DEL PROGRAMA

D. Fernando Quesada Pereira, Presidente de la Comisión Académica del Programa "Tecnologías de la Información y las Comunicaciones".

INFORMA:

Que la Tesis Doctoral titulada, "Techniques for Loss Reduction in Waveguide Filters", ha sido realizada por D. José Antonio Lorente Acosta, bajo la dirección y supervisión de los Doctores Christoph Ernst / Alejandro Álvarez Melcón.

En reunión de la Comisión Académica de fecha 05/06/2013 , visto que la mencionada tesis doctoral tiene acreditados los indicios de calidad, requeridos para el depósito de tesis doctorales, regulados en el artículo 32 del Reglamento de Estudios Oficiales de Máster y Doctorado de la UPCT, y la autorización del Director de la misma, se acordó dar la conformidad para que a dicha tesis le sea autorizado, por la Comisión de Doctorado, su depósito.

La Rama de conocimiento por la que esta tesis ha sido desarrollada es:

☐Ciencias
☐Ciencias Sociales y Jurídicas
X Ingeniería y Arquitectura

En Cartagena, a 6 de Septiembre de 2013

EL PRESIDENTE DE LA COMISIÓN ACADÉMICA DEL PROGRAMA

Fdo: Fernando J. Quesada Pereira

COMISIÓN DE DOCTORADO

Nunca sabrás de lo que eres capaz si no lo intentas

AGRADECIMIENTOS

La decisión de hacer una tesis doctoral no es tarea sencilla. Yo nunca pensé en hacer una, hasta que surgió la oportunidad. Aún así tuve serias dudas sobre si era ésto lo mejor para mi, si era lo que yo realmente quería. La principal razón de que escriba estas palabras es precisamente por la gente que me empujó y apoyó para llevarla a cabo.

En primer lugar me gustaría agradecer a mi familia su insistencia en que hiciera este doctorado. Tengo que decir que ellos supieron mucho antes que yo que era éste mi siguiente paso en la vida. Gracias por todo el soporte que me habéis brindado durante estos años. Gracias por venir a verme cuando estaba fuera, por recogerme y llevarme al aeropuerto a horas en que ni las calles estaban puestas, por vuestras palabras de ánimo cuando los resultados no salían, y gracias simplemente por estar ahí. Sé que me diríais que todo lo hacéis encantados, pero aún así, gracias.

Mi más sincero agradecimiento a mi supervisor de tesis, Alejandro. Gracias por apoyar mi candidatura a la Agencia Espacial Europea en primer lugar cuando hice el proyecto final de carrera. Sin duda, esto fue lo que me abrió las puertas para conseguir lo que hoy en día tengo. Gracias por tantas charlas tan productivas y tantas horas de Skype cuando estaba fuera. He de confesar que al principio del doctorado, cuando estaba en la Agencia Espacial Europea, pensaba: "no creo que me pueda ayudar, si llevamos 3 meses sin hablar". Ignorante yo, pues salía de esa reunión con la vida resuelta. Para mí, así como para otros que vinieron antes que yo, eres el mejor tutor de tesis que se pueda tener.

Special thanks to Christoph, my PhD supervisor at ESA. I still remember our first talk in the phone when you interviewed me. I was very nervous. You asked for my marks and I said I was the best of my class, of course :). Thank you for your guidance and for saying "keep up the good work" when you liked something. I have always found very important positive feedback, that we sometimes forget. Thank you for having confidence in me, and for being not only my supervisor, but also my friend.

I would also like to thank all my colleagues at ESTEC. You made my stay in The Netherlands very comfortable. In special, I would like to thank Andre, César and Petronilo for all their help with the manufacturing and measurements of the filters while I was not there, and Fabrizio, for supporting my work with his professional experience.

Gracias a Mónica, mi compañera de despacho. Nos conocimos en Cartagena, pero nos hicimos amigos en Holanda. Gracias por ayudarme con la síntesis de filtros y a escribir "papers".

Gracias también a todos mis amigos en Holanda que hicieron mi estancia alejado de los míos mucho más cómoda. Gracias a Chevi, Berta, Miguel, Nuria, Dani, Mamen, Joan, Clara, Vittorio, Carlos, Alejandra, Francis, Carlos Domenech, entre otros.

A mis compañeros Geatianos. La universidad era mucho menos aburrida con vosotros. Ojala sigamos haciendo comidas y cenas cuando todos nos reunimos en casa por vacaciones. Gracias a María, Sebas, Raúl, Alejandro y Jorge.

También, y por qué no, estoy muy agradecido a esta tesis, porque por ella os he conocido a todos vosotros. Por ella he vivido en 4 países distintos y he aprendido otras culturas. Ella me ha enseñado a buscar una alternativa a los problemas y me ha abierto las puertas para poder trabajar en lo que me gusta.

Mis últimas palabras van dirigidas, como no, a mi novia Marta. Te doy las gracias por apoyarme desde el principio, aunque eso supusiera el estar separados durante 1 año. Gracias por escuchar todos los problemas que me surgían en el desarrollo de la tesis. Gracias por leer conmigo y corregirme errores. Gracias por intentar entender cuando te explicaba algo. Sé que ha sido duro, sobre todo el último año, pero tú siempre has estado ahí. Gracias, sobre todo, por hacer todo lo anterior y mucho más siempre con una sonrisa. ¡Te quiero!

RESUMEN

El trabajo presentado en esta tesis está estructurado de forma minuciosa para conseguir el objetivo final: la búsqueda de técnicas para la reducción de pérdidas en filtros guía onda de cavidades acopladas de forma directa a través de optimización geométrica. Está claro que, para alcanzar tal objetivo, la geometría de los resonadores así como la de las estructuras de acoplo debe de ser modificada de tal manera que las pérdidas de inserción del filtro se vean reducidas. Sin embargo, la optimización global de un filtro con geometrías complejas y con un gran número de parámetros que se incrementa con el orden del filtro, sería una tarea tremendamente tediosa. Entre estos parámetros se encuentran las dimensiones de las cavidades y de los acoplos, esquinas redondeadas y sesgadas, curvas que siguen funciones matemáticas, etc. Seguir este camino llevaría, probablemente, a una profunda frustración y una buena cantidad de tiempo perdido. El objetivo está claro, pero para conseguirlo, el problema de la reducción de las pérdidas óhmicas de un filtro debe de ser dividido en tareas más pequeñas (u objetivos secundarios) que ayuden a alcanzar el fin primario una vez completadas.

Una de las primeras preguntas que se presentan durante este trabajo es si la geometría final del filtro optimizado podrá ser fabricada, o si por el contrario, se quedará en la mente y ordenador del diseñador sin ninguna posibilidad de ser traída al mundo real (al menos con la tecnología de hoy en día). El capítulo 3 es la respuesta a esta pregunta: resultados obtenidos previamente en este campo se han elegido para llevar a cabo una evaluación de una nueva tecnología llamada *fundido selectivo por láser* (o en inglés *selective laser melting o SLM*) que es capaz de construir geometrías extremadamente complejas para la fabricación de filtros guía onda con geometrías optimizadas. Varios prototipos de dos diseños diferentes han sido fabricados: un filtro con geometrías rectangulares tomado como referencia y un filtro con geometrías optimizadas. Ambos filtros han sido fabricados en dos materiales distintos con esta nueva tecnología: una aleación de aluminio (AlSi10Mg) que resulta ser muy ligera, pero que tiene una rugosidad superficial mayor de lo deseado, y titanio (grado II), por un lado más pesado que el aluminio, pero con una rugosidad superficial considerablemente menor. En el capítulo 3 se muestra el resultado de medir la rugosidad superficial de varias piezas (partes de los filtros diseñados) que han sido fabricadas con la misma tecnología. Además, se ha llevado a cabo una evaluación de la precisión que puede alcanzar dicha tecnología de fabricación utilizando

para ello las piezas citadas anteriormente, lo que ha ayudado a calibrar el sistema para la posterior fabricación de los filtros bajo estudio. A raíz de la medida de las dimensiones físicas de las piezas, se revela que las precisiones de fabricación son mayores en aquellas dimensiones paralelas a la dirección de fabricación de la pieza. No se ha podido establecer un valor claro de tolerancia ya que se ha obtenido cifras de entre 50 μm y 140 μm que dependen fuertemente de la dirección de fabricación de la pieza. Sin embargo, el proceso de fabricación de un filtro guía onda no termina con la construcción del propio filtro, sino que se debe de aplicar tratamientos en su superficie para conseguir una pieza de calidad. Más específicamente, se ha aplicado un tratamiento de pulido químico en dos de los filtros hechos de titanio (Ti3 y Ti4). Las respuestas de estos filtros tras el pulido muestran una gran reducción de pérdidas si se comparan con sus respuestas antes de ser pulidos (alrededor de 40% menos). Además, el ancho de banda de los filtros aumenta y la frecuencia de resonancia se desplaza unos 50 MHz hacia frecuencias más bajas. Como era de esperar, el proceso de pulido en los filtros no sólo reduce la rugosidad de superficie sino que también las dimensiones internas de los filtros, lo que produce los efectos descritos. Como resultado de esto, las pérdidas de inserción mejoran. Paralelamente se ha llevado a cabo un intento de plateado de uno de los filtros optimizados (Al2). Las pérdidas de inserción de dicho filtro se han visto reducidas en aproximadamente un 65% gracias a la mejora en conductividad del material. En este caso, apenas ha variado el ancho de banda así como tampoco lo ha hecho la frecuencia de resonancia del filtro. Por otro lado, un resultado sorprendente obtenido durante el desarrollo del presente trabajo es que la sensibilidad a tolerancias de fabricación de los filtros con geometrías optimizadas es menor que la de los filtros con geometrías rectangulares. Las geometrías optimizadas en este caso equivalen a geometrías redondeadas, ya que permiten una distribución más uniforme de las corrientes de superficie que fluyen a través del filtro. Estas geometrías proporcionan una transición más suave entre las estructuras de acoplo y las cavidades. Por lo tanto, una desviación en la geometría en una dirección causa una desviación en las otras direcciones también, lo que al final reduce la sensibilidad.

Habiendo probado la viabilidad de la fabricación de filtros guía onda de geometrías optimizadas mediante la tecnología SLM, la puerta hacia un nuevo concepto para el diseño de filtros guía onda queda abierta. El siguiente paso ha sido encontrar un método estructurado de optimización que pueda ser aplicado a segmentos de un filtro, resultando en una reducción efectiva de las pérdidas de inserción del filtro final. Es por ello que se ha derivado un circuito equivalente que tiene en cuenta de forma precisa las pérdidas debido a los resonadores y estructuras de acoplo. Para la segmentación del filtro, se ha elegido el centro teórico de los resonadores (no el físico), donde la fase de la señal transmitida es conocida. En el capítulo 4 se muestra la derivación paso a paso del circuito equivalente de los acoplos internos del filtro (para el caso de banda estrecha) mediante un procedimiento basado en un análisis par e impar. En el caso del acoplo externo, se propone utilizar el mismo circuito equivalente que para el caso de los acoplos internos y se muestra cuatro formas para calcular los valores de los elementos del circuito. La idea es igualar la impedancia de entrada obtenida mediante simulación de onda completa en un determinado modelo propuesto (el cual incluye el acoplo externo bajo estudio) a la impedancia de entrada analítica del circuito. Para determinar el sistema de ecuaciones se usa

dos puntos en frecuencia: la frecuencia central del filtro y una segunda frecuencia cerca de la central, donde la dependencia con la frecuencia del modelo en guía onda y del circuito propuesto son similares. De esta manera, usando las partes reales e imaginarias de las impedancias, es posible obtener y resolver un sistema no linear de cuatro ecuaciones con cuatro incógnitas. Para caracterizar los resonadores se ha usado una línea de transmisión con pérdidas cuya longitud es de media longitud de onda. El circuito equivalente final del filtro completo es el resultado de disponer en cascada los circuitos equivalentes de las partes segmentadas. La teoría se ha aplicado de forma satisfactoria a dos filtros guía onda: un filtro de primer orden con sólo una cavidad y acoplos externos y un filtro de orden cinco con irises parabólicos. Tanto el ancho de banda, la frecuencia central y las pérdidas de inserción obtenidas mediante el nuevo circuito equivalente y mediante simulación de onda completa coinciden perfectamente. La teoría ha sido aplicada a la optimización de la respuesta de una gran variedad de filtros, evitando así el uso de simulaciones de onda completa. También se ha hecho análisis de tolerancia de filtros de geometrías arbitrarias incluyendo pérdidas tanto en resonadores como en estructuras de acoplo.

Queda probado así el correcto funcionamiento del circuito equivalente para la predicción de pérdidas en filtros guía onda sin necesidad de simular el filtro completo. Sin embargo, todavía es necesaria la extracción de un parámetro del circuito equivalente que pueda ser usado como función objetivo en la optimización de las distintas partes segmentadas del filtro. El parámetro debe de representar las pérdidas debido a las estructuras de acoplo de forma precisa, independientemente de sus geometrías. Por lo tanto, una mejora de dicho parámetro en este nivel conllevará una reducción de las pérdidas de inserción finales del filtro completo. Esto se ha conseguido gracias a la definición de un nuevo factor de calidad efectivo para ambos tipos de acoplos (tanto internos como externos) que tiene en cuenta pérdidas producidas tanto en los acoplos como en sus resonadores adyacentes, como se muestra en el capítulo 5. Los factores de calidad efectivos de diferentes estructuras de acoplo con geometrías diversas como irises rectangulares, irises sinusoidales, ventanas circulares, ventanas circulares con forma sinusoidal a lo largo de la dirección de propagación, etc., han sido calculados y comparados entre ellos. Nunca antes se había llevado a cabo un estudio sistemático sobre el impacto de las dimensiones y la geometría de las estructuras de acoplo en las pérdidas de un filtro. El análisis muestra que, en general, estructuras de acoplo gruesas tienen menos pérdidas, pero a expensas de alargar el filtro final (en el caso del iris rectangular no pasa esto). Mientras que un incremento en el grosor de los acoplos conlleva reducción en pérdidas de entre un 4% y un 8%, el cambio a una geometría totalmente distinta podría mejorar el factor de calidad efectivo en más de un 12%. La estructura de acoplo con menor factor de calidad efectivo ha resultado ser el iris rectangular, mientras que la mejor estructura es la ventana circular-sinusoidal, con una mejora sobre el iris rectangular (tomado como referencia) de un 12%. Aunque este trabajo no se centra en obtener una geometría óptima para filtros en guía onda de acoplos directos, se ha comprobado que es posible obtener una mejora de más de un 23% sobre el filtro de referencia si se usa geometrías redondeadas también en los resonadores. Además, se ha calculado el rango libre de espurios de las partes segmentadas y se muestra que el rango decrece conforme el grosor de las estructuras aumenta, en todos los casos. Por otro lado, los resultados muestran que la degradación del rango de espurios con el grosor de las es-

tructuras es menos pronunciada para el caso de ventanas circulares-sinusoidales con resonadores tanto rectangulares como redondeados. Es por ello que esta estructura muestra el mejor rendimiento en términos de factor de calidad efectivo y rango libre de espurios. También se muestra que el umbral de multipactor no se ve afectado por el proceso de optimización geométrica ya que dicha optimización se produce lejos del lugar donde se encuentra el máximo de campo eléctrico.

Como se ha mencionado anteriormente, la mejora del factor de calidad efectivo de las estructuras lleva ligado un incremento en la longitud final del filtro. Como el volumen es también un parámetro de gran importancia, se ha llevado a cabo un estudio sobre la contribución de cada acoplo a las pérdidas finales del filtro. Como era de esperar, los acoplos localizados en el centro del filtro contribuyen en mayor medida a las pérdidas totales de éste. Por lo tanto, en el caso de que otras restricciones como volumen y peso sean requisito, serán los acoplos centrales los primeros candidatos a tener en cuenta en la optimización.

Para probar la teoría anterior se ha diseñado varios filtros que se recogen en dos conjuntos: el primer conjunto está compuesto por dos filtros de geometrías totalmente distintas, pero con el mismo factor de calidad efectivo en todos sus acoplos, mientras que el segundo conjunto se compone de filtros de diferentes geometrías y distintos factores de calidad efectivos en sus acoplos. Los resultados de la simulación de onda completa de los filtros del primer conjunto muestran básicamente las mismas pérdidas de inserción en ambos filtros. En cuanto a los filtros del segundo conjunto, la simulación de onda completa muestra mayores pérdidas de inserción en aquellos filtros que poseen menores factores de calidad efectivos en sus acoplos. Además, el rango libre de espurios de los filtros de ambos conjuntos coincide con lo observado en los segmentos en los que se dividen los filtros.

El diseño de filtros de geometrías optimizadas requiere un estudio por separado. En este trabajo se propone un nuevo método de diseño para este tipo de filtros. Se ha observado que las geometrías optimizadas de los acoplos modifican el parámetro de pendiente de reactancia o susceptancia de los resonadores adyacentes, lo que lleva a errores en el diseño final de los filtros (respuestas con anchos de banda que difieren de lo deseado y pérdidas de retorno no ajustadas perfectamente). Esto implicaría la necesidad de optimizar dichos filtros usando simuladores de onda completa, lo que resultaría en largos tiempos de simulación. En el capítulo 6 se propone un nuevo proceso iterativo para el diseño de este tipo de filtros que evita el uso excesivo de simuladores de onda completa. El proceso comienza con un filtro diseñado a partir de la teoría tradicional y calcula cómo cada acoplo afecta al parámetro de pendiente de los resonadores. Con esta información, es posible calcular el parámetro de pendiente de un resonador corregido por la influencia de los acoplos adyacentes. Mediante la teoría tradicional y usando el parámetro de pendiente corregido, se consigue, finalmente, diseñar el filtro sin errores. Al final de este capítulo se muestra el diseño de tres filtros mediante la teoría tradicional y mediante la nueva teoría, con la que se consigue corregir desviaciones de hasta un 10% en ancho de banda.

De esta manera queda cumplido el objetivo principal de esta tesis: la proposición y verificación de técnicas para la reducción de pérdidas en filtros guía onda con cavidades acopladas de forma directa. Esto abre la puerta a nuevas ideas y campos de aplicación en cuanto al diseño de filtros guía onda.

CONTENTS

Page

LIST OF FIGURES

Page

LIST OF TABLES

Page

CHAPTER 1

INTRODUCTION

Space communication is a very competitive growing industry that has become very popular over the last two decades. The need of highly demanding applications like high definition TV, high speed internet connection, high resolution earth mapping, highly precise weather forecast and many more is rapidly growing. To satisfy the market, the capacity of the satellite must be increased. To do so, the number of channels in the payload must be enlarged and the transmitted power must be boosted. In this context, Passive Intermodulation (PIM) is of great concern. Particularly in telecom satellites every percentage of reduced dissipated power can be converted into revenue gain due to increased payload efficiency. Low PIM is required not to pollute the very weak received signals. Also, it is desirable to keep the dissipation losses to a minimum to cope with the increased power signals.

In addition, due to the long path between the Earth and the satellite, the signal that reaches the earth station or the antenna of the satellite is highly attenuated. Therefore, the receiver of the earth station and the satellite must be capable of handling very low power signals. Furthermore, the signal to be transmitted from the earth station to the satellite or viceversa must be amplified so that it can bear the high attenuation that will suffer during its propagation through the atmosphere. Hence, the transmitters of both the earth station and the satellite must be capable of handling high power signals.

Waveguide filters satisfy the two previous requirements: they have low insertion losses and are capable to cope with high power signals. Hence, they are one of the main components of satellite payloads. These two parameters together with mass and volume are key factors to take into account when designing components for satellite applications. Another essential parameter in space communications is the spurious signal emission, which can translate into demanding out of band attenuation requirements of payload filters. The need of further decreasing dissipation losses while maintaining the same spurious free range has triggered the investigation of new techniques to achieve this goal.

In this introductory chapter, the main aspects of satellite communication will be summarized and the role of waveguide filters in satellite communications will be highlighted. The state of the art regarding loss reduction in waveguide filters by shaping strategies is described and put in context with the goal of this work. An

outline of the main results of this work concludes this introductory chapter.

1.1 Satellite Communication

A satellite communication system constitutes of a ground segment, a space segment, and the user terminals (see Figure 1.1). The ground segment consists of all the earth stations, which are usually connected to the user terminal by a terrestrial network, although they can be connected directly to the user terminal (VSAT) in some cases. The size of the stations depends on the volume and type of traffic to be carried on the satellite link (telephone, television or data), i.e. from antennas of several meters in the largest stations to antennas of less than 1 m in receiving stations (portable stations or handsets). Some stations both transmit and receive and others are receive-only stations like, for instance, receiving stations for broadcasting satellite system. The space segment is the satellite itself or network of satellites and it is composed of the bus and the payload. The bus plays a supporting role; its functions include power generation and distribution, attitude control, and propulsion. The bus also contains equipment that allows the satellite to communicate with Earth. The payload is the communication subsystem, which carries out the communications mission (receiving and transmitting information).

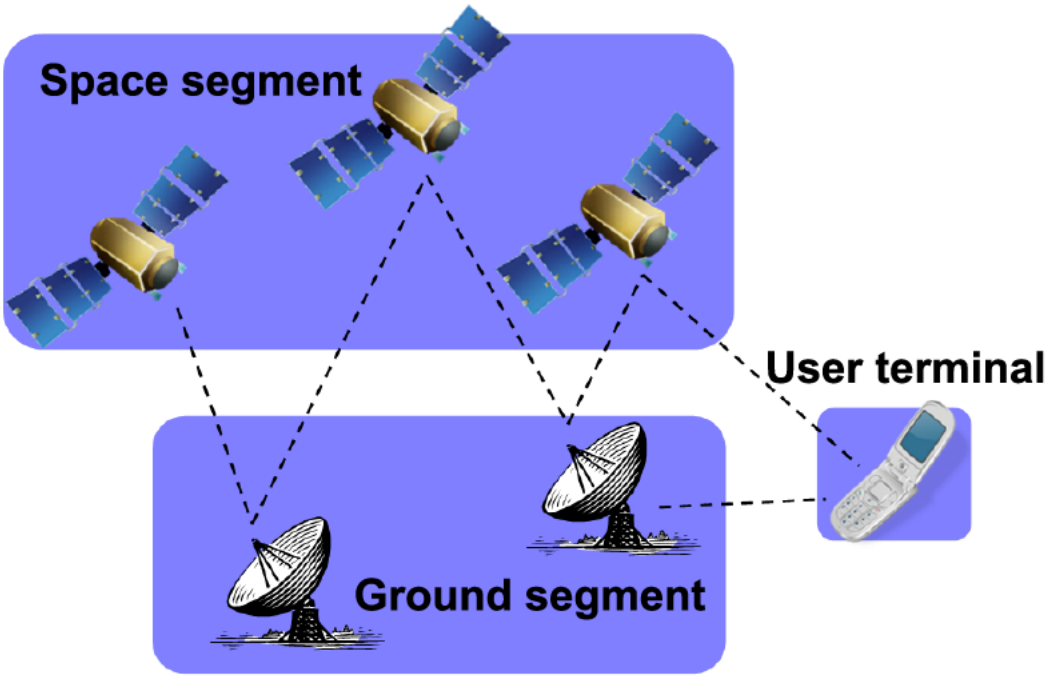

Figure 1.1: Satellite communications system.

1.1.1 The First Satellite

The world's first satellite was launched on 4 October 1957. Its name was *Sputnik-1*, which means *Satellite-1* and was launched by the Soviet Union. The satellite was about the size of a beach ball (58 cm in diameter) and weighted only 83.6 kg. It was put on an elliptical orbit that took 98 minutes to complete. The *Sputnik-1* transmitted temperature data for 22 days before its power sources went dead. The satellite made 1440 orbits and then burned up on the reentry into the Earth atmosphere on 4 January 1958, after 92 days in space. Its launch marked the start of the space age and the U.S.-U.S.S.R space race.

1.1.2 Satellites, Orbits, and Applications

After the *Sputnik-1*, satellites have become more and more popular due to their diverse applications and nowadays there are more than 1000 operative satellites all over the world out of 6934 satellites that have been launched in total since 1957, [NASA, 2013].

Satellites can be put in orbit at different distances from the Earth, depending on the final application the satellite is conceived for. The altitudes at which satellites can orbit the Earth are split into three categories:

- Low Earth Orbit (LEO)
- Medium Earth Orbit (MEO)
- High Earth Orbit (HEO)

Depending on the inclination, satellites can orbit around the equator or the poles, but technically they can orbit the Earth on any elliptical or circular path.

Low Orbit Earth (LEO)

Satellites placed at Low Earth Orbit (LEO) are found at a height of between 160 and 1400 km above the Earth's surface and they typically orbit in a circular pattern. Hence, the linear speed of a satellite at a LEO orbit is larger than 27000 km/h and it completes one orbit roughly every 90 minutes. Therefore, sophisticated ground equipment must be used to track the satellite while moving.

The main advantage of this orbit is that the signal delay is small compared to the rest of the orbits. Thus, typical applications are those where delay must be kept as low as possible, i.e. voice communication. Another advantage is that one satellite orbits the Earth several times a day, what makes possible the observation of the same point several times per day. With a complete network of satellites placed at LEO orbit and communicating between them, it is possible then to track the evolution of any event taking place at one point on the Earth's surface. Satellites placed at LEO orbits also find application for the military field.

On the other hand, satellites in this orbit have a very small *footprint*, meaning that the surface of the Earth that is covered by the signal broadcast from the satellite is small and 35 or more satellites are needed to make worldwide communication possible. It is then a very expensive satellite network to build and to maintain.

Medium Earth Orbit (MEO)

When a satellite is placed at a Medium Earth Orbit (MEO), it is found at a height between LEO and Geostationary Earth Orbit (GEO). That means, they are placed at a height between around 1400 km and 35786 km above the Earth. Like LEOs, medium earth orbit satellites do not maintain a stationary position with respect to the Earth, thus requiring the use of several satellites to cover the whole planet, but not as much as if they were placed at LEO orbits.

One advantage of placing a satellite in this orbit is that its *footprint* is larger than that of another one placed at a LEO orbit, due to their different orbital patterns (circular and elliptical) and higher distance to the Earth. Satellites placed at MEO are usually put in a polar orbit, whose path passes over the poles. Due to the Earth's rotation movement, one satellite placed in a polar orbit can cover the entire surface of the Earth.

This orbit is used by global navigation satellite systems like Galileo, Glonass or GPS. Satellites placed at MEO orbit also find application for weather forecasting, Earth observation, for military purposes, and although the signal delay is larger than that of a LEO satellite, it is still acceptable for communication purposes. Nevertheless, satellites placed at MEO do not maintain a stationary position with respect to the Earth and thus, some applications, like television broadcasting, are not possible.

High Earth Orbit (HEO)

At around 35786 km above the Earth an interesting effect occurs. Crafts placed at this height over the equator maintain their relative position over the Earth's surface and thus, this special high earth orbit (HEO) is called Geostationary or Geosynchronous Earth Orbit (GEO).

Satellites placed in geostationary orbit do not need to be tracked, which considerably reduces the cost of earth station antennas. They also have the advantage of height, therefore broad footprint (the signal broadcast covers most of the Earth's surface) and are suitable for fixed (point-to-point) services like broadcast applications and internet access. A geostationary orbit is extremely valuable for weather monitoring because satellites in this orbit provide a constant view of the same surface area. These satellites also find application in the military field.

Due to the long distance, voice, Voice over IP (VoIP) and other latency-sensitive services are not feasible since the signal propagation time is too high (225 ms round trip or more). Additional power and larger dishes are also required to boost the signal to the satellite and receive the signal on the ground. Signals in geostationary systems also must pass through the entire atmosphere and suffer the greatest dissipation of all three orbital systems. Another disadvantage of this orbit is that communication between the ground station and the satellite becomes more problematic as the ground station get closer to the poles. Thus, satellites placed in other orbits must be used when the ground station is located at a very high latitude.

Other interesting spots beyond high earth orbit are the Lagrange points. At those points, the pull of gravity from the Earth cancels out the pull of gravity from the Sun. Hence, a craft placed at the Lagrange points will feel equally pulled toward

the Earth and the Sun and will revolve with the Earth around the Sun. Satellites placed at these points find application in the study of the Sun and the nature of the universe.

1.1.3 Special Conditions

Vibration during the Launch

The first extreme condition a spacecraft has to deal with is that of launch. During launch, the rocket that holds the satellite will shake it violently and batter it with extremely loud sound waves, which have a huge impact in the satellite and all its delicate machinery. This will introduce high mechanical tensions and loading in the machinery of the spacecraft, which can perturb the extremely sensitive electrical response of the components of the satellite, loose mounting and tuning screws and, in the most extreme cases, it could break apart some components. Therefore, satellites must be designed and built to overcome these situations. Vibration tests are always performed both at component level and eventually when the built of the satellite is complete to assess its readiness for the launch.

Attenuation and High Power

The typical path length from an earth station to a GEO satellite is 35786 km, as mentioned above, and it is well known that radio signals get weaker in proportion to the square of the distance travelled. As there is so much distance, signals reaching a satellite (uplink) are always extremely weak. In the same way, signals coming to the Earth from a satellite are even weaker than uplink signals due to the limit in electrical power that can be generated using solar cells and consequently the limit in RF power available. Moreover, due to the long path that the signals have to follow until they reach the satellite or the earth station and due to the rather high frequency used, they are distorted and attenuated by the atmosphere. Above 10 GHz, rain causes significant attenuation to the signal and the probability that rain will occur in the path between the satellite and an earth station must be factored into the system design. Above 20 GHz, attenuation in heavy rain (usually associated with thunderstorms) can cause sufficient attenuation that the link will fail. Due to the high attenuation that the signal suffers on its way to the satellite and to the earth station, the electronic devices that receive the signal must dissipate as low power as possible and they should have a very small figure of noise so that the communication is possible. Furthermore, the output sections of a ground station as well as of a satellite must also be able to withstand high power signals that are to be sent to the satellite or the ground station.

Temperature and Radiation

Satellites and all its components have to support very high temperature changes due to the absence of an insulating atmosphere in space (many tens of degrees both below and above zero). A satellite that is being heated by the Sun's rays may, at the same time, be experiencing temperatures far below freezing on the side of its body facing away from the Sun. Similarly, when the satellite moves out of the direct sunlight,

the temperature drop experienced by the spacecraft is extremely fast. These sudden temperature changes make necessary that the satellite is extremely flexible, as well as resilient, in order to withstand the inevitable expansions and contractions it will undergo as it moves in and out of the Sun's rays.

Radiation in space such as fast-moving particles and X-rays also affect the satellite and its components. Most of the time these changes are so minor that they have no real consequences to the way the satellite operates. However sometimes conditions in space can change drastically, especially during a severe solar storm or "space weather event". When a high-energy particle penetrates a satellite's metal skin, its energy can be absorbed by microscopic electrical components in the circuitry of a satellite. The switch can be changed from "on" to "off" momentarily, or if the energy is high enough, this can be a permanent change. If that switch is a piece of data in the satellites memory, or a digit in a command or program, it can suddenly cause the satellite to veer out of control until a human operator on the ground can correct this problem. If the particle happens to collide with one of the pixel elements in the satellite's star-tracking camera, a false star might be created and this can confuse the satellite to think it is not pointing in the right direction. Other satellite effects can be even more dramatic. When severe solar storms affect Earth's upper atmosphere, the atmosphere heats up slightly and expands deeper into space. Satellite will feel more friction with the air they are passing through, and this will seriously affect their orbits.

Vacuum

Another important effect that must be taken into account when designing a satellite and all its components is that the satellite will be exposed to extreme vacuum conditions due to the absence of atmosphere in space. This means that matter density in space is very low and hence, the pressure the satellite must work at approximates zero. When designing components that are to be placed in space, the absence of pressure must be taken into account, specially in elements that will deal with high power signals. The multipactor effect is a phenomenon in radio frequency (RF) amplifier vacuum tubes and waveguides, where, under certain conditions, secondary electron emission in resonance with an alternating electric field leads to exponential electron multiplication, possibly damaging and even destroying the RF device.

1.1.4 The Payload of a Satellite

A block diagram of the general structure of the payload of a satellite is shown in Figure 1.2.

The payload of a communication satellite has one or more antennas, receivers, and transmitters, as well as hardware and software that perform some information processing. Redundant units are included for all equipment except for the antennas.

Receivers are designed to amplify the very weak received signals while minimising noise. They also filter the received signal to reject out-of-band noise and interferences from unwanted signals. Processing can be as little as a frequency translation from the uplink frequency to the downlink frequency. However, processing often includes additional filtering and routing different groups of received signals to different

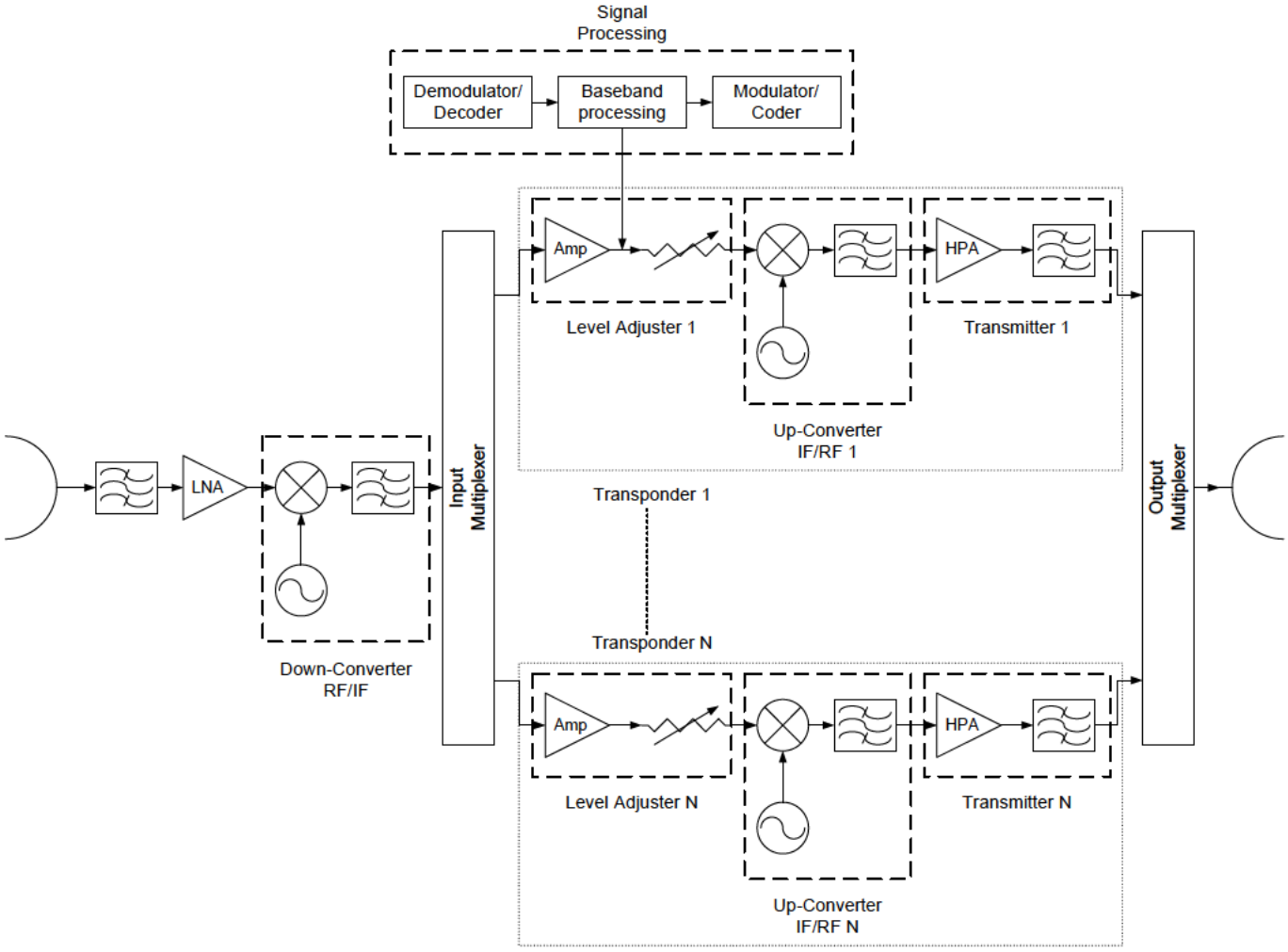

Figure 1.2: General block diagram of a satellite's payload.

transmitters. It can also include demodulating and decoding the uplink information, then remodulating and recoding it for the downlink. Modern communication subsystems divide received signals into many separate groups for efficient transmission and for routing to multiple antenna beams. Each group of signals and the associated transmitter is called a repeater or transponder. The core of each transmitter is a high-power amplifier. A transmitter can also include post-amplifier filters, as well as switches that route the signals to various antennas.

1.1.5 Filters for Space Application

Waveguide filters are found all over the payload of a satellite: in the receiver, in the down-converter, in the input multiplexer, in the up-converter, in the transmitters, and in the output multiplexer. The receiver filter tightly controls the frequencies allowed into the receiver chain while introducing very low loss to the highly attenuated received signal. This has the effect of reducing the unwanted noise from space and prevents interference from outside of the receiver band of frequencies. In the same way, the transmission filter tightly controls the frequencies allowed into the antenna and it is able to cope with the high power signals to be transmitted back to Earth.

This has the effect of reducing the unwanted signals from being accidentally transmitted onto the satellite and prevents interference to outside of the transmitter band of frequencies. Filters that are found in the frequency converters have the mission of preventing spurious resonances generated by the mixer from being transmitted. The input and output multiplexers are composed of several filters which divide the input received signal into its different channels and combine the different channels into one signal to be transmitted, respectively.

The special properties of waveguide filters (low insertion loss and high power handling capability) together with the special conditions that are given in space, make them an essential component in satellite payloads.

1.2 State of the Art on Loss Reduction in Waveguide Filters by Shape Optimization

In this section, previous work showing the possibilities of reducing the loss dissipation in waveguide transmission lines and waveguide filters by shaping techniques in resonators and coupling structures is reviewed. The main achievements in this field will be highlighted and the main drawbacks and work that can be done to further improve losses in waveguide filters due to finite material conductivity will be pointed out.

A study to obtain the optimum cross section of the dominant mode waveguide which has minimum conductor loss was carried out in [Suzuki and Hosono, 1983]. To that end, a finite Fourier series was proposed to characterize the arbitrary cross section of a waveguide. The number of coefficients that were taken for the Fourier approximation was chosen bearing in mind how close the shape of the cross-sectional element for *Finite Element Methods* (FEM) can approach the configuration expressed by the Fourier expansion. As figure of merit for the optimization, a function that is dependant on the dominant mode waveguide attenuation and the cutoff frequency of the second mode was chosen. To minimize the figure of merit, a quasi-Newton method known as the multivariable optimizing numerical solution was adopted [Fletcher, 1972]. The optimized configuration having minimum loss and a transmission bandwidth ratio equal to that of a rectangular shape was a kind of cigar shape. However and in order to facilitate the numerical calculation, manufacturing, and inspection, the cigar-like shape was approximated to a simple cigar construction made up of straight sides and semicircles. The optimized cigar shape gave a 10.5% smaller conductor loss than the standard rectangular cross section and an almost identical cutoff frequency of the second propagating mode, hence almost identical transmission bandwidth.

Thal [Thal, 1982] experimentally proved the significant impact in the unloaded Q degradation of a fixed cavity due to a thin aperture with different height to width ratios, used as inter-resonator coupling. The model used for the study was a circular waveguide TE_{111} cavity coupled to the input feed source by a small excitation aperture on one side and coupled to a detuned resonator by the aperture under study on the other side. Several apertures with different height to width ratios were manufactured for testing. The test procedure consisted on measuring the unloaded Q-factor of the cavity (using a short-circuit instead of a test aperture) and its res-

onant frequency and then carrying out the same measurements on the same cavity loaded with progressively larger apertures. The result of the study showed that the resonant frequency of the cavity decreased as the coupling aperture increased and so did the Q-factor. As the study was carried out for several apertures with different height to width ratios, but with a fixed thickness, the optimum aperture dimension ratio could be found as it was assumed that apertures that yield same frequency shifts, had essentially the same coupling value. This assumption can be taken when apertures with the same thickness and similar geometries are compared to each other, as it was the case. However, as it will be shown later, apertures with different thicknesses or with completely different geometries yield different loadings into the cavity, and thus different shifts in frequency, even if they have the same coupling coefficients. In the present work, the different loadings due to different coupling geometries will be taken into account when studying their impact on the Q-factor of the resonator. Furthermore, in contrast to [Thal, 1982], the impact of shaping the coupling geometry on the range free of spurious will also be shown here.

Another study on how to reduce the dissipation loss was recently proposed in [Zafra and Ernst, 2006] and [Zafra, 2007]. Instead of using canonical shapes (i.e. rectangular resonators and rectangular irises), the use of complex geometries with rounded edges was proposed, with the aim to reduce high current densities that concentrate along the edges and therefore, reducing the final filter losses. In that work, an optimized shaped cavity and iris with respect to the rectangular traditional cavity and iris were obtained. Specifically, a cavity with all its corners rounded was found to have an improvement of about 17% in its unloaded Q-factor over the traditional rectangular one, maintaining essentially the same spurious free range. Besides, a parabolic shape iris was found to improve a kind of effective Q-factor of a cavity in about 10% over the effective Q-factor of a similar cavity with rectangular irises. Both structures were obtained by a shape optimization in an EM simulation program. The same resonant frequency was maintained in the case of the cavity optimization, whereas the coupling value at the centre frequency was fixed for the coupling structures. Once the optimized cavities and irises were obtained, as presented in [Zafra, 2007], the next step was to assemble them and create a shaped cross section filter with also shaped coupling structures. In this way, the use of shaped geometries for the loss reduction in waveguide filters is proved since enhanced cavity filters with reduced losses were designed. Nevertheless, a clear characterization of losses produced by resonators and coupling structures was not conducted. An equivalent circuit representing the losses in the different parts of the filter was not derived. Thus, a suitable figure of merit that could be used to reduce losses was not clearly identified. Instead, the maximum current density in the apertures was optimized when they were not connected to adjacent resonators, hence not taking into account the loading effect on the resonator and the impact that this can have in the effective Q-factor of the structure (resonator and coupling geometries). Also, the impact of shaping the coupling geometry on the spurious free range of the combined resonator and coupling structures was not studied.

In this work, the main ideas of [Zafra, 2007] are further developed and a solid basis for the loss optimization of waveguide direct-coupled-cavity filters is established through the derivation of an equivalent circuit representing losses in resonators and coupling structures from where a goal function can be extracted. This goal function

is then used for the performance (i.e. loss and spurious free range) optimization of cavities and coupling geometries, in a very effective way.

1.3 Goal of the Work

This thesis presents a thorough work on the search of techniques for the loss reduction due to material finite conductivity in traditional waveguide filters by optimizing their cavity and coupling geometries whilst maintaining essentially the same spurious free range. Brute force optimization of the complete filter is not feasible since 3D full-wave software is needed to solve the fields inside the very complex geometry parts expected to be obtained. To follow this strategy would lead to a very long simulation time. Instead, the waveguide filter is divided in smaller parts that can be optimized for low losses and afterwards combined to yield a final improved filter RF response. Hence, a rigorous plan must be followed and the previous main goal must be divided in smaller tasks to be accomplished first, namely:

- The manufacturing of geometry optimized waveguide direct-coupled-cavity filters is not an easy task to be performed by traditional manufacturing methods (i.e. mechanical machining). In this work, an assessment of new additive manufacturing techniques for the manufacturing of geometry optimized waveguide filters is studied in detail.

- A rigorous derivation of an equivalent circuit that accurately represents the behaviour of the waveguide filter with arbitrary cross section and arbitrary coupling geometries to be optimized is needed. The contribution of the coupling structures to the total dissipated power and the total stored energy of the filter must be derived and a clear separation between resonators and couplings must be established.

- The reference points where the filter should be divided for the optimization have to be established. The waveguide direct-coupled-cavity filter is then divided in the smaller parts that are going to be optimized. These reference points must be taken in order to facilitate the 3D full-wave geometry optimization.

- From the two previous points, the equivalent circuit that accurately characterizes dissipation losses in the smaller optimizable parts is known, but an optimization parameter is needed. An effective quality factor that accurately represents the total losses due to the coupling structures must be extracted from the equivalent circuit. Losses in resonators are precisely given by their unloaded quality factor.

- Once the individual parts are optimized, the final dimensions of the filter must be obtained. It will be shown that shaping the geometry of the resonators and the coupling structures modifies the slope parameters involved in the calculation of impedance inverters. This effect hinders the physical dimensioning of the final filter by means of the traditional filter theory. A detailed novel method to overcome this difficulty is also derived in this work.

1.4 Thesis Outline

This thesis work is structured in eight chapters that describe in detail the development of the previously mentioned objectives.

Chapter 1 introduces the main aspects of satellite communications and highlights the hard conditions that are given in space and the challenges to be overcome. A very short historical review of satellite communications is given with special emphasis on the motivation that has lead to such an increment in satellite launchings. A short description of the parts of a satellite is also outlined.

Chapter 2 summarizes the general transmission line theory with special emphasis on rectangular waveguides. A short description on the traditional filter design theory is also exposed. The most important equations that can help to the better understanding of this work are reviewed. It also collects the previous work that has been performed in the geometry optimization of waveguide cavity resonators and coupling structures and that has served as motivation to further research in this direction. Already optimized cavity resonators and waveguide coupling structures will be presented and the main differences with the present work will be highlighted. Simulations of two waveguide direct-coupled-cavity filter designs, one with traditional rectangular structures and one with shaped geometries will also be presented.

Chapter 3 explains the assessment of the manufacturing of complex shaped waveguide filters using a new additive manufacturing technique (Selective Laser Melting or SLM) which builds the part in one piece from the bottom, layer-by-layer to the top. For the accuracy assessment, two waveguide cavity samples have been manufactured using this technology and cut in half to measure their internal dimensions and compare them against their nominal values. Furthermore, a total of six filters have also been manufactured using SLM: three prototypes of each design presented in Chapter 2, two of which are manufactured in an aluminium alloy (AlSi10Mg) and one in titanium (Grade II). To assess surface treatments to parts built with SLM technology, a chemical polish process has been applied to two of the filters and another one has been silver-plated. The effective Q-factor of the manufactured filters has been calculated, confirming the improvement in insertion loss due to the geometry shaping in cavities and coupling structures.

Chapter 4 presents a rigorous approach to accurately extract the equivalent circuit of a narrow-band waveguide direct-coupled-cavity filter including losses due to resonators and coupling apertures. To that end, a lossy transmission line resonator is used as equivalent circuit for the waveguide cavities. The lossy transmission line resonators are characterized by the complex propagation constant of the waveguide, which can be obtained directly from full-wave simulation for arbitrarily shaped waveguides, and its cutoff frequency. The remaining parameters can be derived from these two. In order to extract the lossy equivalent circuit of the inter-resonator coupling structures, a segmentation of the filter in smaller parts is carried out by applying magnetic wall

boundaries to the electrical center of its cavities. The components that compose the equivalent circuit and their values are derived by using an even and odd analysis formalism. For the external coupling, a different approach is followed. A similar equivalent circuit to the inter-resonator coupling case is used, instead of deriving it step-by-step. Its analytical input impedance is calculated and equated to the input impedance of a cavity coupled to the input waveguide by the external coupling geometry under study. The final values of the equivalent circuit are obtained by solving a system of four non-linear equations. The equivalent circuits of different waveguide filters have been obtained to prove the theory and different practical applications for the use of the novel equivalent circuits are proposed.

Chapter 5 describes the derivation of a new effective Q-factor of the smaller structures in which the filter has been segmented. The approach uses the lossy equivalent circuits derived in Chapter 4 for the inter-resonator and external coupling cases and takes into account the losses and stored energy in the resonator as well as in coupling structures. The theory has been applied to different coupling geometries. Furthermore, a goal function that takes into account the new defined effective Q-factor and the spurious free range of the smaller structures is also proposed. Finally, it is shown that filters composed of structures with the same effective Q-factor yield the same insertion loss and that a filter composed of structures with larger effective Q-factor yield smaller insertion loss. This result completely validates the theory behind the new effective Q-factor derived in this work.

Chapter 6 addresses the physical dimensioning of waveguide direct-coupled-cavity filters with optimized geometries with no need of full-wave optimization. It is clear that shaped cavities and coupling geometries yield to a non-uniform characteristic impedance of the waveguide, hence a non-uniform slope parameter of the resonators. The proposed approach calculates a uniform effective slope parameter that can be used for the dimensioning of this kind of filters. In addition, the effective slope parameter of the resonators is calculated taking into account the effects of all the coupling structures adjacent to them. The approach is a two step iterative process which makes use of the traditional filter theory to obtain the modified effective slope parameter of the resonators. The design of filters with optimized geometries using the traditional filter theory and following the new proposed approach is shown for validation of the new approach.

Chapter 7 concludes this work and some future research lines are discussed.

1.5 Original Contributions of this Thesis

This section summarizes the novel contributions of this thesis organized by chapters:

Chapter 3 : Assessment of Selective Laser Melting Technology for Geometry Optimized Filter Manufacturing. In this chapter, the assessment of using modern 3D prototyping techniques like *Selective Laser Melting*

for the manufacturing of RF equipment is discussed and, for the first time, applied to waveguide filters with optimized geometries [Lorente et al., 2009b], [Lorente et al., 2009a], [Lorente et al., 2010]. In total, six waveguide filters have been manufactured using *SLM* in Titanium and Aluminium. The same post-processing steps as if they were fabricated with traditional machining techniques were applied to the filters, i.e. they have successfully been chemically polished, silver plated, and tuned. It is shown that working waveguide filters with optimized geometries can be obtained using the modern prototyping techniques at no increased cost, hence opening the door to new possibilities in waveguide filter design like optimized geometries, optimized filter topologies, and integration of several components into one piece (which yield to considerable mass reductions). Also Passive Intermodulation (PIM) is of importance in high power applications. Already from this point of view, single part hardware can be very desirable, as it has the potential to achieve optimum Q and a PIM free design due to minimized number of surface to surface contacts. Hardware made as a single part potentially also reduces cost due to the simpler assembly procedures and less probability of assembly errors.

Chapter 4 : Rigorous Derivation of Lossy Equivalent Circuit for Narrow-band Waveguide Direct-Coupled-Cavity Filters. A novel equivalent circuit that includes losses due to material finite conductivity in cavities and coupling apertures is derived in this chapter [Lorente et al., 2012], [Lorente et al., 2013]. The lossy equivalent circuit of the inter-resonator coupling structures is for the first time stepwise derived using an even and odd formalism on a proposed waveguide model, which results from choosing cut reference planes at the centers of the cavities. For the external coupling, the equivalent circuit is proposed and the values of the elements are obtained by a novel technique that compares the analytical input impedance of the circuit with that of the waveguide model. In both cases, the contribution of the coupling structures to the total dissipated power and total stored energy of the filter can be derived and a clear separation between resonators and couplings is established. Theoretical, simulated and measured results confirm the accuracy of the loss prediction of the new equivalent circuit. The circuit finds application on filter design optimization including losses for filters with fixed geometries, loss reduction in waveguide filters by geometry optimization, and filter yield analysis including losses, among others.

Chapter 5 : Loss Reduction in Narrow-band Waveguide Direct-Coupled-Cavity Filters by Shaping Coupling Structures. One of the main applications of the novel lossy equivalent circuit is discussed in this chapter: filter geometry optimization. The division of the filter in smaller parts as commented previously allows not only to easily obtain their lossy equivalent circuit but also to define a novel effective Q-factor that can be used as goal function for the filter geometry optimization [Lorente et al., In Process]. The new technique is applied to different coupling geometries and a complete study on how their effective Q-factor varies with the coupling dimensions and geometries is carried out. The spurious free range is also included in the study and

a novel goal function that accounts for effective Q-factor and spurious free range is defined. The technique is also applied to a geometry with a kind of cigar-shape cavities and a novel sinusoidal-circular coupling window (sinusoidal in the axial dimension and circular in the transverse dimensions). The new geometry improves in around 23% the effective Q-factor of a rectangular geometry defined as baseline and almost 20% in the new defined goal function is used (that includes spurious free range information). It is shown that filters with coupling geometries with same effective Q-factor yield to essentially the same filter insertion loss and that filters with coupling geometries with higher effective Q-factor yield to lower filter insertion loss, therefore validating the theory. Furthermore, the contribution of each coupling structure to the overall filter loss is also discussed and results show that the central couplings of the filter contribute significantly more than the external ones. Since loss reduction by shaping geometries generally yield to thicker coupling structures, the previous statement can be used when filter length restrictions apply.

Chapter 6 : Dimensional Synthesis of Narrow-Band Waveguide Direct-Coupled-Cavity Filters with Optimized Geometries. The slope parameter of the filter resonators are usually affected by the shaping process in a similar way as they are when the filter bandwidth is high. This chapter proposes a new technique to correct the resonators slope parameters for the physical dimensioning of waveguide filters with optimized geometries [Lorente et al., 2013 submitted]. The technique is based on the traditional filter theory. This means that the calculated dimensions from the traditional filter theory are used as starting point to calculate the corrected ones that yield the desired filter bandwidth and return loss response. Using the new technique developed in this chapter deviations of around 10% in filter bandwidths have been corrected, avoiding the use of full-wave optimization at filter level.

A complete list of publications (international and national journals and conferences) is collected in Appendix A.

CHAPTER 2
BACKGROUND

2.1 Introduction

In this chapter, the main definitions, equations, and concepts of lossy transmission line theory and filter theory, and their application to waveguide technology that are useful for the understanding of this work are reviewed. In addition, background work regarding loss reduction in waveguide filters by geometry optimization is also summarized.

2.2 Transmission Line and Waveguides

It is well known that bandpass filters are components made of resonators whose energy couple to each other. A waveguide bandpass filter is then a structure composed of waveguide cavities that act as resonators and apertures on their walls that allow the coupling of the energy to the adjacent resonators. Furthermore, a waveguide cavity made of a metal with finite conductivity can be seen as a portion of lossy transmission line (generally of length of $\approx \lambda/2$). It is of great importance then to review the main definitions, equations and concepts of lossy transmission line theory, and its application to waveguide technology, that are necessary for a complete understanding of the work developed in this thesis. Also, the special properties of waveguide cavity resonators are later discussed. The most relevant bibliography about these topics is referenced.

2.2.1 Lossy Transmission Line Theory

Figure 2.1 shows the voltage and current definitions in a portion of lossy transmission line with characteristic impedance Z_C and complex propagation constant γ.

The steady-state solution of the voltage and current at any given point in a lossy transmission line [Pozar, 1998], [Collin, 2001] are of the form

$$V(z) = V^+ e^{-\gamma z} + V^- e^{\gamma z} \tag{2.1}$$

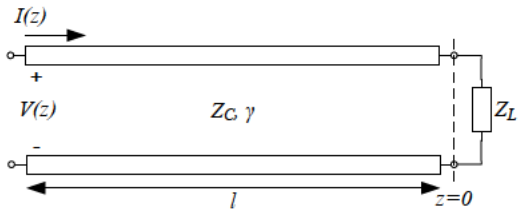

Figure 2.1: Voltage and current definitions in a lossy transmission line of length 'l'.

$$I(z) = I^+ e^{-\gamma z} + I^- e^{\gamma z} = \frac{1}{Z_C}\left(V^+ e^{-\gamma z} - V^- e^{\gamma z}\right) \tag{2.2}$$

where $V^+e^{-\gamma z}$ and $I^+e^{-\gamma z}$ are the voltage and current waves propagating in the positive z direction and $V^-e^{\gamma z}$ and $I^-e^{\gamma z}$ are the voltage and current waves propagating in the negative z direction. The complex propagation constant γ is defined as

$$\gamma = \alpha + j\beta \tag{2.3}$$

In (2.3), β is the phase constant of the mode and α is the attenuation factor due to metal finite conductivity or lossy dielectric materials.

The impedance through the transmission line can be calculated as the ratio of the voltage and the current at a given point z,

$$Z(z) = \frac{V(z)}{I(z)} = Z_C \frac{V^+e^{-\gamma z} + V^-e^{\gamma z}}{V^+e^{-\gamma z} - V^-e^{\gamma z}} = Z_C \frac{e^{-\gamma z} + \Gamma e^{\gamma z}}{e^{-\gamma z} - \Gamma e^{\gamma z}} \tag{2.4}$$

At the load, when $z = 0$, (2.4) becomes

$$Z(0) = Z_L = Z_C \frac{V^+ + V^-}{V^+ - V^-} = Z_C \frac{1+\Gamma}{1-\Gamma} \tag{2.5}$$

where Γ is the voltage reflection coefficient at the load, which is defined as the amplitude of the reflected voltage wave at the load normalized to the amplitude of the incident wave at the load. Therefore,

$$\Gamma = \frac{V^-}{V^+} = \frac{Z_L - Z_C}{Z_L + Z_C} \tag{2.6}$$

Finally, substituting (2.6) into (2.4) and using the Euler's identity for the exponential functions, the impedance at any given point z in a lossy transmission line is given by

$$Z(z) = Z_C \frac{Z_L + Z_C \tanh \gamma z}{Z_C + Z_L \tanh \gamma z} \tag{2.7}$$

2.2.2 Fields in Transmission Lines and Rectangular Waveguides

As seen in the previous section, a lossy transmission line is characterized by a complex propagation constant and a characteristic impedance. Equations for these

quantities in a rectangular waveguide will be given here. To that end, the field solutions inside a rectangular waveguide are necessary. However, the general wave solution inside a waveguide with arbitrary cross section but with axial uniformity is first reviewed here since the field solutions inside a rectangular waveguide are just a specific case of the general wave solution. For a more detailed derivation, references [Pozar, 1998], [Collin, 2001], [Marcuvitz, 1951], and [Rizzi, 1988] can be of help.

General Wave Solution

Assuming that the waveguide region is source free, the time harmonic Maxwell's equations can be written as

$$\nabla \times \overrightarrow{E} = -j\omega\mu\overrightarrow{H} \tag{2.8}$$

$$\nabla \times \overrightarrow{H} = -j\omega\epsilon\overrightarrow{E} \tag{2.9}$$

The electric and magnetic fields in a propagating medium are given in (2.10) and (2.11), which for simplicity are expressed in terms of its transversal and longitudinal components and the z dependence has been separated (assuming time dependance $e^{j\omega t}$).

$$\overrightarrow{E}(x,y,z) = \overrightarrow{E}_t(x,y,z) + \overrightarrow{E}_z(x,y,z) = \overrightarrow{e}_t(x,y)\,e^{-j\beta z} + \overrightarrow{e}_z(x,y)\,e^{-j\beta z} \tag{2.10}$$

$$\overrightarrow{H}(x,y,z) = \overrightarrow{H}_t(x,y,z) + \overrightarrow{H}_z(x,y,z) = \overrightarrow{h}_t(x,y)\,e^{-j\beta z} + \overrightarrow{h}_z(x,y)\,e^{-j\beta z} \tag{2.11}$$

Using (2.10) and (2.11) into Maxwell's equations in (2.8) and (2.9), the general transverse field solutions in terms of the longitudinal fields (e_z and h_z) for a wave propagating in the positive z-direction are found to be as

$$e_x = \frac{-j}{k_c^2}\left(\beta\frac{\partial e_z}{\partial x} + \omega\mu\frac{\partial h_z}{\partial y}\right) \tag{2.12}$$

$$e_y = \frac{j}{k_c^2}\left(-\beta\frac{\partial e_z}{\partial y} + \omega\mu\frac{\partial h_z}{\partial x}\right) \tag{2.13}$$

$$h_x = \frac{j}{k_c^2}\left(\omega\epsilon\frac{\partial e_z}{\partial y} - \beta\frac{\partial h_z}{\partial x}\right) \tag{2.14}$$

$$h_y = \frac{-j}{k_c^2}\left(\omega\epsilon\frac{\partial e_z}{\partial x} + \beta\frac{\partial h_z}{\partial y}\right) \tag{2.15}$$

where $k_c^2 = k^2 - \beta^2$ is defined as the cutoff wavenumber and $k = \omega\sqrt{\mu\epsilon}$ is the wavenumber of the material filling the transmission line or waveguide region.

TEM Wave Modes

Transverse electromagnetic (TEM) wave modes are particular modes from transmission lines with two or more conductors. They are characterized by $e_z = h_z = 0$, hence having a uniquely defined voltage, current, and characteristic impedance. These modes will not be covered here as all the work presented in this project is based in single-conductor transmission lines.

TE Wave Modes in Rectangular Waveguide

Transverse electric (TE) wave modes are supported by transmission lines consisting of a single conductor like rectangular and circular waveguides, although they can also propagate in multiple-conductor transmission lines like parallel plate waveguides and coaxial lines.

In TE modes, the longitudinal electric field is equal to zero ($e_z = 0$) and the solution to the Helmholtz equation ($\nabla^2 A + k^2 A = 0$) of the longitudinal magnetic field (applying boundary conditions of a rectangular waveguide) is of the form

$$h_z = A_{mn} \cos \frac{m\pi x}{a} \cos \frac{n\pi y}{b} e^{-j\beta z}, \qquad m, n = 0, 1, 2, ... \tag{2.16}$$

where A_{mn} is an arbitrary amplitude constant and n and m stand for the number of half-wavelength variations along the height b and the width a of the rectangular waveguide.

Substituting now (2.16) in (2.12)-(2.15), the solution to the transverse fields is found to be as

$$e_x = \frac{j\omega\mu}{k_c^2} \left(\frac{n\pi}{b}\right) A_{mn} \cos \frac{m\pi x}{a} \sin \frac{n\pi y}{b} e^{-j\beta z}, \qquad m, n = 0, 1, 2, ... \tag{2.17}$$

$$e_y = -\frac{j\omega\mu}{k_c^2} \left(\frac{m\pi}{a}\right) A_{mn} \sin \frac{m\pi x}{a} \cos \frac{n\pi y}{b} e^{-j\beta z}, \qquad m, n = 0, 1, 2, ... \tag{2.18}$$

$$h_x = \frac{j\beta}{k_c^2} \left(\frac{m\pi}{a}\right) A_{mn} \sin \frac{m\pi x}{a} \cos \frac{n\pi y}{b} e^{-j\beta z}, \qquad m, n = 0, 1, 2, ... \tag{2.19}$$

$$h_y = \frac{j\beta}{k_c^2} \left(\frac{n\pi}{b}\right) A_{mn} \cos \frac{m\pi x}{a} \sin \frac{n\pi y}{b} e^{-j\beta z}, \qquad m, n = 0, 1, 2, ... \tag{2.20}$$

where the propagation constant β is given by

$$\beta = \sqrt{k^2 - k_c^2} = \sqrt{\omega^2 \mu\epsilon - \left(\frac{m\pi}{a}\right)^2 - \left(\frac{n\pi}{b}\right)^2} \tag{2.21}$$

Based on the frequency of the wave, three different situations can be given in (2.21):

- If $k < k_c$, the propagation constant is purely imaginary and the amplitude of the wave decays exponentially away in the direction of propagation. It is said that the mode is evanescent.
- If $k > k_c$, the propagation constant is purely real and the wave propagates along the waveguide. It is said that the mode is propagating.
- If $k = k_c$, the propagation constant is equal to zero. From this equation, the following relation can be derived

$$f_c = \frac{1}{2\pi\sqrt{\mu\epsilon}}\sqrt{\left(\frac{m\pi}{a}^2\right) + \left(\frac{n\pi}{b}^2\right)} \tag{2.22}$$

  which is known as the cutoff frequency from where the mode starts propagating along the waveguide.

Note that the electric and magnetic fields and the cutoff frequency are identical to zero when $m = n = 0$, thus the TE_{00} cannot exist in the waveguide and the first propagating mode, which is called fundamental or dominant mode, is the TE_{10}.

The wave impedance that relates the transverse magnetic field to the transverse electric field is

$$Z_{\mathrm{TE}} = \frac{e_x}{h_y} = \frac{-e_y}{h_x} = \frac{\omega\mu}{\beta} \tag{2.23}$$

and is real when β is real (propagating mode) and imaginary when β is imaginary (evanescent mode).

Another important parameter is the attenuation, which can be due to dielectric (α_d) or conductor (α_c) loss. In this work, only attenuation due to conductor loss is treated, which can be obtained for the fundamental TE_{10} using the perturbation method as

$$\alpha_c = \frac{R_s}{a^3 b\beta_{10} k\eta}\left(2b\pi^2 + a^3k^2\right) Np/m \tag{2.24}$$

where β_{10} is the phase constant of the TE_{10} mode, $\eta = \sqrt{\mu_0/\epsilon_0}$ is the free space impedance, and R_s is the surface resistance of the waveguide (in ohmios), defined as

$$R_s = \sqrt{\frac{\omega\mu_0}{2\sigma}} \tag{2.25}$$

TM Wave Modes in Rectangular Waveguide

Transverse magnetic (TM) wave modes are supported by transmission lines consisting of a single conductor like rectangular and circular waveguides, although they can also propagate in multiple-conductor transmission lines like parallel plate waveguides and coaxial lines.

In TM modes, the longitudinal magnetic field is equal to zero ($h_z = 0$) and the solution to the Helmholtz equation ($\nabla^2 A + k^2 A = 0$) of the longitudinal electric field (applying boundary conditions of a rectangular waveguide) is of the form

$$e_z = A_{mn} \sin \frac{m\pi x}{a} \sin \frac{n\pi y}{b} e^{-j\beta z}, \qquad m, n = 1, 2, 3, ... \tag{2.26}$$

where A_{mn} is an arbitrary amplitude constant and n and m stand for the number of half-wavelength variations along the height b and the width a of the rectangular waveguide.

Substituting now (2.26) in (2.12)-(2.15), the solution to the transverse fields is found to be as

$$e_x = -\frac{j\beta}{k_c^2} \left(\frac{m\pi}{a}\right) A_{mn} \cos \frac{m\pi x}{a} \sin \frac{n\pi y}{b} e^{-j\beta z}, \qquad m, n = 1, 2, 3, ... \tag{2.27}$$

$$e_y = -\frac{j\beta}{k_c^2} \left(\frac{n\pi}{b}\right) A_{mn} \sin \frac{m\pi x}{a} \cos \frac{n\pi y}{b} e^{-j\beta z}, \qquad m, n = 1, 2, 3, ... \tag{2.28}$$

$$h_x = \frac{j\omega\epsilon}{k_c^2} \left(\frac{n\pi}{b}\right) A_{mn} \sin \frac{m\pi x}{a} \cos \frac{n\pi y}{b} e^{-j\beta z}, \qquad m, n = 1, 2, 3, ... \tag{2.29}$$

$$h_y = -\frac{j\omega\epsilon}{k_c^2} \left(\frac{m\pi}{a}\right) A_{mn} \cos \frac{m\pi x}{a} \sin \frac{n\pi y}{b} e^{-j\beta z}, \qquad m, n = 1, 2, 3, ... \tag{2.30}$$

where the propagation constant β is the same as for TE modes (2.21). Therefore, the cutoff frequency (2.22) is also the same.

Note that the electric and magnetic fields are identical to zero when either $m = 0$ or $n = 0$, thus the TM_{00}, TM_{01}, and TM_{10} cannot exist in the waveguide and the first propagating mode is the TM_{11}.

The wave impedance that relates the transverse magnetic field to the transverse electric field is

$$Z_{\mathrm{TM}} = \frac{e_x}{h_y} = \frac{-e_y}{h_x} = \frac{\beta}{\omega\epsilon} \tag{2.31}$$

and is real when β is real (propagating mode) and imaginary when β is imaginary (evanescent mode).

2.2.3 Rectangular Waveguide Cavities

Resonant Frequency

From the electrical point of view, the main property of a resonator is that the signal or wave propagating through it oscillates (resonates) at a given frequency, with larger amplitude than at others. The frequency at which this effect is produced is called *Resonant Frequency*.

The resonant frequency of a rectangular waveguide cavity resonator [Pozar, 1998], [Collin, 2001] can be calculated as

$$f_{mnl} = \frac{1}{2\pi\sqrt{\mu\epsilon}}\sqrt{\left(\frac{m\pi}{a}^2\right) + \left(\frac{n\pi}{b}^2\right) + \left(\frac{l\pi}{d}^2\right)} \tag{2.32}$$

where m, n, l stand for the number of half-wavelength variations along the width a, the height b, and the length d of the rectangular waveguide cavity. When $b < a < d$, the first propagating mode is the TE_{101} mode.

Unloaded Q-factor

The rate of energy loss relative to the stored energy of the resonator at the resonant frequency is measured with the *Unloaded Quality Factor (Q-factor).* Hence, this parameter gives an idea of the power loss in a resonator. The larger this parameter, the better the performance of a resonator and hence, of the final filter.

For rectangular waveguide cavities with lossy conducting walls (but lossless dielectric), the Q-factor of the TE_{10l} mode [Pozar, 1998], [Collin, 2001] is given by the formula

$$Q_U = \omega_0 \frac{W_T}{P_L} = \frac{(kad)^3\, b\eta}{2\pi^2 R_s} \frac{1}{2l^2a^3b + 2bd^3 + l^2a^3d + ad^3} \tag{2.33}$$

where W_T and P_L are the total stored energy and the total power loss in the resonator.

Spurious Free Range (SFR)

Loss reduction in waveguide filters for satellite applications is considered of extreme importance but also of great importance is the cleanliness of the filter response around the passband from unwanted spurious frequency resonances (harmonic resonances of the same propagating mode or higher order modes). The cleanliness of the frequency response of a resonator from unwanted resonances is measured with the *Spurious Free Range (SFR).* The larger this parameter, the better the performance of a resonator and hence, of the final filter.

The spurious free range is defined as

$$SFR(\%) = 100 \cdot \frac{|f_{\text{unwanted mode}} - f_{\text{selected mode}}|}{f_{\text{selected mode}}} \tag{2.34}$$

where $f_{\text{selected mode}}$ is the resonant frequency of the selected mode to work with and $f_{\text{unwanted mode}}$ is the resonant frequency of the closest unwanted mode.

Physical Parameters

The three previous parameters completely define the electrical behaviour of a resonator. However, some other physical parameters like volume, mass, and foot-print are of extreme importance in satellite communication. Therefore, depending on the technology used to build the resonator, a trade-off has to be made between the electrical properties of a resonator and its physical ones. For example, a resonator manufactured in planar technology (i.e. microstrip) will have a very low mass, volume, and foot-print, but an insufficient Q-factor to be used as receiver filter in a

satellite. On the other hand, a waveguide cavity resonator has an increased mass, volume, and foot-print than those of the planar resonator, but a quite larger Q-factor.

2.3 Design of Narrow-band Waveguide Direct-Coupled-Cavity Filters

A filter is a device that allows the transmission of some desired frequencies while rejecting the rest. Filters can be generally classified depending on the position of their passbands and their frequency transfer function [Zverev, 1967], [Hong and Lancaster, 2001], [Hunter, 2001]. Regarding the position of their passbands, filters can be categorized in:

- *Low-pass*: Low-pass filters allow the transmission of frequencies below a defined cutoff frequency (passband), while rejecting frequencies above it.
- *High-pass*: High-pass filters allow the transmission of frequencies above a defined cutoff frequency (passband), while rejecting frequencies below it.
- *Band-pass*: Band-pass filters allow the transmission of frequencies between two frequency points that define the passband and bandwidth of the filter, while rejecting frequencies outside this passband.
- *Band-stop*: Band-stop filters reject frequencies between two frequency points that define the stopband and bandwidth of the filter, while allowing the transmission of frequencies outside this stopband.

In addition, depending on their frequency transfer function, filters are divided in:

- *Butterworth*: Butterworth filters exhibit the flattest possible shape at the center of the passband with no ripple neither in the passband nor in the stopband (monotically increasing function). For this reason, they are also called maximally flat filters.
- *Chebyshev*: Chebyshev filters exhibit a steeper roll-off than Butterworth filters. However, they also have a equalized ripple (equiripple) in both the passband (type I) and the stopband (type II). As the ripple approaches zero, the Chebyshev filter converges to a Butterworth filter.
- *Elliptic*: Elliptic filters exhibit a ripple in both the passband and the stopband. For a given filter order, elliptic filters possess the steepest roll-off possible. As either the ripple in the stopband or in the passband approaches zero, the elliptic filter converges to a Chebyshev filter of the type I or II, respectively. When both ripples approach zero, the filter becomes a Butterworth filter.
- *Bessel, Gaussian, Legendre, etc.*

The theory developed in this thesis will be applied to Chebyshev filters with no transmission zeroes (no equalized ripple in the stopband). Therefore, only the filter theory concerning Chebyshev responses and their physical dimensioning in waveguide technology will be summarized in the following. On the other hand, this theory and dimensioning is similar and easily transportable to other filter responses.

2.3.1 Chebyshev Polynomial

The amplitude transfer function that describes the filter response is given by [Matthaei et al., 1980], [Hunter, 2001]

$$|S_{21}(j\Omega)|^2 = \frac{1}{1+\varepsilon^2 C_n^2(\Omega)} \tag{2.35}$$

where $C_n(\Omega)$ is the Chebyshev polynomial of the first kind of order n shown in (2.36) and ε is related to the ripple in the filter passband L_{Ar} in dB shown in (2.37).

$$C_n(\Omega) = \begin{cases} \cos\left(n\cos^{-1}(\Omega)\right), & |\Omega| \leq \Omega_c \\ \cosh\left(n\cosh^{-1}(\Omega)\right), & |\Omega| \geq \Omega_c \end{cases} \tag{2.36}$$

$$\varepsilon = \sqrt{10^{\frac{L_{Ar}}{10}} - 1} \tag{2.37}$$

The order n of the polynomial must be chosen in order to satisfy certain rejection requirements at some given frequencies.

It can be noted that the Chebyshev expression is driven by a periodic function inside the passband ($|\Omega| \leq \Omega_c$) and by a non periodic function in the stopband ($|\Omega| \geq \Omega_c$).

2.3.2 Low-pass Prototype

The low-pass prototype element values of a Chebyshev filter with a passband ripple L_{Ar} in dB and a cutoff frequency $\Omega_c = 1$ may be computed as follows [Matthaei et al., 1980], [Hunter, 2001]:

$$\begin{aligned} g_0 &= 1 \\ g_1 &= \frac{2}{\gamma}\sin\left(\frac{\pi}{2n}\right) \\ g_i &= \frac{1}{g_{i-1}} \frac{4\sin\left[\frac{(2i-1)\pi}{2n}\right]\sin\left[\frac{(2i-3)\pi}{2n}\right]}{\gamma^2 + \sin^2\left[\frac{(i-1)\pi}{n}\right]}, \quad i = 2,3,...,n \\ g_{n+1} &= \begin{cases} 1, & \text{for } n \text{ odd} \\ \coth^2\left(\frac{\beta}{4}\right), & \text{for } n \text{ even} \end{cases} \end{aligned} \tag{2.38}$$

where

$$\beta = \ln\left[\coth\left(\frac{L_{Ar}}{17.37}\right)\right] \tag{2.39}$$

$$\gamma = \sinh\left(\frac{\beta}{2n}\right) \tag{2.40}$$

The low-pass prototype ladder network for Chebyshev type filters with element values (2.38) is depicted in Figure 2.2(a) for orders n even and odd. Its dual circuit having exactly the same response can also be seen in Figure 2.2(b).

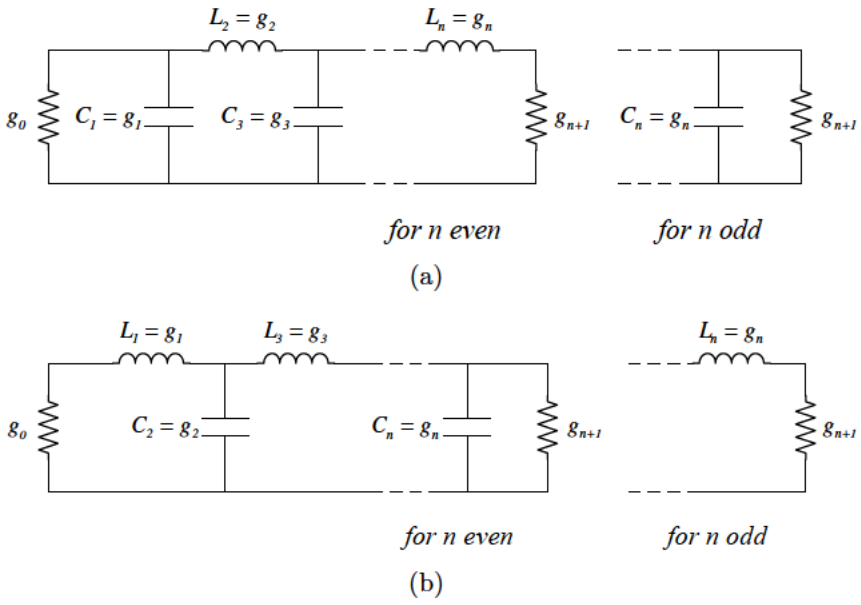

Figure 2.2: (a) Low-pass prototype ladder network for Chebyshev type filters and (b) its dual circuit.

2.3.3 Band-Pass Filters

Low-Pass to Band-Pass Transformation

To convert the low-pass prototype filters of Figure 2.2 into band-pass networks with arbitrary center frequency and bandwidth, a frequency transformation is necessary (2.41),

$$\omega \rightarrow \alpha\left(\frac{\omega}{\omega_0} - \frac{\omega_0}{\omega}\right) \tag{2.41}$$

where α and ω_0 are unknowns. To find them, the band-edges frequencies of the low-pass response are mapped into the desired band-edges of the band-pass domain as

$$-1 = \alpha\left(\frac{\omega_L}{\omega_0} - \frac{\omega_0}{\omega_L}\right) \tag{2.42}$$

$$+1 = \alpha \left(\frac{\omega_H}{\omega_0} - \frac{\omega_0}{\omega_H} \right) \tag{2.43}$$

The solution to the previous system of equations yield to

$$\omega_0 = \sqrt{\omega_L \omega_H} \tag{2.44}$$

$$\alpha = \frac{1}{w} = \frac{\omega_0}{\omega_H - \omega_L} \tag{2.45}$$

being ω_0 the geometric midband frequency, ω_H the frequency at the higher edge of the passband, ω_L the frequency at the lower edge of the passband, and w the fractional bandwidth of the filter.

The mapping must now be applied to all the frequency dependant impedances of the circuit. Therefore, a series inductor L transforms into a series connected LC circuit with values

$$L' = \frac{\alpha L}{\omega_0} \tag{2.46}$$

$$C' = \frac{1}{\alpha L \omega_0} \tag{2.47}$$

and a shunt capacitor C transforms into a shunt connected LC circuit with values

$$L' = \frac{1}{\alpha C \omega_0} \tag{2.48}$$

$$C' = \frac{\alpha C}{\omega_0} \tag{2.49}$$

The complete transformation of the lowpass prototype in Figure 2.2(a) to a bandpass filter is shown in Figure 2.3(a). The transformation of the dual network is also shown in Figure 2.3(b). The band-pass transformation of a low-pass LC ladder circuit results in a band-pass filter with both series and shunt resonators.

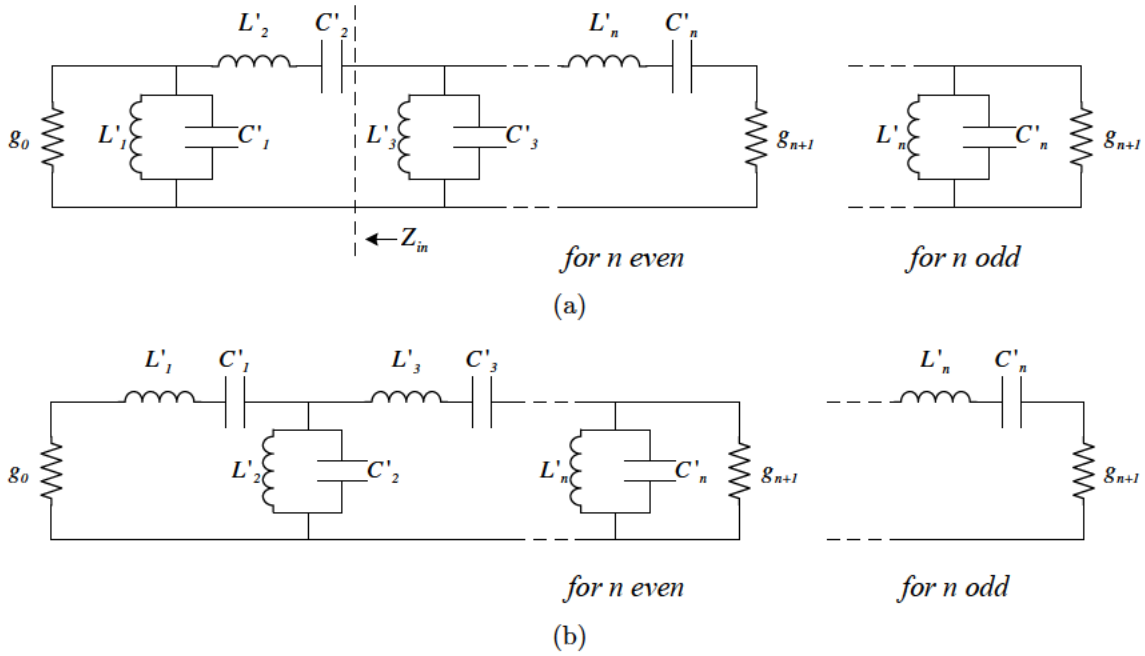

Figure 2.3: (a) Transformed band-pass filter from the low-pass prototype and (b) its dual circuit.

Use of Immittance Inverters

However, it would be desirable to have either only series or shunt resonators for implementation with microwave structures. This can be achieved with the aid of immittance (impedance and admittance) inverters. The transmission parameters of an ideal impedance inverter are shown in (2.50) and the ones of an ideal admittance inverter, in (2.51).

$$ABCD_{imp} = \begin{bmatrix} 0 & -jK \\ \dfrac{1}{jK} & 0 \end{bmatrix} \tag{2.50}$$

$$ABCD_{adm} = \begin{bmatrix} 0 & \dfrac{1}{jJ} \\ -jJ & 0 \end{bmatrix} \tag{2.51}$$

Moreover, immittance inverters have also the ability to shift impedance or admittance levels, allowing to transform the circuits in Figure 2.3 to more convenient equivalent circuits for practical purposes, as shown in Figure 2.4.

The circuits in Figure 2.4 have exactly the same response as the filters in Figure 2.3, except for an impedance shift. In order to relate the impedance inverters values and the new component values with the previous ones, the impedances seen from the second resonator to the source of both circuits is compared to each other (Z_{in} and Z_{rin}).

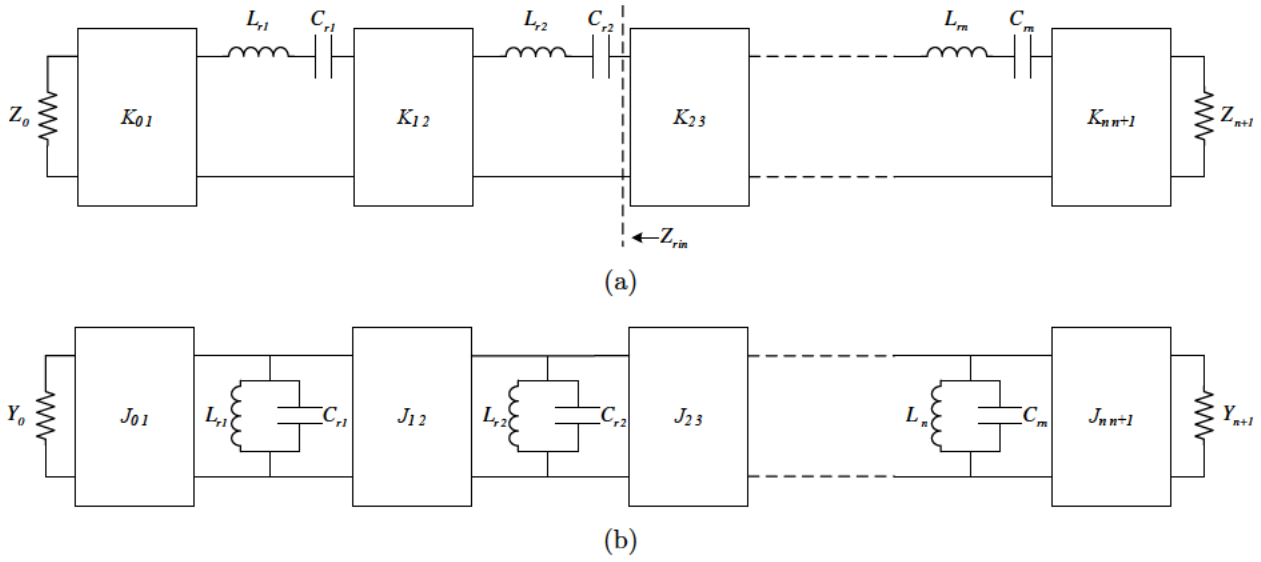

Figure 2.4: (a) Band-pass filter with series resonators and impedance inverters and (b) its dual circuit using parallel resonators and admittance inverters.

$$
\begin{aligned}
Z_{in} &= j\omega L_2' + \frac{1}{j\omega C_2'} + \frac{1}{j\omega C_1' + \dfrac{1}{j\omega L_1'} + \dfrac{1}{g_0}} \\
&= \sqrt{\frac{L_2'}{C_2'}}\left[j\left(\frac{\omega}{\omega_0} - \frac{\omega_0}{\omega}\right) + \frac{\sqrt{\dfrac{C_2' L_1'}{L_2' C_1'}}}{j\left(\frac{\omega}{\omega_0} - \frac{\omega_0}{\omega}\right) + \dfrac{1}{g_0}\sqrt{\dfrac{L_1'}{C_1'}}} \right]
\end{aligned}
\tag{2.52}
$$

$$
\begin{aligned}
Z_{rin} &= j\omega L_{r2} + \frac{1}{j\omega C_{r2}} + \frac{K_{1,2}^2}{j\omega L_{r1} + \dfrac{1}{j\omega C_{r1}} + \dfrac{K_{0,1}^2}{Z_0}} \\
&= \sqrt{\frac{L_{r2}}{C_{r2}}}\left[j\left(\frac{\omega}{\omega_0} - \frac{\omega_0}{\omega}\right) + \frac{K_{1,2}^2\sqrt{\dfrac{C_{r2} C_{r1}}{L_{r2} L_{r1}}}}{j\left(\frac{\omega}{\omega_0} - \frac{\omega_0}{\omega}\right) + \dfrac{K_{0,1}^2}{Z_0}\sqrt{\dfrac{C_{r1}}{L_{r1}}}} \right]
\end{aligned}
\tag{2.53}
$$

A closer look into expressions (2.52) and (2.53) reveals that the only difference between them is a shift in impedance level produced by the new component values (as mentioned above) if (2.54) and (2.55) are satisfied.

$$
\frac{K_{0,1}^2}{Z_0}\sqrt{\frac{C_{r1}}{L_{r1}}} = \frac{1}{g_0}\sqrt{\frac{L_1'}{C_1'}} \tag{2.54}
$$

$$
K_{1,2}^2\sqrt{\frac{C_{r2} C_{r1}}{L_{r2} L_{r1}}} = \sqrt{\frac{C_2' L_1'}{L_2' C_1'}} \tag{2.55}
$$

From (2.54) and (2.55), the values of the impedance inverters can be expressed in terms of the band-pass filter components from Figure 2.4(a) and the low-pass prototype filter elements from Figure 2.2(a) by using (2.46)-(2.49). Hence,

$$K_{0,1} = \sqrt{Z_0 \omega_0 w \frac{L_{r1}}{g_0 g_1}} = \sqrt{Z_0 w \frac{\chi_{r1}}{g_0 g_1}} \tag{2.56}$$

$$K_{i,i+1} = \omega_0 w \sqrt{\frac{L_{ri} L_{ri+1}}{g_i g_{i+1}}} = w \sqrt{\frac{\chi_{ri} \chi_{ri+1}}{g_i g_{i+1}}} \tag{2.57}$$

$$K_{n,n+1} = \sqrt{R_{n+1} \omega_0 w \frac{L_{rn}}{g_n g_{n+1}}} = \sqrt{R_{n+1} w \frac{\chi_{rn}}{g_n g_{n+1}}} \tag{2.58}$$

where χ_{ri} is the reactance slope parameter of a series resonator (2.59), defined as the variation of its reactance with frequency, evaluated at the center frequency. Similarly, the susceptance slope parameter of a shunt resonator (2.60) is defined as the variation of its susceptance with frequency, evaluated at the center frequency. Note that the relation between the impedance inverters and the slope parameter of the resonators is independent of the type of resonator used.

$$\chi = \frac{\omega_0}{2} \left. \frac{dX}{d\omega} \right|_{\omega 0} = \omega_0 L_r \tag{2.59}$$

$$b = \frac{\omega_0}{2} \left. \frac{dB}{d\omega} \right|_{\omega 0} = \omega_o C_r \tag{2.60}$$

In addition, the impedance inverter values can be expressed in terms of the amplitude of the transmission scattering parameters, if these are terminated in impedances Z_C on each side, by using some network transformation [Levy, 1973] as

$$\left| S_{21_{i,i+1}} \right| = \frac{2 Z_C}{K_{i,i+1} + \dfrac{Z_C^2}{K_{i,i+1}}} \tag{2.61}$$

Expressions for the dual circuit with admittance inverters can also be obtained if the same procedure is applied to the circuits in Figure 2.3(b) and in Figure 2.4(b) and the susceptance slope parameter is used instead.

2.3.4 Practical Realization of Narrow-band Waveguide Direct-Coupled-Cavity Filters

Lumped elements are difficult to realize at microwave frequencies, where the wavelength compares to the length of the elements and radiation may become a problem. In that case, it is usually desirable to use distributed transmission line resonators rather than the lumped-element version shown in Figure 2.4. Figure 2.5 shows a generalized circuit for band-pass filters having distributed half-wavelength transmission line resonators and impedance inverters.

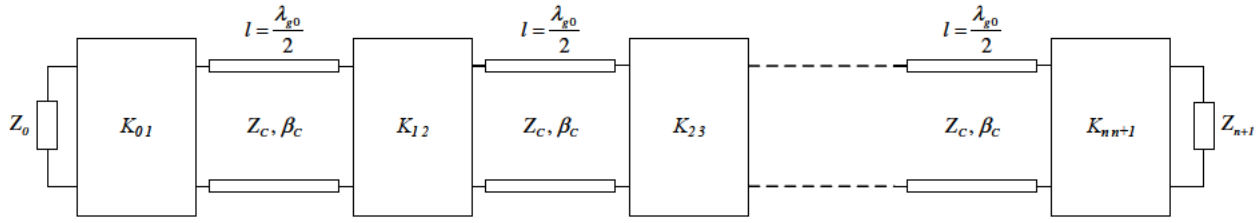

Figure 2.5: Band-pass filter with distributed transmission line resonators and impedance inverters.

Practical Realization of Immittance Inverters

An ideal impedance/admitance inverter has the property of inverting the impedance/admittance attached to one of its ports, when looking it through the other, for all frequencies. Unfortunately, this is not the case in real filter design and various networks acting as impedance and admittance inverters (some with better inverting properties over wider bandwidths than others) have been proposed to date [Matthaei et al., 1980]. The inverters shown in Figure 2.6 are particularly useful in circuits where the line of negative electrical length ϕ can be added to or subtracted from adjacent lines of the same impedance.

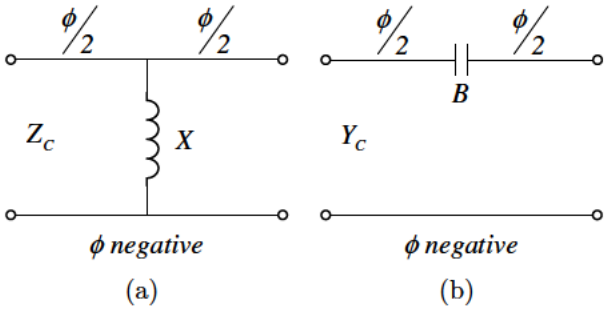

Figure 2.6: Equivalent circuits for (a) impedance inverters and (b) admittance inverters.

The reactance X and electrical length ϕ from the impedance inverter may be computed as

$$K = Z_C \tan\left|\frac{\phi}{2}\right| \tag{2.62}$$

$$\phi = -arctan\left(\frac{2X}{Z_C}\right) \tag{2.63}$$

$$\left|\frac{X}{Z_C}\right| = \frac{\frac{K}{Z_C}}{1 - \left(\frac{K}{Z_C}\right)^2} \tag{2.64}$$

The susceptance B and electrical length ϕ from the admittance inverter can be obtained by

$$J = Y_C \tan\left|\frac{\phi}{2}\right| \tag{2.65}$$

$$\phi = -arctan\left(\frac{2B}{Y_C}\right) \tag{2.66}$$

$$\left|\frac{B}{Y_C}\right| = \frac{\dfrac{J}{Y_C}}{1 - \left(\dfrac{J}{Y_C}\right)^2} \tag{2.67}$$

Transmission Line Resonators

Waveguide cavity resonators can be characterized by transmission lines of length $l = \lambda_{g0}/2$, where λ_{g0} is the guide wavelength evaluated at the resonant frequency. The electrical length associated to this physical length is then

$$\theta = \beta l = \frac{2\pi}{\lambda_{g0}}\frac{\lambda_{g0}}{2} = \pi \tag{2.68}$$

As seen previously, the impedance/admittance inverters introduce an either positive or negative electrical length ($\phi_{i-1,i}$) that must be absorbed by the adjacent resonators of the same impedance, yielding to an enlargement or a shortening of the latter. Hence, the electrical length of a resonator θ_i connected to impedance/admitance inverters at its both ends is given as

$$\theta_i = \pi + \frac{\phi_{i-1,i}}{2} + \frac{\phi_{i,i+1}}{2} \tag{2.69}$$

Physical Dimensioning of Narrow-band Direct-Coupled-Cavity Filters

In waveguide filter design, the impedance/admittance inverters may be modeled by waveguide discontinuities like irises, windows, posts, etc., [Marcuvitz, 1951]. When the energy reach these discontinuities, higher order modes are excited. These are generally below cutoff and so they remain confined to the coupling structure as stored energy, either magnetic or electric. Hence, the use of the reactance or susceptance in the equivalent circuits in Figure 2.6. The additional transmission lines of electrical length $\phi/2$ are the consequence of imposing an impedance (or admittance) phase shift of 90° between the input and the output ports, to create an impedance inverter.

To approach the physical dimensioning problem, for lossless cases, a unit element composed of a waveguide discontinuity (coupling structure) and one half cavity on each side is chosen, as seen in Figure 2.7(a). The equivalent circuit of the previous structure is also shown in Figure 2.7(b).

The transmission parameters of the equivalent circuit $ABCD_{cir}$ are known since the circuit elements have been derived through the filter synthesis phase. The physical dimensions of the CAD model unit element (length of cavity d and coupling aperture a_C) can then be varied, for a fixed coupling length l_C, until the transmission parameters of the CAD model $ABCD_{sim}$ equate those of the equivalent circuit $ABCD_{cir}$ (2.70).

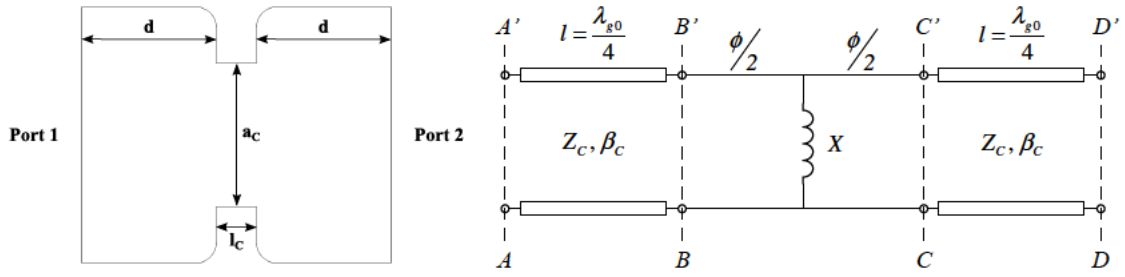

(a) (b)

Figure 2.7: Unit element chosen for the physical dimensioning of the waveguide cavities and coupling structures of a filter: (a) CAD model and (b) equivalent circuit.

$$ABCD_{sim} = ABCD_{cir} =$$
$$= \begin{bmatrix} 0 & jZ_C \\ j\frac{1}{Z_C} & 0 \end{bmatrix}_{AA'-BB'} \begin{bmatrix} 0 & -jK \\ -j\frac{1}{K} & 0 \end{bmatrix}_{BB'-CC'} \begin{bmatrix} 0 & jZ_C \\ j\frac{1}{Z_C} & 0 \end{bmatrix}_{CC'-DD'} =$$
$$= \begin{bmatrix} 0 & j\frac{Z_C^2}{K} \\ j\frac{K}{Z_C^2} & 0 \end{bmatrix}_{AA'-DD'} \tag{2.70}$$

Another approach is to use the magnitude and phase of the scattering parameters. In this case, the coupling aperture a_C is varied (for a fixed coupling length l_C) until the amplitude of the transmission scattering parameter of the CAD model $|S_{21,sim}|$ equates the amplitude of the transmission scattering parameter of the equivalent circuit $|S_{21,cir}|$, (2.71). Note that the half resonator transmission lines are lossless and the amplitude of the transmission scattering parameter depends only on the coupling structure (2.61). In a second iteration, the length of the cavity d is optimized until the phase of the transmission scattering parameter of the CAD model $\varphi(S_{21,sim})$ equates the phase of the transmission scattering parameter of the equivalent circuit $\varphi(S_{21,cir})$, which for the circuit of Figure 2.7(b) is $-90°$ (2.72).

$$|S_{21,sim}| = |S_{21,cir}| \tag{2.71}$$

$$\varphi(S_{21,sim}) = \varphi(S_{21,cir}) = -90° \tag{2.72}$$

In the first approach, an optimization with two parameters (a_C and d) and two goals (values B and C from the transmission parameters (2.70)) is needed. On the other hand, if the second approach is followed instead, the problem is reduced to two optimizations of one parameter each (a_C or d) and one goal each ($|S_{21,cir}|$ or $\varphi(S_{21,cir})$), which reduces considerably the computational time.

The final filter response can be recovered by just cascading all the optimized unit elements, with no need of further optimization.

2.4 Loss Reduction in Waveguide Filters by Geometry Optimization

Previous work in the field of geometry optimization [Zafra, 2007] is reviewed in this section and some of the mayor achievements are summarized. In the case of resonators, a rectangular baseline cavity and a shaped cavity are considered, and their unloaded Q-factor and spurious performance are compared against each other. Regarding the coupling structures, a rectangular iris is chosen as baseline and a kind of effective Q-factor is calculated and compared to the one obtained from a parabolic shaped iris. Two filters including the baseline and shaped geometries were designed and simulated. In this thesis, the work in [Zafra, 2007] has been extended and new simulations improving the mesh quality have been performed. Also, small bandwidth corrections have been applied to the filters, hence allowing for their insertion loss comparison.

2.4.1 Cavities

A rectangular cross section *WR-75* waveguide cavity with $a = 19.05$ mm, $b = 9.525$ mm, and $d = 19.5$ mm, as shown in Figure 2.8, was taken as baseline.

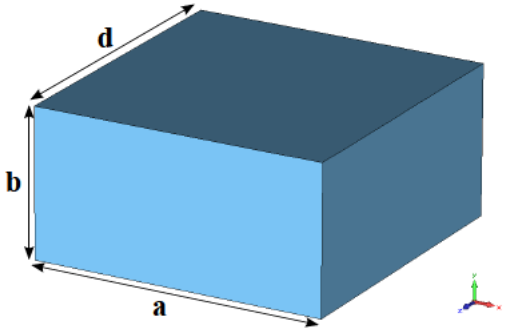

Figure 2.8: Baseline cavity.

The length of the cavity (d) was obtained for a resonant frequency of $f_0 = 11$ GHz.

The analytical unloaded Q-factor of the fundamental mode (TE_{101}) of a rectangular cavity is obtained in [Pozar, 1998] as (2.73). This equation is obtained through the power loss method. This method assumes the field distribution of a lossless cavity in a lossy cavity. Once the field distribution of the lossless cavity is obtained, the surface currents induced by this field distribution are used to calculate the power dissipation introducing the real conductivity of the cavity.

$$Q_U = \omega_0 \frac{W_T}{P_L} = \frac{(kad)^3 b\eta}{2\pi^2 R_s \left(2a^3b + 2bd^3 + a^3d + ad^3\right)} \tag{2.73}$$

In (2.73), ω_0 is the angular frequency, W_T is the total stored energy in the cavity (electric and magnetic), P_L is the dissipated power in the cavity, $k = 2\pi/\lambda$ is the wave-number, $\eta = \mu_0/\epsilon_0$ is the free-space impedance, and the surface resistance (R_s) can be computed as

$$R_s = \sqrt{\frac{\omega\mu}{2\sigma}} \tag{2.74}$$

where σ is the electrical conductivity of the material of the structure.

The spurious free range (SFR) (2.75) is the range of frequencies (measured from the center frequency) where the filter response (or cavity) is free from resonances.

$$SFR(\%) = 100 \cdot \frac{|f_{next\ mode} - f_0|}{f_0} \tag{2.75}$$

Table 2.1 lists the analytical and simulated unloaded Q-factor of the baseline cavity using two different conductivities that correspond to the two materials employed in the manufacturing of the filters shown in the last part of this chapter: an aluminium alloy (AlSi10Mg) and titanium grade II. The spurious free range is also shown.

Table 2.1: Theoretical and simulated Q-factor and SFR of the baseline cavity

Material	Conductivity (S/m)	Theoretical Q_U	Simulated Q_U*	SFR (%)
AlSi10Mg	16000000	3995	3993	57
Titanium G. II	1785714	1335	1334	57

*Ansoft HFSS V11.1.2

Several shapes improving the unloaded Q-factor of a single cavity over the baseline cavity have been studied in [Zafra, 2007], but maintaining the same resonant frequency and volume. An optimized cavity with a larger Q-factor than the baseline cavity is shown in Figure 2.9.

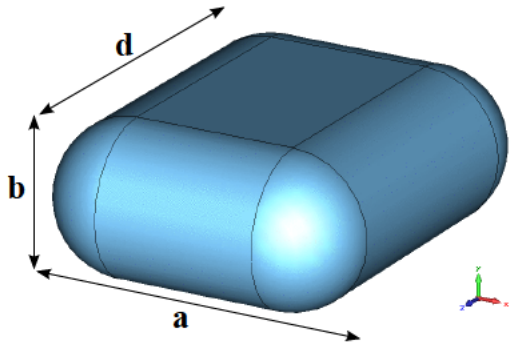

Figure 2.9: Shaped cavity.

The width of the cavity is fixed to $a = 20.5$ mm and the height is chosen to satisfy the optimum cross section specifications ($b = 0.487a = 9.9835$ mm) [Suzuki and Hosono, 1983], whereas its length is optimized to obtain a resonant frequency of $f_0 = 11$ GHz ($d = 22.2236$ mm). A fillet operation of $b/2$ is applied in all its edges.

Table 2.2 collects the unloaded Q-factor of the optimized cavity for both materials under study and the improvement over the baseline cavity. Its spurious free range can also be seen.

Table 2.2: Simulated Q-factor and SFR of the optimized cavity

Material	Conductivity (S/m)	Simulated Q_U*	Impr.	SFR (%)
AlSi10Mg	16000000	4688	17%	52
Titanium G.II	1785714	1566	17%	52

*Ansoft HFSS V11.1.2

An improvement in unloaded Q-factor of around 17% is achieved for the new geometry whilst maintaining essentially the same spurious free range. It was proved then that high Q_U improvement can be achieved for geometry optimized cavities without a large degradation of their spurious free range.

2.4.2 Coupling Structures

Coupling structures are also important elements inside a waveguide cavity filter. They strongly affect the losses in a loaded cavity and thus, have to be taken into account in the geometry optimization process.

In this case, the optimized parameter was the maximum current density in the coupling aperture when connected to an input and an output waveguide port, as seen in Figure 2.10.

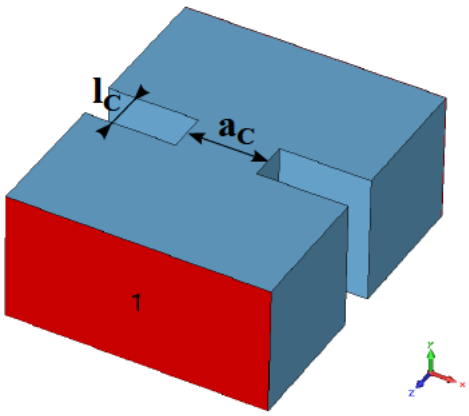

Figure 2.10: Baseline coupling structure.

To validate the improvement, a kind of effective Q-factor (Q_{eff}) was extracted from a first degree filter composed of a rectangular cavity coupled to the input feed source and output load by means of the coupling geometries under study, as shown in Figure 2.11.

The study was performed for a coupling value of $S_{21} = -10$ dB at a center frequency of $f_0 = 11$ GHz. First, the coupling dimensions were optimized to obtain the desired coupling coefficient. Next, the coupling structure was inserted into a first degree filter where the length of the cavity (d) was adjusted to yield the desired resonant frequency. Finally, the effective Q-factor of the cavity was calculated as the ratio of the stored energy and the power loss from half of the input coupling to half of the output coupling.

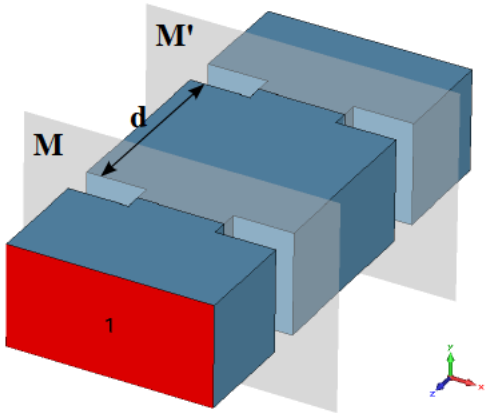

Figure 2.11: First degree filter for the extraction of Q_{eff}.

Several structures were proposed and studied in [Zafra and Ernst, 2006] and in [Zafra, 2007]. As a baseline, a symmetrical rectangular iris as the one shown in Figure 2.10 was chosen. The height of the baseline coupling structure was taken as the height of the cavity, the thickness was fixed to $l_C = 3$ mm and the aperture, after optimizing it to yield the desired coupling value, was $a_C = 9.106$ mm. The coupling structure was then inserted into a first degree filter following the previous procedure and the effective Q-factor was extracted for the two materials under study, giving the results listed in Table 2.3.

Table 2.3: Effective Q-factor of a first degree filter with baseline coupling structures

Material	Conductivity (S/m)	Simulated Q_{eff}*
AlSi10Mg	16000000	3367
Titanium Grade II	1785714	1139

*Ansoft HFSS V11.1.2

As in the case of the cavities, applying rounding in the sharp corners of the rectangular irises was found to improve the effective Q-factor in [Zafra and Ernst, 2006]. An optimized parabolic shaped structure (Figure 2.12) with $a_C = 7.988$ mm, $l_C = 5.056$ mm, and with the same height as the cavities was found to improve the effective Q-factor in around 10%.

Table 2.2 collects the effective Q-factor of a first degree filter with the optimized coupling geometries for the two materials under study.

Table 2.4: Effective Q-factor of a first degree filter with shaped coupling structures

Material	Conductivity (S/m)	Simulated Q_{eff}*	Improvement over baseline
AlSi10Mg	16000000	3719	10.5%
Titanium Grade II	1785714	1248	9.6%

*Ansoft HFSS V11.1.2

In this case, the improvement achieved by only modifying the geometry of the

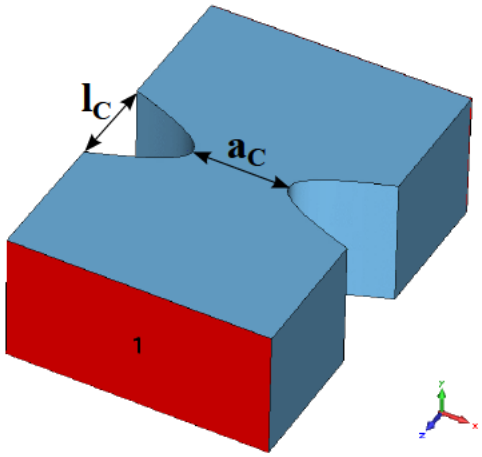

Figure 2.12: Shaped coupling structure.

waveguide coupling structures was around 10%. Again, the optimization of the coupling geometries is proved to increase the effective Q-factor of a first degree filter.

However, the above described optimization process does not take into account that resonators exist in the vicinity of the coupling structure and loadings in resonators are then neglected (also current densities will be different due to the presence of resonators). Furthermore, external coupling current densities are asymmetrical due to the presence of one resonator in one side of the coupling structure and not in the other, and the models in Figure 2.10 and in Figure 2.12 do not accurately represent this fact. In the next chapters, a more accurate optimization process is derived and proved to give excellent results.

2.4.3 Designed Filters

To validate the previous theory, the optimized shaped cavities and shaped irises are then assembled to create a waveguide direct-coupled-cavity filter. A filter with rectangular cavities and rectangular irises is chosen as baseline (Figure 2.13).

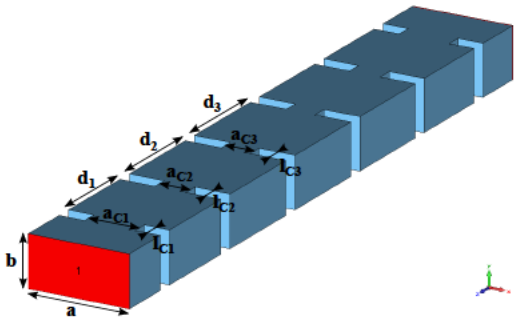

Figure 2.13: Designed baseline filter.

The second filter (shaped filter) is composed of rounded cavities and parabolic irises. To design it, a filter with rectangular cavities and parabolic irises is first

created (Figure 2.14(a)), and then a fillet operation with a radius of $b/2$ is applied in all its edges, resulting in the filter shown in Figure 2.14(b).

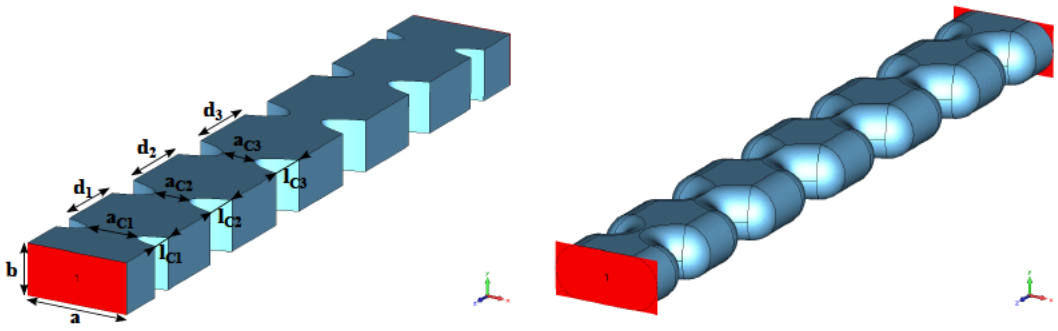

(a) (b)

Figure 2.14: Designed shaped filter: (a) before the fillet operation, and (b) final filter.

The targeted filter performance is shown in Table 2.5.

Table 2.5: Filter specifications

Parameter	Value
f_0	$11GHz$
Ripple BW	$100MHz$
RL	$25dB$
n	5

For the design, the standard filter design method was employed [Cohn, 1957], [Matthaei et al., 1980]. Table 2.6 shows the final dimensions of the filters, which were extracted from [Zafra, 2007].

Table 2.6: Baseline filter and shaped filter physical dimensions

Parameter	Baseline (mm)	Shaped (mm)
a	19.05	20.5
b	9.525	9.984
d_1	16.727	15.313
d_2	18.299	16.113
d_3	18.414	16.116
l_{C1}	3	4.904
l_{C2}	3	7.687
l_{C3}	3	8.244
a_{C1}	9.538	10.508
a_{C2}	5.884	7.205
a_{C3}	5.397	6.774
total length*	126.47	140.64

*Same launch length of 10mm

Figure 2.15 shows the simulated responses of the designed filters. In this case, the conductivity from the aluminium alloy (AlSi10Mg) has been used (see Table 2.3).

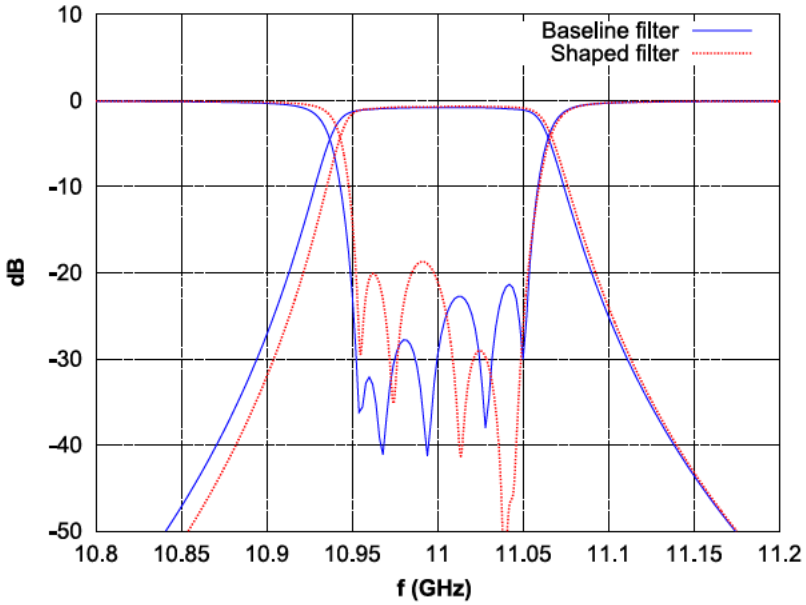

Figure 2.15: Simulated RF responses of the baseline and shaped filters.

The dimensioning of the filters in [Zafra, 2007] was carried out with a poor mesh. Additional simulations keeping the original dimensions have been performed in this work that improve the mesh quality of the models, thus slightly detuning the filters. Due to this fact, Figure 2.16(a) shows both responses in a normalized frequency axis. A detail of their $S_{2,1}$ can be seen in Figure 2.16(b).

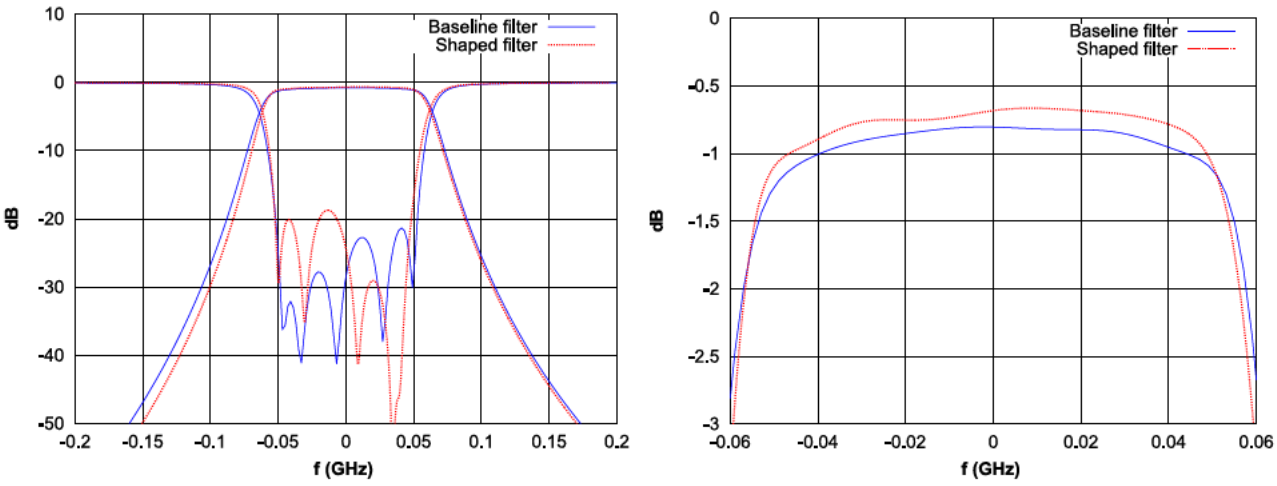

(a) (b)

Figure 2.16: (a) Simulated RF responses of the baseline and shaped filters in a normalized frequency axis and (b) $S_{2,1}$ detail.

In this work, the minimum insertion loss and the 3dB bandwidths from both filters have been collected and are shown in Table 2.7, for comparison.

Table 2.7: Insertion loss of the baseline and shaped filters

Filter	min. IL (dB)	3dB BW
Baseline	0.803	125.38
Shaped	0.664	121.56

As the insertion loss of a filter is a function of its bandwidth, a comparison cannot be directly performed since both filters have slightly different bandwidths. In [Hunter et al., 2002], an equation for the losses at center frequency depending on the degree and bandwidth of the filter is derived (2.76).

$$IL_1 = \frac{4.343 f_0}{(BW_1 Q_U)} \sum_{r=1}^{N} g_r \tag{2.76}$$

For slight bandwidth variations, the low-pass prototype elements as well as the unloaded Q-factor of the resonators can be considered invariable. Hence,

$$IL_2 = \frac{4.343 f_0}{(BW_2 Q_U)} \sum_{r=1}^{N} g_r \tag{2.77}$$

By combining (2.76) and (2.77), a relationship between the insertion loss (IL_1) of a filter with bandwidth BW_1 and the insertion loss (IL_2) of a filter with bandwidth BW_2 can be derived as

$$IL_2 = IL_1 \frac{BW_1}{BW_2} \tag{2.78}$$

which can be used for insertion loss corrections for filters with slight different bandwidths. Applying (2.78) to the shaped filter to match the same bandwidth of the baseline filter, a corrected insertion loss for the new bandwidth can be obtained. Table 2.8 collects the insertion loss of the baseline filter, the corrected insertion loss of the shaped filter and the achieved improvement.

Table 2.8: Insertion loss of the baseline and shaped filters

Filter	min. IL (dB)	Impr. (%)
Baseline	0.803	n/a
Shaped	0.644	19.8

The out of band performance of the simulated filters is shown in Figure 2.17 and the extracted spurious free range measured from the centre frequency of each filter to the first resonance of the second harmonic can be seen in Table 2.9.

Table 2.9: Spurious free range of the baseline and shaped filters

Filter	SFR (%)	Impr. (%)
Baseline	54.6	n/a
Shaped	47	-13.92

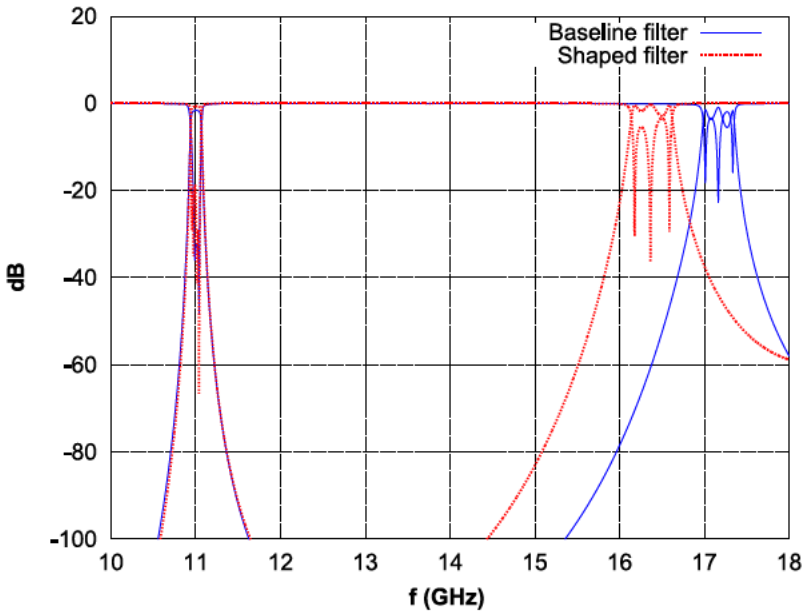

Figure 2.17: Simulated out of band response of the baseline and shaped filters.

2.5 Conclusion

Previous work has reported successful loss reduction on waveguide direct-coupled-cavity filters by shape optimization on their cavities and coupling structures [Zafra, 2007]. The predicted unloaded Q-factor improvement of a shaped cavity over a rectangular one was reported to be approximately 17%. Moreover, the shaped irises were reported to also contribute significantly to the improvement of a kind of effective Q-factor of a first degree filter. However, an overall insertion loss comparison of the designed filters was not possible since they have slightly different bandwidths. The work in [Zafra, 2007] has been extended here and small bandwidths corrections have been applied to the filters to allow for their insertion loss comparison. Improvements in the range of at least 19% were verified by full-wave simulation for filters with optimized geometries (after applying bandwidth correction). On the other hand, simulation results show that the spurious free range of the shaped filter is degraded as this parameter was not used in the goal function during the optimization of the coupling elements.

CHAPTER 3

ASSESSMENT OF SELECTIVE LASER MELTING TECHNOLOGY FOR GEOMETRY OPTIMIZED FILTER MANUFACTURING

This chapter is devoted to the assessment of a new manufacturing technique known as *Selective Laser Melting (SLM)* for the fabrication of geometry optimized waveguide filters. This technique is able to reproduce complex geometries at no increased cost. The designed filters in Chapter 2 have been fabricated with the new technology and are shown here.

3.1 Introduction

The manufacturing of filters with complex geometries is a challenging task and must be carefully considered. Traditional machining processes are in a very mature state and are able to achieve tolerances as good as $10\mu m$ for simple geometries, including some simple shaped geometries. However, they are limited in the range of geometries they can reproduce and the final prototype will always be composed of more than one part. In high power applications single part hardware is very desirable, as it has the potential to achieve optimum Q and a PIM free design since the number of surface to surface contacts is minimized. Hardware made as a single part potentially also reduces cost due to the simpler assembly procedures and less probability of assembly errors. In this context, today electroforming or moulding techniques can be employed to achieve single piece hardware. However they are either expensive or have long lead times or can only offer limited geometrical freedom, [Ecclestone et al., 2007]. This is not the case for a new class of emerging additive manufacturing techniques [Crawford and Beaman, 1999]. Among these, one promising technology is *Direct Metal Laser Sintering (DMLS)*. Recently DMLS was used to manufacture an Ortho Mode Transducer (OMT) which is part of a Ka-band antenna system [Gilmore and Booth, 2008]. A nickel bronze alloy was employed for the OMT manufacturing process. Although mass saving could be achieved since no assembly screws are needed, the nickel bronze alloy has a quite high specific density ($7.6g/cm^3$ in skin areas, $6.3g/cm^3$ in core areas). In order to overcome this disad-

vantage, a similar additive manufacturing technique called *Selective Laser Melting (SLM)* which is able to fabricate rectangular as well as complex shapes at no additional cost was chosen in this case study and used for the fabrication of the designed filters in Chapter 2.

A total of six filters (Table 3.1) divided in three sets have been manufactured. Each set is composed of two filters: one baseline and one shaped. Filters from set 1 have been manufactured in an aluminium alloy (AlSi10Mg) and filters from sets 2 and 3, in titanium (grade II). Also, surface treatment of the prototypes is evaluated as a post-processing step after the manufacturing to improve inherent surface roughness to the manufacturing technique and conductivity of the material. In this context, the shaped filter from set 1 (Al2) has been silver plated and both filters from set 3 have been chemically polished.

Table 3.1: List of manufactured prototypes and sets

SET 1 (AlSi10Mg)	Baseline (Al1)
	Shaped (Al2)
SET 2 (Titanium)	Baseline (Ti1)
	Shaped (Ti2)
SET 3 (Titanium chemically polished)	Baseline (Ti3)
	Shaped (Ti4)

The accuracy of the process has been assessed by comparing the final physical dimensions of two waveguide samples manufactured using SLM to their nominal design dimensions. Furthermore, the final surface roughness of the fabricated prototypes has also been measured.

Simulated and measured results of the manufactured filters are shown here. A method to extract the effective Q-factor (Q_{eff}) of the filters from their response is studied, thus allowing to fairly compare their performances in terms of losses.

3.2 Selective Laser Melting (SLM)

SLM technology is investigated in this work for the manufacturing of single part microwave filters. One of the most powerful features of this technology is the ability to produce very complex shaped waveguide structures, thus increasing the freedom in microwave filter design. SLM is an additive manufacturing technology where each part of the structure is built layer-by-layer instead of removing material from a bulk block. To do so, the 3D CAD file is sliced in thin successive layers. Then, thin metallic powder layers corresponding to the layer-wise assembly are added one on top of the other in the SLM machine. Finally, a laser is used to sinter (or melt) the metal to build the solid part before applying the next layer. This process can be seen in Figure 3.1.

With this technology, providing that the unconsolidated powder can be removed through an orifice, design has no limitation due to the tooling. Extremely complex geometries can be created in few hours instead of the days or weeks that are required using traditional processes; however, a trade-off has to be made as the higher the building rate the lower the shape accuracy.

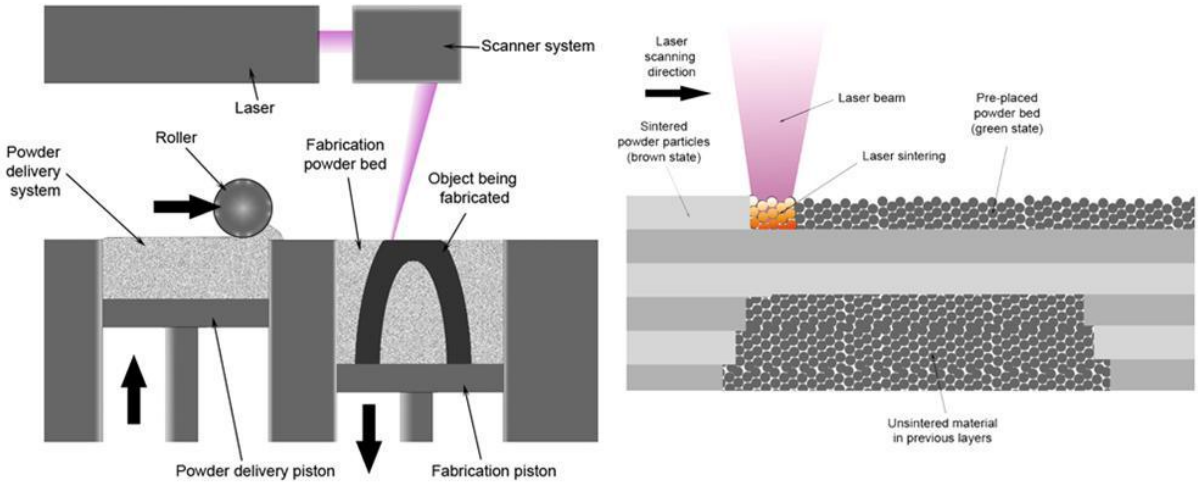

Figure 3.1: SLM process.

Until recently, this technology was restricted to cobalt, chromium, bronze alloys, titanium, etc., but now also commercial aluminium processes are available. The manufactured filters presented in this work, are made from titanium and aluminium alloy (AlSi10Mg). The aluminium alloy is a preferred material because it provides mass reduction, in contrast to other materials. SLM together with other rapid manufacturing technologies are used commonly in medical and orthodontic implants, for tooling, formula 1 parts or jewellery and art design. However, to the author's knowledge, it is the first time SLM is used to manufacture RF filters.

3.2.1 SLM Accuracy Assessment

To assess the geometric accuracy of the manufacturing process, two aluminium samples (sample A and B) taken from the designed filters were first built and cut to take a set of internal dimension measurements, as depicted in Figure 3.2. The mean deviation (MD) and the standard deviation (σ) were calculated employing the measured data and the nominal dimensions of the designed CAD samples as

$$\mathrm{MD} \equiv \frac{1}{N}\sum_{i=1}^{N}|x_i - NV| \tag{3.1}$$

$$\sigma \equiv \sqrt{\frac{1}{N}\sum_{i=1}^{N}(x_i - NV)^2} \tag{3.2}$$

where N is the number of measurements considered, x_i is the value of each sample and NV is the nominal value of the dimension. However, as the process is an additive process, the accuracy might not be the same in each direction. Therefore, these two parameters are measured for every direction.

In Table 3.2, the nominal values of the dimensions of the samples are listed, as well as the numbers of the measurements that correspond to that dimension.

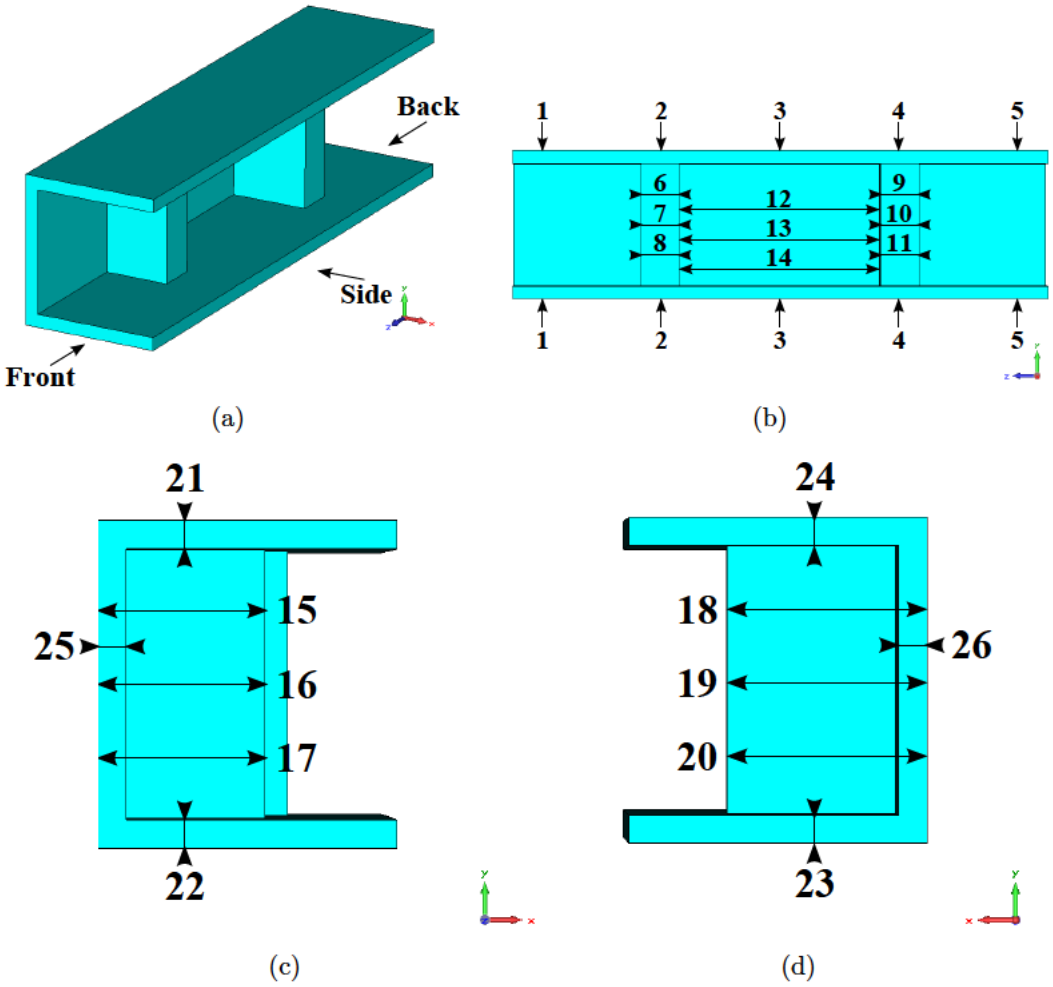

Figure 3.2: Samples views and measurements: (a) perspective view, (b) side view, (c) front view, and (d) back view.

Table 3.2: Nominal dimensions and sample numbers

Dimension	Number	Nominal value (mm)
a = Cavity height + 2 Metal thick.	1, 2, 3, 4, 5	$9.525 + 2 \cdot 1 = 11.525$
b = Iris thick.	6, 7, 8, 9, 10, 11	3
c = Cavity length	12, 13, 14	16.727
d = 1^{st} Iris width + Metal thick.	15, 16, 17	$4.756 + 1 = 5.756$
e = 2^{nd} Iris width + Metal thick.	18, 19, 20	$6.583 + 1 = 7.583$
f = Metal thick.	21, 22, 23, 24, 25, 26	1

Table 3.3 collects the measurements taken from sample A.

The measurements of a second sample (B) are collected in Table 3.4.

For each xyz-direction, the absolute value of the difference between the different physical dimensions measured in the actual xyz-direction and their nominal values are used in the calculation of the mean deviation and the standard deviation. Table 3.5 collects the calculated mean deviation and standard deviation for both samples in the three different dimensions. The calculation of these values is given

Table 3.3: Measurements for sample A

Number	Value (mm)	Number	Value (mm)	Number	Value (mm)
1	11.66	10	3.16	19	7.49
2	11.65	11	3.18	20	7.51
3	11.56	12	16.56	21	1.01
4	11.50	13	16.55	22	1.11
5	11.53	14	16.60	23	1.08
6	3.18	15	5.73	24	1.01
7	2.97	16	5.72	25	0.99
8	3.04	17	5.74	26	0.95
9	3.17	18	7.51		

Table 3.4: Measurements for Sample B

Number	Value (mm)	Number	Value (mm)	Number	Value (mm)
1	11.64	10	3.09	19	7.50
2	11.70	11	3.09	20	7.47
3	11.68	12	16.61	21	1.20
4	11.61	13	16.64	22	1.04
5	11.63	14	16.57	23	1.00
6	3.04	15	5.78	24	1.16
7	3.05	16	5.72	25	1.01
8	3.17	17	5.70	26	0.94
9	3.12	18	7.48		

in detail in Appendix B.

Table 3.5: Accuracy measurements summary

	MD_x (mm)	MD_y (mm)	MD_z (mm)	σ_x (mm)	σ_y (mm)	σ_z (mm)
Sample A	0.0471	0.0594	0.1368	0.0549	0.0778	0.1480
Sample B	0.0606	0.1150	0.1023	0.0698	0.1305	0.1103

The number of measurements that has been taken is not enough to make an exact estimation of the accuracy of this manufacturing technology. However, a rough estimation can be done. The results show that the accuracy of the manufacturing technology depends on the xyz-direction as it is extremely dependent on the growing direction of the prototype.

The same process was also done by the manufacturing company, which used the data to calibrate the manufacturing process with the goal to maximize the manufacturing accuracy.

3.2.2 Measurement of the Surface Roughness

The ESTEC Metrology Laboratory measured the surface roughness (ISO 4287) of four testing filters (Al2, Ti2, Ti3, and Ti4) constructed by Selective Laser Melting (SLM) Technology and one sample manufactured with traditional machining processes. In the following, a summary of the work done on the measurement of the surface roughness is given. The full document can be found in [Tavares, 2009].

A Mitutoyo Surftest SV3000 S/N 200 101 measuring equipment as the one shown in Figure 3.3 has been used for the roughness measurement.

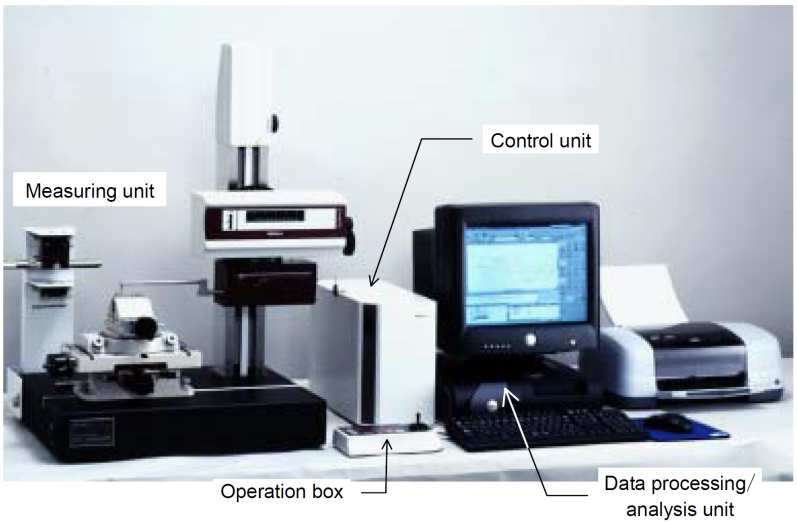

Figure 3.3: Mitutoyo Surftest SV3000 test equipment for the measurement of the surface roughness.

The measurements were taken under the following environmental conditions:

- Clean room class 100000
- Temperature: $19° < T < 21°$
- Relative humidity: $30\% < R.H. < 60\%$

Three parameters have been measured in order to characterize the roughness of the samples under test:

- Ra: mean height of the surface profile (peaks and inverted valleys). Ra is the arithmetic average value of the departure from profile from the center line. So, for any four values, (3.3) applies:

$$Ra = \frac{W + X + Y + Z}{4} \tag{3.3}$$

- Rz: highest peak-to-valley value.

- Rs: root mean square of the surface profile (peaks and inverted valleys). For the same four values in (3.3), Rs can be calculated as (3.4):

$$Rs = \sqrt{\frac{W^2 + X^2 + Y^2 + Z^2}{4}} \tag{3.4}$$

To calculate the previous parameters, measurement paths were randomly taken in the inner part of the filter, in a total of five measurements paths, as shown in Figure 3.4. The average of the five measurements of the roughness parameters (Ra, Rz, and Rs) from each sample is shown in Table 3.6.

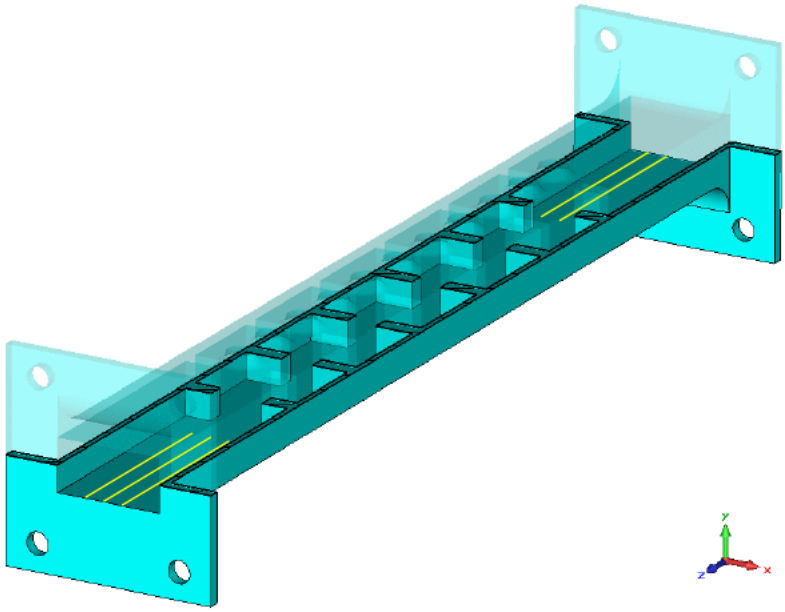

Figure 3.4: Paths were the roughness measurement has been carried out.

Table 3.6: Roughness results of the SLM manufactured filters with a 95% confidence interval

Sample	Ra (μm)	Rz (μm)	RMS = Rs (μm)
Al 1	14.86 ± 4.85	87.58 ± 27.79	19.458
Ti 2	7.14 ± 0.55	48.06 ± 4.57	9.791
Ti 3	8.10 ± 0.30	53.35 ± 4.01	11.833
Ti 4	9.13 ± 1.28	60.31 ± 9.69	12.445
Machined Flange	0.24	2.13	n/a

The surface roughness depends on the grain size of the material powder, as well as on the laser beam width and the rate of the process. It can be noted from Table 3.6 that the surface roughness inherent to the aluminium sample is almost double than the one obtained for the titanium ones. The surface roughness of the machined flange is negligible if compared to any sample manufactured using SLM. The main disadvantage of surface roughness is the inherent increase of loss due to increased material resistivity.

3.3 Filter Measurements

A total of six filters (Table 3.1) have been manufactured in an aluminium alloy (AlSi10Mg) and titanium (grade II). Due to the poor surface roughness inherent to the manufacturing technology, a chemical polishing process has been applied to the filters in set 3. Also, the shaped aluminium filter from set 1 (Al2) has been successfully silver plated by an electroplating process. In addition, tuning was applied where needed in some of the filters, but kept to a minimum. The goal was to measure the ohmic losses of the filters without perturbing them with additional external sources, as it is the case of tuning screws. A picture of the aluminium alloy filter with shaped internal geometry as received from the manufacturer is shown in Figure 3.5.

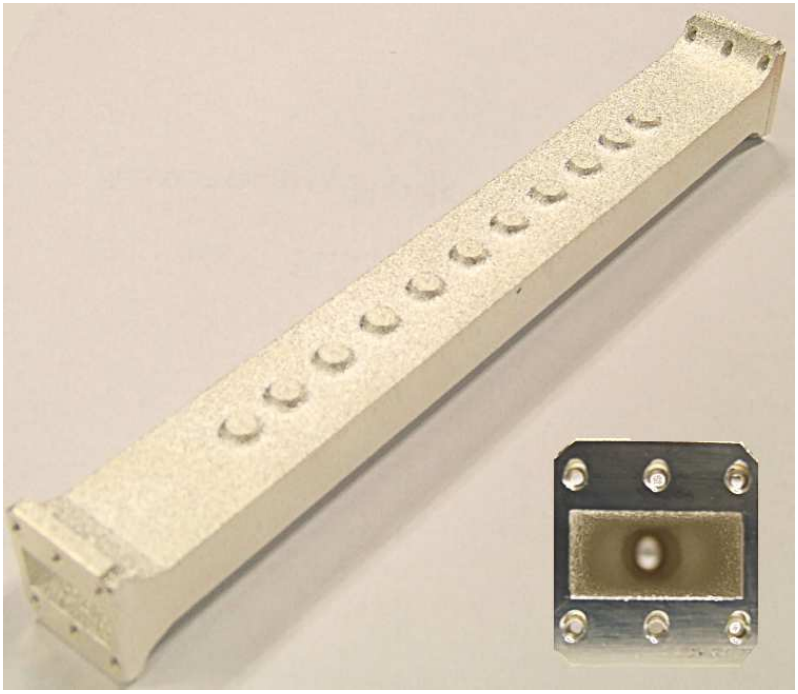

Figure 3.5: Manufactured single piece part aluminum alloy shaped filter as received from the manufacturer.

In the following, the measured responses of the prototypes as received, after the polishing process, after silver plating, and after tuning are presented, when applicable, from Figure 3.6 to Figure 3.16. The Agilent 8722ES Vector Network Analyzer has been used for the measurements. The list of measured filters is shown in Table 3.7.

Simulation results are also presented in the graphs for comparison purposes. The conductivities used in the simulations are listed in Table 3.8. In addition, the surface roughness obtained in section 3.2.2 (Table 3.6) was also included in the simulation of the filters due to the poor surface roughness inherently obtained from the SLM process, which affects the conductivity of the material, thus increasing the losses of the filter.

Table 3.7: List of filters measured

			As received	Tuned	Plated
Set 1	Baseline Aluminium (Al 1)		✓	✓	✗
	Shaped Aluminium (Al 2)		✓	✗	✓
Set 2	Baseline Titanium (Ti 1)		✓	✓	✗
	Shaped Titanium (Ti 2)		✓	✓	✗
Set 3	Baseline Titanium (Ti 3)	Non polished	✓	✗	✗
		Polished	✓	✓	✗
	Shaped Titanium (Ti 4)	Non polished	✓	✗	✗
		Polished	✓	✗	✗

Table 3.8: Conductivities of the materials employed in the simulations

Material	Conductivity (S/m)
AlSi10Mg	16000000
Titanium Grade II	1785714
Silver	61000000

3.3.1 Unmodified Filters

Figure 3.6, Figure 3.7 and Figure 3.8 shows the measured results of the baseline and shaped filters from the three sets as received (no tuning). The response of the baseline filters is almost centered at the desired frequency, but the return loss level is only in the order of 8-12dB. On the other hand, some larger offset from the desired centre frequency than in the baseline filters can be observed in the case of the shaped filters but much better return loss is obtained in comparison to them. Note that the filters were not tuned.

Figure 3.9 shows the surprising repeatability of the Titanium filters from set 2 and set 3 (before polishing). The baseline filter responses are almost identical, whereas the shaped filter responses vary in the order of 6%.

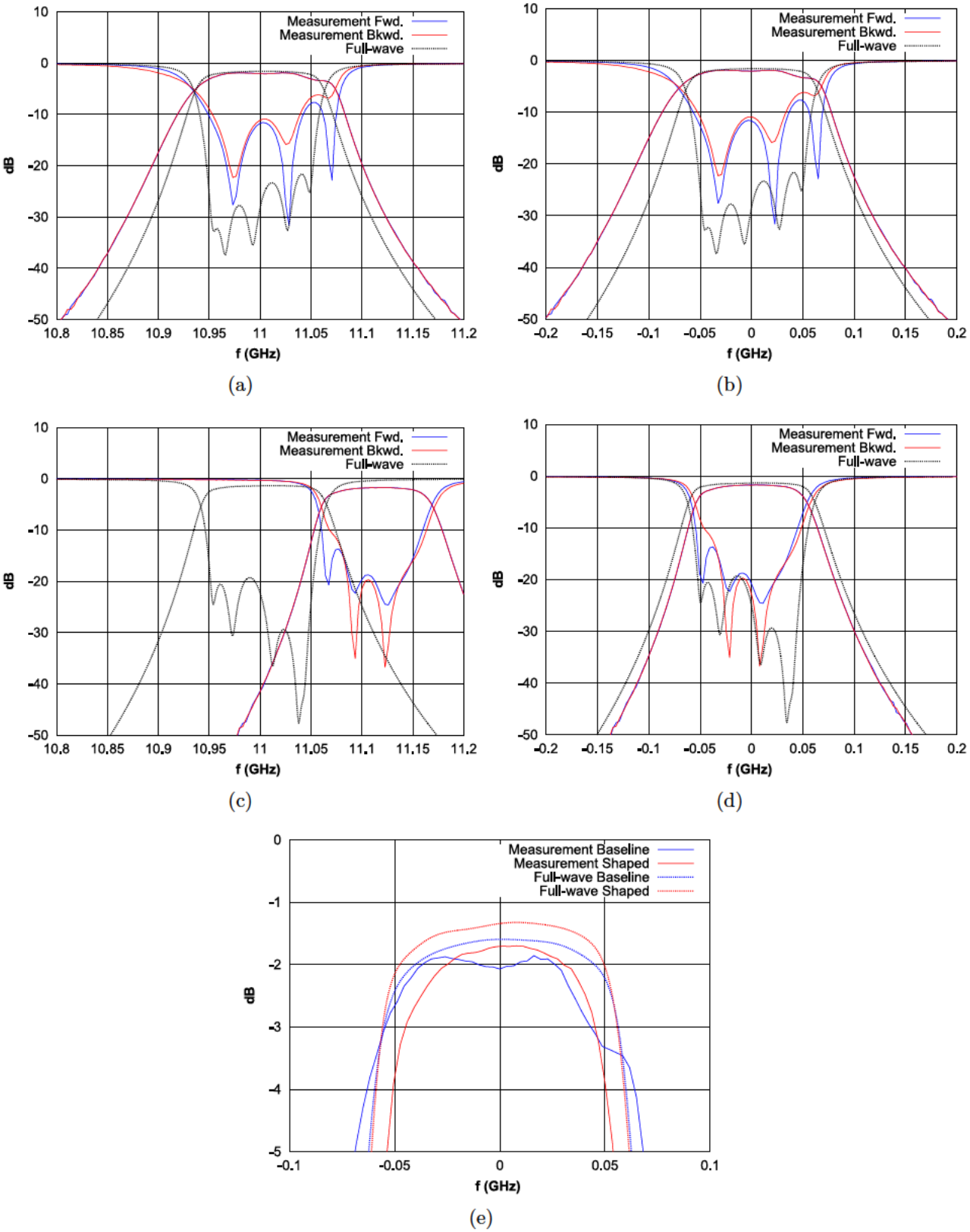

Figure 3.6: Measured RF responses of the set 1 Aluminium (AlSi10Mg) filters as received (no tuning): (a) baseline filer (Al1), (b) baseline filter in a normalized frequency axis, (c) shaped filter (Al2), (d) shaped filter in a normalized frequency axis, and (e) $S_{2,1}$ detail in normalized frequency axis.

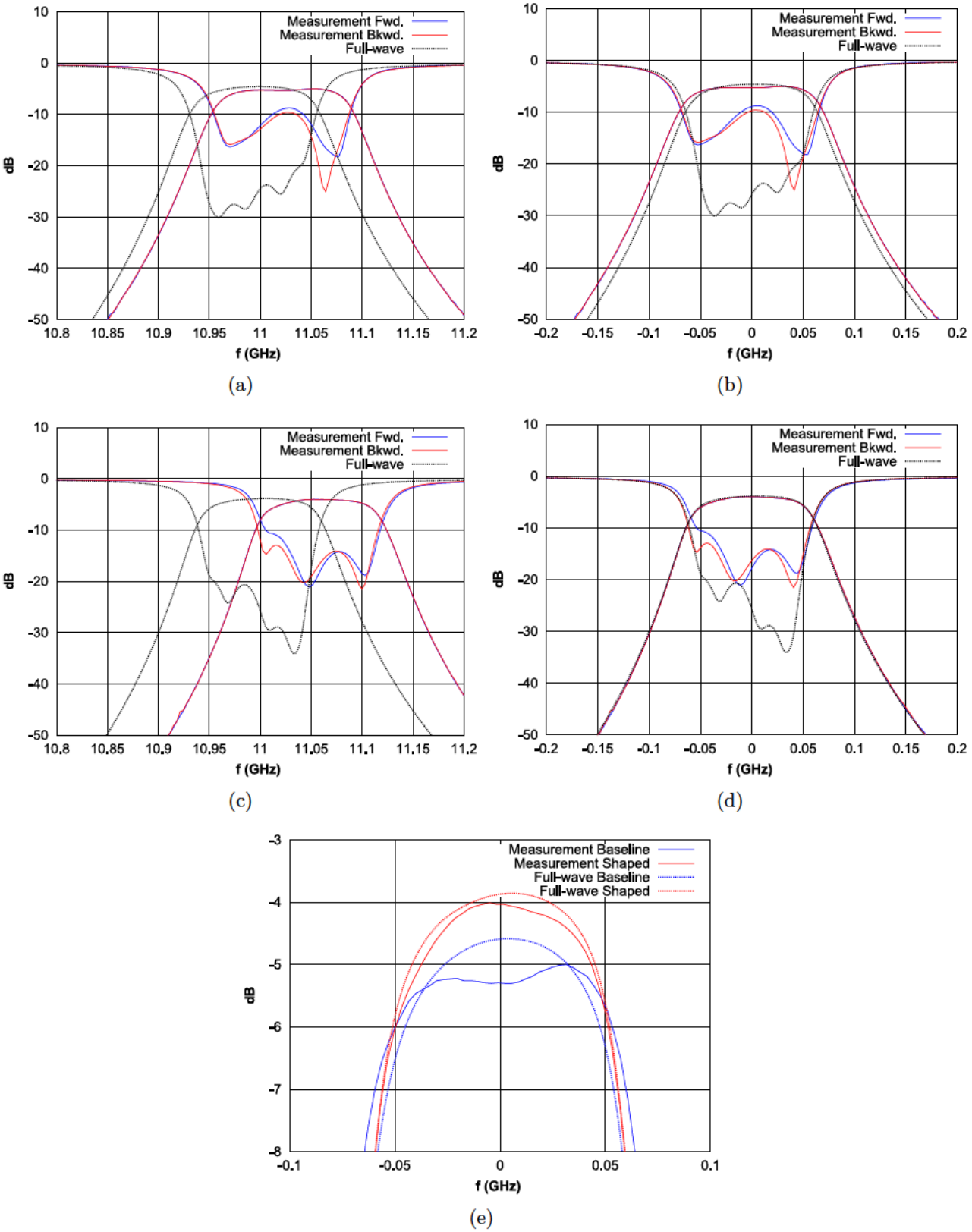

Figure 3.7: Measured RF responses of the set 2 Titanium Grade II filters as received (no tuning): (a) baseline filer (Ti1), (b) baseline filter in a normalized frequency axis, (c) shaped filter (Ti2), (d) shaped filter in a normalized frequency axis, and (e) $S_{2,1}$ detail in normalized frequency axis.

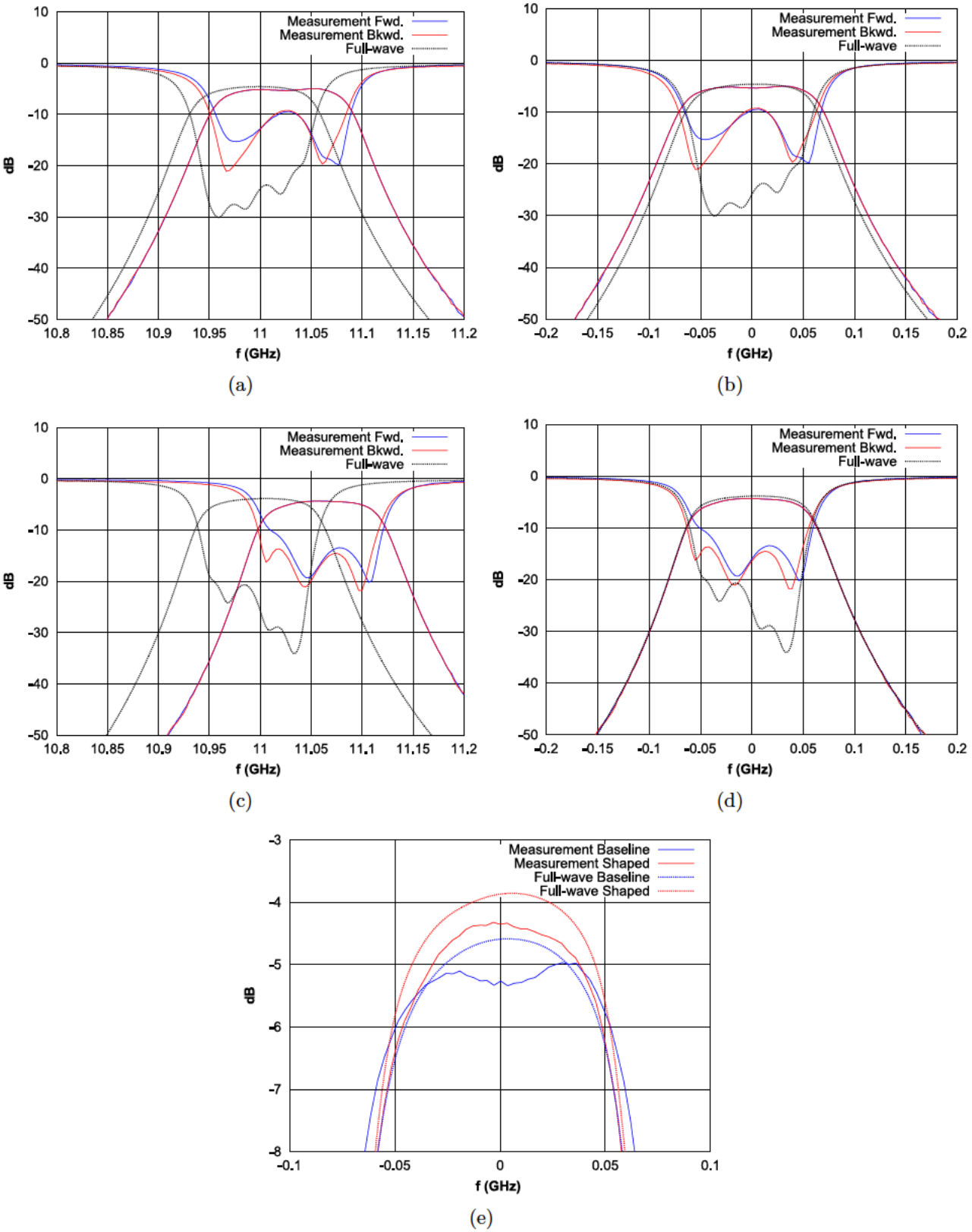

Figure 3.8: Measured RF responses of the set 3 Titanium Grade II filters as received (no tuning): (a) baseline filer (Ti3), (b) baseline filter in a normalized frequency axis, (c) shaped filter (Ti4), (d) shaped filter in a normalized frequency axis, and (e) $S_{2,1}$ detail in normalized frequency axis.

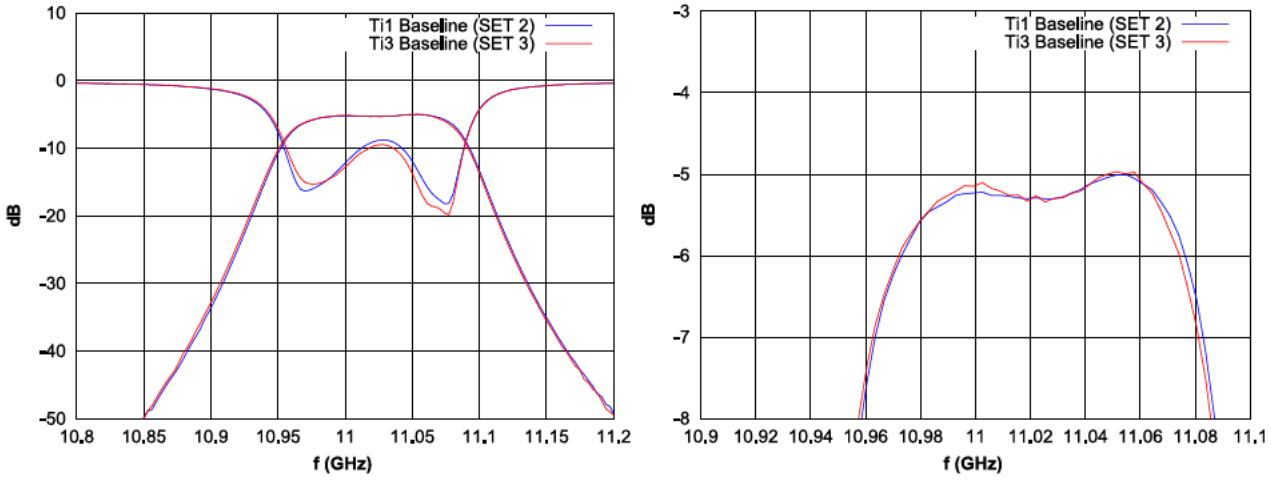

(a)

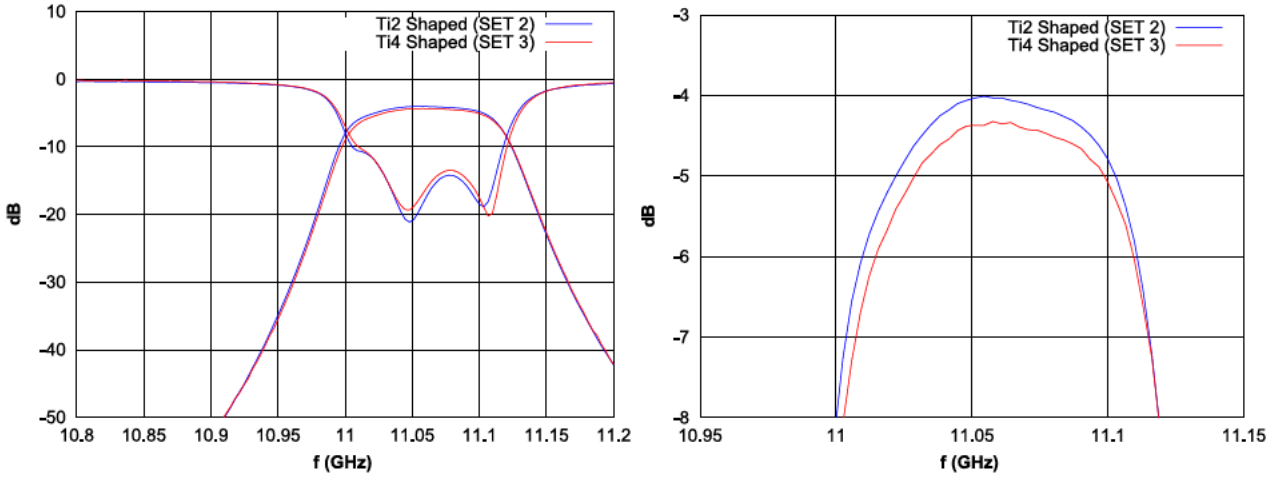

(b)

Figure 3.9: Repeatability between set 2 and set 3: a) baseline filters and b) shaped filters.

3.3.2 Surface-Treated Filters

A chemical polish process was applied to a baseline and a shaped titanium filter (Ti3 and Ti4) from set 3. The results are shown in Figure 3.10. Figure 3.10(a) and Figure 3.10(b) show the RF response of the both baseline and shaped filters, respectively. In Figure 3.10(c), an $S_{2,1}$ detail of both filters before and after applying the chemical polishing process is shown. Note that the insertion loss is largely reduced in both cases. Figure 3.10(d) shows the $S_{2,1}$ variation of both filters before and after applying the chemical polishing process. In comparison to the titanium filters as received, the polished filters have a wider bandwidth, a lower centre frequency and lower insertion losses (about 40% lower), as can be seen in Table 3.9. Hence, it can be inferred that the polish process not only decreased the surface roughness but also increased the internal dimensions of the filters, thus widening the bandwidth and down-shifting the center frequency. As a result of this, also insertion loss must improve. Therefore, a comparison between the losses of the filters before and after applying the polish process is not feasible. Simulation results are not included as the internal dimensions of the filters after the polish process are unknown.

Table 3.9: Bandwidth, center frequency, and insertion loss of filters Ti3 and Ti4 before and after chemical polishing

Filter	3dB BW (MHz)	f_0 (GHz)	IL (dB)
Baseline (Ti3)	128.5	11.022	5.26
Baseline polished (Ti3)	150.8	10.973	3.36
Shaped (Ti4)	111.3	11.061	4.35
Shaped polished (Ti4)	130.5	11.022	2.27

The shaped aluminium alloy filter (Al2) was silver-plated. The measured response of the filter after the plating process is shown in Figure 3.11(a) together with simulation results. Figure 3.11(c) shows the absolute $S_{2,1}$ of the shaped filter before and after applying the silver plating process and simulation results. The $S_{2,1}$ variation is shown in Figure 3.11(d). As expected, the insertion losses of the filter improved significantly since the conductivity of silver is higher than the conductivity of aluminium. It can also be noted that the bandwidth of the filter barely changed and that the center frequency slightly shifted up, as expected (see Table 3.10). Thus, it can be said that the silver plating process has been successfully completed for an aluminium filter.

Table 3.10: Bandwidth, center frequency, and insertion loss of filter Al2 before and after silver plating

Filter	3dB BW (MHz)	f_0 (GHz)	IL (dB)
Shaped (Al2)	106.6	11.115	1.71
Shaped plated (Al2)	108.9	11.123	0.57

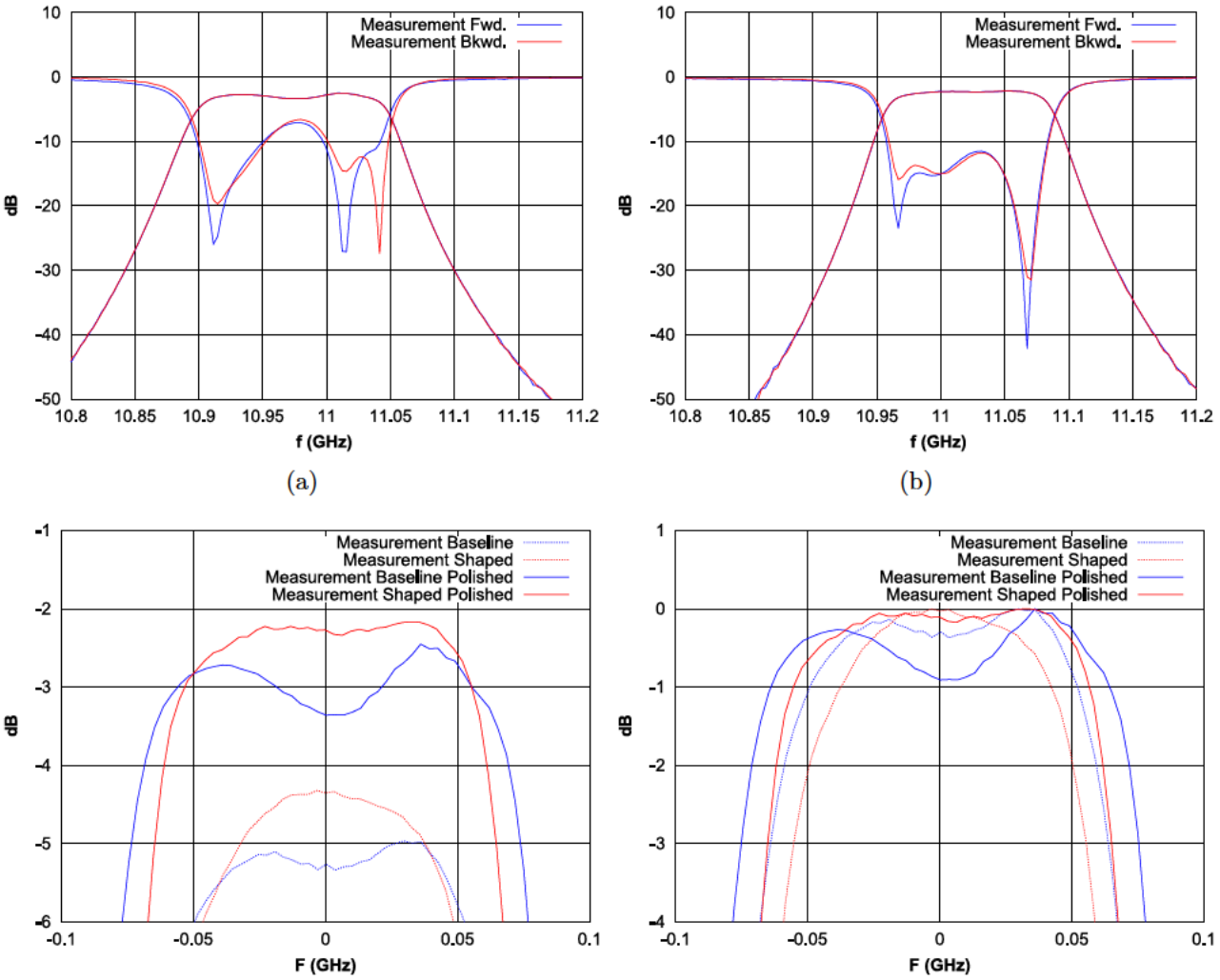

Figure 3.10: Measured RF responses of the set 3 Titanium Grade II filters after a chemical polish process (no tuning): (a) baseline filer (Ti3), (b) shaped filter (Ti4), (c) $S_{2,1}$ detail in normalized frequency axis including baseline (Ti3) and shaped (Ti4) filters before and after polishing, and (d) $S_{2,1}$ variation detail in normalized frequency axis including baseline (Ti3) and shaped (Ti4) filters before and after polishing.

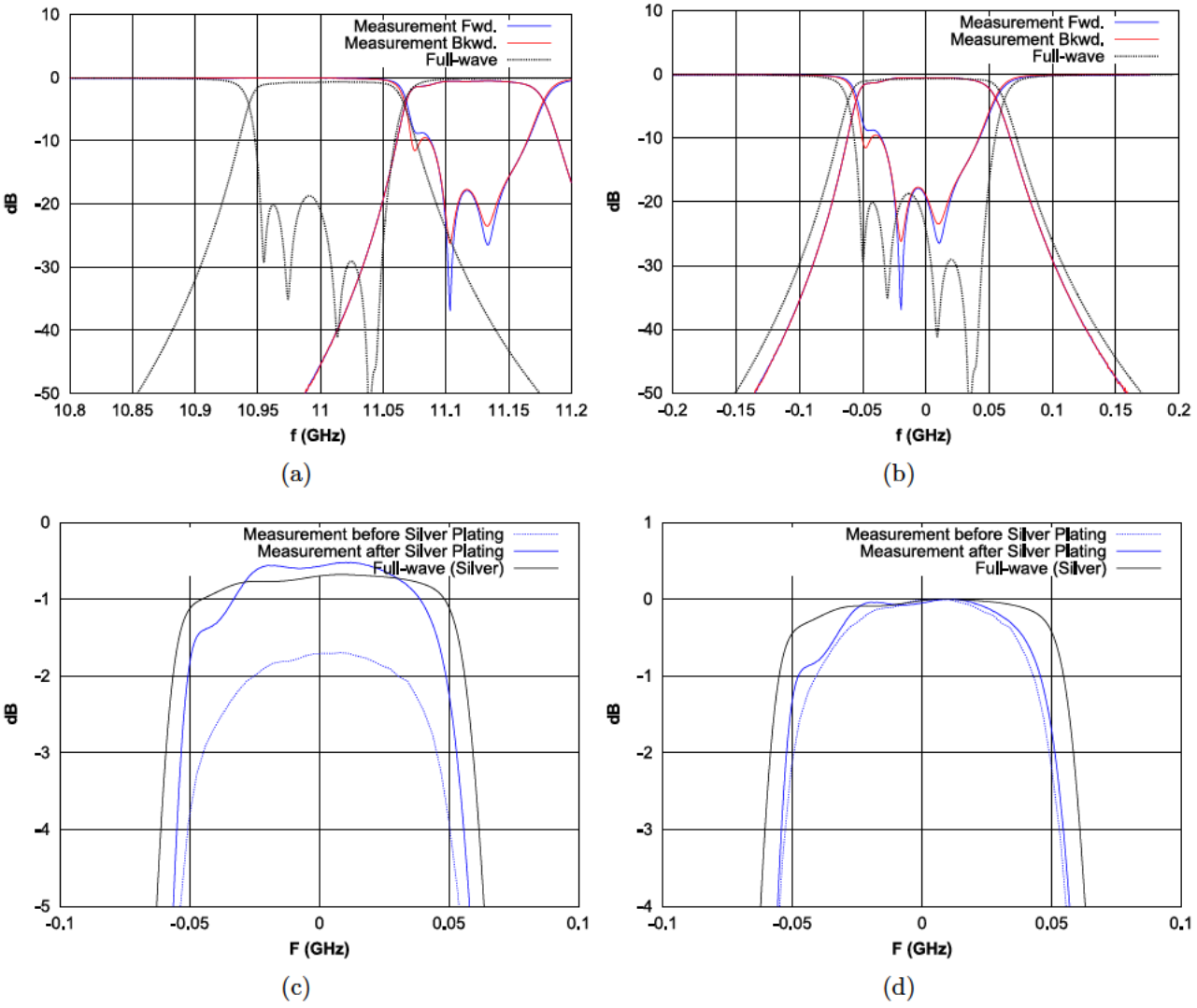

Figure 3.11: (a) Measured RF response of the set 1 Aluminium (AlSi10Mg) shaped filter (Al2) after a silver plating process (no tuning), (b) in normalized frequency axis, (c) $S_{2,1}$ detail in normalized frequency axis including shaped filter (Al2) before and after silver plating, and (d) $S_{2,1}$ variation detail in normalized frequency axis including shaped filter (Al2) before and after silver plating.

3.3.3 Tuned Filters

Only the cavities of the filters were tuned. Goal was to obtain good return loss with minimum tuning effort and then to extract the effective filter resonator Q. Hence, no effort was undertaken to tune the filters to the desired centre frequency or adjust the bandwidth with additional coupling screws.

Measured results of the tuned filters are shown in the next figures. In Figure 3.12 the measured response of the aluminium baseline filter (Al1) is presented, together with a detailed view of its $S_{2,1}$. Figure 3.13 and Figure 3.14 show the response of the titanium baseline filter (Ti1) and the shaped filter (Ti2), respectively. After the tuning process, the insertion losses of the measured responses showed a better agreement with the simulated results. Even better agreement could have been achieved if also the bandwidth of the filters had been tuned (couplings). Moreover, return losses better than 20 dB were achieved.

Finally, Figure 3.15 depicts the measured response of the titanium baseline filter (Ti3) after the polish process and an $S_{2,1}$ detail. Again, simulated results are not included for comparisons since the internal dimensions of the polished filter are unknown.

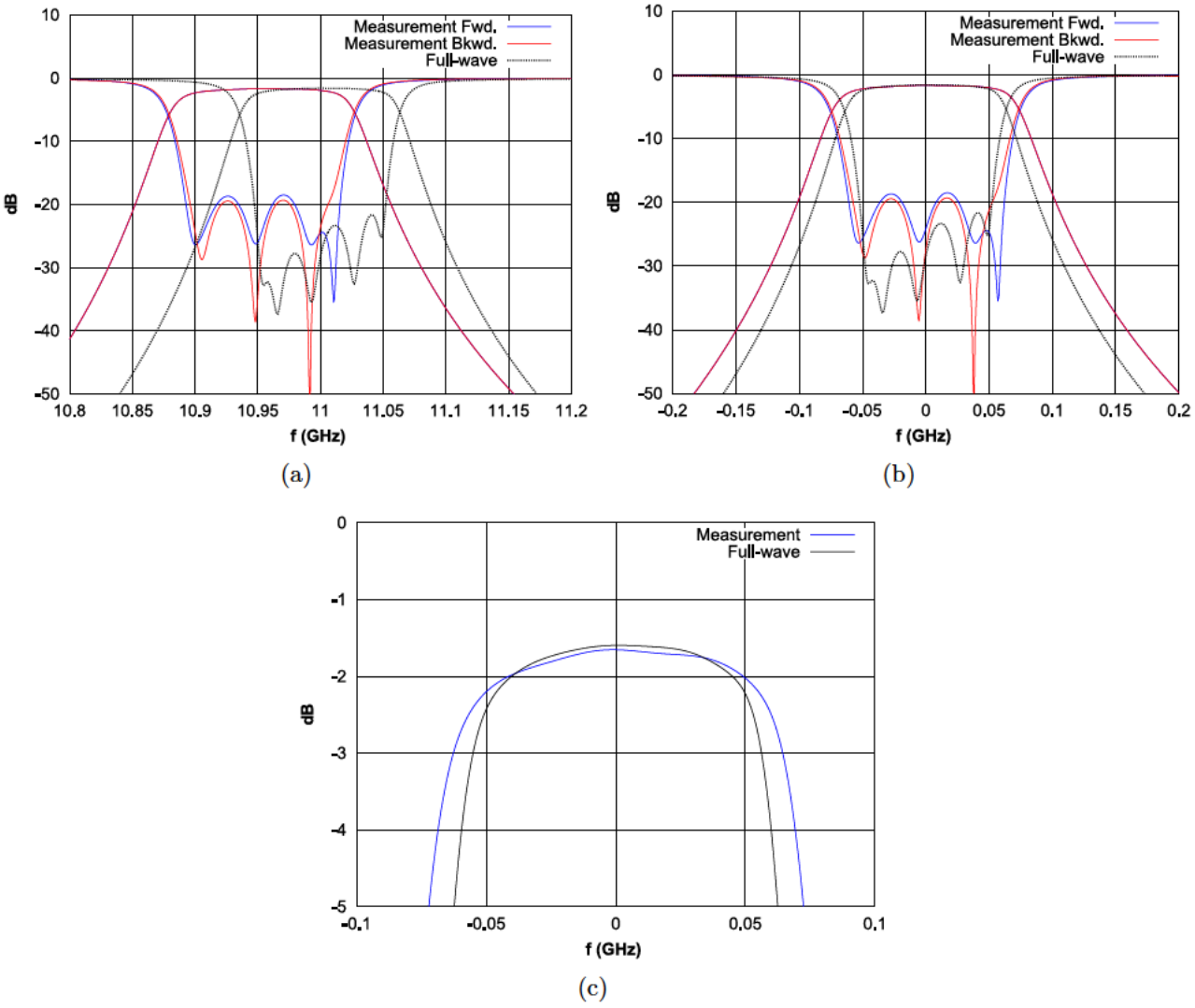

Figure 3.12: (a) Measured RF response of the set 1 Aluminium (AlSi10Mg) baseline filter (Al1) after minimal tuning of the resonators, (b) in normalized frequency axis, and (c) $S_{2,1}$ detail in normalized frequency axis.

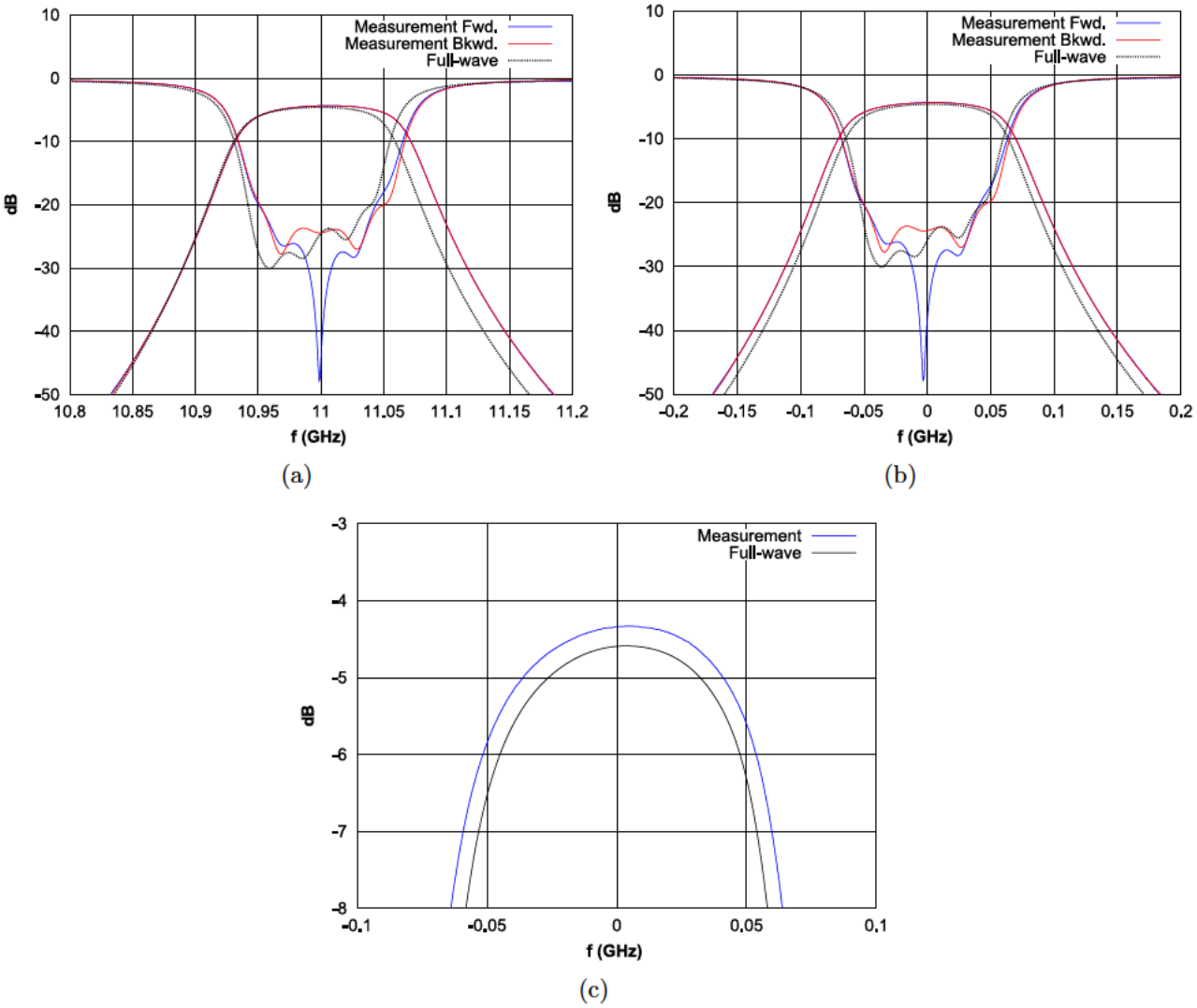

Figure 3.13: (a) Measured RF response of the set 2 Titanium Grade II baseline filter (Ti1) after minimal tuning of the resonators, (b) in normalized frequency axis, and (c) $S_{2,1}$ detail in normalized frequency axis.

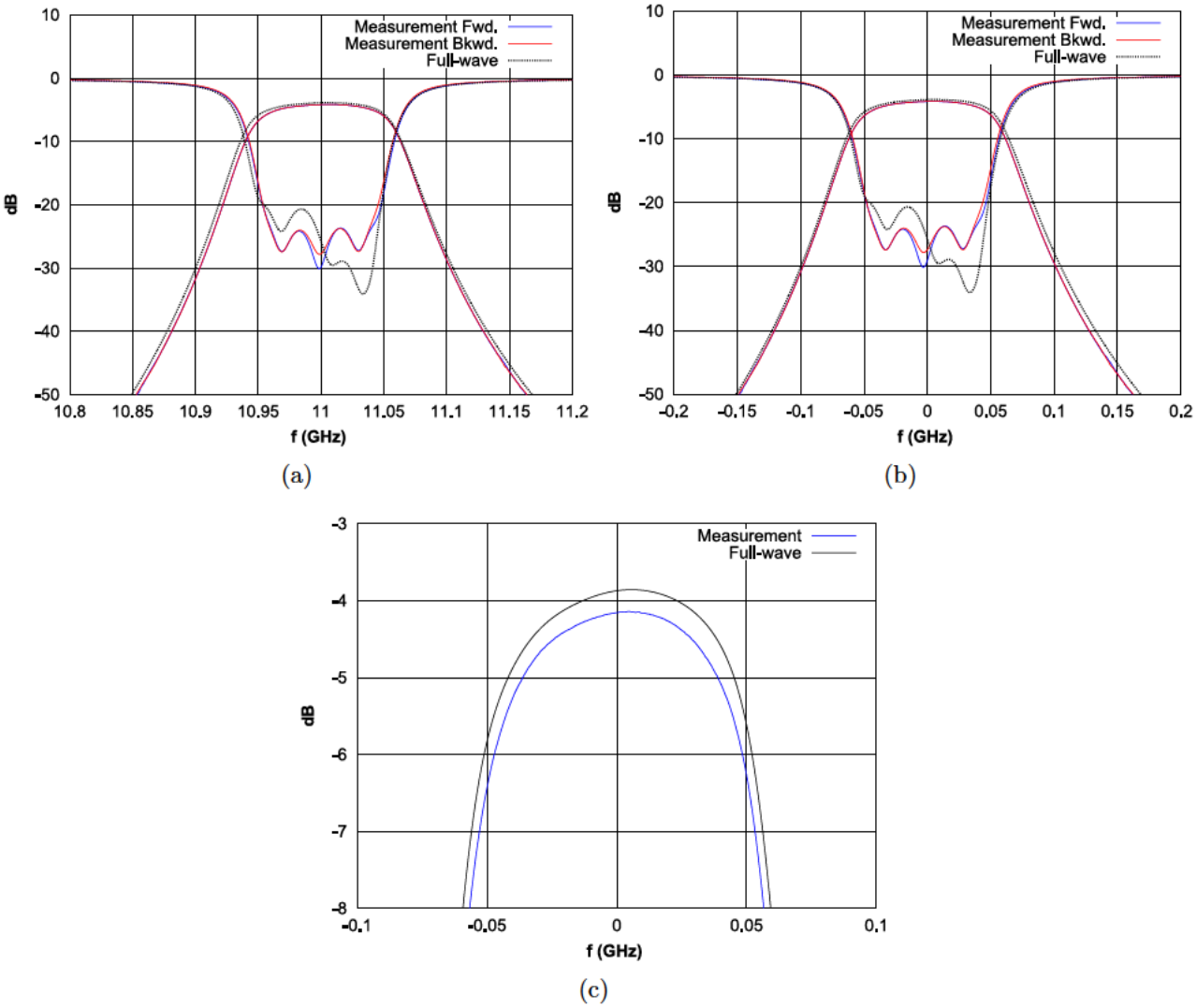

Figure 3.14: (a) Measured RF response of the set 2 Titanium Grade II shaped filter (Ti2) after minimal tuning of the resonators, (b) in normalized frequency axis, and (c) $S_{2,1}$ detail in normalized frequency axis.

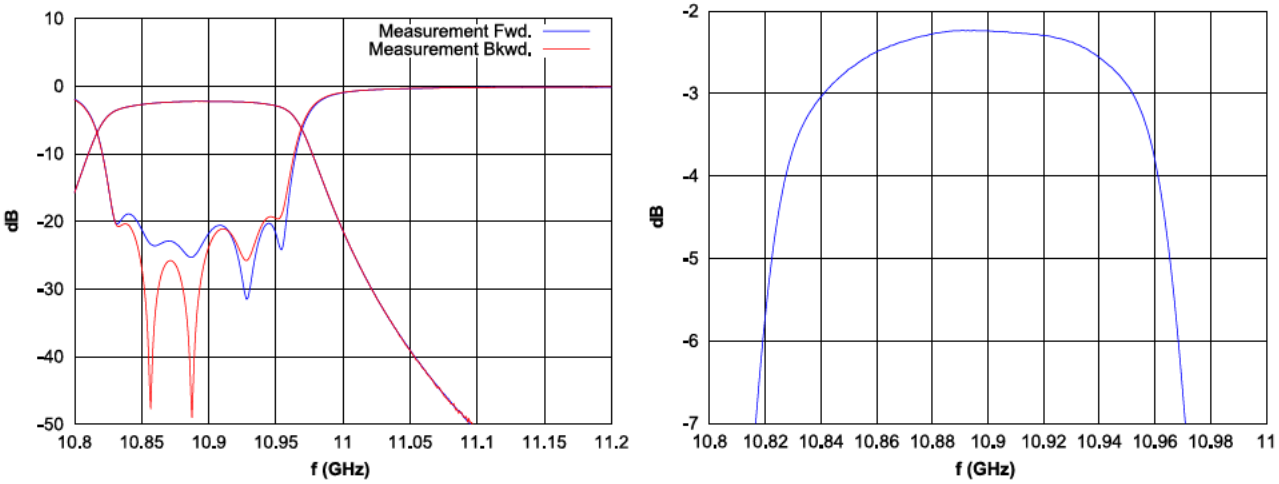

(a) (b)

Figure 3.15: (a) Measured RF response of the set 3 Titanium Grade II baseline filter (Ti3) after a chemical polish process and minimal tuning of the resonators, and (b) $S_{2,1}$ detail.

3.3.4 Out-of-Band Response

Out-of-band measurements have been taken from some of the manufactured filters and the results are shown in Figure 3.16. Figure 3.16(a) depicts the out-of-band response of the baseline filters and Figure 3.16(b) depicts the results of the shaped filters. The measurements prove the results obtained by simulations. On the one hand, a range free of spurious of around 55% is obtained with the baseline filters. On the other hand, a range free of spurious of approximately 47% is obtained with the shaped filters.

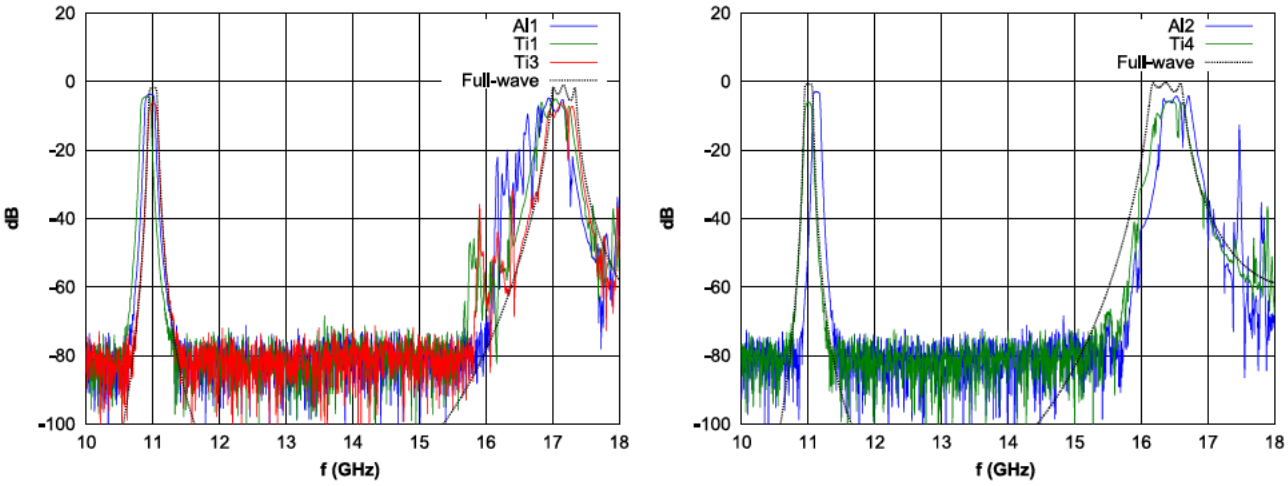

(a) (b)

Figure 3.16: (a) Measured out-of-Band RF performance of the baseline filters and (b) the shaped filters.

3.4 Sensitivity Comparison of Designed Filters

3.4.1 Yield Analysis

A yield analysis to find the sensitivity of the manufactured filters has been performed. A tolerance value of $\pm 20\ \mu m$ was estimated by the manufacturer for the fabrication process after a calibration of the machine.

For the baseline design, a yield analysis using *Mician µWave Wizard* has been performed and the result is shown in Figure 3.17. Poor return loss variations in the order of 10dB and frequency shifts of about $f = f_0 \pm 75\ MHz$ are obtained.

In the case of the shaped filter, a yield analysis using *Mician µWave Wizard* was not feasible since the geometry optimized shapes cannot be modeled using this software. Therefore, a statistical analysis with gaussian distribution using *HFSS* was performed. The tolerance value ($\sigma = 20\ \mu m$) has been used as standard deviation and the nominal values of the dimensions were taken as the mean values of the distribution. Since *HFSS* is a full wave EM software based on the finite element method, only a few iterations have been carried out due to the long simulation time (Figure 3.18).

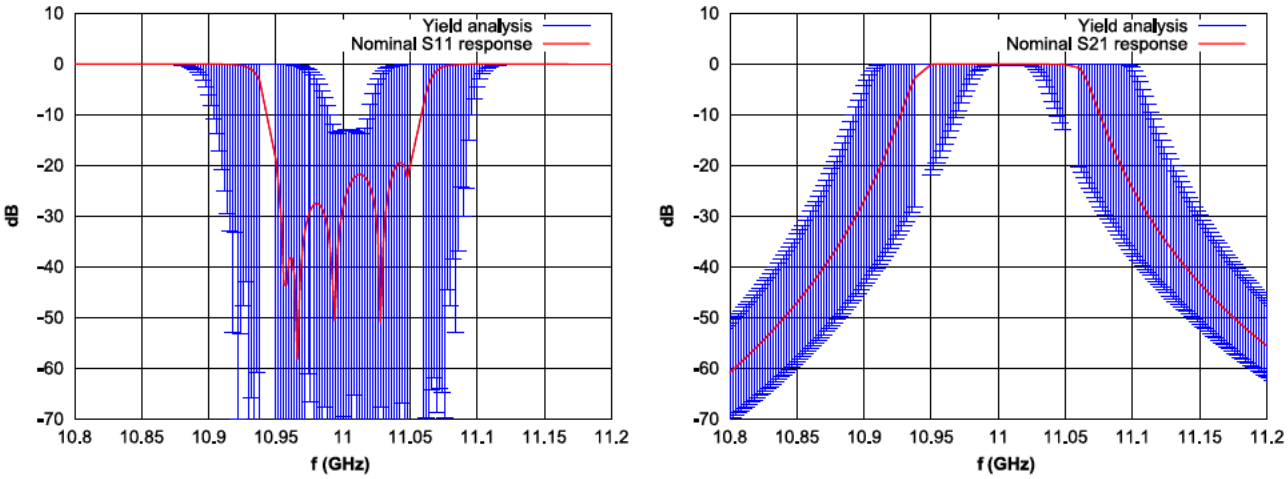

(a) (b)

Figure 3.17: Baseline filter yield analysis using Mician μWave Wizard: (a) S11 response, and (b) S21 response.

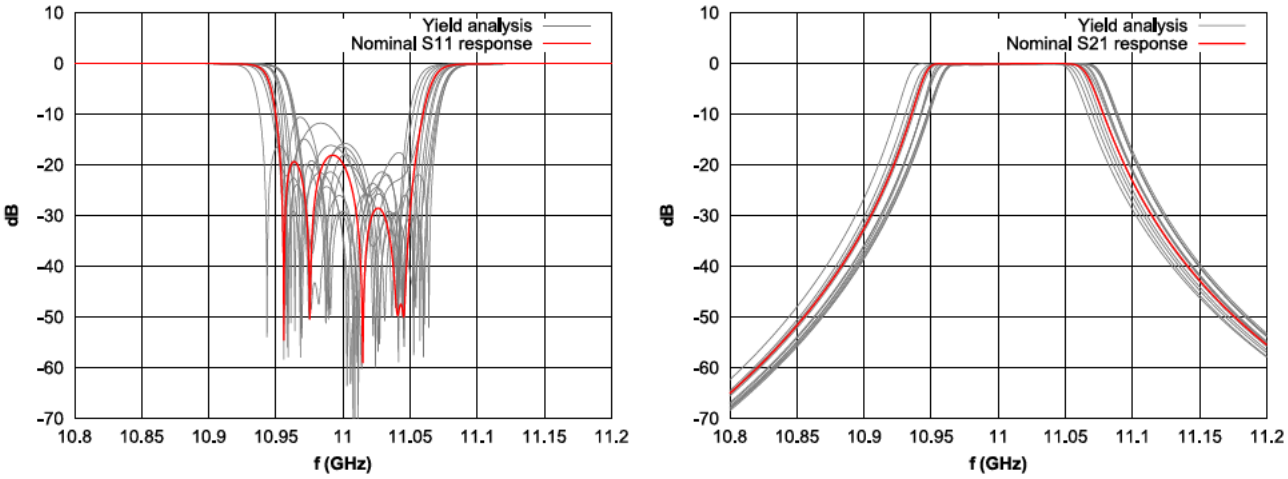

(a) (b)

Figure 3.18: Shaped filter yield analysis using Ansoft HFSS: (a) S11 response, and (b) S21 response.

Good results are found for the shaped filters. A lower frequency shift than in the baseline filter of around $f = f_0 \pm 30\ MHz$ and return loss values in the order of 15dB are obtained.

3.4.2 Conclusion

It can be noted that lower sensitivity to tolerance values is obtained for the shaped filter. This observation can be explained keeping in mind that several parameters affect the sensitivity of a filter: such as the filter transfer function and topology, and thus the stored energy as stated in [Mendoza et al., 2012], and the filter own geometry. In the example that is being treated here, the transfer function and filter

topology (hence the stored energy) are all the same and therefore the reduction in sensitivity observed for the shaped filter is essentially driven by the geometry optimization. A tolerance of $\pm 20\ \mu m$ in the baseline filter will definitely strongly affect mostly one parameter (cutoff frequency, resonant frequency, or coupling coefficient) due to the clear separation between resonators and coupling structures. The previous tolerance yields to a larger degradation than that obtained in a shaped filter where the continuous interface between cavities and irises causes that the same tolerance value affects all the mentioned parameters in a more distributed fashion.

On the other hand, a large frequency deviation of around 120 *MHz* was measured in the shaped filter prototype, although the filter response agreed better with simulations in terms of bandwidth and return loss than that of the baseline filter. Note that the manufacturing company did not calibrate the machine for this geometry.

3.5 Effective Filter Resonator Q

3.5.1 Q Extraction from Measured Data by Curve Fitting using Lumped Element Circuits

The measured insertion loss of the fabricated filters could not be easily compared one against another as the filter responses did not match each other due to manufacturing tolerances. To carry out the loss comparison, a more independent parameter on the filter response was used: the effective filter resonator Q. This parameter is defined as the ratio of the total stored energy of the filter to the total power loss, at the filter center frequency. In order to calculate it, use has been made of the *Agilent Advanced Design System* simulation tool. A fifth degree lumped-element filter composed of parallel RLC circuits and lossless admittance inverters has been designed with this software. The goal was to fine tune the different parameters of the circuit to match the desired S-parameter response: the response of the filter whose effective filter resonator Q is to be calculated. The parameters to tune were as follows:

- The resonant frequency of each single resonator, f_{0i}.
- The bandwidth of the final filter, BW.
- Each admittance inverter value, J_i.
- The Q of the resonators (same Q for all of them).

When a matched response is obtained, the Q of the resonators is then extracted from the equivalent circuit. It is assumed that all resonators have the same loaded Q and losses only occur in the resonators and not in the couplings. The so obtained Q in the equivalent circuit will be referred to as the effective filter resonator Q of a prototype (Q_{eff}). Figure 3.19 shows a flowchart summarizing the process. An example of a matched response is also depicted. The rest of the matched responses are included in Appendix C.

It will be shown in Section 4.4 that lossy couplings degrade the filter insertion loss and produce an asymmetry on the filter response. However, in this case, losses due to coupling structures are absorbed into the resonators, thus maintaining the

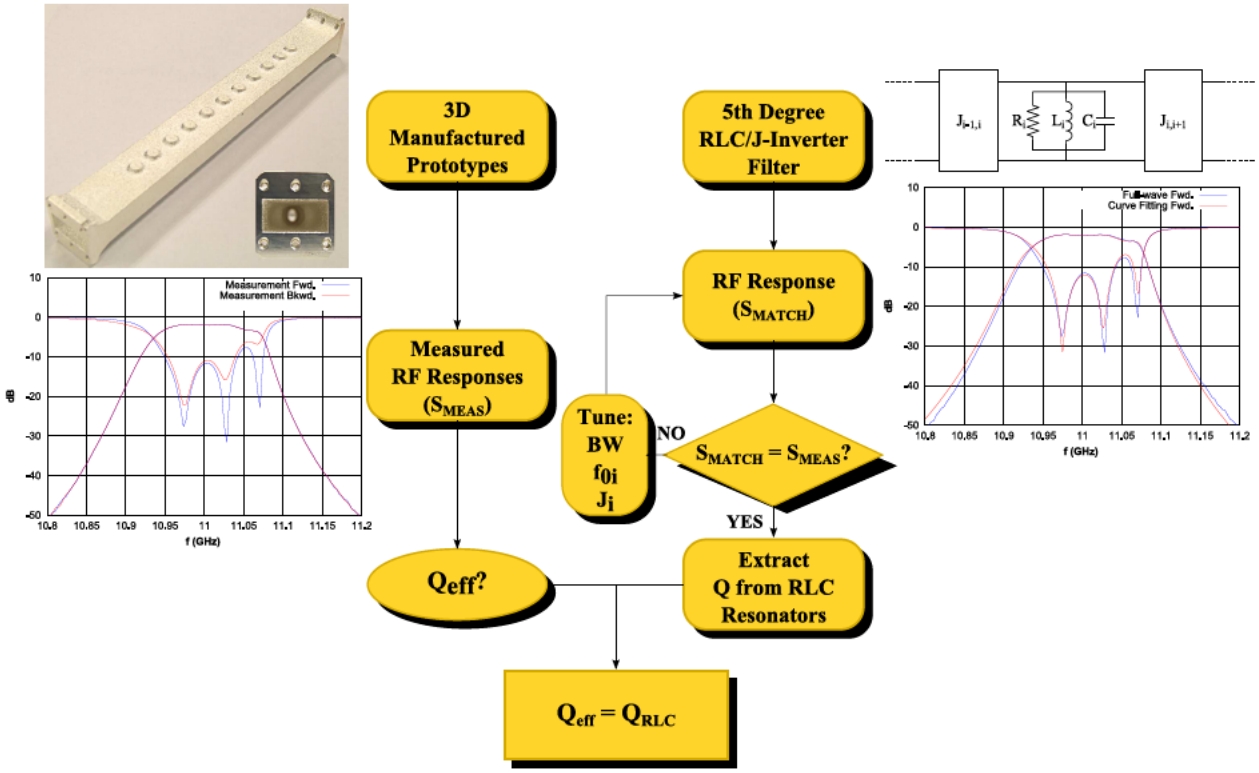

Figure 3.19: Block diagram of the tuning approach to extract the effective filter resonator Q of the filters.

correct insertion loss at center frequency although the final response will not have the above mentioned asymmetry. The effective filter resonator Q is only calculated at the center frequency.

The theoretical unloaded resonator Q as well as the measured and predicted effective filter resonator Q from full-wave simulations are listed in Table 3.11. Great care was taken in conducting precise measurements. The uncertainty of the Q values of the unplated aluminium and titanium filters has been conservatively estimated to be better than 5%. Uncertainties are mainly due to difficulties in accurately matching the filter response to a circuit network. The conductivities of the materials used in the simulations are given in Table 3.8.

Good agreement between the measured Q-factors and the predicted Q-factors from the simulations is obtained. Besides, it is interesting to observe that the shaped filters (Al2, Ti2, Ti4) have an improved effective filter resonator Q at least in the order of 15% over the baseline filters (Al1, Ti1, Ti3) taking into consideration a conservative measurement uncertainty. However for the untreated hardware as received, only around 40%-50% of the theoretical unloaded Q is obtained from the SLM process, in contrast to 50%-80% that could be achieved using traditional processes. This can be explained by the poor surface roughness inherently obtained from the process.

To address this problem, two further experiments were carried out. A chemical polish process was applied to a baseline and a shaped titanium filter (Ti3 and Ti4) and the effective filter resonator Q is also reported in Table 3.11. After polishing, at least 75% of the theoretical unloaded Q is obtained. In the second experiment,

Table 3.11: Extracted effective filter resonator Q by curve fitting using lumped element circuits

		Resonator* HFSS Q_u	Filter* HFSS Q_{eff}	Filter** HFSS Q_{eff}	Measured Filter As received Q_{eff}	Measured Filter Tuned Q_{eff}
SET 1	Al1 (AlSi10MG)	3995	3400	1740	1380	1400
	Al2 (AlSi10MG)	4633	4400	2200	1790	–
	Al2 (Ag Plated)	9050	8500	4290	6300	–
SET 2	Ti1 (Ti Grade II)	1335	1155	590	560	580
	Ti2 (Ti Grade II)	1549	1470	750	680	700
SET 3	Ti3 (Ti Grade II)	1335	1155	590	570	–
	Ti4 (Ti Grade II)	1549	1470	750	720	–
	Ti3 (Ti Polished)	1335	1155	***	1070	1030
	Ti4 (Ti Polished)	1549	1470	***	1320	–

*No roughness **Roughness as in Table 3.6 ***Roughness not known

the shaped aluminium alloy filter (Al2) was silver-plated. Again the effective filter resonator Q was extracted and is reported in Table 3.11. In this case around 70% of the theoretical unloaded Q is obtained. The results were confirmed by an independent laboratory measurement to within 3%.

3.5.2 Q Extraction from Measured Data using the Modified Cauchy Method

Another method has been used to extract the effective filter resonator Q from the measured data of the manufactured SLM filters and was compared to the first extracted effective filter resonator Q factor based on curve fitting. This method introduces a modification over the Cauchy Method so that losses can be taken into account.

This method was first developed to extract the coupling coefficients from the measured S-parameters of a low loss, cross coupled filter with a known topology. Later modifications allowed taking losses into account, [Macchiarella and Traina, 2006] and [Traina et al., 2007]. A further modification that allows a good accuracy even with large losses (several dBs) has been introduced in [Macchiarella, 2010]. In fraction of seconds, this method is able to extract the coupling coefficients and the external Q-factors of the measured data once the number of resonators and the number of transmission zeros (for cross coupling filters) are defined. By specifying the same unloaded Q for all the resonators, the final effective filter resonator Q can be found by comparing the measured S-parameters with the simulated ones.

Table 3.12 shows the extracted effective filter resonator Q that has been obtained using the modified Cauchy method. Very good agreement is observed in comparison to the previous approach with a maximum difference of 6%. It is remarkable that the values of the extracted Q-factors by curve fitting are, in general, lower than those obtained using the modified Cauchy method. This is due to the conservative

Table 3.12: Extracted effective filter resonator Q using the modified Cauchy method

		Resonator*	Measured Filter	
		HFSS	As received	Tuned
		Q_u	Q_{eff}	Q_{eff}
SET 1	Al1 (AlSi10MG)	3995	1400	1440
	Al2 (AlSi10MG)	4633	1900	–
	Al2 (Ag Plated)	9050	6500	–
SET 2	Ti1 (Ti Grade II)	1335	580	590
	Ti2 (Ti Grade II)	1549	720	715
SET 3	Ti3 (Ti Polished)	1335	1060	–
	Ti4 (Ti Polished)	1549	1400	–

*No roughness

position adopted in the Q extraction using the first method. Appendix C collects all the figures comparing the measured responses with those obtained using this method.

3.6 Conclusion

Selective Laser Melting (SLM) is an additive technology which has already been successfully used in the medical field or the tooling industry. In this work, SLM is tested for a completely new purpose: the manufacturing of microwave filters for RF applications.

A new structure improving the insertion losses of a fifth degree rectangular cross section filter with rectangular irises was designed in [Zafra, 2007]: a fifth degree shaped cross section filter with parabolic irises. The predicted improvement achieved in the simulations was about 16%. To confirm this enhancement, three sets of filters were manufactured using SLM. Excellent results in terms of effective filter resonator Q and impressive geometry accuracy have been obtained with this single piece part construction. Besides, a chemical polish process and a silver plating process have been successfully proved to improve the effective filter resonator Q.

This effective filter resonator Q has been extracted using two different methods: by curve fitting using lumped element circuits and by using the modified Cauchy method. Both of them agree very well with a maximum deviation of 6%.

It can be concluded that the application of the SLM technology for RF component manufacturing is very promising, since it offers potential for single piece part manufacturing of new complex geometries.

CHAPTER 4

SYSTEMATIC DERIVATION OF LOSSY EQUIVALENT CIRCUIT FOR NARROW-BAND WAVEGUIDE DIRECT-COUPLED-CAVITY FILTERS

In this chapter, a new technique to rigorously derive a complete lossy equivalent circuit of narrow-band direct-coupled-cavity filters with constant arbitrary cross section and arbitrary coupling geometries is presented. Traditionally, only dissipation loss and stored energy due to closed unperturbed cavities have been taken into account in the design of complete filters and the loss contribution due to coupling structures has been neglected. An additional challenge is the non-trivial discrimination of cavities and couplings in a direct-coupled-cavity filter. With the proposed circuit, the contribution of the coupling structures to the total dissipated power and total stored energy of the filter can be derived and a clear separation between resonators and couplings is established. The technique developed uses the even and odd mode theory to successfully derive lossy equivalent circuits for inter-cavity couplings. The lossy circuit of external (input/output) couplings is also derived. A fifth degree direct-coupled-cavity filter has been designed, simulated and manufactured. Its lossy equivalent circuit has been extracted and comparisons with simulations and measurements show excellent agreement. Applications of the novel equivalent circuit in the prediction of losses in waveguide filters and in yield analyses are also illustrated.

4.1 Introduction

Today most demanding applications require very stringent loss specifications in the design of microwave filters. Due to their low dissipation loss and high power handling capability, microwave waveguide cavity filters are widely used in many applications. Hence, an accurate and fast loss prediction of a filter can be decisive when very tight specifications are to be satisfied. To do so, an accurate circuit model that completely characterizes a direct-coupled-cavity filter including losses due to resonators and

coupling elements is derived in this chapter.

The broad number of publications presented for the derivation [Cohn, 1957], [Ernyei, 1983], [Sengul, 2009] or use of equivalent circuits for microwave filters [Amari, 2000], [Kahrizi et al., 2002] confirms the importance of deriving an accurate network representation for this kind of structures. The applications that require the use of equivalent circuits are diverse and include the derivation of expressions for the sensitivity of coupled resonator filters [Amari, 2000] or the derivation of methods for the tuning of RF microwave filters [Kahrizi et al., 2002], among others.

Most of the previous work centered their research on lossless filters. This is not the case in [Lee and Tsai, 2008], where they already developed a network where losses due to resonators and coupling structures were taken into account. However, the approach they followed requires $m = 2n$ simulations of the complete nth-order filter structure to derive a Vandermonde matrix, which is often ill-conditioned and, if the number of points are increased, its resolution could be problematic.

The new approach presented in this work overcomes these difficulties by a proper segmentation of the complete structure, so the analyses of only individual parts are needed to extract the equivalent lossy circuit. This is verified at the end of the chapter where all the equivalent circuits of the different segmented parts of a filter used as an example are assembled and the filter response is recovered.

A number of publications have been reported on the characterization of both external and inter-resonator couplings [Thal, 1982], [Deslandes and Boone, 2008], [Miraftab and Yu, 2009], and [Sun and Chao, 1995], [Chua and Mirshekar-Syahkal, 2003], [Canos et al., 2003]. Deslandes and Boone [Deslandes and Boone, 2008] proposed an equivalent lossy circuit for inter-resonator couplings, and by using an even and odd formalism they were able to characterize a structure comprised of two resonators coupled together. However, a rigorous deduction of the filter elements of the equivalent circuit is not considered. Also, the technique used in [Deslandes and Boone, 2008] does not properly distribute the power loss due to resonators and coupling structures as a gain is obtained if the calculated losses in resonators are removed from the equivalent circuit. During the development of this work, Miraftab and Yu [Miraftab and Yu, 2009] have also proposed the same equivalent circuit for coupling structures as presented here, which they use for the synthesis of lossy filter responses with improved insertion loss flatness. However, they do not calculate the loss contribution of coupling structures due to their inherent surface resistivity which can then be used for the geometry optimization, but they attribute the losses needed in the coupling structures to yield a specific filter transfer function. Hence, this work presents a novel deduction of the equivalent circuit elements for the characterization of inherent losses in waveguide filters, not seen before. Other publications centered their work solely on the characterization of the external coupling with the goal to measure the unloaded Q-factor of a cavity. [Sun and Chao, 1995] and [Chua and Mirshekar-Syahkal, 2003] proposed an equivalent circuit where losses due to the coupling mechanism are taken into account, but the resonant frequency deviation due to the coupling is not corrected. Thal [Thal, 1982] uses a similar circuit for the characterization of losses in different coupling geometries. This type of circuits is used under the assumption that same coupling loadings yield to same coupling coefficients. However, this assumption is not valid for different iris thicknesses or different

coupling geometries. On the other hand, [Canos et al., 2003] accommodates for different coupling loadings but their considerations are limited to lossless coupling apertures.

In this work the ideas in [Deslandes and Boone, 2008] are further developed and an alternative way to [Miraftab and Yu, 2009] to determine the element values to account for inherent loss in coupling structures due to material finite conductivity is provided. A practical technique to derive the lossy equivalent circuit of inter-cavity coupling apertures is presented, and in contrast to [Thal, 1982] and [Deslandes and Boone, 2008], the derivation of the lossy external coupling is also included in this work. This allows to achieve excellent agreement of the extracted equivalent circuit response of a filter with its full-wave response. Thanks to the use of transmission line resonators, also the out of band performance is improved in comparison to [Deslandes and Boone, 2008]. Thus, the equivalent circuit can be used for the tuning of microwave lossy filters.

The different and novel formulation presented here allows separating resonator and coupling contributions to the overall losses. The losses in the cavities are represented by the attenuation factor in the associated transmission lines, while lumped element circuit models are used for the calculation of the losses in the couplings. With this approach it is then possible to individually study the loss contributions of the resonators and coupling structures of the complete filter. This can be useful, for example, to find optimized geometries of cavities and coupling structures, which might yield to insertion loss reductions of even more than 20% [Thal, 1982], [Lorente et al., 2009b]. The techniques described here can be applied, but should not be limited, to any arbitrarily shaped coupling structure and constant waveguide cross section.

Measured and simulated results of a filter of fifth order confirm the excellent accuracy obtained with the new circuit. The derived circuit is also applied to the loss prediction of practical waveguide coupled cavity filters of different orders, bandwidths, and center frequencies with minimum use of full-wave simulation. Finally, an application of the new circuit to yield analysis is also presented in this work, showing that losses can be included in the prediction with a significant reduction in the use of lengthy full-wave simulations.

4.1.1 Concept of Coupling

The coupling coefficient is defined as the ratio of the energy transfer between two resonators or between an input source and a resonator to the energy stored in a resonator. Hence, it can be well described as the mutual inductance produced between two inductances [Terman, 1943] as shown in Figure 4.1.

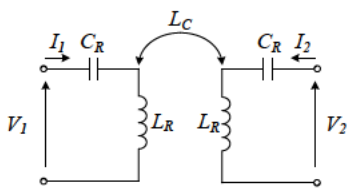

Figure 4.1: Resonators coupled by mutual inductance.

The mesh equations of the above circuit can be written as

$$V_1 = I_1 j\left(\omega L_R - \frac{1}{\omega C_R}\right) + I_2 j\omega L_C \tag{4.1}$$

$$V_2 = I_2 j\left(\omega L_R - \frac{1}{\omega C_R}\right) + I_1 j\omega L_C \tag{4.2}$$

and the circuit in Figure 4.2 can be derived from these equations by inspection.

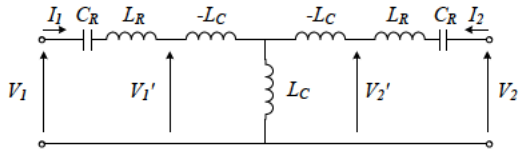

Figure 4.2: Equivalent circuit of the circuit in Figure 4.1.

The $ABCD$ matrix of the coupling circuit in Figure 4.2 is

$$\begin{bmatrix} V_1' \\ I_1 \end{bmatrix} = \begin{bmatrix} 0 & -j\omega L_C \\ \dfrac{-j}{\omega L_C} & 0 \end{bmatrix} \begin{bmatrix} V_2' \\ I_2 \end{bmatrix} \tag{4.3}$$

which is the $ABCD$ matrix of an ideal impedance inverter with $K = \omega L_C$ being the impedance inverter value and has been deeply studied in the past (see for instance [Matthaei et al., 1980], [Hunter et al., 2002]). Therefore, the mutual inductance between two resonators is equivalent to an ideal impedance inverter.

The even and odd resonant frequencies of the circuit in Figure 4.2 can be calculated as

$$\omega_{odd} = \frac{1}{\sqrt{(L_R - L_C)\,C}} \tag{4.4}$$

$$\omega_{even} = \frac{1}{\sqrt{(L_R + L_C)\,C}} \tag{4.5}$$

Combining (4.4) and (4.5), and as $\omega_0 = 1/\sqrt{LC}$, an expression for the resonant frequency in terms of the odd and even frequencies of the circuit can be obtained as

$$\frac{1}{\omega_0^2} = \frac{1}{2}\left(\frac{1}{\omega_{odd}^2} + \frac{1}{\omega_{even}^2}\right) \tag{4.6}$$

The coupling coefficient can also be written in terms of the even and odd frequencies. By definition,

$$k_{ij} = \frac{L_C}{L_R} \tag{4.7}$$

and thus,

$$k_{ij} = \frac{\omega_{odd}^2 - \omega_{even}^2}{\omega_{odd}^2 + \omega_{even}^2} \tag{4.8}$$

where again, use of expressions (4.4), (4.5), and $\omega_0 = 1/\sqrt{LC}$ has been made.

Figure 4.3 shows the even and odd frequencies of the previous circuit versus the coupling coefficient (4.8) when the center frequency of the resonators is fixed to $f_0 = 11GHz$. As predicted by (4.8), the even and odd mode frequencies separate as the coupling increases.

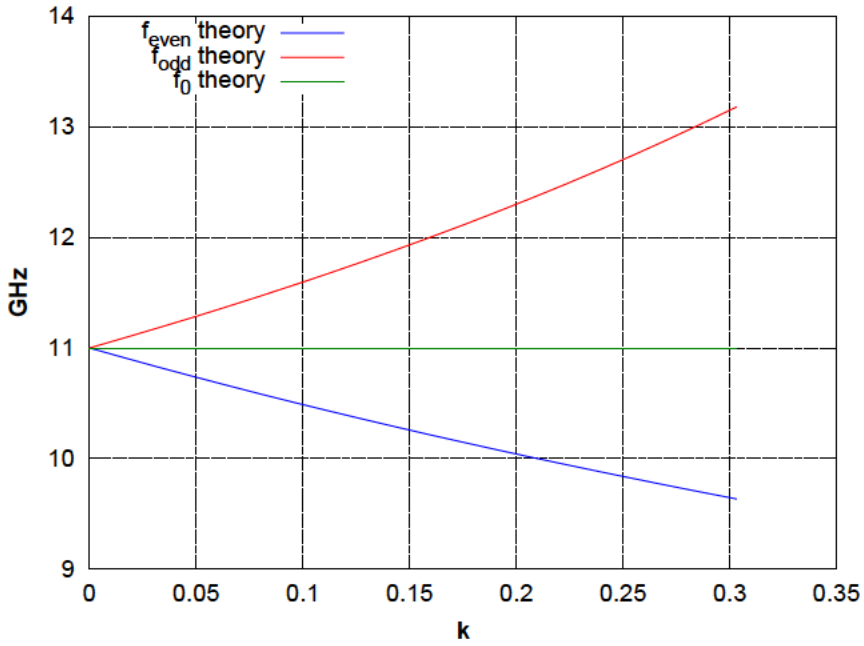

Figure 4.3: Even and odd mode frequencies and center frequency of ideal impedance inverter.

The lossless equivalent circuit presented here will be used in this chapter to extract a lossy equivalent circuit version that completely characterizes losses in coupling structures.

4.2 Step by Step Derivation of the Equivalent Lossy Circuit

The approach used to derive the complete equivalent lossy circuit of a filter consists on deriving the equivalent lossy circuits of the individual coupling structures and the resonators, and assembling them to yield the final equivalent lossy network of the complete structure. To that end, the unloaded resonator, the inter-resonator coupling, and the external coupling must be studied separately. Each process is introduced in the next subsections.

4.2.1 Unloaded Resonator

The first step is to characterize the isolated resonator that will be used in the final equivalent circuit. A waveguide cavity resonator (Figure 4.4(a)) can be represented by a portion of a lossy transmission line with $l_r = n\lambda_{g0}/2$ as the one shown in

Figure 4.4(b). For rectangular cavity resonators, the fundamental TE_{10} waveguide mode can be used for the derivation of the equivalent circuit in analytic form, [Pozar, 1998, Collin, 2001]. In the more general case of arbitrary resonator cross section, the complex propagation constant of the dominant mode ($\gamma_C = \alpha_C + j\beta_C$) can be directly extracted from full-wave simulations, where α_C is the attenuation constant and β_C is the propagation constant of the waveguide mode considered.

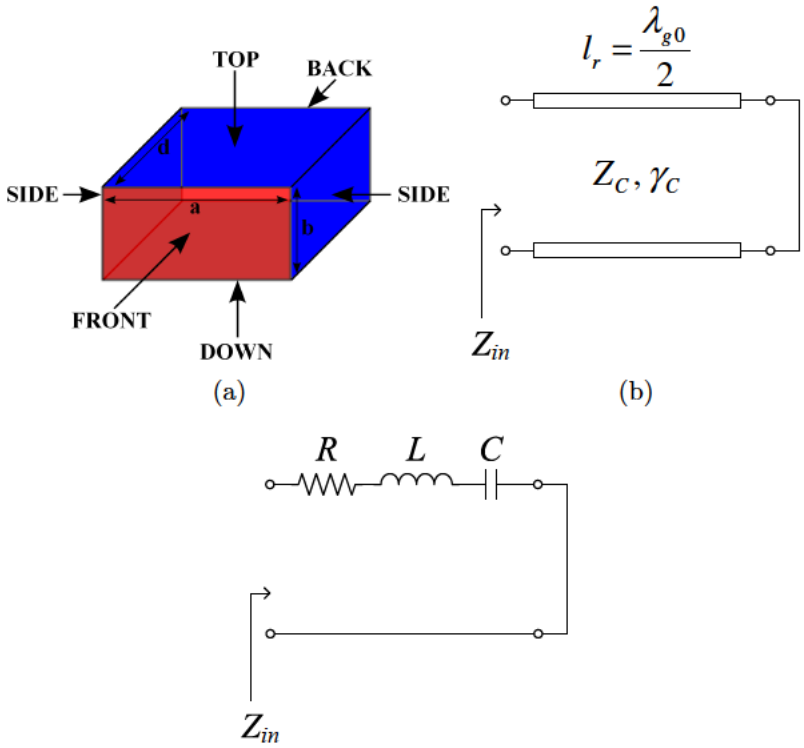

Figure 4.4: (a) Waveguide cavity, (b) transmission line resonator, and (c) its equivalent lumped elements circuit.

To completely characterize the transmission line resonator shown in Figure 4.4(b), the characteristic impedance must also be defined. In this work, CST Microwave Studio and Ansoft HFSS are used to extract the parameters needed to create the equivalent circuit. The former uses the wave impedance of the mode as the characteristic impedance of the waveguide, whilst the latter uses the power-current impedance definition. Hence, depending on what program is used for the parameter extraction of the equivalent circuit, the wave impedance (4.9) or the impedance defined as a ratio of power and current will be used consequently (4.10), [Rizzi, 1988].

$$Z_C = \begin{cases} \dfrac{k\eta}{\beta} & \text{for TE modes} \\ \dfrac{\beta\eta}{k} & \text{for TM modes} \end{cases} \tag{4.9}$$

$$Z_C = \frac{P}{I^2} = 465\frac{b}{a}\sqrt{\frac{\mu_R}{\epsilon_R}}\frac{\lambda_g}{\lambda} \tag{4.10}$$

The reactance slope parameter χ and the unloaded Q-factor Q_U of the transmission line resonator can be defined by comparing its input impedance with the input impedance of a lumped element RLC series resonator (Figure 4.4(c)).

The input impedance of a transmission line resonator short-circuited at the end is given by

$$Z_{in} = Z_C \tanh(\alpha + j\beta) l_r \tag{4.11}$$

and using a well known identity for the hyperbolic tangent gives

$$Z_{in} = Z_C \frac{\tanh \alpha l_r + j \tan \beta l_r}{1 + j \tan \beta l_r \tanh \alpha l_r} \tag{4.12}$$

Note that $Z_{in} = j Z_C \tan \beta l_r$ if a lossless transmission line is assumed ($\alpha = 0$).

In most cases, waveguide lines have very low loss and $\alpha l_r \ll 1$ and so $\tanh \alpha l_r \approx \alpha l_r$. Then (4.12) becomes

$$Z_{in} = Z_C \frac{\alpha l_r + j \tan \beta l_r}{1 + j \alpha l_r \tan \beta l_r} \tag{4.13}$$

Now let $\omega = \omega_0 + \Delta\omega$, then,

$$\begin{aligned} \beta l_r = \frac{2\pi}{\lambda_g} \frac{n\lambda_{g0}}{2} = \frac{\sqrt{\omega^2 - \omega_C^2}}{c} \frac{n\pi c}{\sqrt{\omega_0^2 - \omega_C^2}} = \frac{\sqrt{(\omega_0 + \Delta\omega)^2 - \omega_C^2}}{c} \frac{n\pi c}{\sqrt{\omega_0^2 - \omega_C^2}} \approx \\ \approx n\pi \sqrt{1 + \frac{2\omega_0 \Delta\omega}{\omega_0^2 - \omega_C^2}} \approx n\pi \left(1 + \frac{\omega_0 \Delta\omega}{\omega_0^2 - \omega_C^2}\right) \end{aligned} \tag{4.14}$$

since $\Delta\omega$ is small and

$$\frac{2\omega_0 \Delta\omega}{\omega_0^2 - \omega_C^2} \ll 1 \tag{4.15}$$

Also,

$$\tan \beta l_r = \tan n \left(\pi + \pi \frac{\omega_0 \Delta\omega}{\omega_0^2 - \omega_C^2}\right) \approx n\pi \frac{\omega_0 \Delta\omega}{\omega_0^2 - \omega_C^2} \tag{4.16}$$

Combining (4.16) with (4.13), the input impedance of a transmission line resonator can finally be expressed as

$$Z_{in} = Z_C \frac{\alpha l_r + jn\pi \dfrac{\omega_0 \Delta\omega}{\omega_0^2 - \omega_C^2}}{1 + j\alpha l_r n\pi \dfrac{\omega_0 \Delta\omega}{\omega_0^2 - \omega_C^2}} \approx Z_C \left(\alpha l_r + jn \frac{\lambda_{g0}^2 \omega_0 \Delta\omega}{4\pi c^2}\right) \tag{4.17}$$

since $\alpha l_r n\pi \omega_0 \Delta\omega / (\omega_0^2 - \omega_C)^2 \ll 1$.

Now, consider the input impedance of the RLC circuit shown in Figure 4.4(c),

$$Z_{in} = R + j\omega L \left(1 - \frac{\omega_0^2}{\omega^2}\right) \approx R + j2L\Delta\omega \tag{4.18}$$

where $\omega_0 = \omega - \Delta\omega$ and $\Delta\omega$ is small.

By comparing (4.17) with (4.18), the lumped element components of the RLC resonator can be obtained in terms of the transmission line parameters as

$$R = Z_C \alpha l_r = Z_C \alpha n \frac{\lambda_{g0}}{2} \tag{4.19}$$

and

$$L = Z_C \frac{n}{4f_0} \frac{\lambda_{g0}^2}{\lambda_0^2} \tag{4.20}$$

and thus the reactance slope parameter and the unloaded Q-factor can be eventually obtained as

$$\chi = \omega_0 L = \frac{n\pi Z_C}{2} \left(\frac{\lambda_{g0}}{\lambda_0} \right)^2 \tag{4.21}$$

$$Q_U = \frac{\chi}{R} = \frac{\pi \lambda_{g0}}{\alpha \lambda_0^2} \tag{4.22}$$

It is of importance to note that the above derived Q-factor (4.22) can only be compared against the Q-factor of the model in Figure 4.4(a) when both its front and back wall are considered as PEC. This is due to the perfect short-circuit used at the end of the transmission line. In a practical waveguide resonator, however, front and back walls will be formed by real lossy conductors. As an example, consider the fundamental TE_{10} mode of a WR-75 waveguide with $\alpha = 28.969$ N/m and $\beta = 161.131$ at $f_0 = 11$ GHZ for a material electrical conductivity of $\sigma = 18.797$ MS. The unloaded Q-factor of a TE_{101} cavity has been computed for two cases. In the first approach (Q_{U1}), the losses in all the walls of the cavity have been included whereas for the second approach (Q_{U2}) losses in the front and back walls of the cavity are neglected. The results are shown in Table 4.1.

Table 4.1: Unloaded Q

Q_{U1}	Q_{U2}	Q_U from (4.22)
4328.5	5694.4	5693.1

As stated previously, the unloaded Q-factor calculated as in (4.22) given the specifications of the waveguide agrees with the simulated unloaded Q-factor of a cavity with lossless front and back walls. Therefore, the formulation derived in this section can only be used if the front and back walls of the resonator are assumed to be lossless. In the following, when a short-circuit is needed, a perfect electric wall will be used.

4.2.2 Inter-Resonator Coupling

To derive the equivalent lossy circuit of an inter-resonator coupling, a symmetric model consisting of two cavities coupled through a waveguide aperture as shown in Figure 4.5(a) can be used. In Figure 4.5(a) a rectangular iris is shown, but the

theory is valid for coupling elements of any general shape. This model is chosen because it accurately represents the circuit in Figure 4.2 when no loss is present. In contrast to previous work [Deslandes and Boone, 2008], transmission line resonators are used in the equivalent circuit (Figure 4.5(b)). Thanks to this, the agreement obtained in the out of band response agrees much better with full-wave simulations than if lumped-element resonators are used. Note that due to the need of working with distributed and lumped elements in the same circuit, the nomenclature of the normalized impedances will be given in lowercase, while absolute impedances will be expressed in uppercase.

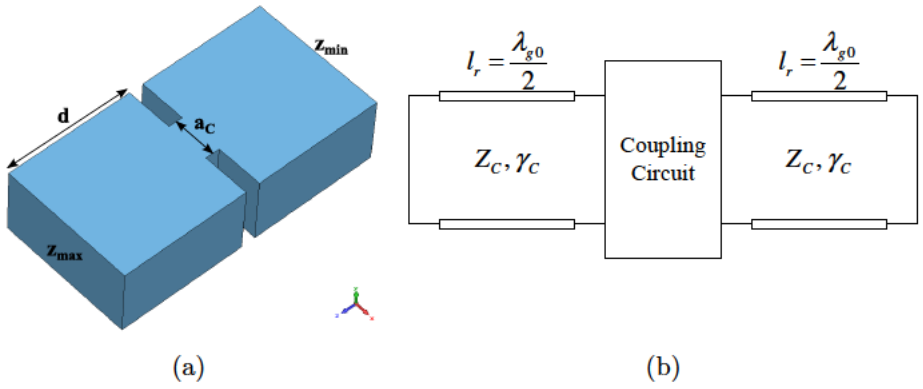

Figure 4.5: (a) Example of inter-cavity coupling model geometry and (b) its unknown equivalent circuit with complete resonators.

An similar graph to that shown in Figure 4.3 can be obtained if the iris aperture (a_C) (Figure 4.6(a)), and thus the coupling coefficient (Figure 4.6(b)), is swept.

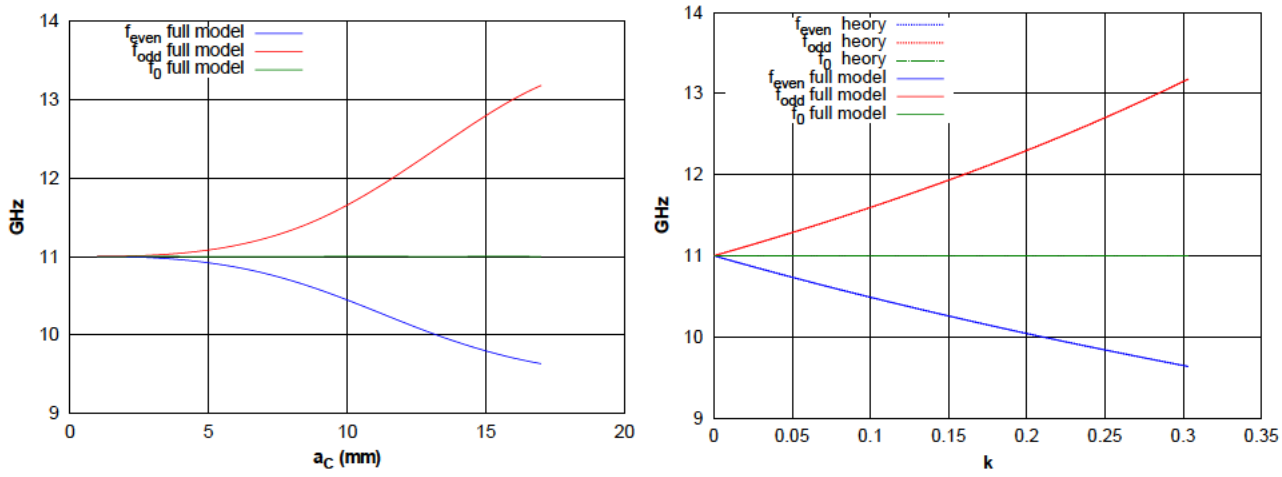

Figure 4.6: (a) Even and odd mode frequencies and center frequency of the model in Figure 4.5 versus the coupling aperture (a_C) and (b) versus the coupling coefficient (k) compared to an ideal impedance inverter circuit (Figure 4.2).

Again note that the center frequency is fixed to a constant value for each value of coupling aperture (a_C). However, if the length of the cavities remained unchanged,

the center frequency would decrease as the coupling aperture increases. This is because a waveguide iris is not equivalent to an ideal impedance inverter alone but to an ideal impedance inverter surrounded by negative transmission lines [Cohn, 1957]. These negative transmission lines exercise a loading effect over the adjacent cavities and therefore, the latter must be shortened if the center frequency is to be maintained. The loading effect depends on the coupling coefficient and on the coupling geometry. Two different coupling structures can yield the same coupling coefficient but with different loadings over the adjacent cavities. In other words, two coupling structures with same cavity loading do not necessarily yield the same coupling coefficient. Figure 4.7 shows the previously discussed loading effect and demonstrates that assumptions made in previous works [Thal, 1982], such that same coupling coefficients yield to same loading effects, are wrong.

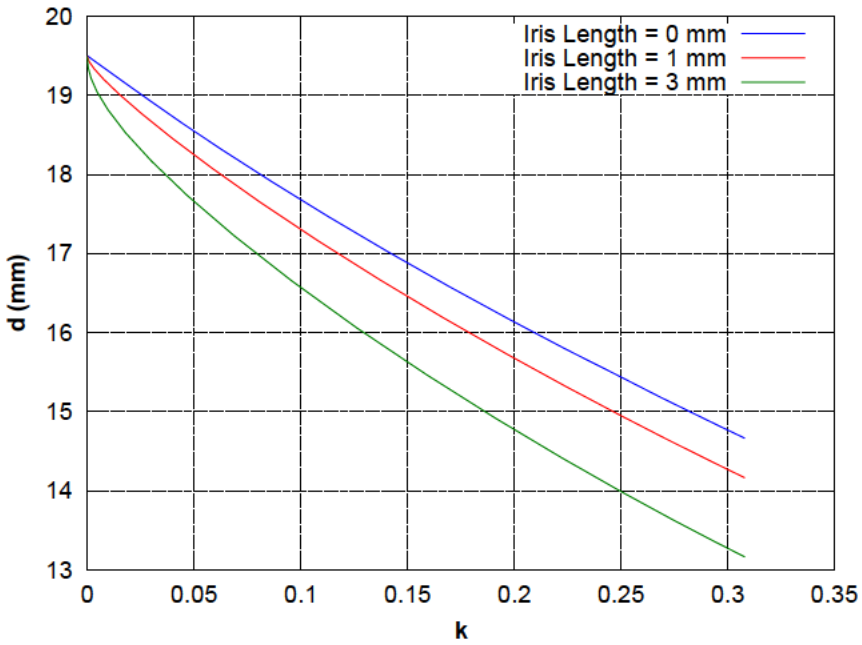

Figure 4.7: Loading effect of the coupling thickness on the length of the cavities. In the graph, (d) is the length of the resonator needed to maintain constant the resonant frequency at 11 GHz.

On the other hand, note that perfect straight electric walls are assumed at the opposite sides of the coupling under study (z_{min} and z_{max}). This is not always the case. Note that an inter-resonator coupling is surrounded by either other inter-resonator couplings or external couplings and the walls of the cavity at z_{min} and z_{max} are unknown. In this context, an analysis of the even and odd fields of the structure shown in Figure 4.5 reveals that a perfect magnetic wall can be placed in the electrical center of both cavities without perturbing the electromagnetic fields. To prove it, the even and odd modes of the fields inside the structure in Figure 4.5(a) are shown in Figure 4.8. It is to note that, in all cases, the conditions of a perfect magnetic wall are satisfied:

- The electric field is tangential to the M plane (Figure 4.8(a) and Figure 4.8(c)).

- The magnetic field is normal to the M plane (Figure 4.8(b) and Figure 4.8(d)).

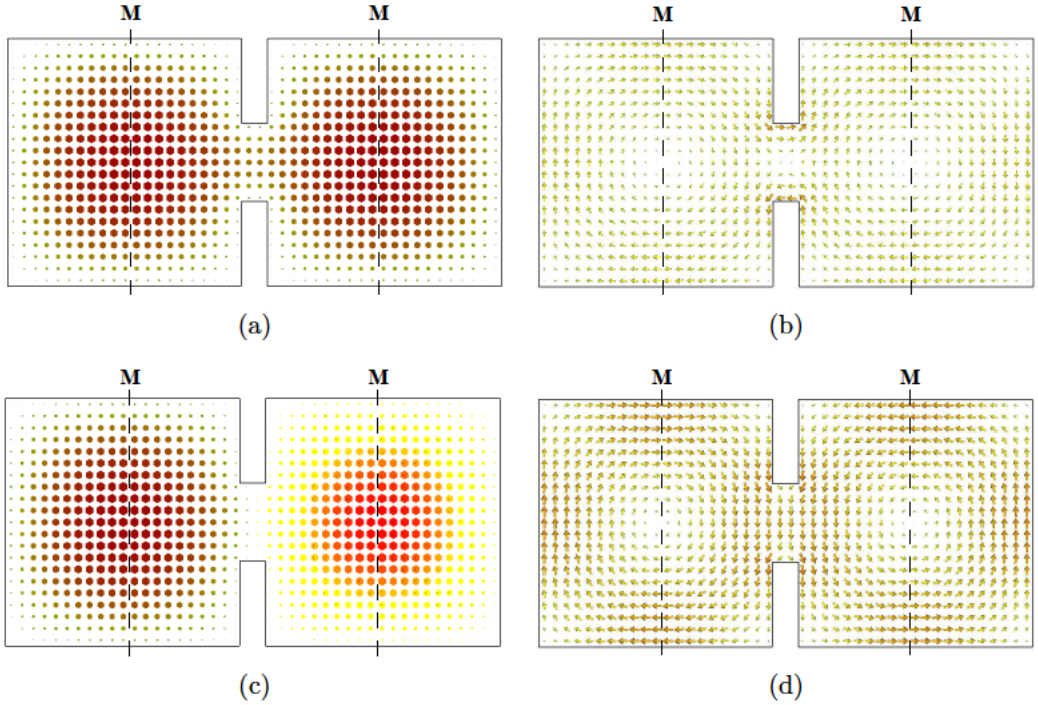

Figure 4.8: Even and odd fields in the inter-cavity coupling model geometry: (a) even E field, (b) even H field, (c) odd E field, and (d) odd H field.

Therefore, by placing these magnetic walls in the electrical center of the cavities (M plane), the problem can be reduced as shown in Figure 4.9, thus saving computational time and allowing an accurate calculation of the overall losses. Likewise, the length of the resonators in the equivalent circuit is reduced to $l_r = \lambda_{g0}/4$ as demonstrated in Appendix D. Hence, the resultant cavities exhibit the following characteristics:

- half the losses of the original cavities,
- half the stored energy of the original cavities,

but they have:

- same resonant frequency of the original cavities,
- same unloaded Q-factor of the original cavities.

The model in Figure 4.9 assumes that the magnetic wall conditions of the even and odd modes (electrical center of the resonator) of the structure in Figure 4.5 are both always satisfied at the same physical point, no matter the coupling aperture. This is not the case, as the electrical center of the even mode deviates from the electrical center of the odd mode as the coupling aperture increases. Figure 4.10

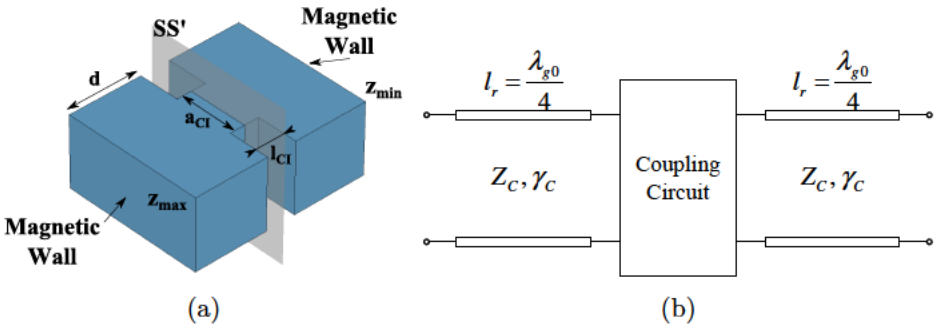

Figure 4.9: (a) Example of inter-resonator coupling model geometry and (b) its unknown equivalent circuit with halved resonators.

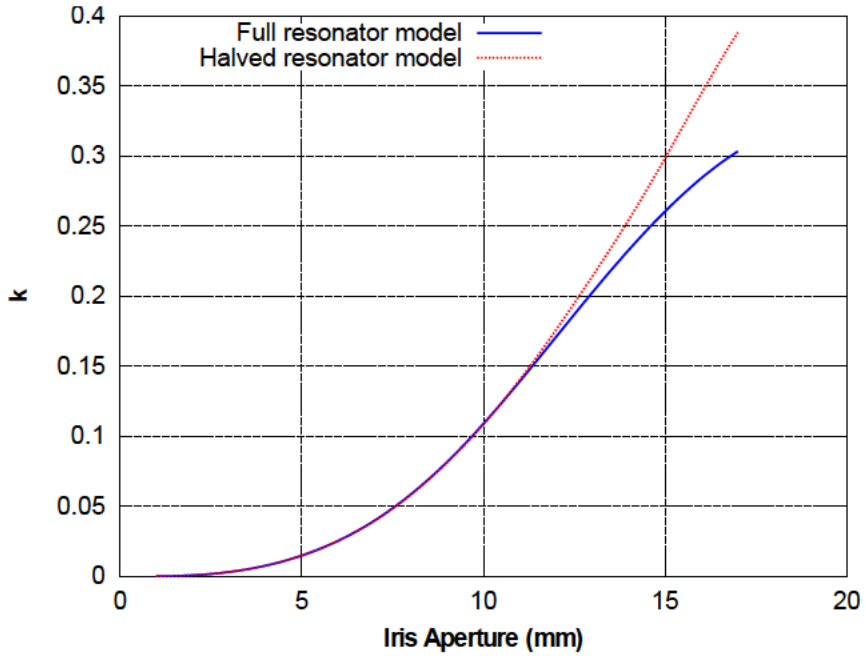

Figure 4.10: Coupling coefficient versus iris aperture for full and halved resonator models.

shows the coupling coefficient deviation between the model with full resonators and the model with halved resonators.

Note that both graphs are in excellent agreement up to a coupling value of $k = 0.15$, which is more than enough for practical narrow-band filter design. Note however that in a real filter similar couplings exist adjacent to the coupling under study and thus, the real coupling coefficient of a given structure in a filter will better agree with the coupling coefficient obtained from the proposed model based on magnetic walls, instead of the full-cavity model. Therefore, the reduced structure shown in Figure 4.9 can be used to extract the lossy equivalent circuit of an inter-resonator coupling using an odd and even analysis formalism.

Odd Mode

The odd mode of the structure in Figure 4.9(a) can be recovered by placing an electric wall in the symmetry plane *SS'* and the equivalent circuit shown in Figure 4.11 is obtained.

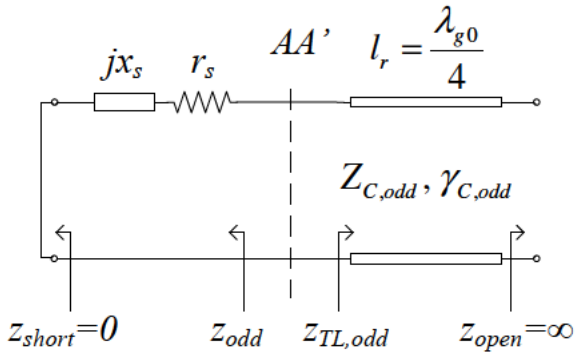

Figure 4.11: Odd mode equivalent circuit of the model in Figure 4.9(b).

The electric wall forces new field patterns and different current distributions, thus varying the resonant frequency and the Q-factor of the structure. x_S and r_S are new components in the equivalent circuit that account for this shift in resonant frequency and change in Q-factor, as compared to a single cavity (f_0, Q_U). For inductive couplings, the reactance can be taken as $x_S = \omega l_S$. The resonant condition of the circuit in Figure 4.11 is satisfied when the imaginary part of its equivalent impedance is null. Thus, l_S can be extracted from (4.23),

$$\Im(z_{TL,odd})|_{\omega_{odd}} + \omega_{odd} l_S = 0 \tag{4.23}$$

where ω_{odd} is the odd mode frequency of the structure in Figure 4.9(a) that can be obtained from full-wave simulation and the normalized impedance $z_{TL,odd}$ can be derived from lossy transmission line theory [Pozar, 1998] as

$$z_{TL,odd} = \frac{z_{open} + \tanh \gamma_{C,odd} l_r}{1 + z_{open} \tanh \gamma_{C,odd} l_r} \tag{4.24}$$

However, since $z_{open} = \infty$ then

$$z_{TL,odd} = \frac{1}{\tanh(\gamma_{C,odd} l_r)} = \frac{1 + j \tan(\beta_{C,odd} l_r) \tanh(\alpha_{C,odd} l_r)}{\tanh(\alpha_{C,odd} l_r) + j \tan(\beta_{C,odd} l_r)} \tag{4.25}$$

The value of r_S can be obtained from the Q-factor of the odd mode (4.26), which can be defined as the ratio of the slope parameters to the resistances of the impedances seen to the right and left of the *AA'* plane in Figure 4.11 [Matthaei et al., 1980]. This equation reads,

$$Q_{odd} = \frac{\chi_{odd} + \chi_{TL.odd}}{\Re(z_{odd}) + \Re(z_{TL,odd})} \tag{4.26}$$

where χ_{odd} is the reactance slope parameter of z_{odd}, $\chi_{TL,odd}$ is the reactance slope parameter of $z_{TL,odd}$, $\Re(z_{odd}) = r_S$ and Q_{odd} is the odd mode Q-factor of the structure in Figure 4.9(a) that can be obtained from full-wave simulation.

Even Mode

Similarly, the even mode of the structure in Figure 4.9(a) is obtained when a magnetic wall is placed at the symmetry plane *SS'*, yielding the equivalent circuit shown in Figure 4.12.

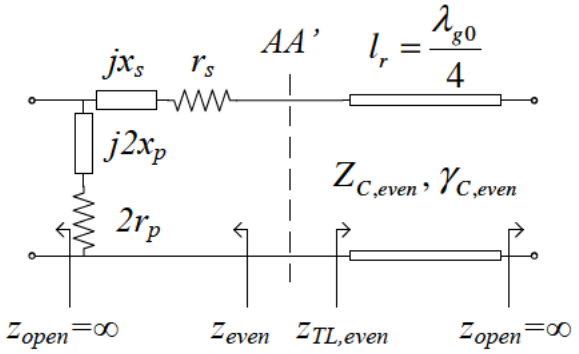

Figure 4.12: Even mode equivalent circuit of the model in Figure 4.9(b).

As in the odd mode case, the magnetic wall forces new field patterns and different current distributions as compared to a single cavity (f_0, Q_U), thus varying the resonant frequency and the Q-factor of the structure. Two new components are added to the equivalent circuit, namely x_P and r_P, that account for this shift in resonant frequency and change in Q-factor. Thus, proceeding as previously, the new components of the equivalent circuit can be obtained from the resonant condition (4.27) and the Q-factor (4.28). Note that the values of l_S and r_S are known from the previous step.

$$\Im(z_{TL,even})\big|_{\omega_{even}} + \omega_{even}\,(l_s + 2l_p) = 0 \tag{4.27}$$

$$Q_{even} = \frac{\chi_{even} + \chi_{TL,even}}{\Re\,(z_{even}) + \Re\,(z_{TL,even})} \tag{4.28}$$

In equations (4.27) and (4.28), $z_{TL,even}$ is a normalized impedance that can be derived similarly to $z_{TL,odd}$, χ_{even} is the reactance slope parameter of z_{even}, $\chi_{TL,even}$ is the reactance slope parameter of $z_{TL,even}$, $\Re(z_{even}) = r_S + 2r_P$, and ω_{even} and Q_{even} are the even mode frequency and Q-factor of the model in Figure 4.9(a) and can be extracted from full-wave simulation.

Final Equivalent Lossy Circuit

Combining the results from the two previous analyses, the equivalent lossy circuit of an inter-resonator coupling is finally obtained as shown in Figure 4.13.

The center frequency and coupling coefficient of the above circuit can be better derived using its homologous lumped element circuit for simplicity (Figure 4.14).

The odd mode resonant frequency of the rlc circuit in Figure 4.14 is given by (4.29) and the even mode resonant frequency, by (4.30).

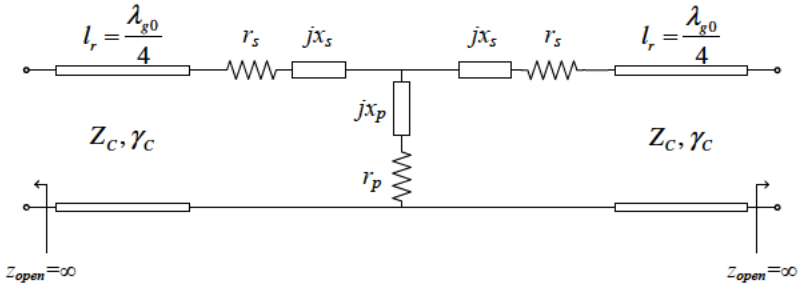

Figure 4.13: Equivalent lossy circuit of two halved TL resonators coupled through a waveguide iris.

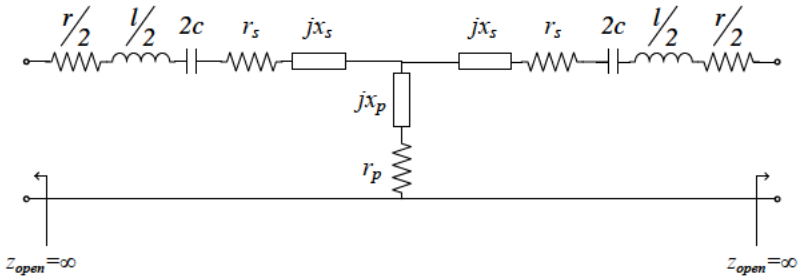

Figure 4.14: Equivalent lossy circuit of two halved rlc resonators coupled through a waveguide iris.

$$\omega_{odd} = \frac{1}{\sqrt{\left(\frac{l}{2} + l_S\right) 2c}} \tag{4.29}$$

$$\omega_{even} = \frac{1}{\sqrt{\left(\frac{l}{2} + l_S + 2l_P\right) 2c}} \tag{4.30}$$

Combining (4.29) and (4.30), assuming $l_S = -l_P$ (which is true for practical narrow-band filters), and as $\omega_0 = 1/\sqrt{lc}$, a final expression for the center frequency can be obtained as

$$\frac{1}{\omega_0^2} = \frac{1}{2}\left(\frac{1}{\omega_{odd}^2} + \frac{1}{\omega_{even}^2}\right) \tag{4.31}$$

The coupling coefficient is defined as the ratio of the coupled magnetic energy to the stored energy of an uncoupled single resonator. Hence,

$$k_{ij} = \frac{2\frac{1}{2}l_S|I|^2 + \frac{1}{2}l_P|2I|^2}{l|I|^2} = \frac{1}{2}\frac{\omega_{odd}^2 - \omega_{even}^2}{\omega_{odd}^2 + \omega_{even}^2} \tag{4.32}$$

where again, use of expressions (4.29), (4.30), and $\omega_0 = 1/\sqrt{LC}$ have been made and $l_S = -l_P$ has been assumed.

Note that in (4.32), the formulation to derive the magnetic coupling coefficient is slightly different to that obtained in (4.8) [Zaki and Chen, 1987],

[Hong and Lancaster, 2001]. The difference comes due to the use of halved resonators (and therefore half of the resonator stored energy) in the derivation of the equivalent circuit (see Appendix D).

4.2.3 External Coupling

The final step is to derive the equivalent lossy circuit of the external coupling. To that end, several approaches have been considered in this work and are presented in the following.

Approach 1: Singly Terminated Cavity

For the first approach, a model consisting of a single resonator coupled to the input feed source has been considered. An example of the structure is shown in Figure 4.15(a). The suggested equivalent circuit is based on the equivalent circuit of an ideal impedance inverter (Figure 4.2) and can be seen in Figure 4.15(b).

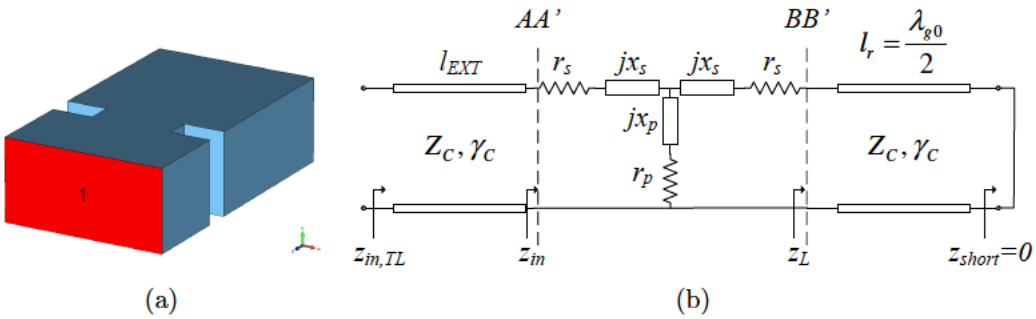

Figure 4.15: (a) External coupling model of approach 1 and (b) its suggested lossy equivalent circuit.

In this figure, $z_{in,TL}$, z_{in} and z_L are the impedances seen from the input port, from the transformed impedance after the port transmission line (plane AA') and from the transformed impedance before the resonator (plane BB'), respectively.

The analytical input impedance of the circuit in Figure 4.15(b) seen from the AA' plane can be calculated as

$$z_{in} = r_s + r_p + j\left(x_s + x_p\right) - \frac{\left(r_p + jx_p\right)^2}{r_s + r_p + j\left(x_s + x_p\right) + z_L} \tag{4.33}$$

where r_S, x_S, r_P and x_P are unknowns and the normalized impedance z_L at BB' (see Figure 4.15(b)) is given by

$$z_L = \tanh\left(\gamma_C l_r\right) \tag{4.34}$$

The normalized input impedance at the plane AA' can also be expressed as

$$z_{in} = \frac{z_{in,TL} - \tanh\left(\gamma_C l_{EXT}\right)}{1 - z_{in,TL}\tanh\left(\gamma_C l_{EXT}\right)} \tag{4.35}$$

where γ_C is the propagation constant of the mode under study and $z_{in,TL}$ is the input impedance of the model in Figure 4.15(a) that can be obtained from full-wave

simulation. Moreover, l_{EXT} is the length of the input line. However, the physical length given in the waveguide model cannot be used due to the loading effects of the waveguide coupling over the line. Hence the corrected length of the external line has to be derived using the phase of the S_{11} parameter. In this context, let a signal traveling through the structure in Figure 4.15(a) have a total phase shift of

$$\phi\left(S_{11}\right) = 2\phi\left(l_{EXT}\right) + 2\phi\left(coupling\right) + 2\phi\left(\frac{\lambda_{g0}}{2}\ resonator\right) + \phi\left(electric\ wall\right) \quad (4.36)$$

where the phase shifts due to the coupling, the resonator and the electric wall are 90°, −180°, and 180°, respectively, at ω_0 and if low loss is assumed. Therefore,

$$\phi\left(S_{11}\right) = 2\phi\left(l_{EXT}\right) \quad (4.37)$$

and since $\beta_0 l_{EXT} = \phi(l_{EXT})$, then

$$l_{EXT} = \frac{\lambda_{g0}}{2\pi}\phi(l_{EXT}) = \frac{\lambda_{g0}}{2\pi}\frac{\phi(S_{11})}{2} \quad (4.38)$$

where $\phi(S_{11})$ is the unwrapped phase of the reflection parameter from the full-wave simulation.

Combining (4.33) with (4.35), a system of two non-linear equations ($\Re(z_{in})$ and $\Im(z_{in})$) can be obtained for one frequency point. Hence, at least two frequency points are needed to find the four unknowns. Two equations will be extracted from the center frequency (f_0) ((4.39) and (4.40)) and two more from a frequency point near resonance (f_S) ((4.41) and (4.42)). The nonlinear system of four equations and four unknowns can be solved numerically.

The second frequency point should be chosen near resonance, where the frequency dependence of the waveguide coupling model and the equivalent circuit are very similar. For instance, for the example treated here good results have been obtained when f_S is selected to be equal to $f_0 \pm 5MHz$, $f_0 \pm 10MHz$ or $f_0 \pm 20MHz$, showing that the technique is robust.

$$\mathrm{Re}\left(z_{in}|_{\omega_0}\right) = r_s + r_p - \frac{\left(r_p^2 - x_p^2\right)\cdot\left(r_s + r_p + \mathrm{Re}\left(z_L|_{\omega_0}\right)\right) + 2\cdot r_p\cdot x_p\cdot\left(x_s + x_p + \mathrm{Im}\left(z_L|_{\omega_0}\right)\right)}{\left(r_s + r_p + \mathrm{Re}\left(z_L|_{\omega_0}\right)\right)^2 + \left(x_s + x_p + \mathrm{Im}\left(z_L|_{\omega_0}\right)\right)^2} \quad (4.39)$$

$$\mathrm{Im}\left(z_{in}|_{\omega_0}\right) = x_s + x_p + \frac{\left(r_p^2 - x_p^2\right)\cdot\left(x_s + x_p + \mathrm{Im}\left(z_L|_{\omega_0}\right)\right) - 2\cdot r_p\cdot x_p\cdot\left(r_s + r_p + \mathrm{Re}\left(z_L|_{\omega_0}\right)\right)}{\left(r_s + r_p + \mathrm{Re}\left(z_L|_{\omega_0}\right)\right)^2 + \left(x_s + x_p + \mathrm{Im}\left(z_L|_{\omega_0}\right)\right)^2} \quad (4.40)$$

$$\mathrm{Re}\left(z_{in}|_{\omega_S}\right) = r_s + r_p - \frac{\left(r_p^2 - x_p^2\right)\cdot\left(r_s + r_p + \mathrm{Re}\left(z_L|_{\omega_S}\right)\right) + 2\cdot r_p\cdot x_p\cdot\left(x_s + x_p + \mathrm{Im}\left(z_L|_{\omega_S}\right)\right)}{\left(r_s + r_p + \mathrm{Re}\left(z_L|_{\omega_S}\right)\right)^2 + \left(x_s + x_p + \mathrm{Im}\left(z_L|_{\omega_S}\right)\right)^2} \quad (4.41)$$

$$\mathrm{Im}\left(z_{in}|_{\omega_S}\right) = x_s + x_p + \frac{\left(r_p^2 - x_p^2\right)\cdot\left(x_s + x_p + \mathrm{Im}\left(z_L|_{\omega_S}\right)\right) - 2\cdot r_p\cdot x_p\cdot\left(r_s + r_p + \mathrm{Re}\left(z_L|_{\omega_S}\right)\right)}{\left(r_s + r_p + \mathrm{Re}\left(z_L|_{\omega_S}\right)\right)^2 + \left(x_s + x_p + \mathrm{Im}\left(z_L|_{\omega_S}\right)\right)^2} \tag{4.42}$$

Approach 2: Doubly Terminated Cavity (Even-Odd)

For the second approach, use is made of the model in Figure 4.16(a) to derive the equivalent circuit of external lossy couplings. It consists of a single resonator coupled to the input feed source and output load, where a symmetry plane SS' along the direction of propagation can be observed. Thus, an even and odd mode approach can be used. The corresponding equivalent circuit is shown in Figure 4.16(b), where one half of the circuit has been omitted due to the symmetry of the model.

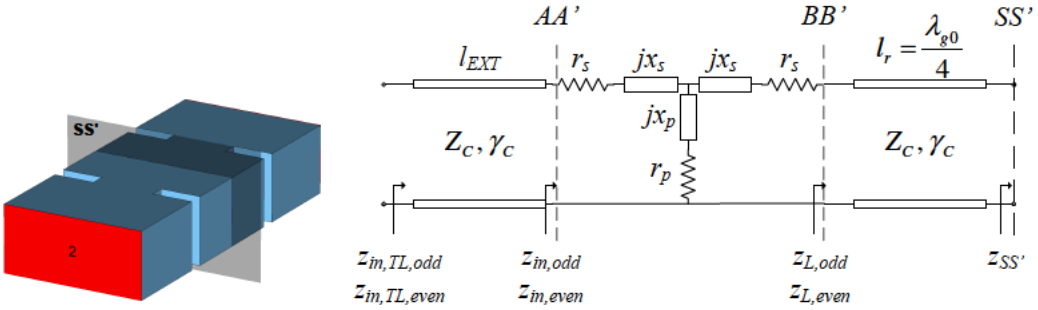

Figure 4.16: (a) External coupling model of approach 2 and (b) its suggested lossy equivalent circuit.

The procedure to find the four unknowns of the equivalent circuit is very similar to the one followed in the previous approach, but with the difference that the analytical input impedance must be calculated for both the even (4.43) and odd (4.44) modes of the equivalent circuit of Figure 4.16(b).

$$z_{in,even} = r_S + r_P + j\left(x_S + x_P\right) - \frac{\left(r_P + jx_P\right)^2}{r_S + r_P + j\left(x_S + x_P\right) + z_{L,even}} \tag{4.43}$$

$$z_{in,odd} = r_S + r_P + j\left(x_S + x_P\right) - \frac{\left(r_P + jx_P\right)^2}{r_S + r_P + j\left(x_S + x_P\right) + z_{L,odd}} \tag{4.44}$$

where $z_{L,even}$ and $z_{L,odd}$ are the load impedances seen from the BB' plane when the symmetry plane SS' is substituted by a magnetic wall ($z_{SS'} = \infty$) or an electric wall ($z_{SS'} = 0$), respectively. Analytically, they can be derived as

$$z_{L,even} = \frac{z_{SS'} + \tanh\gamma_C l_r}{1 + z_{SS'}\tanh\gamma_C l_r} = \frac{1}{\tanh\left(\gamma_C l_r\right)} \tag{4.45}$$

$$z_{L,odd} = \frac{z_{SS'} + \tanh \gamma_C l_r}{1 + z_{SS'} \tanh \gamma_C l_r} = \tanh (\gamma_C l_r) \tag{4.46}$$

The even and odd input impedances can also be expressed as

$$z_{in,even} = \frac{z_{in,TL,even} - \tanh (\gamma_C l_{EXT})}{1 - z_{in,TL,even} \tanh (\gamma_C l_{EXT})} \tag{4.47}$$

$$z_{in,odd} = \frac{z_{in,TL,odd} - \tanh (\gamma_C l_{EXT})}{1 - z_{in,TL,odd} \tanh (\gamma_C l_{EXT})} \tag{4.48}$$

where again γ_C is the propagation constant of the mode under study and $z_{in,TL,even}$ and $z_{in,TL,odd}$ are the input impedances of the model in Figure 4.16(a) when the symmetry plane *SS'* is replaced by a magnetic or an electric wall, respectively, and can be obtained from full-wave simulation. Moreover, l_{EXT} is the length of the input line and must be calculated following the same procedure outlined in the previous approach. To that end, consider only one half of the structure in Figure 4.16(a) (input line, coupling and half resonator) and a signal traveling through it, which has a total phase shift of

$$\begin{aligned} \phi (S_{11}) &= 2\phi (l_{EXT}) + 2\phi (coupling) + 2\phi \left(\frac{\lambda_{g0}}{4}\ resonator \right) + \phi (SS') = \\ &= 2\phi (l_{EXT}) + \phi (SS') \end{aligned} \tag{4.49}$$

since the phase shift introduced by the coupling and the halved resonator must be 90° and −90°, respectively, if low loss is assumed. The term $\phi (SS')$ is the phase shift of an electric (−180°) or a magnetic wall (0°). The length of the external line can then be calculated as

$$l_{EXT} = \frac{\phi(l_{EXT})}{\beta_0} = \frac{\lambda_{g0}}{2\pi}\phi(l_{EXT}) = \frac{\lambda_{g0}}{2\pi}\frac{\phi(S_{11}) - \phi (SS')}{2} \tag{4.50}$$

where $\phi(S_{11})$ is the unwrapped phase of the reflection parameter from the full-wave simulation.

Combining the even and odd input impedances, the impedance parameters of the complete model with no symmetry planes are derived as

$$z_{11} = \frac{z_{in,even} + z_{in,odd}}{2} \tag{4.51}$$

$$z_{21} = \frac{z_{in,even} - z_{in,odd}}{2} \tag{4.52}$$

$$z_{12} = z_{21} \tag{4.53}$$

$$z_{22} = z_{11} \tag{4.54}$$

and the normalized input impedance (seen from the *AA'* plane) with no symmetries can finally be obtained as

$$z_{in} = \frac{1}{Z_C}\left(Z_{11} - \frac{Z_{12}Z_{21}}{Z_{22}+Z_C^*}\right) = z_{11} - \frac{z_{12}z_{21}}{z_{22}+1} \tag{4.55}$$

Equation (4.55) can be calculated analytically from (4.43) and (4.44) and can also be obtained from (4.47) and (4.48) and full-wave simulation. Combining the analytical expressions with the full-wave results, a system of non-linear equations is finally obtained. Again, two frequency points are needed to find the four unknowns. Two equations can be extracted from the center frequency (f_0) ((4.56) and (4.57)) and two more from a frequency point near resonance (f_S) ((4.58) and (4.59)). The nonlinear system of four equations and four unknowns can be solved numerically.

$$\begin{aligned}\Re\left(z_{in}|_{\omega_0}\right) = {} & \Re\left(z_{11}|_{\omega_0}\right) \\ & - \frac{\left(\Re\left(z_{12}|_{\omega_0}\right)\Re\left(z_{21}|_{\omega_0}\right) - \Im\left(z_{12}|_{\omega_0}\right)\Im\left(z_{21}|_{\omega_0}\right)\right)\left(\Re\left(z_{22}|_{\omega_0}\right)^2+1\right)}{\left(\Re\left(z_{22}|_{\omega_0}\right)+1\right)^2 - \Im\left(z_{22}|_{\omega_0}\right)^2} + \\ & + \frac{\left(\Re\left(z_{12}|_{\omega_0}\right)\Im\left(z_{21}|_{\omega_0}\right) + \Re\left(z_{21}|_{\omega_0}\right)\Im\left(z_{12}|_{\omega_0}\right)\right)\Im\left(z_{22}|_{\omega_0}\right)}{\left(\Re\left(z_{22}|_{\omega_0}\right)+1\right)^2 - \Im\left(z_{22}|_{\omega_0}\right)^2}\end{aligned} \tag{4.56}$$

$$\begin{aligned}\Im\left(z_{in}|_{\omega_0}\right) = {} & \Im\left(z_{11}|_{\omega_0}\right) - \frac{\left(\Im\left(z_{12}|_{\omega_0}\right)\Im\left(z_{21}|_{\omega_0}\right) - \Re\left(z_{12}|_{\omega_0}\right)\Re\left(z_{21}|_{\omega_0}\right)\right)\Im\left(z_{22}|_{\omega_0}\right)}{\left(\Re\left(z_{22}|_{\omega_0}\right)+1\right)^2 - \Im\left(z_{22}|_{\omega_0}\right)^2} + \\ & + \frac{\left(\Re\left(z_{12}|_{\omega_0}\right)\Im\left(z_{21}|_{\omega_0}\right) + \Re\left(z_{21}|_{\omega_0}\right)\Im\left(z_{12}|_{\omega_0}\right)\right)\left(\Re\left(z_{22}|_{\omega_0}\right)^2+1\right)}{\left(\Re\left(z_{22}|_{\omega_0}\right)+1\right)^2 - \Im\left(z_{22}|_{\omega_0}\right)^2}\end{aligned} \tag{4.57}$$

$$\begin{aligned}\Re\left(z_{in}|_{\omega_S}\right) = {} & \Re\left(z_{11}|_{\omega_S}\right) \\ & - \frac{\left(\Re\left(z_{12}|_{\omega_S}\right)\Re\left(z_{21}|_{\omega_S}\right) - \Im\left(z_{12}|_{\omega_S}\right)\Im\left(z_{21}|_{\omega_S}\right)\right)\left(\Re\left(z_{22}|_{\omega_S}\right)^2+1\right)}{\left(\Re\left(z_{22}|_{\omega_S}\right)+1\right)^2 - \Im\left(z_{22}|_{\omega_S}\right)^2} + \\ & + \frac{\left(\Re\left(z_{12}|_{\omega_S}\right)\Im\left(z_{21}|_{\omega_S}\right) + \Re\left(z_{21}|_{\omega_S}\right)\Im\left(z_{12}|_{\omega_S}\right)\right)\Im\left(z_{22}|_{\omega_S}\right)}{\left(\Re\left(z_{22}|_{\omega_S}\right)+1\right)^2 - \Im\left(z_{22}|_{\omega_S}\right)^2}\end{aligned} \tag{4.58}$$

$$\begin{aligned}\Im\left(z_{in}|_{\omega_S}\right) = {} & \Im\left(z_{11}|_{\omega_S}\right) - \frac{\left(\Im\left(z_{12}|_{\omega_S}\right)\Im\left(z_{21}|_{\omega_S}\right) - \Re\left(z_{12}|_{\omega_S}\right)\Re\left(z_{21}|_{\omega_S}\right)\right)\Im\left(z_{22}|_{\omega_S}\right)}{\left(\Re\left(z_{22}|_{\omega_S}\right)+1\right)^2 - \Im\left(z_{22}|_{\omega_S}\right)^2} + \\ & + \frac{\left(\Re\left(z_{12}|_{\omega_S}\right)\Im\left(z_{21}|_{\omega_S}\right) + \Re\left(z_{21}|_{\omega_S}\right)\Im\left(z_{12}|_{\omega_S}\right)\right)\left(\Re\left(z_{22}|_{\omega_S}\right)^2+1\right)}{\left(\Re\left(z_{22}|_{\omega_S}\right)+1\right)^2 - \Im\left(z_{22}|_{\omega_S}\right)^2}\end{aligned} \tag{4.59}$$

Approaches 3 and 4: Doubly Terminated Cavity (Only Even - Only Odd)

In lumped elements circuits, the even and odd mode theory for symmetric circuits must be fully applied since information about the whole circuit is shared between the two modes. However, when the even and odd mode theory is applied in a lossy transmission line, both modes have information about the whole circuit and thus, they can be studied separately.

Only using the information of the even (4.43) or the odd (4.44) mode input impedances as obtained in approach 2, a system of equations similar to the one derived in approach 1 that can be solved numerically is obtained. With these two new approaches, computing resources are reduced as only one simulation of one half of the structure in Figure 4.16(a) is needed.

However, it is expected that the odd mode will not yield the right coupling element values since $z_{SS'} = 0$ and $z_L \gg z_S$ and therefore, z_S is *hidden* in z_L and the system does not converge to the right solution. In other words, z_L is so big that the current passing through z_L and z_S is almost negligible. This is not the case for the even mode, where $Z_{SS'} = \infty$ and $z_L \sim Z_S$ and a valid solution can be found.

External Q-factor of Lossy Couplings

In [Cameron et al., 2007], a method for extracting the external coupling of a filter is presented. The external Q-factor of the filter is calculated from the phase of the S_{11} coefficient or the group delay of an equivalent circuit of a resonator coupled to the input feed source. However, the equivalent circuit is assumed to be lossless and hence it can only be used in low loss applications, which is usually the case for waveguides.

When the external coupling of a filter including losses has to be calculated, the previous theory can be applied to find the lossy equivalent circuit of the external coupling and thus, its external Q-factor. For simplicity, the transmission line based resonator has been substituted for its equivalent lumped element circuit as explained in Section 4.2.1 and it is shown in Figure 4.17.

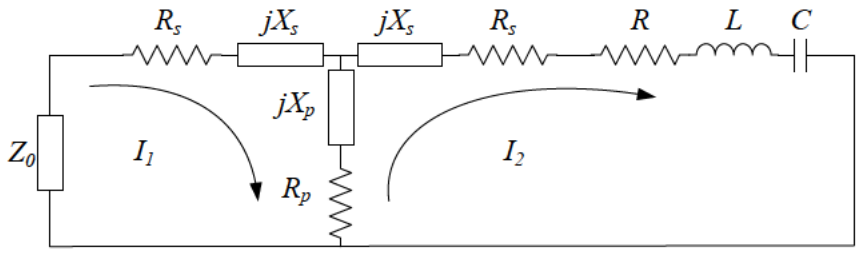

Figure 4.17: Equivalent circuit of a lossy external coupling with RLC resonator.

The external Q-factor is defined as the ratio of the stored energy in a resonator to the power loss in the input/output feed source. Therefore, it can be calculated using the lossy equivalent circuit from Figure 4.17 as

$$Q_{EXT} = \omega_0 \frac{W_{RES}}{P_{EXT}} = \omega_0 \frac{L\left|I_2\right|^2}{Z_0\left|I_1\right|^2} = \omega_0 \frac{L}{Z_0 \frac{R_P^2 + \omega_0^2 L_P^2}{\left(Z_0 + R_S + R_P\right)^2 + \left(\omega_0 L_S + \omega_0 L_P\right)^2}} \tag{4.60}$$

where (4.61) has been used.

$$\left|I_1\right|^2 = \left|I_2\right|^2 \frac{\left|Z_P\right|^2}{\left|Z_0 + Z_S + Z_P\right|^2} = \left|I_2\right|^2 \frac{R_P^2 + \omega_0^2 L_P^2}{\left(Z_0 + R_S + R_P\right)^2 + \left(\omega_0 L_S + \omega_0 L_P\right)^2} \tag{4.61}$$

4.3 Theory Validation

A first order WR-187 waveguide cavity filter with rectangular irises as the one shown in Figure 4.18 with a center frequency of $f_0 = 4.5$ GHZ and with -10 dB couplings has been designed and manufactured to verify the external coupling theory developed above. Table 4.2 collects the physical dimensions of the structure.

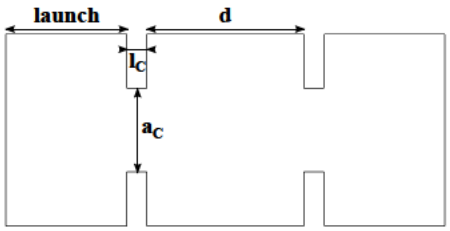

Figure 4.18: Designed Chebyshev type 1^{st} order waveguide direct-coupled-cavity filter with rectangular inductive couplings and $f_0 = 4.5$ GHz, -10 dB couplings, and $\sigma = 18306$ S.

Table 4.2: Physical dimensions (in mm) of the structure in Figure 4.18

Dimension	Value
launch	30
d	19.479
l_C	5
a_C	20.700

The material used in the fabrication of the filter was a steel alloy with unknown electrical properties. Therefore, the electrical conductivity in the simulation was optimized to match the center insertion loss of the measured data and hence a fair comparison in terms of center frequency and bandwidth could be done. The equivalent circuit was then obtained using the four previous outlined procedures. Table 4.3 lists all the information extracted from full-wave simulations needed to find the equivalent circuit of the filter in Figure 4.18 following all the exposed approaches. The second frequency point used in the derivation of the equivalent circuit has been chosen to be $f_S = f_0 + 10$ MHz ($f_S/f_0 = 1.0022$).

Table 4.3: External coupling parameters of the filter in Figure 4.18 obtained using CST Microwave Studio

Parameter	Value
$Z_{in,TL,even}(\omega_0)$	$277.48 + j357.26\ \Omega$
$Z_{in,TL,even}(\omega_S)$	$426.81 + j585.17\ \Omega$
$Z_{in,TL,odd}(\omega_0)$	$14.57 - j620.65\ \Omega$
$Z_{in,TL,odd}(\omega_S)$	$14.20 - j606.60\ \Omega$
$Z_{in,TL,singly}(\omega_0)$	$397.46 + j252.16\ \Omega$
$Z_{in,TL,singly}(\omega_S)$	$892.18 + j528.09\ \Omega$
$\phi(S_{11,even}(\omega_0))$	$-258.79°$
$\phi(S_{11,odd}(\omega_0))$	$-80.84°$
$\phi(S_{11,singly}(\omega_0))$	$102.21°$

The resulting circuit values are collected in Table 4.4, Table 4.5, Table 4.6, and Table 4.7, for all the four approaches developed above.

Table 4.4: Approach 1: final equivalent lossy circuit values

Section	Parameter	Value
TL Resonator	length	$\lambda_{g0}/2$ m
	$Z_C\|_{\omega=\omega_0}$	526.9 Ω
	$\alpha\|_{\omega=\omega_0}$	$241 \cdot 10^{-3}$ Nepers/m
	$\beta\|_{\omega=\omega_0}$	67.147 rad/s
Coupling 1	r_{S1}	1.986 mΩ
	x_{S1}	−0.162 H·rad
	r_{P1}	1.110 mΩ
	x_{P1}	0.163 H·rad

Table 4.5: Approach 2: final equivalent lossy circuit values

Section	Parameter	Value
TL Resonator	length	$\lambda_{g0}/2$ m
	$Z_C\|_{\omega=\omega_0}$	526.9 Ω
	$\alpha\|_{\omega=\omega_0}$	$241 \cdot 10^{-3}$ Nepers/m
	$\beta\|_{\omega=\omega_0}$	67.147 rad/s
Coupling 1	r_{S1}	3.467 mΩ
	x_{S1}	−0.173 H·rad
	r_{P1}	0.123 mΩ
	x_{P1}	0.167 H·rad

Figure 4.19 and Figure 4.20 show the full-wave simulation, the measured data and the response from the equivalent circuit obtained using all the different approaches. As expected, a good convergence is not observed when only an electric wall is used

Table 4.6: Approach 3: final equivalent lossy circuit values

Section	Parameter	Value
TL Resonator	length	$\lambda_{g0}/2$ m
	$Z_C\|_{\omega=\omega_0}$	526.9 Ω
	$\alpha\|_{\omega=\omega_0}$	$241 \cdot 10^{-3}$ Nepers/m
	$\beta\|_{\omega=\omega_0}$	67.147 rad/s
Coupling 1	r_{S1}	0.2889 mΩ
	x_{S1}	−0.1696 H·rad
	r_{P1}	2.882 mΩ
	x_{P1}	0.1634 H·rad

Table 4.7: Approach 4: final equivalent lossy circuit values

Section	Parameter	Value
TL Resonator	length	$\lambda_{g0}/2$ m
	$Z_C\|_{\omega=\omega_0}$	526.9 Ω
	$\alpha\|_{\omega=\omega_0}$	$241 \cdot 10^{-3}$ Nepers/m
	$\beta\|_{\omega=\omega_0}$	67.147 rad/s
Coupling 1	r_{S1}	−4.230 mΩ
	x_{S1}	−0.210 H·rad
	r_{P1}	7.385 mΩ
	x_{P1}	0.200 H·rad

to obtain the input impedance of the model under study (approach 4: only odd mode). On the other hand, excellent agreement between the full-wave simulation, the response from the equivalent circuit, and the measured data is obtained both in magnitude and in phase when the other approaches are used. A picture of the manufactured prototype is shown in Figure 4.21.

A study on how the second frequency point affect the accuracy of the results has been carried out for the second approach (only even mode) and it is summarized in Table 4.8. Good results are obtained when $f_0 - 50$ MHz $< f_S < f_0 + 50$ MHz ($f_S/f_0 = 1.0111$).

Furthermore, to assess the validity of the inter-resonator as well as the external coupling theory, a fifth order direct-coupled-cavity filter like the one shown in Figure 4.22 with parabolic irises has also been designed and manufactured.

The filter was designed using the standard filter theory [Matthaei et al., 1980]. The physical dimensions were obtained with the aid of a full-wave simulation program and are shown in Table 4.9.

The equivalent lossy circuits of the inter-resonator couplings were obtained following the steps in subsections 4.2.1 and 4.2.2 and using a similar model to that in Figure 4.9(a) adapted to the new geometry. The parameters needed to derive their equivalent lossy circuits are shown in Table 4.10.

For the external coupling, use was made of subsections 4.2.1 and 4.2.3. The first approach has been followed to derive the equivalent circuit and a similar model to

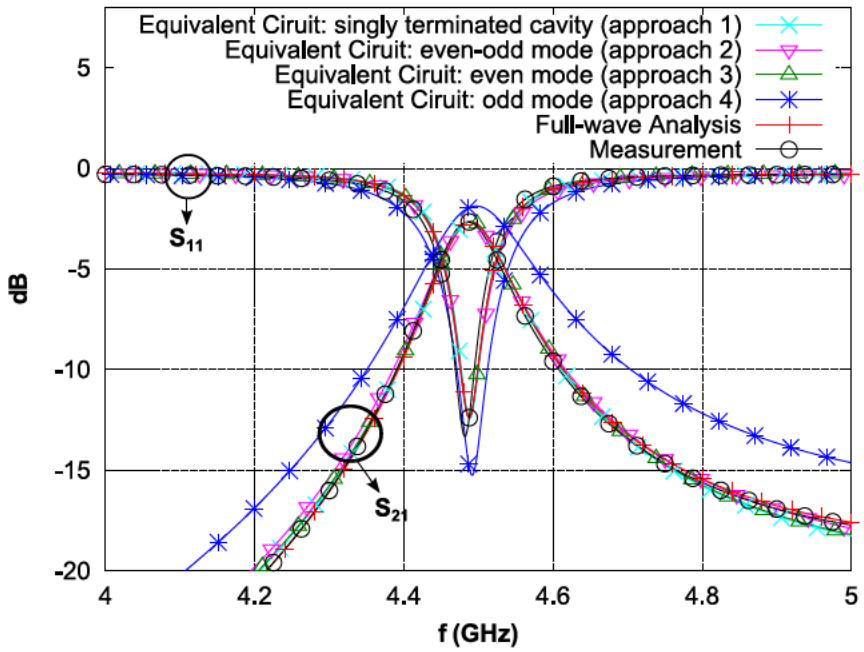

Figure 4.19: Equivalent circuit, simulated, and measured RF responses of the filter in Figure 4.18.

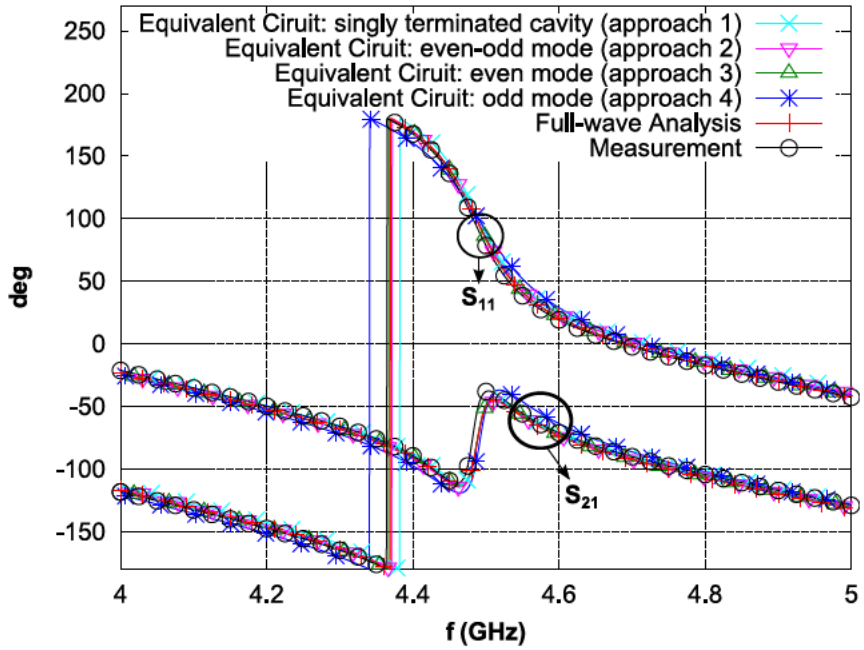

Figure 4.20: Equivalent circuit, simulated, and measured RF phase responses of the filter in Figure 4.18.

that shown in Figure 4.15(a) has been used with the new geometry. Table 4.11 collects the relevant information to derive the equivalent lossy circuit of the external coupling where $f_S = f_0 - 5$ MHz.

The values of the final equivalent lossy circuit based on transmission line resonators of the filter in Figure 4.22 are given in Table 4.12. Figure 4.23 and Figure 4.24 show the response from the equivalent lossy circuit, the full-wave

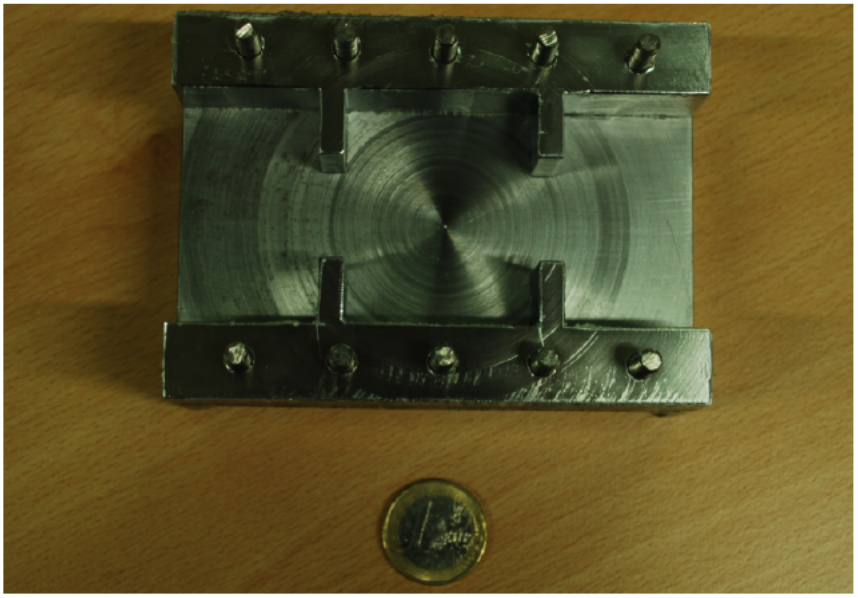

Figure 4.21: Manufactured 1^{st} order filter.

Table 4.8: Extracted parameters from simulation, measurement, and equivalent circuit for different f_S

Data from...	f_0 (GHZ)	BW (MHz)	IL (dB)	GD (ns)
Simulation	4.4896	103.2	2.649	3.437
Measurement	4.485	103.75	2.649	3.493
Equivalent Circuit ($f_S = f_0 + 150MHz$)	4.4904	117.6	2.655	3.051
Equivalent Circuit ($f_S = f_0 + 50MHz$)	4.4898	108.6	2.647	3.287
Equivalent Circuit ($f_S = f_0 + 10MHz$)	4.4898	104.4	2.643	3.395
Equivalent Circuit ($f_S = f_0 + 2MHz$)	4.4898	103.8	2.643	3.418
Equivalent Circuit ($f_S = f_0 - 2MHz$)	4.4898	103.2	2.642	3.430
Equivalent Circuit ($f_S = f_0 - 10MHz$)	4.4898	102.6	2.642	3.453
Equivalent Circuit ($f_S = f_0 - 50MHz$)	4.4898	99	2.637	3.574
Equivalent Circuit ($f_S = f_0 - 150MHz$)	4.4898	89.4	2.625	3.924

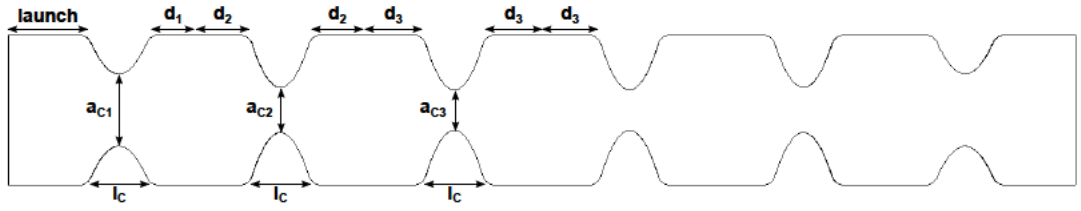

Figure 4.22: Designed Chebyshev type 5^{th} order waveguide direct-coupled-cavity filter with parabolic inductive couplings and $f_0 = 11$ GHz, $BW = 100$ MHz, $RL = 30$ dB and $\sigma = 18.797$ MS.

simulated response, and the measurements obtained from a manufactured prototype. The response from the equivalent circuit derived with the theory in

Table 4.9: Physical dimensions (in mm) of the structure in Figure 4.22

Parameter	Value
a	19.05
b	5
launch	20
d_1	5.259
d_2	6.981
d_3	7.149
a_{C1}	9.544
a_{C2}	5.669
a_{C3}	5.080
l_C	8
cavity-iris radii	1.5

Table 4.10: Inter-resonator coupling parameters obtained using Ansoft HFSS

	Coupling 2	Coupling 3
f_{even} (GHz)	10.8936	10.9270
f_{odd} (GHz)	11.1105	11.0732
Q_{even}	2782	2826
Q_{odd}	3092	3067

Table 4.11: External coupling parameters obtained using Ansoft HFSS

$Z_{in,TL}\|_{\omega=\omega_0}$	$9.41 - j185.43\ \Omega$
$Z_{in,TL}\|_{\omega=\omega_S}$	$11.05 - j214.32\ \Omega$
$\phi(S_{11})\|_{\omega=\omega_0}$	$-86.46°$

[Deslandes and Boone, 2008] has also been included for comparison. The group delay is given in Figure 4.25.

The agreement between full wave simulation and the response from the equivalent circuit is excellent. The insertion loss from the full-wave simulation is now accurately predicted by the new approach described in this chapter. The response of the manufactured filter also agrees very well, as it only deviates 3 MHz from the full-wave and the equivalent circuit responses. This deviation is mainly due to measuring the filter under normal air conditions instead of under vacuum conditions. It is interesting to observe that no tuning process has been carried out in the manufactured filter.

The out of band response is not accurately predicted by the derived lossy equivalent circuit. As discussed before, a waveguide coupling structure is not an ideal impedance inverter but it has a loading effect over its adjacent cavities that depends on the geometry of the coupling structure itself and on the coupling value, and also on the frequency. The loading effect of the coupling at center frequency is taken into account in the derived equivalent circuit. However, such is not the case at the spurious frequencies and so the spurious of the equivalent circuit do not perfectly

Table 4.12: Final equivalent lossy circuit values of the structure in Figure 4.22

Section	Parameter	Value
TL Resonator	length	$\lambda_{g0}/2$ m
	$Z_C\|_{\omega=\omega_0}$	174.5 Ω
	$\alpha\|_{\omega=\omega_0}$	$45.8 \cdot 10^{-3}$ Nepers/m
	$\beta\|_{\omega=\omega_0}$	161.148 rad/s
Coupling 1	r_{S1}	130.285 μΩ
	l_{S1}	−3.021 pH
	r_{P1}	10.696 μΩ
	l_{P1}	3.005 pH
Coupling 2	r_{S2}	62.201 μΩ
	l_{S2}	−0.4677 pH
	r_{P2}	36.012 μΩ
	l_{P2}	0.4586 pH
Coupling 3	r_{S3}	68.418 μΩ
	l_{S3}	−0.3138 pH
	r_{P3}	27.113 μΩ
	l_{P3}	0.3093 pH

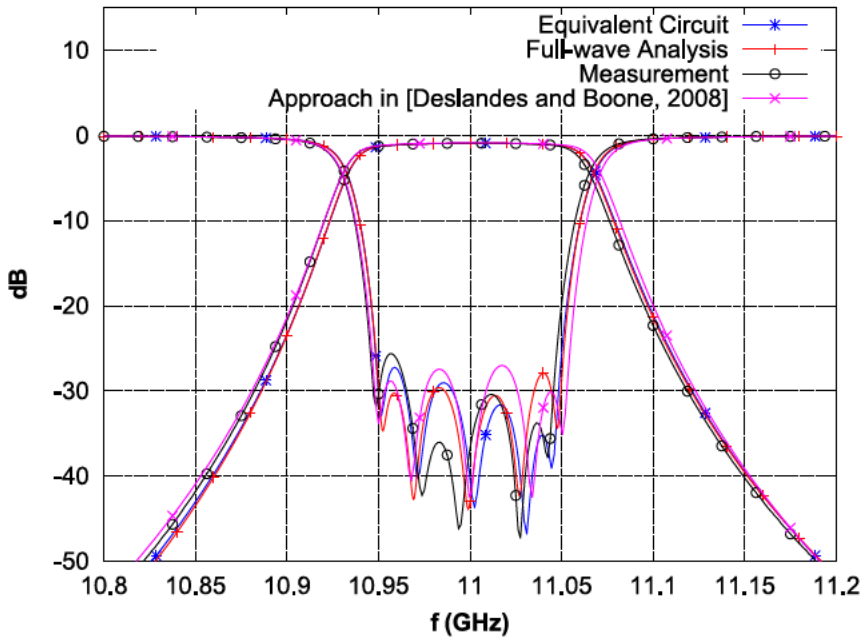

Figure 4.23: Equivalent circuit, simulated, and measured RF responses of the structure in Figure 4.22.

match the measured results (Figure 4.26). In spite of this, the spurious behavior of the equivalent circuit is not too far from the measured response, and so it could be used as a first approach to predict spurious free range.

A photograph showing the internal geometry of the manufactured filter is shown

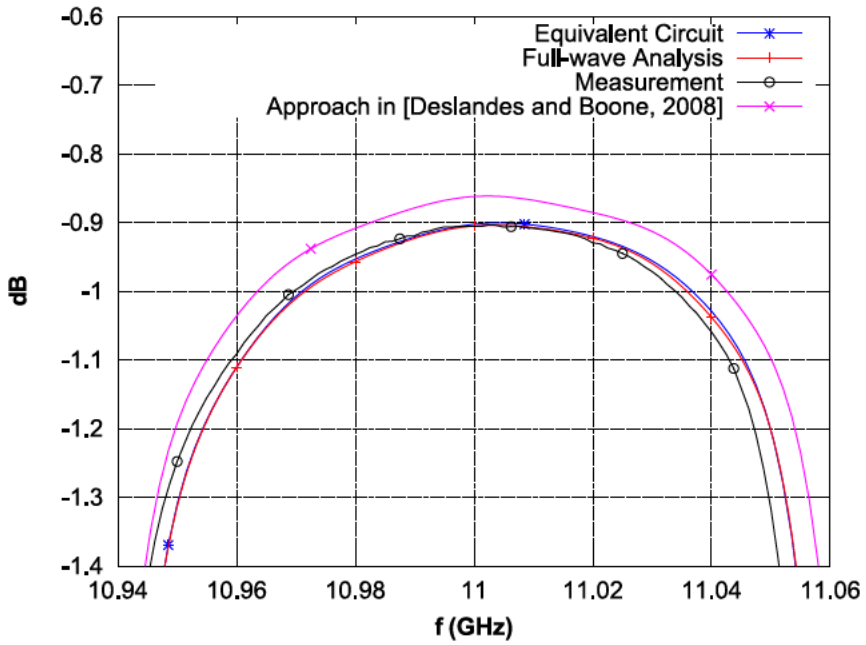

Figure 4.24: Equivalent circuit, simulated, and measured $S_{2,1}$ detail.

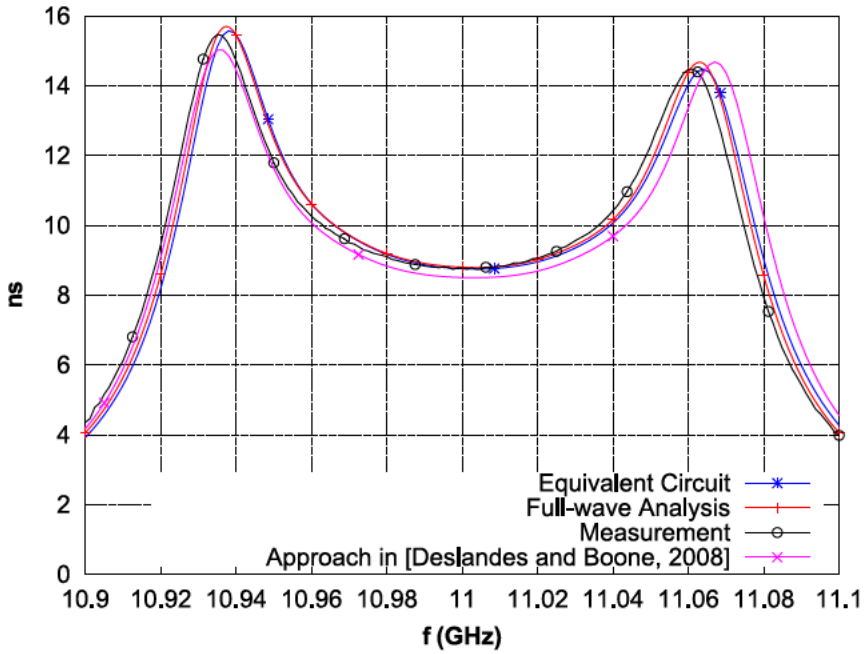

Figure 4.25: Equivalent circuit, simulated, and measured transmission group delay.

in Figure 4.27.

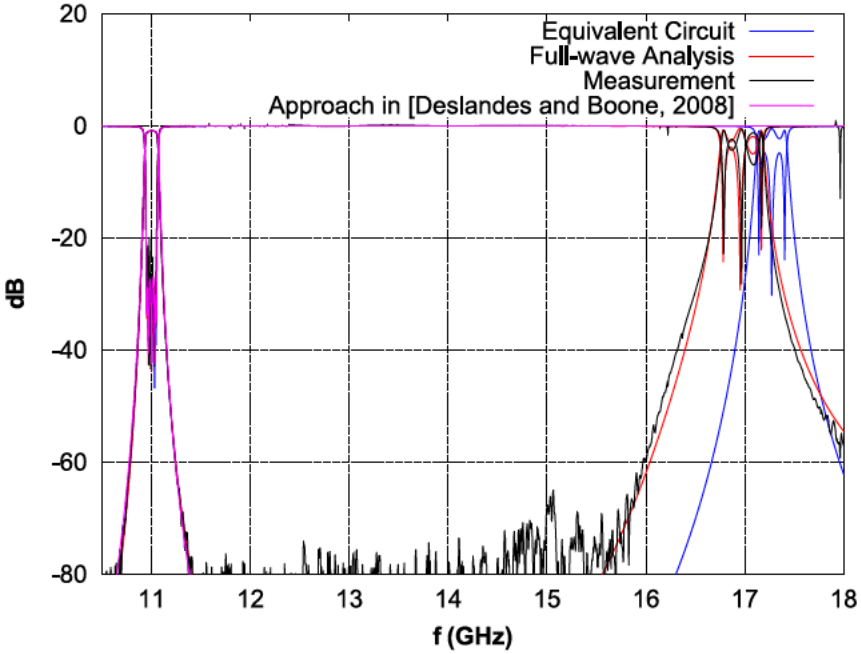

Figure 4.26: Equivalent circuit and simulated out of band responses.

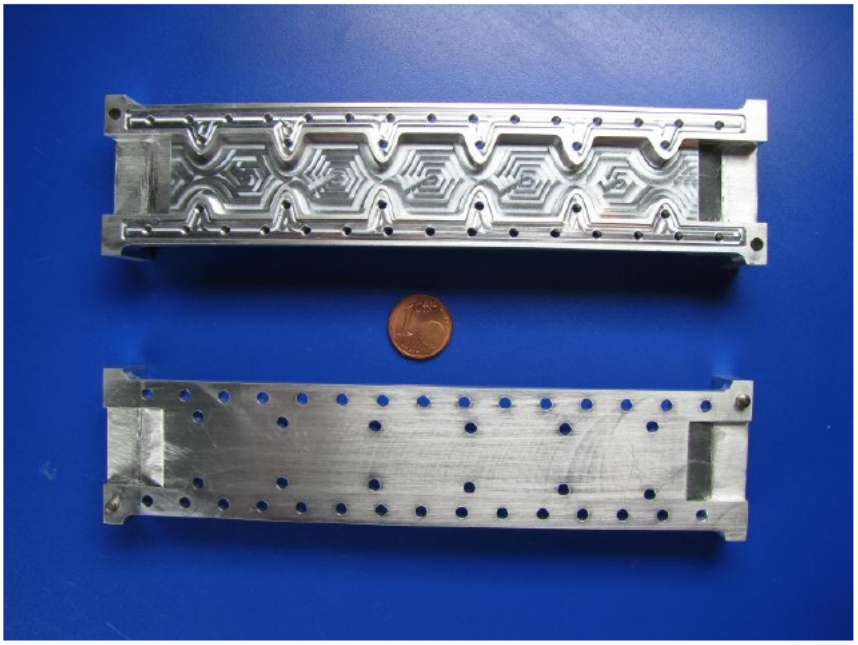

Figure 4.27: Fabricated filter.

4.4 Impact of Lossy Couplings on the Filter Response

The impact of adding losses to the couplings in the equivalent circuit on the filter response is discussed in this section. The response of the equivalent circuit is plotted in Figure 4.28 for different configurations:

- When all the cavity and coupling resistors are set to zero (blue line).

- When all the cavity resistors are set to zero, but with lossy couplings (red line).
- When all the coupling resistors are set to zero, but with lossy cavities (green line).
- When both cavities and couplings are lossy (black line).

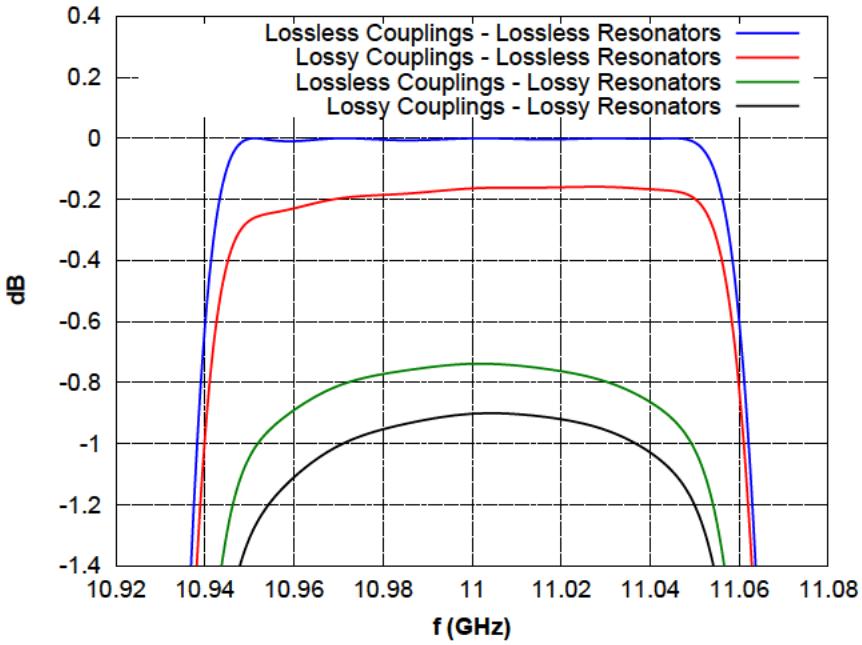

Figure 4.28: RF response of the extracted equivalent circuit with the theory in this work.

When all the losses are removed from the equivalent circuit (blue line), the response match that of the lossless synthesis ($f_0 = 11$ GHz, $BW = 100$ MHz, and $RL = 30$ dB). If now, only losses due to the coupling structures are included (red line), the insertion loss increases around 0.2 dB and an asymmetry in the passband can be observed. This is not the case if only losses in the resonators are taken into account (green line). Finally, when all the losses due to cavities and couplings are taken into account in the equivalent circuit, the final lossy response matches well the simulation results and the asymmetry in the passband appears again. It is proved then that this dispersion in the passband is due to lossy couplings and it is of importance to take it into account in the design process. As it will be shown in the next chapter, the passband dispersion due to lossy couplings can be reduced if different coupling geometries are used.

For comparison, the responses of the equivalent circuit obtained using the theory in [Deslandes and Boone, 2008] for the different losses configurations explained above are shown in Figure 4.29. Note that when losses in couplings are included in the equivalent circuit (either with lossless or lossy resonators), only the in-band dispersion can be observed, but the absolute value of insertion loss at the design center frequency does not change with respect to the lossless couplings case. When lossless resonators are used in the equivalent circuit, a gain can be observed in the

upper band of the response, proving that the loss distribution between cavities and coupling structures is not correct if the theory in [Deslandes and Boone, 2008] is used.

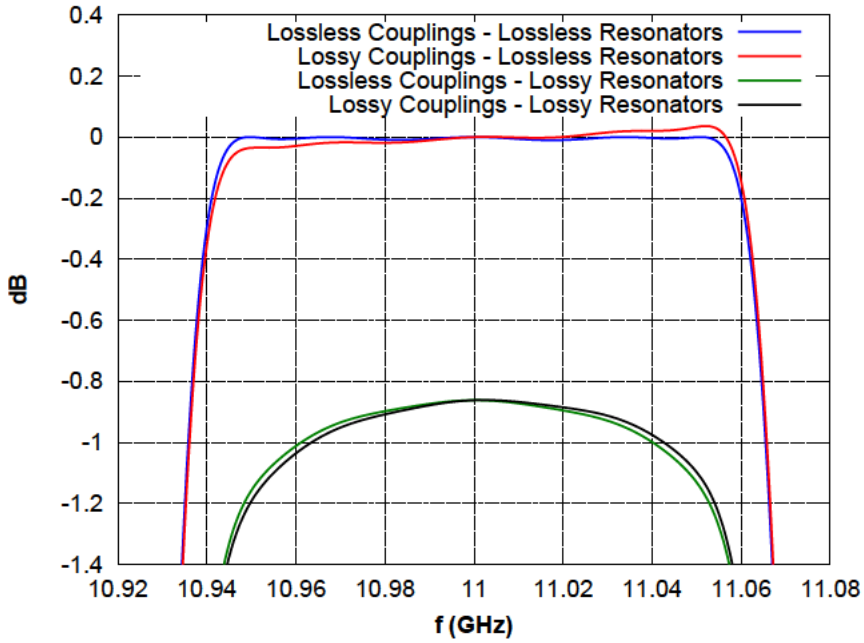

Figure 4.29: RF response of the extracted equivalent circuit with the theory in [Deslandes and Boone, 2008].

4.5 Practical Applications

4.5.1 Filter Response Optimization

The theory presented in this chapter can help to accurately find the individual contributions of each coupling structure and resonators to the overall loss in a filter. This allows to optimize the individual components separately, without the need of carrying out full-wave simulations of the complete filter. In this context, an individual geometry optimization of the different parts of a filter can be carried out to improve the final response of the filter once they are assembled. To do so, a database containing the equivalent circuits of coupling structures with different geometries and covering a wide range of coupling coefficients can be obtained with the aid of the derived equivalent circuit. Hence, the theory developed in this work can help to find the filter response which best suits some given specifications much faster than if full-wave simulations of complete filter structures had to be used.

As an example, consider a sinusoidal shaped coupling structure. To create the database, the models for internal couplings (Figure 4.30(a)) and external couplings (Figure 4.30(b)) are used with the geometry under study. Next, a sweep over the iris aperture (a_{CI} and a_{CE}) and the cavity length (d) is carried out to cover a wide range of coupling coefficients and frequencies (i.e. 10 points for the iris aperture and 10 points for the cavity length). Note that the iris length has been kept constant in

this example ($l_{CI} = 4.2mm$ and $l_{CE} = 4mm$). Finally, the equivalent circuits can be obtained following the above theory.

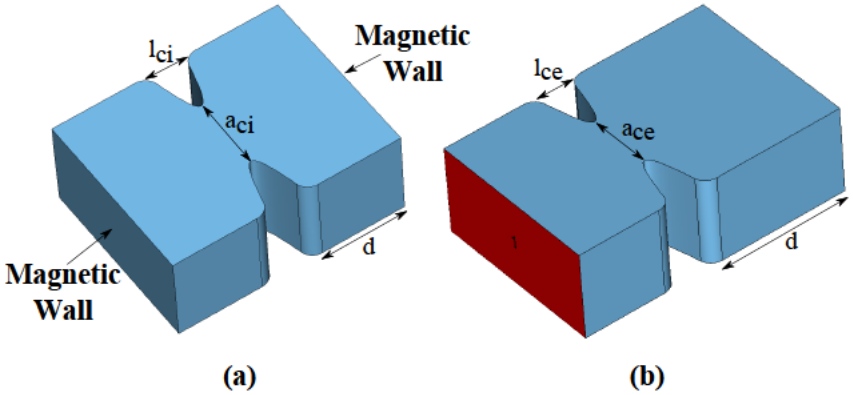

Figure 4.30: (a) Internal coupling model and (b) external coupling model.

Figure 4.31 and Figure 4.32 collect the information derived from the previous tests for the internal and external couplings, respectively. A very wide range of coupling coefficients at different frequencies can be obtained if interpolation between samples is used.

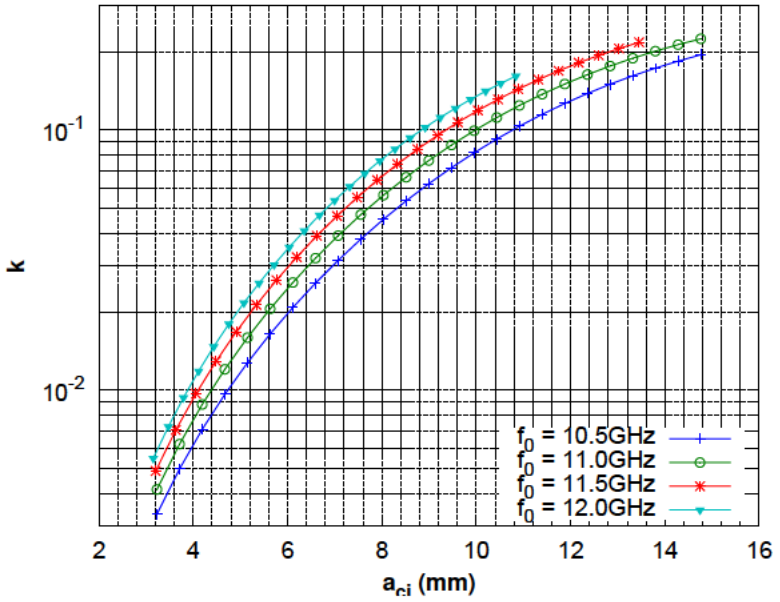

Figure 4.31: Internal coupling coefficient versus iris aperture for different frequencies.

A wide variety of filters of different orders, bandwidths, center frequencies can now be designed in matter of seconds just by using the equivalent lossy circuits with no need of further full-wave simulations. Thanks to this, a filter response can be optimized to meet some certain specifications of insertion loss, rejection, bandwidth, or center frequency very efficiently. Figure 4.33(a) shows three filters with different center frequencies but same bandwidth, return loss and order whose

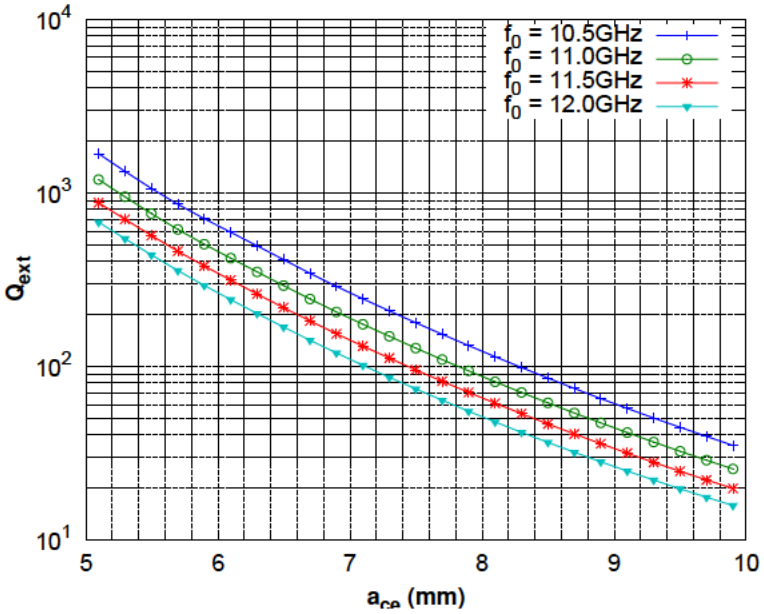

Figure 4.32: External coupling coefficient versus iris aperture for different frequencies.

equivalent circuits have been obtained from the database. Also, the equivalent circuits of three filters with different bandwidth but with same center frequency, return loss, and order can be seen in Figure 4.34(a). Finally, Figure 4.35(a) shows the RF response of the equivalent circuits of three filters of different orders and with same center frequency, bandwidth and return loss. Note that the insertion loss prediction in all the three cases (Figure 4.33(b), Figure 4.34(b) and Figure 4.35(b)) of the equivalent circuits perfectly matches the insertion loss obtained in the simulations.

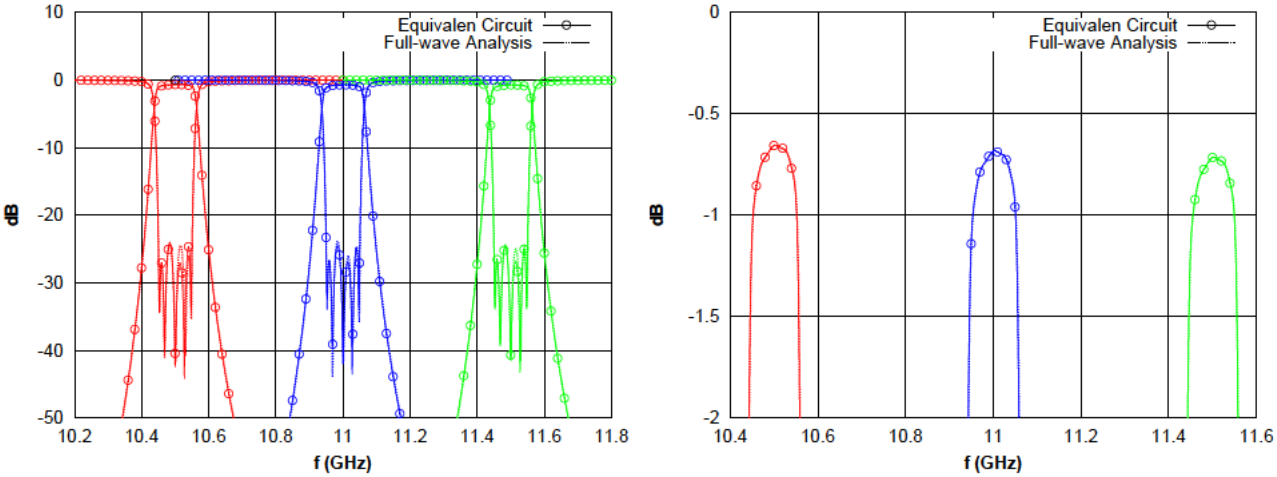

Figure 4.33: (a) Equivalent circuit and simulated RF responses of filters with $f_0 = 10.5$ GHz, $f_0 = 11$ GHz, and $f_0 = 11.5$ GHz with the same BW, RL, and order and (b) $S_{2,1}$ detail.

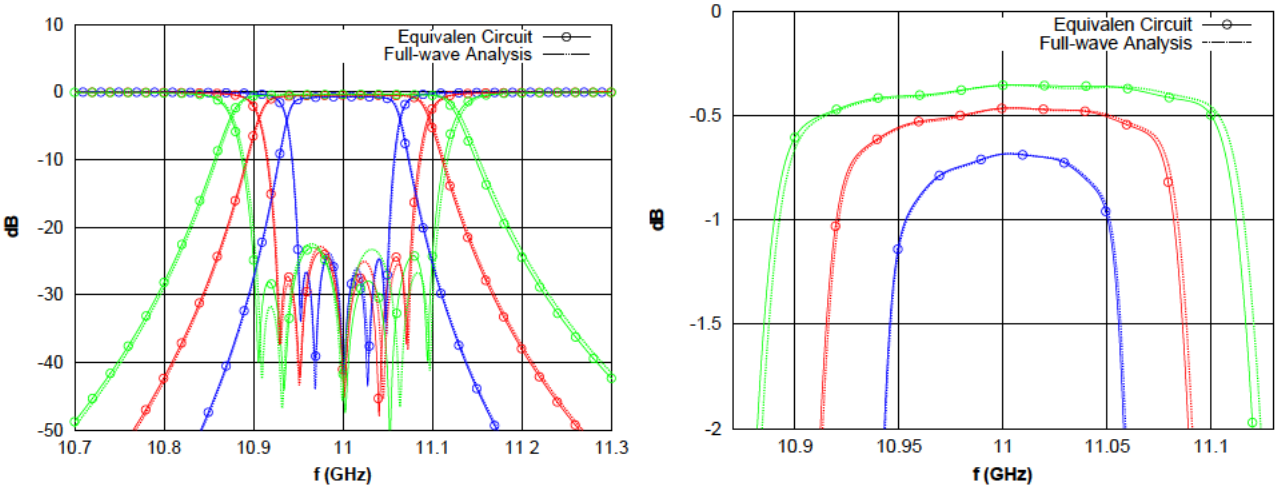

(a) (b)

Figure 4.34: (a) Equivalent circuit and simulated RF responses of filters with $BW = 100$ MHz, $BW = 150$ MHz, and $BW = 200$ MHz with the same f_0, RL, and order and (b) $S_{2,1}$ detail.

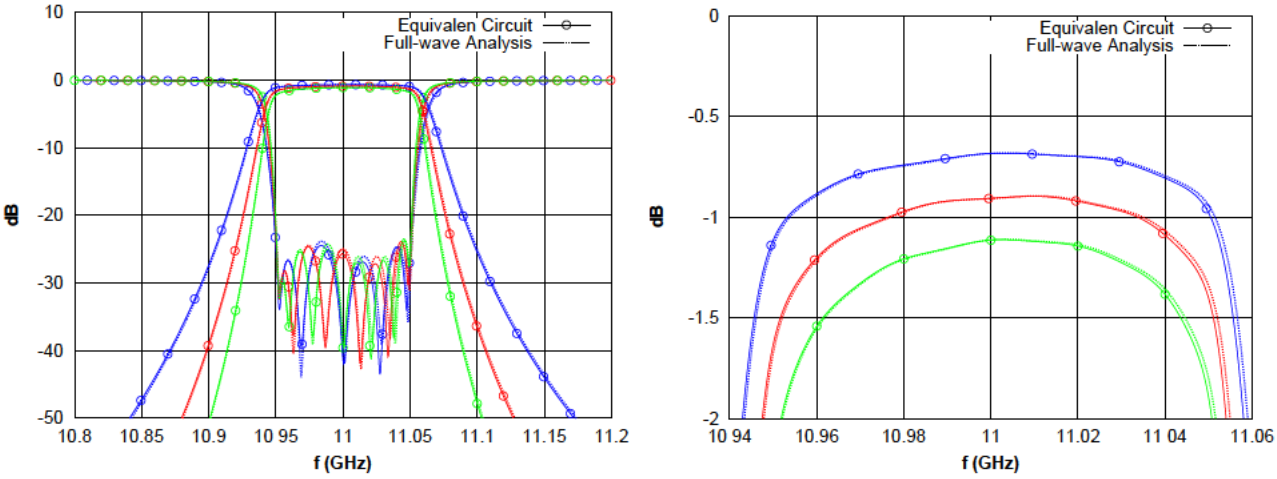

(a) (b)

Figure 4.35: (a) Equivalent circuit and simulated RF responses of filters with $N = 5$, $N = 6$, and $N = 7$ with the same f_0, BW, and RL and (b) $S_{2,1}$ detail.

These results show that the lossy equivalent circuits derived in the work can be used for a very accurate loss prediction in a wide range of filters, without additional lengthy full wave simulations of complete filter structures.

4.5.2 Lossy Yield Analysis

Another application of the theory developed in this work is the yield analysis of the designed filter with manufacturing tolerances. It can be presented as an extension to the work in [Folgero and Kocbach, 2003]. However, using the equivalent circuit theory derived in this work the yield analysis of the filter can be performed with

an accurate evaluation of the resulting losses. As an example, the results of the yield analysis (applying a tolerance factor of $tol = \pm 20\mu m$ and 500 simulations) performed directly on the equivalent circuit, including losses in cavities as well as in coupling structures are included in Figure 4.36(a). Note that no additional full-wave simulations are needed to obtain these results (details of the achieved losses are shown in Figure 4.36(b)). If a tolerance factor of $tol = \pm 40\mu m$ is used instead (500 simulations), the yield distribution in Figure 4.37(a) is obtained and a detail of the $S_{2,1}$ is shown in Figure 4.37(b). A random response has been chosen and simulated in a full-wave program. The result has also been included in the graphs and it shows very close agreement with the predicted response from the equivalent circuit.

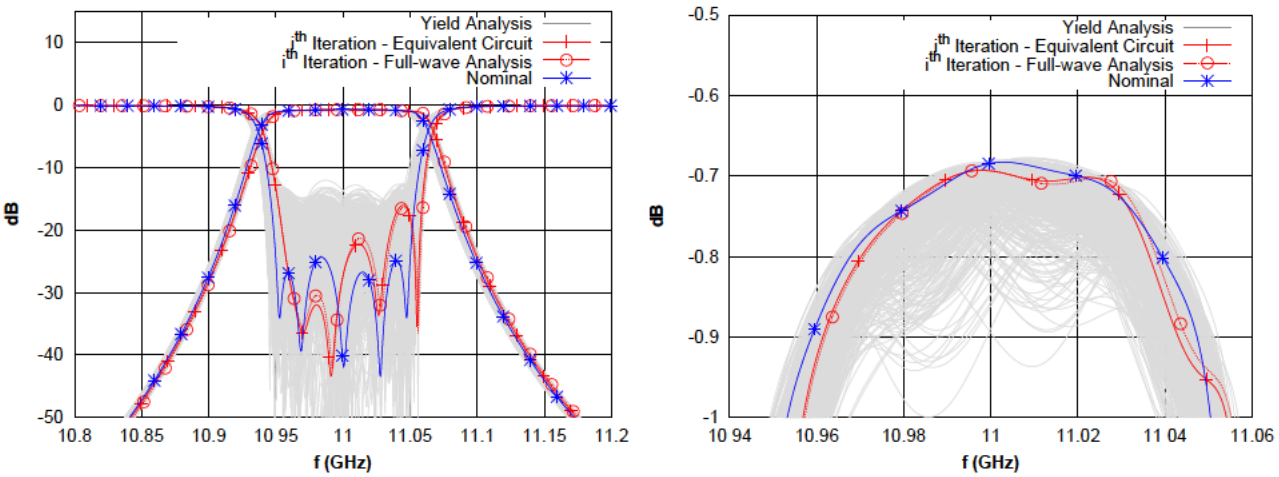

(a) (b)

Figure 4.36: (a) Yield analysis including losses everywhere in the filter (Tol = $\pm 20\mu m$) and (b) $S_{2,1}$ detail.

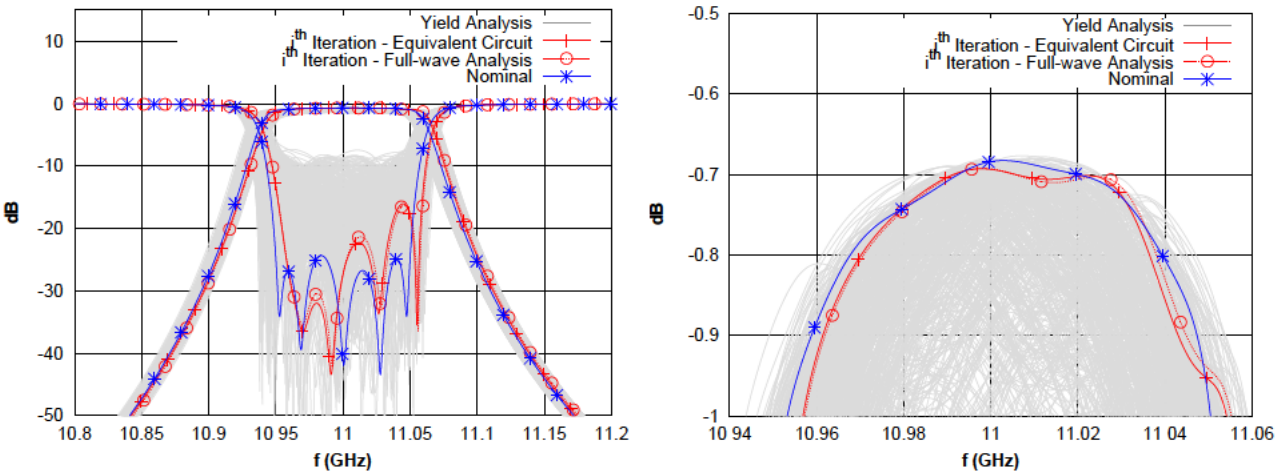

(a) (b)

Figure 4.37: (a) Yield analysis including losses everywhere in the filter (Tol = $\pm 40\mu m$) and (b) $S_{2,1}$ detail.

4.6 Conclusion

A rigorous derivation of an equivalent circuit of a direct-coupled-cavity filter with arbitrary shaped cross section and coupling geometries including losses due to cavities and coupling structures has been presented in this chapter. With the correct understanding of the fields inside the cavities of a filter and using the even and odd mode theory, equivalent lossy circuits of the inter-cavity couplings as well as the external couplings have been derived. Assigning the losses of a half-wavelength lossy transmission line to the resonators, the losses due to the coupling structures can be extracted. A fifth degree direct-coupled-cavity filter has been designed, and the above theory has been successfully applied. The agreement between simulation and the response from the extracted equivalent circuit is excellent. The filter has also been manufactured and measured. No tuning process has been carried out. The measured response agrees very well with full wave simulations and with the novel extracted equivalent lossy circuit. The theory has been successfully applied to the response optimization of a wide range of filters avoiding the use of full-wave simulations of complete filter structures. Also, the theory derived has been applied to the yield analyses of arbitrarily-shaped filters including losses in both resonators and coupling structures.

CHAPTER 5

LOSS REDUCTION IN NARROW-BAND WAVEGUIDE DIRECT-COUPLED-CAVITY FILTERS BY SHAPING COUPLING STRUCTURES

In this chapter a new technique to reduce losses in waveguide filters by introducing appropriate shaping in the coupling structures is described. To assess the losses in the coupling structures an effective quality factor (Q_{eff}) is defined based on circuit parameter extraction techniques, as discussed in Chapter 4. Results show that the new quality factor is able to represent accurately the losses introduced by coupling structures, independently on their shapes. The theory is applied to the study of several types of coupling waveguide windows using a wide range of geometrical shapes, including parabolic and sinusoidal irises, and circular windows. Using the theory proposed, the coupling structure with the lowest insertion losses has been identified. Besides, the impact of the coupling geometry on the spurious free range (SFR) of the final filter has also been discussed. Several filters are designed using different coupling windows for comparison purposes. Measured results are also included to validate the theory presented. Results show that around 15% of loss reduction can be achieved in a 5 pole inline filter if circular windows are used as coupling elements, with respect to a baseline filter that uses standard rectangular irises.

5.1 Introduction

Waveguide cavity filters are widely used in space industry due to their low dissipation loss and high power handling capability [Yu, 2007]. However, today most demanding applications require very stringent loss specifications and new techniques to minimize dissipated power in waveguide band-pass filters are continuously investigated. In [Flory and Taber, 1997], a new resonator based on Bragg reflectors that increases the unloaded Q-factor with respect to that obtained with traditional rectangular waveguides was presented. Dielectric resonators [Cohn, 1968] are also used when high Q-factors are needed and when volume is a constrain. However, the main

disadvantage of this kind of structures is that the center frequency variation over temperature is excessive for many applications, requiring temperature stabilization.

Traditionally, only losses in the unloaded cavities were taken into account in the synthesis of practical filters [Cohn, 1959]. However, it is well known that the final filter performance could lead to responses of 15-20% increased losses, as it is shown in Fig. 5.1 for a typical design in Ku-band.

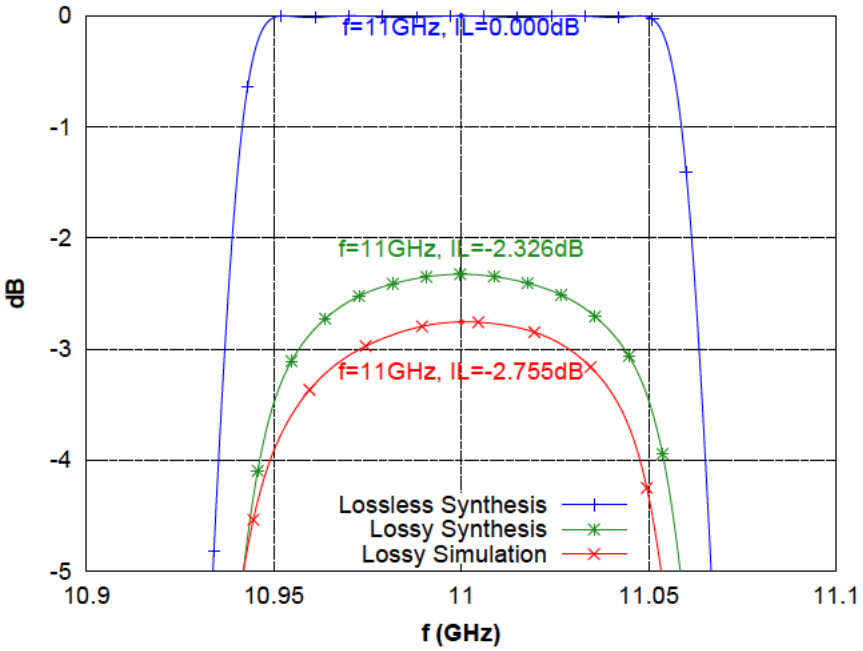

Figure 5.1: Lossless synthesis, lossy synthesis including losses in resonators and lossy simulation including losses everywhere.

The insertion loss difference between lossy synthesis and full-wave simulation with losses is attributed to the power loss in the coupling structures. In this context, it is clear that overall filter losses can be reduced if losses in couplings are minimized.

Previous studies [Suzuki and Hosono, 1983], [Lorente et al., 2009b], [Zafra and Ernst, 2006] proved that a clever shaping of the geometry of waveguide structures yields to reduced filter insertion loss. In [Suzuki and Hosono, 1983], a truncated Fourier series is taken as an approximation of a waveguide cross section and by applying optimization with the aid of a full-wave simulation program the optimum cross section, which has minimum conductor loss, was obtained. A slightly modified shape was then used in the design of direct coupled waveguide filters [Lorente et al., 2009b], [Zafra and Ernst, 2006], where also shaping in coupling structures was introduced. However, a suitable optimization parameter that could be used to reduce losses was not properly identified. Only the maximum current density in the apertures was optimized when they were not connected to adjacent resonators.

Thal [Thal, 1982] experimentally proved the impact in the unloaded Q degradation of a fixed cavity due to a thin aperture with different height to width ratios, used as inter-resonator coupling. This study was carried out under the assumption that same coupling loadings yield to same coupling coefficients. However, this assumption is not valid anymore for different iris thicknesses or for completely different

coupling geometries.

This chapter extends the work presented in [Lorente et al., 2009b], [Zafra and Ernst, 2006], [Thal, 1982] and overcomes their limitations. The aim is to find optimized coupling geometries that minimize overall losses in waveguide cavity filters. However, full-wave geometry optimization of a complete waveguide filter is not feasible due to the extreme complex geometries expected to be obtained and the very long simulation time entailed to it. Instead, coupling structures can be individually optimized for low losses, and then combined to yield a final improved filter RF response. For this purpose, a new effective quality factor is defined that accurately represents losses introduced by coupling apertures based on circuit parameter extraction techniques.

The new theory has been applied to the study of several types of coupling waveguide windows using a wide range of geometrical shapes, including parabolic and elliptic irises, and circular windows. Results show optimum values of the coupling physical dimensions for a given geometry, leading to minimum losses. The impact of these type of geometries on the spurious free range of the final filter is also highlighted in this chapter.

Several filters with different coupling geometries have been designed, simulated and manufactured for validation. The results are presented in this chapter, confirming the validity of the techniques derived. Results show that up to 12% of loss reduction can be achieved in a 5 pole inline filter if circular windows are used as coupling elements, with respect to a baseline filter that uses standard rectangular windows, and even more than 20% if the geometry of the cavities is also varied.

High power simulations have also been carried out for filters with rectangular and shaped irises, and the results are collected in Appendix E. As expected, simulations show that the shaping applied in the coupling structures has little or no effect on the multipactor threshold in a direct-coupled-cavity filter. This is because the lowest multipactor threshold is found where the highest E field concentrates, which for this type of filters occurs in the center of the cavities, where shaping has not been applied.

5.2 Definition of Novel Effective Q for Loss Prediction in Coupling Structures

A new effective Q-factor (Q_{eff}) that accurately represents the power loss introduced by coupling geometries is presented in this section for both inter-resonator as well as external couplings. The effective Q-factor can be defined as

$$Q_{\text{eff}} = \omega_0 \frac{W_T}{P_T} \tag{5.1}$$

where W_T and P_T are the stored energy and dissipated power, respectively, in the coupling structure and the adjacent cavities. The equivalent circuits obtained in the previous chapter will be of use to obtain an expression of the effective Q-factor that will be used to optimize the coupling geometries. It will be shown that improving the effective Q-factor of these structures will yield to an improved loss performance in the final filter.

5.2.1 Inter-Resonator Coupling

Figure 5.2 shows the equivalent circuit of two halved resonators coupled through a lossy coupling as derived in the previous chapter. The transmission line resonators have been replaced by their equivalent lumped element circuits for simplicity, as explained in section 4.2.1.

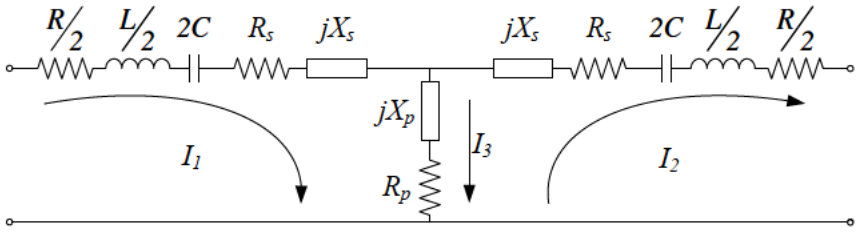

Figure 5.2: RLC equivalent circuit of inter-resonator coupling.

For narrow-band applications and inductive coupling $X_S = \omega L_S$ and $X_P = \omega L_P$ can be considered.

By further expanding (5.1), the effective Q-factor of an inter-resonator coupling can be expressed in terms of the components of the equivalent circuit as

$$Q_{\text{eff}} = \frac{\frac{\omega_0 L}{2}\left(|I_1|^2 + |I_2|^2\right) + \frac{1}{2}X_s\left(|I_1|^2 + |I_2|^2\right) + \frac{1}{2}X_p\,|I_3|^2}{\frac{R}{2}\left(|I_1|^2 + |I_2|^2\right) + R_s\left(|I_1|^2 + |I_2|^2\right) + R_p\,|I_3|^2} \tag{5.2}$$

where I_1, I_2, and $I_3 = I_1 - I_2$ are the currents flowing through the circuit in Figure 5.2 when it is cascaded to the rest of the filter. To calculate them, the equivalent circuit of the complete filter must be first extracted and that would require simulating the rest of the non-optimum coupling structures. To avoid that, (5.2) can be further reduced and made current independent if low loss approximation is assumed.

To that end, consider the $ABCD$ matrix of an impedance inverter:

$$\begin{bmatrix} V_1 \\ I_1 \end{bmatrix} = \begin{bmatrix} 0 & -jK \\ \frac{-j}{K} & 0 \end{bmatrix} \begin{bmatrix} V_2 \\ I_2 \end{bmatrix}, \tag{5.3}$$

If the inverter is terminated by a load impedance (Z_L), a relation between the current at the input and the current at the output can be found as

$$I_1 = \frac{-j}{K}V_2 = \frac{-j}{K}I_2 Z_L \tag{5.4}$$

Thus, the phase shift between I_1 and I_2 is

$$\angle I_1 = \angle I_2 + \angle Z_L - \angle K - 90^\circ \tag{5.5}$$

For in-line filters, each resonator sees approximately a matched load at the pass-band center frequency and therefore, Z_L and K are real ($\angle Z_L = 0^\circ$ and $\angle K = 0^\circ$) yielding to a 90° phase shift between the two currents. Under this condition, the amplitude of the current in the shunt branch can be expressed as

$$|I_3|^2 = |I_1 - I_2|^2 = |I_1|^2 + |I_2|^2 \tag{5.6}$$

Hence, 5.2 can be rewritten as

$$Q_{\text{eff}} = \frac{\omega_0 L + X_s + X_p}{R + 2R_s + 2R_p} \tag{5.7}$$

Note that 5.7 is only valid for frequencies in the passband, where the filter is matched and the 90° phase condition is approximately fulfilled.

Consider now the analytical expression for the resonant even and odd frequencies and Q-factors of the circuit in Figure 5.2, which are derived in terms of the circuit components as

$$\omega_{odd}^2 = \frac{1}{\frac{L}{2} + L_s} \tag{5.8}$$

$$\omega_{even}^2 = \frac{1}{\frac{L}{2} + L_s + 2L_p} \tag{5.9}$$

$$Q_{odd} = \omega_{odd} \frac{\frac{L}{2} + L_s}{\frac{R}{2} + R_s} \tag{5.10}$$

$$Q_{odd} = \omega_{odd} \frac{\frac{L}{2} + L_s + 2L_p}{\frac{R}{2} + R_s + 2R_p} \tag{5.11}$$

By further combining (5.8)-(5.11) into (5.7), an expression of the effective Q-factor that only depends on the center frequency and on the even and odd mode frequencies and Q-factors of the structure can be finally obtained as

$$Q_{\text{eff}} = \omega_0 \frac{\frac{1}{\omega_0^2} + \frac{1}{2}\left(\frac{1}{\omega_{odd}^2} + \frac{1}{\omega_{even}^2}\right)}{\frac{1}{\omega_{odd} Q_{odd}} + \frac{1}{\omega_{even} Q_{even}}} \tag{5.12}$$

It will be shown that maximizing (5.12) for each inter-resonator coupling of a filter will assure the minimization of the final insertion loss of the complete filter.

5.2.2 External Coupling

Figure 5.3 shows the equivalent circuit of a resonator coupled through an inductive circuit to the input feed source as derived in the previous chapter for the external coupling, where $X_S = \omega L_S$ and $X_P = \omega L_P$ is selected for narrow-band applications and inductive couplings. Again, the transmission line resonators have been replaced by their equivalent lumped element circuits for simplicity, as explained in section 4.2.1.

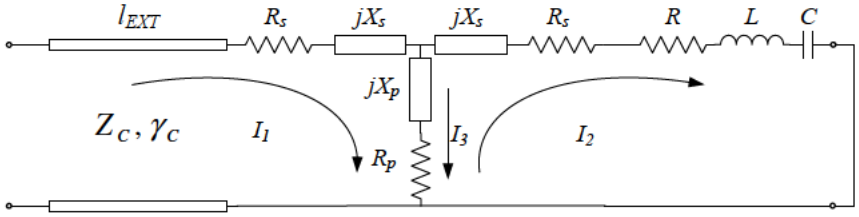

Figure 5.3: RLC equivalent circuit of external coupling.

From Figure 5.3 the effective Q-factor of the external coupling can be expressed as

$$Q_{\text{eff}} = \frac{\omega_0 L \left|I_2\right|^2 + \frac{1}{2} X_s \left(\left|I_1\right|^2 + \left|I_2\right|^2\right) + \frac{1}{2} X_p \left|I_3\right|^2}{R \left|I_2\right|^2 + R_s \left(\left|I_1\right|^2 + \left|I_2\right|^2\right) + R_p \left|I_3\right|^2} \tag{5.13}$$

where I_1, I_2, and $I_3 = I_1 - I_2$ are the currents flowing through the external coupling circuit. Assuming low loss as in the inter-resonator case, the 90° phase shift condition between currents I_1 and I_2 also applies here and so (5.6). Hence, currents in the circuit of Figure 5.3 can be expressed as

$$\left|I_3\right|^2 = \left|I_1\right|^2 + \left|I_2\right|^2 = \left|I_2\right|^2 C \tag{5.14}$$

where

$$C = \left(\frac{\left(R_s + R_p + R\right)^2 + \left(X_s + X_p\right)^2}{R_p^2 + X_p^2} + 1 \right) \tag{5.15}$$

has been obtained by circuit relations. Finally, the effective Q-factor of the external coupling is given as

$$Q_{\text{eff}} = \frac{2\omega_0 L + \left(X_s + X_p\right) C}{2R + \left(R_s + R_p\right) C} \tag{5.16}$$

Again, maximizing this expression for the external coupling will yield to an improved insertion loss response of the final filter, as it will be shown later.

5.3 Performance of Coupling Geometries

The aim of this section is to find an optimized coupling geometry that can be used in a complete filter to reduce its final losses and improve its spurious free range. To that end, an extensive study of different coupling structures whose geometries are driven by mathematical curves has been carried out. The effective Q-factor of inter-resonator and external couplings with the proposed geometries has been calculated as described in Section 5.2 and evaluated.

It will be shown that different geometries lead to different effective Q-factors of the coupling structures, but also the ratio between the thickness of the apertures and their width for the same geometry. To prove this, the thickness of the apertures (l_C) has been swept. For each value of (l_C), the width (a_C) and the length of

the cavity (d) are adjusted to yield the desired coupling coefficient at the design center frequency for each geometry (see Figure 5.5 as an example of geometry). The effective Q-factor is then calculated in each iteration using (5.7) and (5.16) for the inter-resonator and external couplings, respectively.

For the comparison, coupling geometries yielding the same coupling coefficient have been used. Coupling values of a fifth degree filter with the specifications given in Table 5.1 have been chosen for the study.

Table 5.1: Filter Specifications

Parameter	Value
Type	Chebyshev
Degree	5
f_0	$11GHz$
BW	$100MHz$
RL	$25dB$
Conductivity	$18.797MS$

The performance in terms of spurious free range is also predicted for the selected geometries. The procedure is as follows:

- In the case of the inter-resonator coupling, the magnetic walls at z_{min} and z_{max} (see Figure 4.9(a)) that define the electrical center of the resonators of the fundamental mode are now substituted by electric walls to recover the even and odd modes of the second harmonic. In that case, the conditions of a perfect electric wall are satisfied:
  - The tangential electric field becomes null at the M plane (see Figure 5.4(a) and Figure 5.4(c)).
  - The magnetic field is tangential to the M plane (see Figure 5.4(b) and Figure 5.4(d)).

  Therefore, the M plane is substituted by an electric wall in order to calculate the frequency of the second harmonic, which can then be derived from the even and odd frequencies using (4.31).
- The spurious performance of an external coupling geometry can also be predicted if the coupling geometry is attached to a cavity as in Figure 4.15(a) and the S-parameters response is obtained.

In this way, the performance in terms of losses and spurious free range of different coupling geometries is compared and an optimized geometry is proposed for the design of filters with reduced losses and improved spurious free range performance.

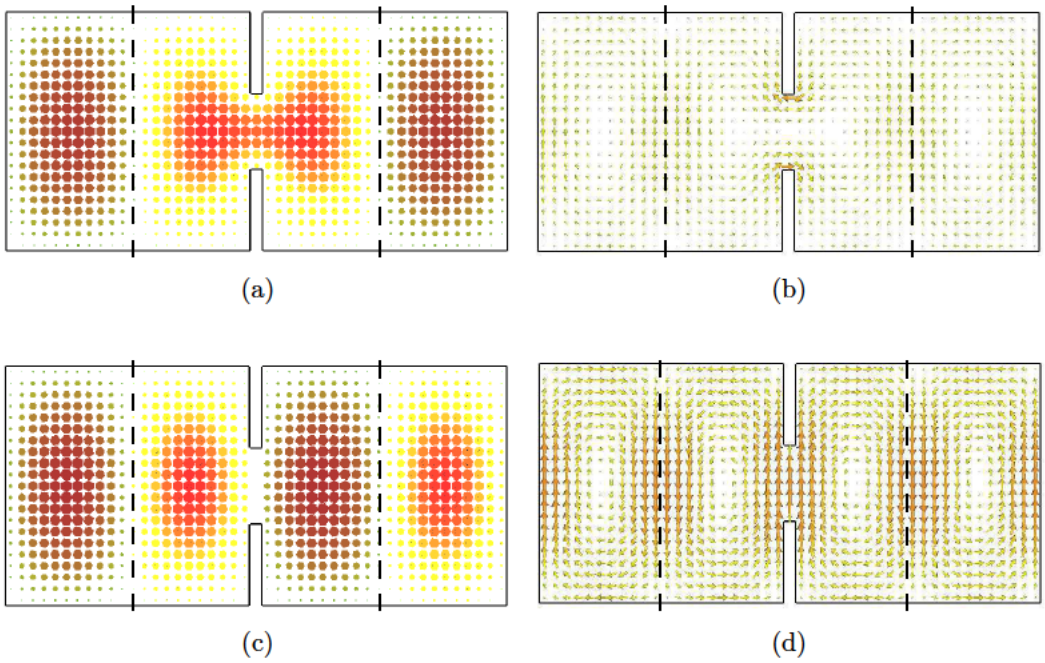

Figure 5.4: Second harmonic even and odd fields in the inter-cavity coupling model geometry: (a) even E field, (b) even H field, (c) odd E field, and (d) odd H field.

5.3.1 Rectangular Iris

The baseline geometry of this study is the well known rectangular iris shown in Figure 5.5 within a WR-75 rectangular waveguide ($a = 19.05$ mm and $b = 9.525$ mm).

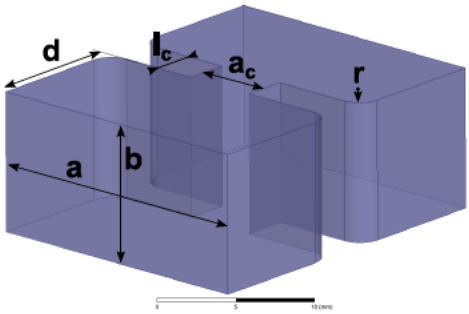

Figure 5.5: Rectangular iris coupling geometry.

The effective Q-factor of the inter-resonator couplings of a filter whose specifications are given in Table 5.1 has been derived for different iris thicknesses as described previously and it is shown in Figure 5.6. Besides, for each thickness value, filters with the corresponding inner coupling thicknesses and with a fixed external coupling have been designed. In this way, we can verify how the different internal coupling thicknesses affect the overall filter losses. The $S_{2,1}$ at center frequency of these filters is also shown in Figure 5.6.

The same study has been applied to the external coupling and the results are presented in Figure 5.7. Similarly, filters with the corresponding external coupling

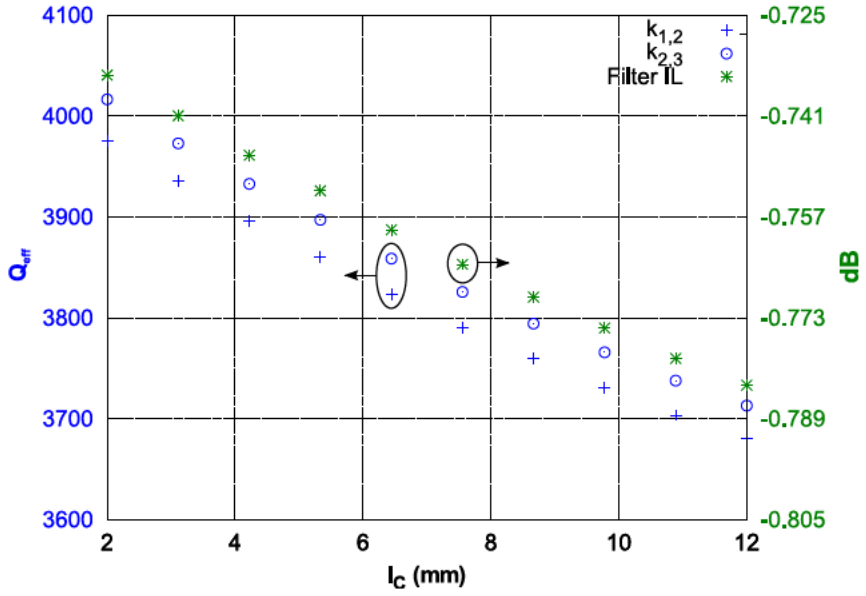

Figure 5.6: Inter-resonator effective Q-factor for different thicknesses of a rectangular iris and $S_{2,1}$ at center frequency of a filter designed with the corresponding inter-resonator couplings and with a fixed external coupling.

thicknesses have been designed, with fixed inter-resonator coupling geometries. In this way, we can assess the influence of the external window thicknesses in the overall filter losses. The resulting $S_{2,1}$ at center frequency of the filters are presented in Figure 5.7.

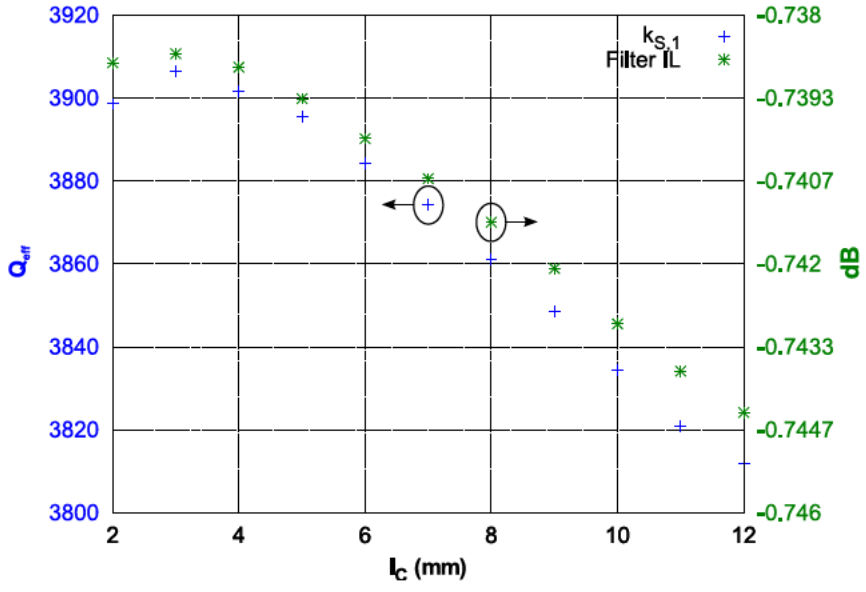

Figure 5.7: External effective Q-factor for different thicknesses of a rectangular iris and $S_{2,1}$ at center frequency of a filter designed with fixed inter-resonator couplings and with the corresponding external coupling.

In the case of the inter-resonator coupling, Q_{eff} decreases for thicker irises which agrees with the common idea of using thin rectangular irises in practical waveguide

filter design. However, this is not the case for the external coupling where a maximum can be observed at $l_C = 3$ mm. Clearly, this result shows that the performance of a coupling geometry also depends on the coupling coefficient. Moreover, it is clear from Figure 5.6 and Figure 5.7 that the behavior of the $S_{2,1}$ at center frequency of the filter can be accurately predicted by Q_{eff}, thus proving the validity of (5.7) and (5.16). In particular we can observe that an increment in the effective Q-factor leads to a reduction in the insertion loss of the filter.

Figure 5.8 shows how the length of the rectangular coupling geometry affects the resonant frequency of the second harmonic for the three different coupling coefficients under study. The results show that the longer the coupling structure, the lower the spurious free range. Also, the larger the coupling coefficient, the more sensitive the structure is to the thickness of the coupling.

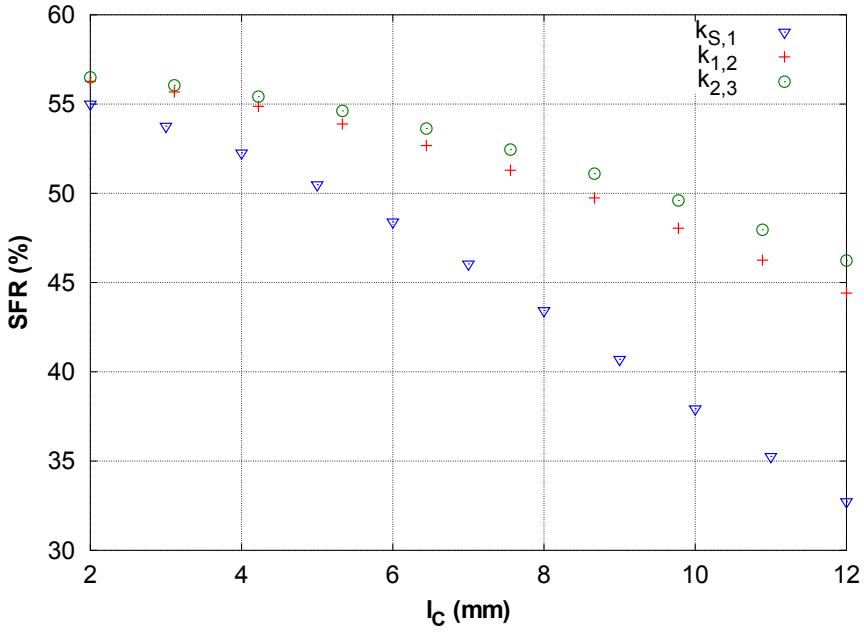

Figure 5.8: Spurious free range of the inter-resonator and external coupling models when rectangular irises are used.

The losses introduced by the rectangular coupling iris are rather high. This is because high current densities concentrate along the edges of the rectangular iris, increasing the losses of the structure. To overcome this problem, a rounding (r_C) can be applied at the edges. It has been verified that just by introducing this rounding the effective Q-factor increases in about 4% with respect to the one obtained with a conventional rectangular iris whilst maintaining essentially the same spurious free range. In the case of the external couplings, the effective Q factor increases around 2.3%.

5.3.2 Sinusoidal Iris

The rounding applied in the previous case is just the first step in the pursuance of an optimized coupling geometry. A sinusoidal shaped iris inserted within a WR-75

rectangular waveguide ($a = 19.05$ mm and $b = 9.525$ mm) like the one shown in Figure 5.9 has also been studied.

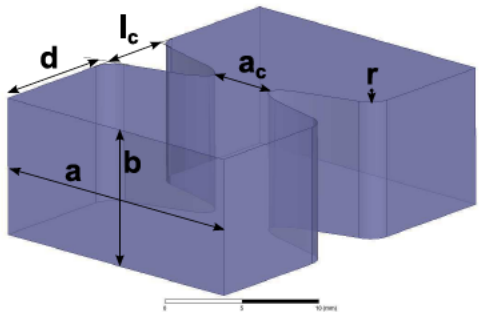

Figure 5.9: Sinusoidal iris coupling geometry.

Its geometry is defined by

$$y = \frac{a - a_c}{2} \sin\left(\frac{\pi}{l_c}x + \frac{\pi}{2}\right) \tag{5.17}$$

Figure 5.10 depicts the inter-resonator effective Q-factor of this structure for different iris thicknesses (l_C). In contrast to the previous example, Q_{eff} increases for thicker irises and a maximum can be observed. This maximum exceeds the best Q_{eff} obtained in the baseline geometry in around 6.5%. Again, filters with the corresponding inner coupling thicknesses and with a fixed external coupling have been designed for each thickness value, and an excellent agreement in the trend of the Q_{eff} and $S_{2,1}$ at center frequency curves is perceived.

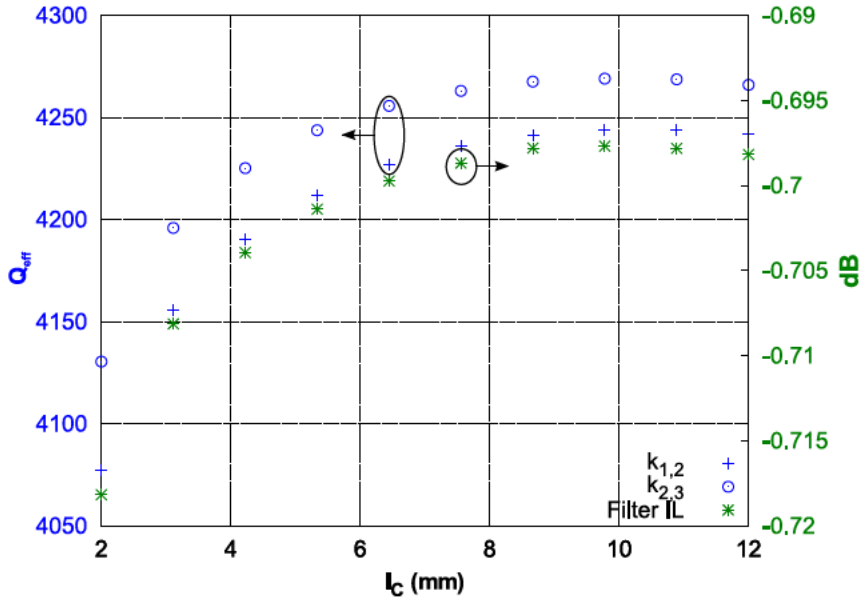

Figure 5.10: Inter-resonator effective Q-factor for different thicknesses of a sinusoidal iris and $S_{2,1}$ at center frequency of a filter designed with the corresponding inter-resonator couplings and with a fixed external coupling.

Figure 5.11 shows the effective Q-factor of an external coupling with sinusoidal geometry for different iris thicknesses, together with the $S_{2,1}$ at center frequency

of filters with the corresponding external coupling thicknesses and with fixed inter-resonator coupling geometries. In this case the maximum Q_{eff} improvement over the baseline structure is around 5.5%.

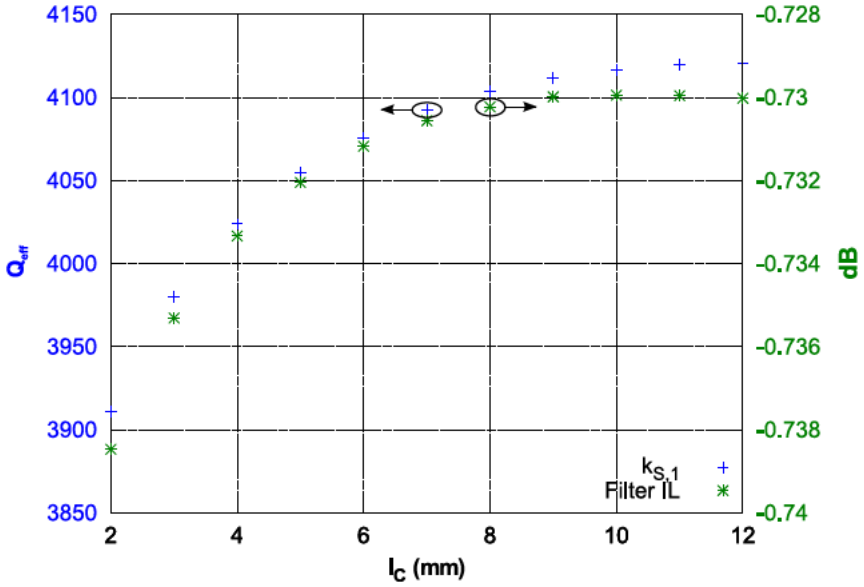

Figure 5.11: External effective Q-factor for different thicknesses of a sinusoidal iris and $S_{2,1}$ at center frequency of a filter designed with fixed inter-resonator couplings and with the corresponding external coupling.

The spurious free range is also presented in Figure 5.12. Again, it decreases as the thickness of the iris increases but the drop is more moderate than in the baseline geometry.

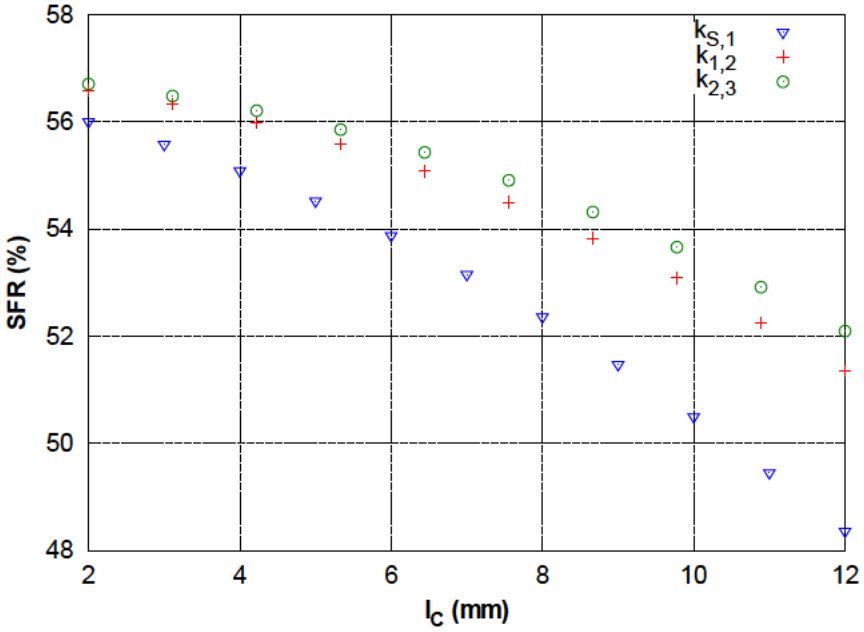

Figure 5.12: Spurious free range of the inter-resonator and external coupling models when sinusoidal irises are used.

It has also been verified that if a parabolic shape is used instead, very similar results are obtained. In that case, the optimum inter-resonator Q_{eff} increases in about 6.25% over the baseline geometry whilst the external Q_{eff} improves in around 5.25%.

5.3.3 Elliptic Double Posts

Inductive double posts of elliptic shape as shown in Figure 5.13 are also considered in this work (WR-75 rectangular waveguide with $a = 19.05$ mm and $b = 9.525$ mm).

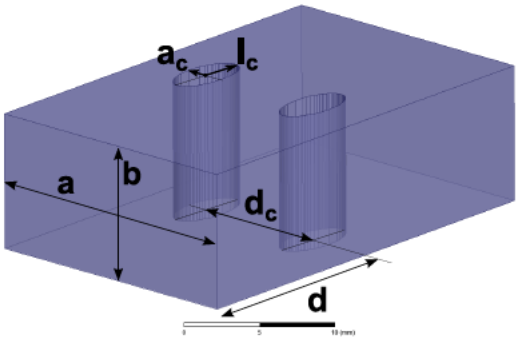

Figure 5.13: Elliptic double posts coupling geometry.

In this example, one semi axis (l_C) has been swept and the other one (a_C) as well as the length of the cavity (d) have been adjusted for a given coupling value at the design center frequency. The position of the posts in the waveguide has been fixed to $d_C = a/2$.

Optimum l_C values that maximize Q_{eff} can be observed for both the inter-resonator and external couplings in Figure 5.14 and Figure 5.15. Although this geometry is not as good as the parabolic and sinusoidal shapes in terms of Q_{eff}, an improvement of approximately 3.25% can still be achieved over the baseline shape for the internal couplings. However, due to the very small dimensions obtained for the external couplings, high currents appear in the posts, dropping the external effective Q in 1% with respect to the baseline geometry.

The same trend as in previous geometries can be observed for the spurious free range in Figure 5.16. As the posts extend in the direction of propagation (increasing l_C), the range free of spurious decreases, being this drop steeper for larger couplings.

If both semi axes are equal, the posts become of circular shape. Sweeping the radius of the circular posts while adjusting the distance (d_C) between them and the length of the cavities (d) lead to an improvement over the baseline geometry of about 3.5% for the inter-resonator couplings whereas the external effective Q increases in around 1%.

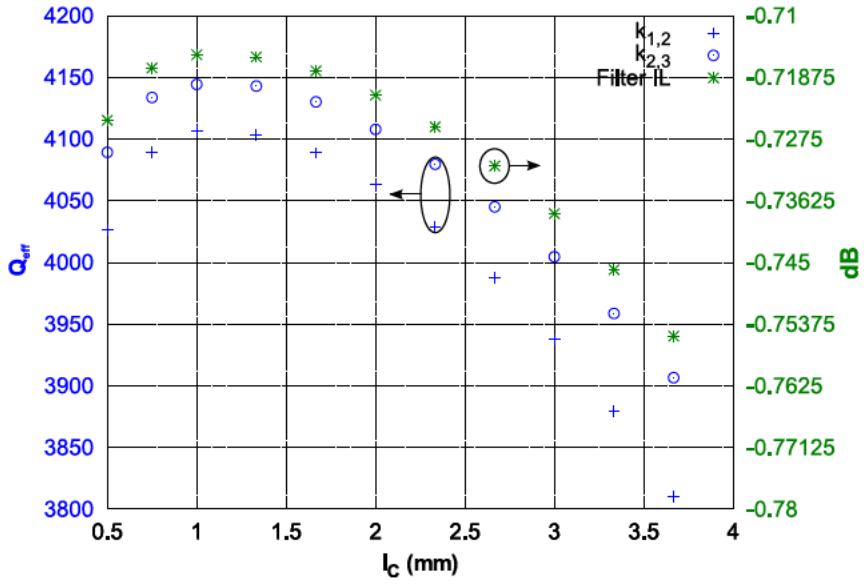

Figure 5.14: Inter-resonator effective Q-factor for different thicknesses of an elliptic posts coupling and $S_{2,1}$ at center frequency of a filter designed with the corresponding inter-resonator couplings and with a fixed external coupling.

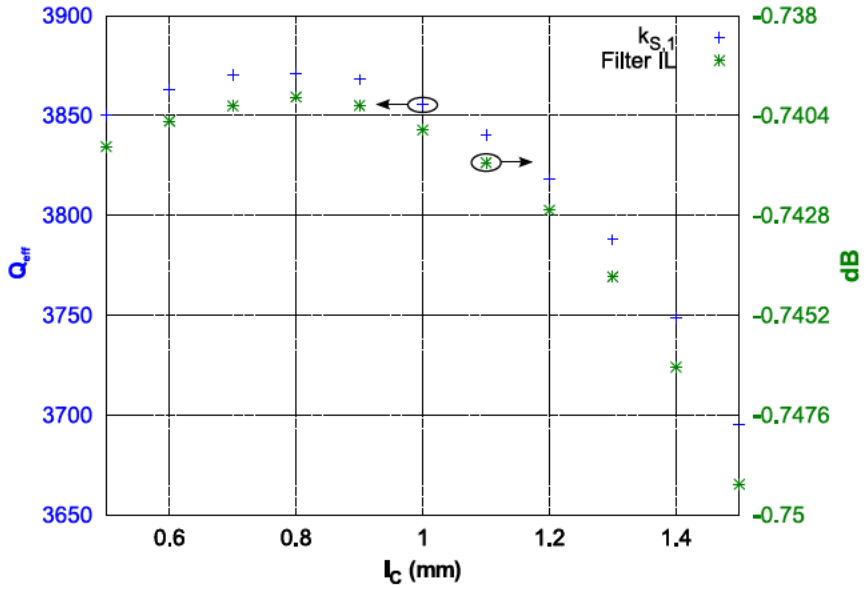

Figure 5.15: External effective Q-factor for different thicknesses of an elliptic posts coupling and $S_{2,1}$ at center frequency of a filter designed with fixed inter-resonator couplings and with the corresponding external coupling.

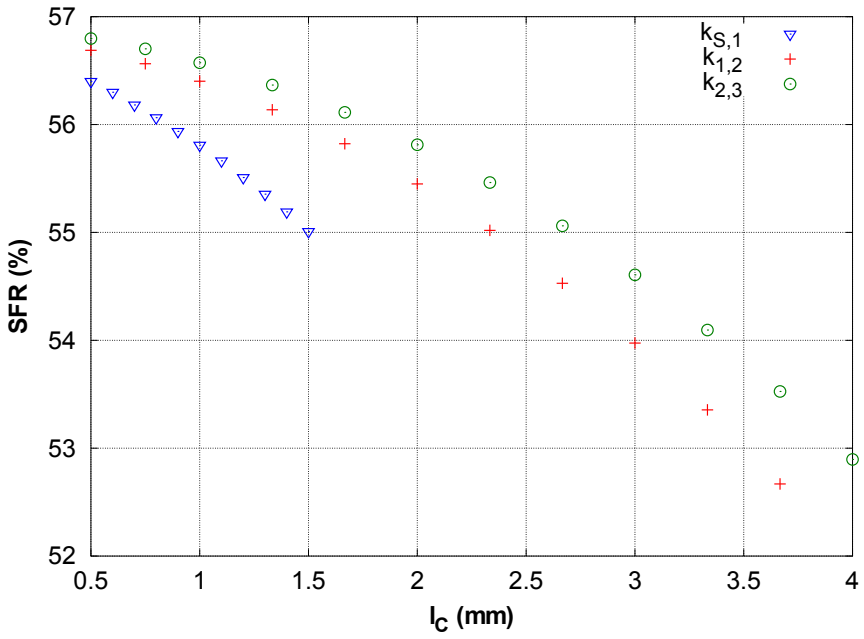

Figure 5.16: Spurious free range of the inter-resonator and external coupling models when elliptic posts are used.

5.3.4 Rounded Circular Window

The rounded circular window geometry is presented in Figure 5.17. A rectangular WR-75 waveguide ($a = 19.05$ mm and $b = 9.525$ mm) has been used.

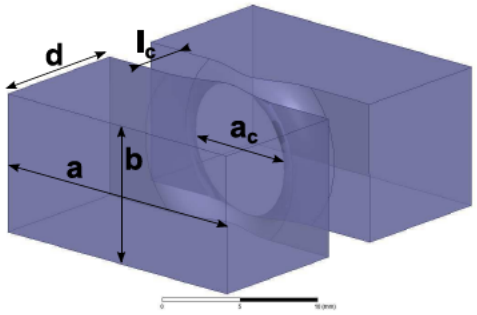

Figure 5.17: Rounded circular window coupling geometry.

A rounding of $l_C/2$ has been applied along the propagation direction with the aim of avoiding high current densities that concentrate in the edges of the aperture, as performed with the rectangular structure.

The effective Q-factor of this geometry for the inter-resonator and external couplings is presented in Figure 5.18 and Figure 5.19. A gain of approximately 10.5% with respect to the rectangular baseline geometry is obtained for the internal couplings. The improvement in the external Q_{eff} is slightly smaller, around 9%. Figure 5.18 and Figure 5.19 also show the $S_{2,1}$ at center frequency of filters with the corresponding coupling geometries and fixed external couplings or internal couplings, respectively. In all cases, the trend between $S_{2,1}$ at center frequency and effective Q-factor is very good.

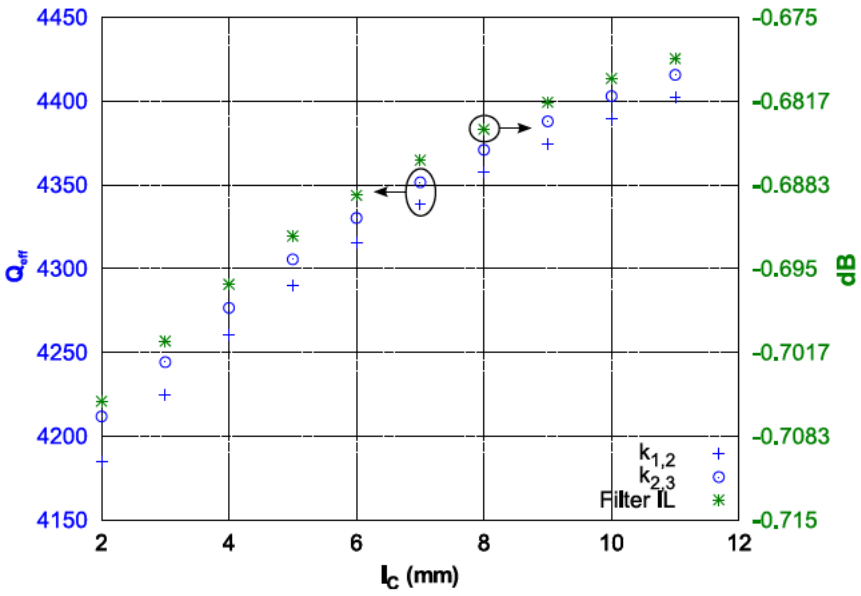

Figure 5.18: Inter-resonator effective Q-factor for different thicknesses of a rounded circular window and $S_{2,1}$ at center frequency of a filter designed with the corresponding inter-resonator couplings and with a fixed external coupling.

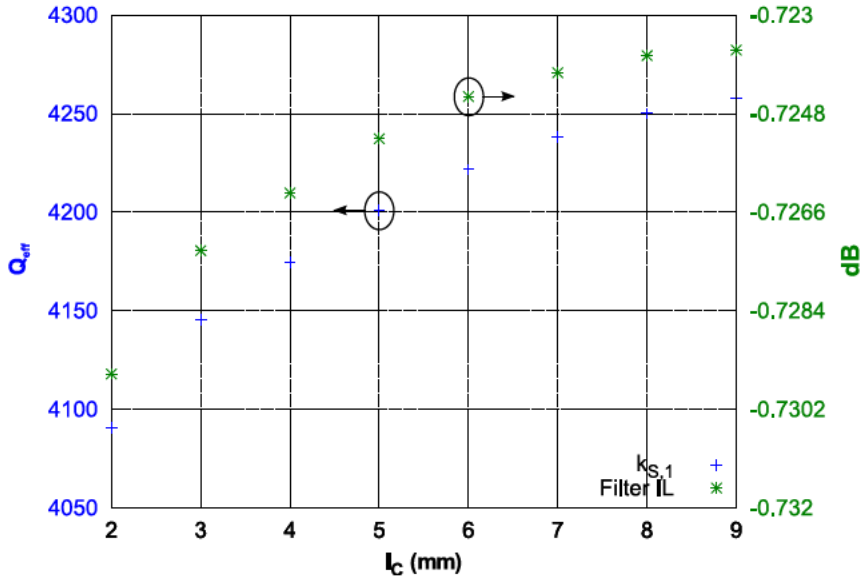

Figure 5.19: External effective Q-factor for different thicknesses of a rounded circular window and $S_{2,1}$ at center frequency of a filter designed with fixed inter-resonator couplings and with the corresponding external coupling.

Figure 5.20 depicts the spurious free range for both the internal and the external couplings showing a similar trend as in all the other coupling geometries.

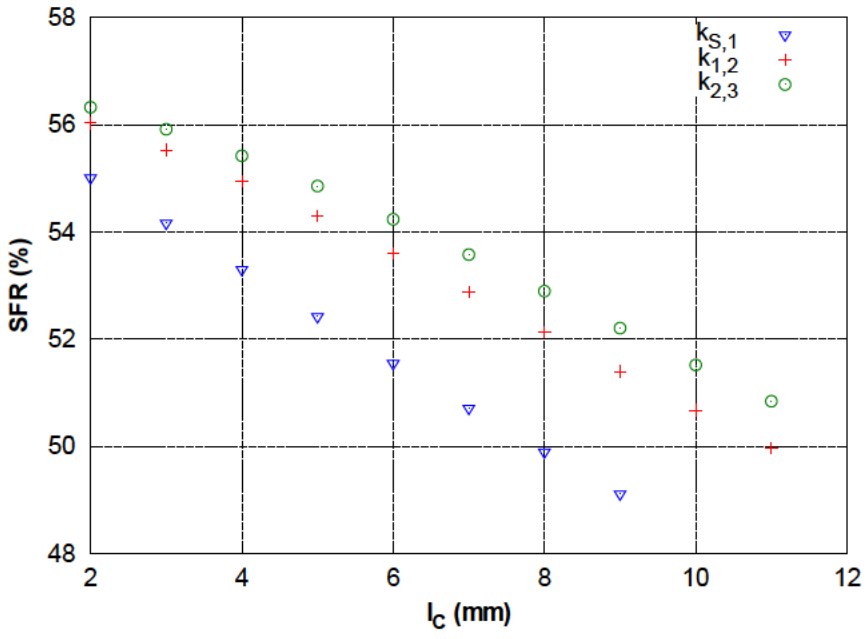

Figure 5.20: Spurious free range of the inter-resonator and external coupling models when rounded circular windows are used.

5.3.5 Sinusoidal-Circular Window

The sinusoidal-circular window coupling structure is a mixture of the bests geometries obtained so far: sinusoidal iris and circular window. To obtain this geometry, a

sinusoidal shape as the one shown in Figure 5.21(a) has been created and revoluted over the center axis R to create the circular window (Figure 5.21(b)).

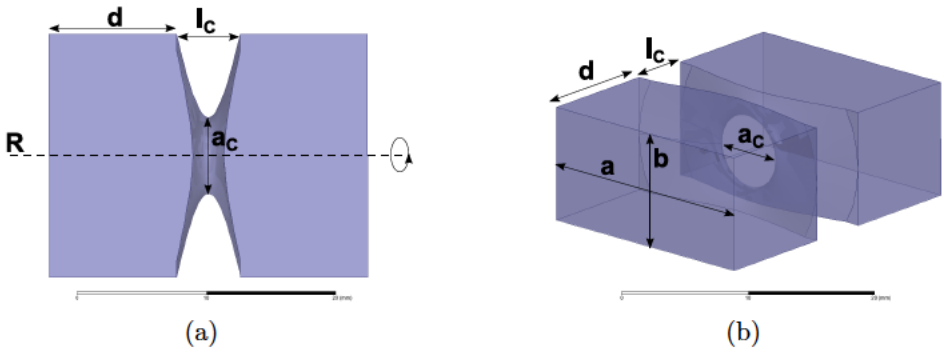

Figure 5.21: Sinusoidal-circular window coupling geometry.

The inter-resonator effective Q-factor can be seen in Figure 5.22 for different coupling thicknesses (l_C). In the same way, Figure 5.23 shows the external effective Q-factor. In both figures, also the $S_{2,1}$ at center frequency of filters with the corresponding coupling geometries and fixed external couplings or internal couplings, respectively, is shown. The trend between $S_{2,1}$ at center frequency and effective Q-factor agrees very good in all cases.

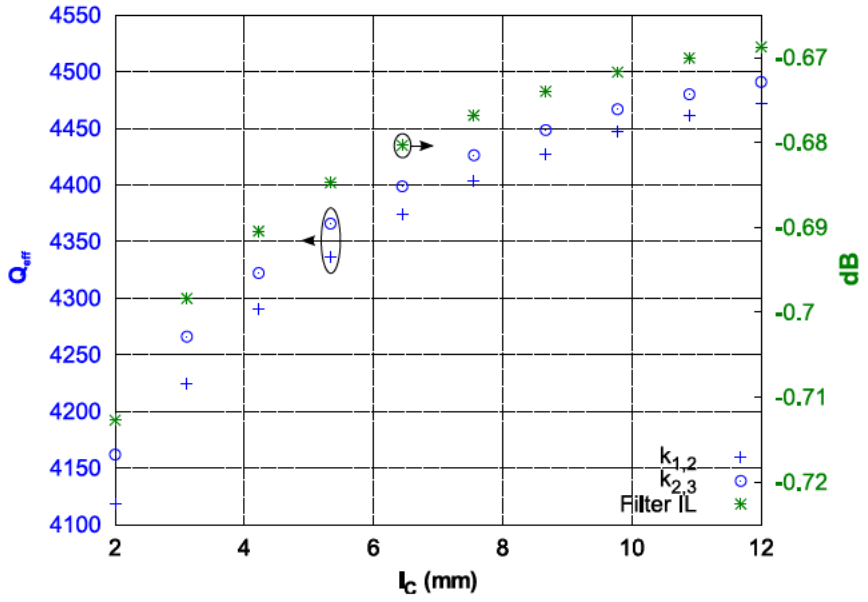

Figure 5.22: Inter-resonator effective Q-factor for different thicknesses of a sinusoidal-circular window and $S_{2,1}$ at center frequency of a filter designed with the corresponding inter-resonator couplings and with a fixed external coupling.

The spurious free range for both, the internal and the external couplings, is shown in Figure 5.24. The same trend as in all previous cases is observed.

It is to note, that the maximum improvement in effective Q-factor obtained for this geometry is around 12% with respect to the baseline geometry, which is larger than the improvement obtained with the sinusoidal iris and the one obtained

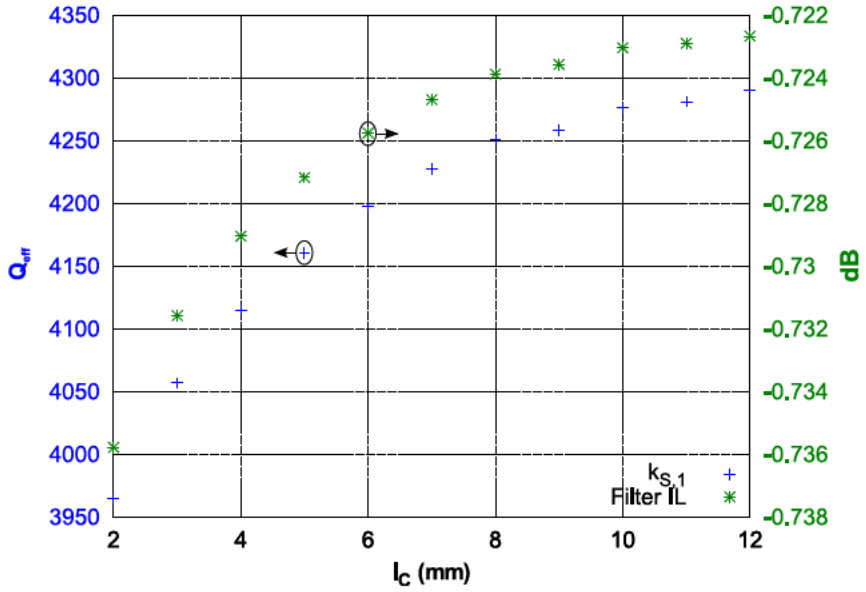

Figure 5.23: External effective Q-factor for different thicknesses of a sinusoidal-circular window and $S_{2,1}$ at center frequency of a filter designed with fixed inter-resonator couplings and with the corresponding external coupling.

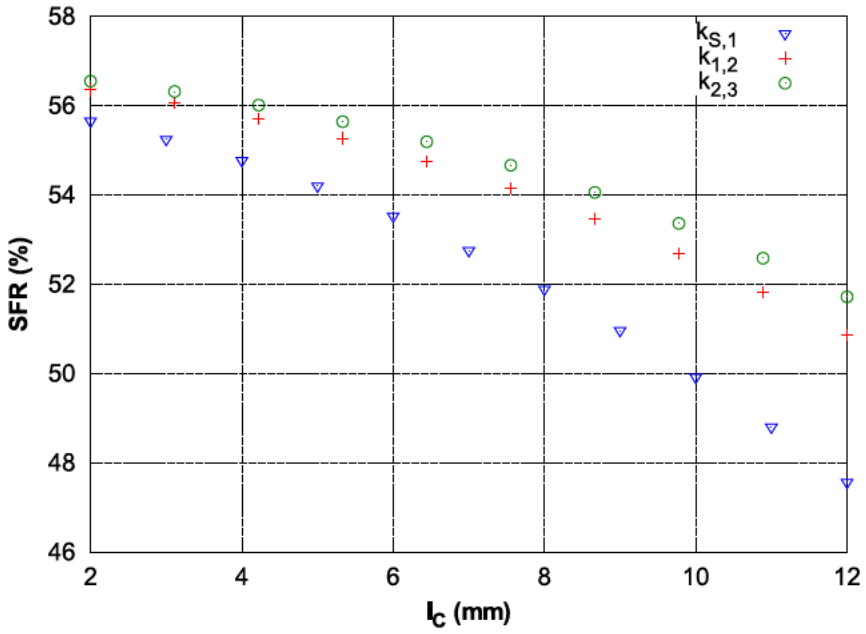

Figure 5.24: Spurious free range of the inter-resonator and external coupling models when sinusoidal-circular windows are used.

with the rounded circular window, as initially supposed. In addition, the spurious free range degradation with increasing coupling coefficient and coupling thickness is lower than that of the rounded circular window and very similar to that of the sinusoidal iris. Hence, the new geometry improves the effective Q-factor of both the sinusoidal iris and the rounded circular window and, in addition, does not degrade the spurious free range.

5.3.6 Sinusoidal-Circular Window with Rounded Cavities

A work on the optimization of the cross section of a rectangular waveguide [Suzuki and Hosono, 1983] and another one on the optimization of rectangular waveguide cavities [Zafra, 2007] were introduced in Chapter 1. If the techniques from previous works are applied to the last geometry, a sinusoidal-circular window with rounded cavity is obtained (Figure 5.25). A fillet operation over the edges of the structure (r_G and r_C) has been applied to test the impact of a rounded cavity over the effective Q-factor. In this case, the dimensions of the waveguide have been modified ($a = 21.287$ mm and $b = 9.876$ mm) to yield optimum spurious free range and roughly the same volume [Zafra, 2007].

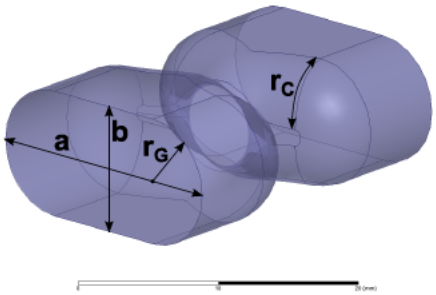

Figure 5.25: Sinusoidal-circular window coupling geometry with rounded cavity.

The effective Q-factor of the inter-resonator couplings of a filter whose specifications are given in Table 5.1 has been derived for different iris thicknesses as described previously and it is shown in Figure 5.26. Note that, for each thickness value, filters with the corresponding inner coupling thicknesses and with a fixed external coupling have been designed in order to verify how the different internal coupling thicknesses affect the overall filter losses. The $S_{2,1}$ at center frequency of these filters is also shown in Figure 5.26.

The results concerning the external coupling are presented in Figure 5.27. Again, filters with the corresponding external coupling thicknesses have been designed, with fixed inter-resonator coupling geometries in order to assess the influence of the external window thicknesses in the overall filter losses. The resulting $S_{2,1}$ at center frequency of the filters are also presented in the same figure.

The spurious free range versus the length of the coupling geometry is shown in Figure 5.28 for the three different coupling coefficients under study. The results are in concordance with all the other coupling geometries shown in this work: the spurious free range decreases for thicker coupling geometries and the larger the coupling coefficient, the more sensitive the structure is to the thickness of the coupling.

This geometry shows the maximum increase in effective Q-factor of all the geometries studied in this work. In the case of the inter resonator Q_{eff}, the increment is around 23%, whereas around 18% is obtained for the external coupling geometry. This geometry also has an excellent behavior regarding the spurious free range, as the sensitivity to the coupling thickness is lower than the rest of the geometries (with the exception of the double posts geometry, which is the least sensitive structure) and very similar to the one obtained before the rounding in the cavities. Note that

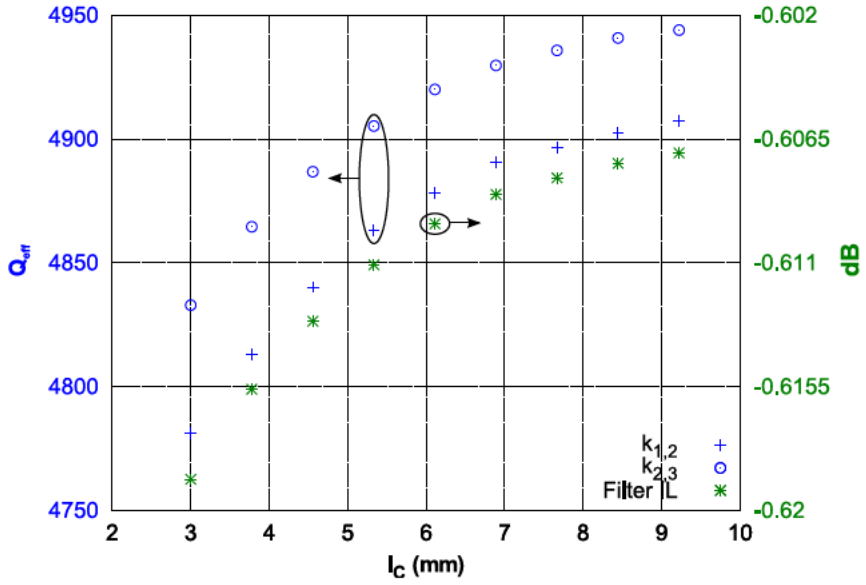

Figure 5.26: Inter-resonator effective Q-factor for different thicknesses of a sinusoidal-circular window with rounded cavities and $S_{2,1}$ at center frequency of a filter designed with the corresponding inter-resonator couplings and with a fixed external coupling.

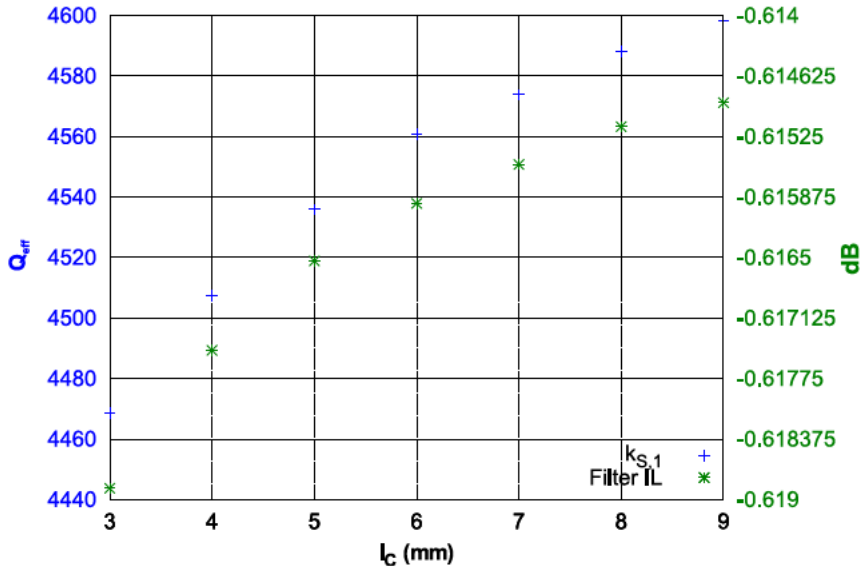

Figure 5.27: External effective Q-factor for different thicknesses of a sinusoidal-circular window with rounded cavities and $S_{2,1}$ at center frequency of a filter designed with fixed inter-resonator couplings and with the corresponding external coupling.

the waveguide dimensions (a and b) have been chosen to maximize spurious free range [Zafra, 2007] and roughly maintain the same volume.

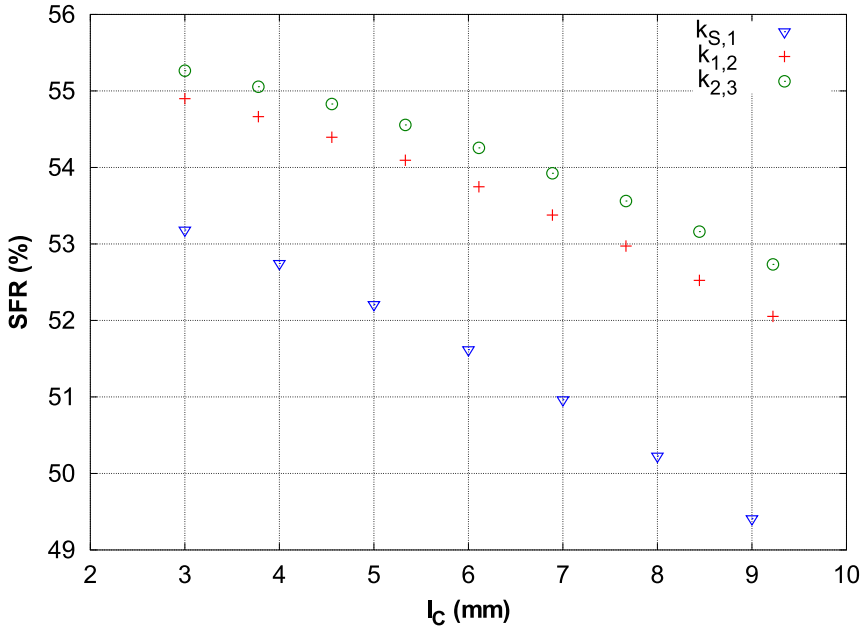

Figure 5.28: Spurious free range of the inter-resonator and external coupling models when sinusoidal-circular windows with rounded cavities are used.

5.4 Practical Considerations of the Novel Effective Q-factor

5.4.1 Impact of Coupling Coefficient on Effective Q-factor

In the previous section, it was stated that the performance of a coupling geometry in terms of losses also depends on the coupling value. Here, the impact of coupling values on the effective Q-factor is studied in more detail.

Figure 5.29 plots the effective Q-factor of the rectangular iris versus the coupling coefficient in dB for different iris thicknesses at $f_0 = 11$ GHz. It is interesting to observe that the optimum iris thickness (in terms of Q_{eff}) is $l_C = 2$ mm when the coupling is below -10 dB. However, $l_C = 12$ mm becomes the optimum iris thickness when the coupling value is above -5 dB. A 3D plot can be seen in Figure 5.30.

The same graph is presented for the sinusoidal geometry in Figure 5.31 and Figure 5.32. From -40 dB to -15 dB coupling, the optimum iris thickness lays in the range between $l_C = 9.78$ mm and $l_C = 10.89$ mm. On the other hand, the optimum iris is always the thicker one for coupling values above -15 dB. Again, a 3D plot from the graph shown in Figure 5.31 is shown in Figure 5.32.

In this context, it is concluded that a certain combination of coupling geometry and dimensions may give the optimum structure for a given coupling coefficient. However, this combination might not be optimum if a different coupling value is selected.

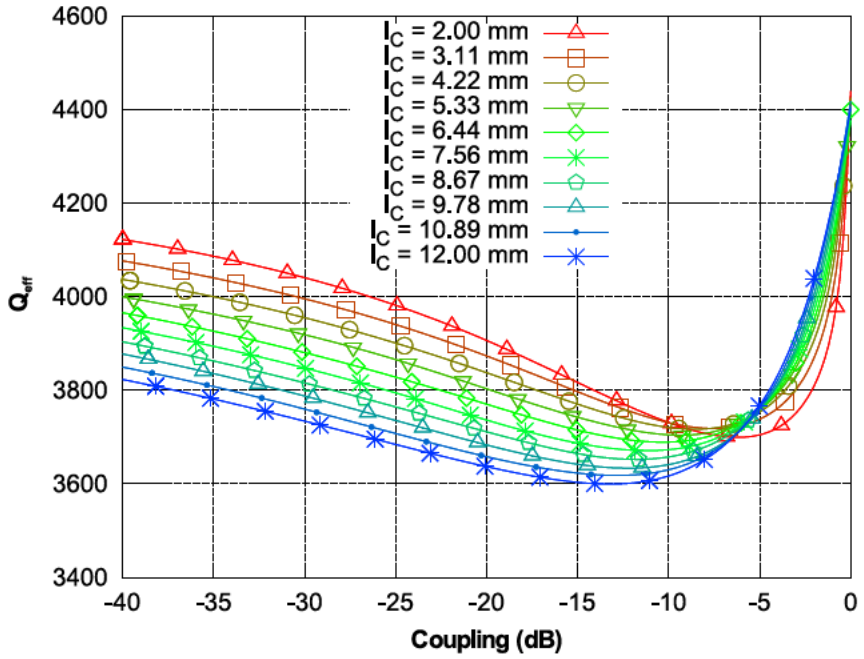

Figure 5.29: Effective Q-factor of a rectangular iris versus the coupling coefficient for different iris thicknesses.

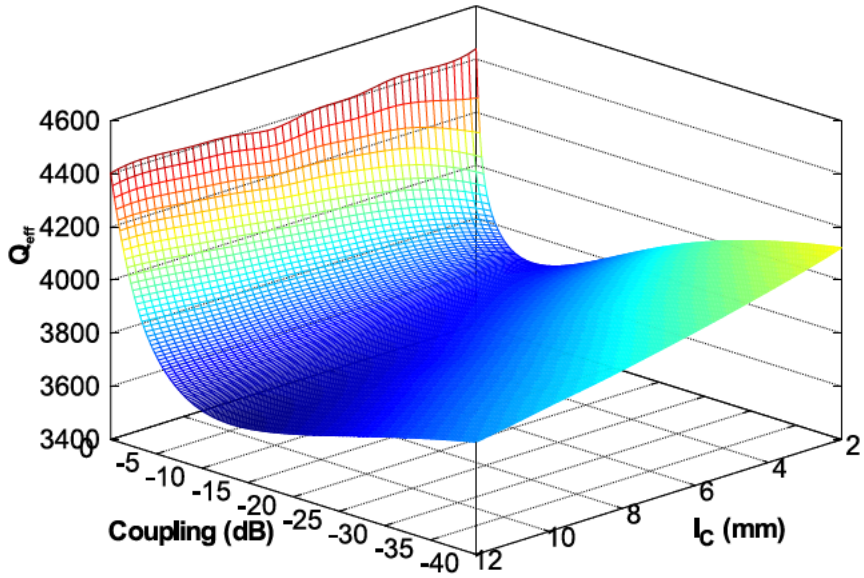

Figure 5.30: Effective Q-factor of a rectangular iris versus the coupling coefficient for different iris thicknesses.

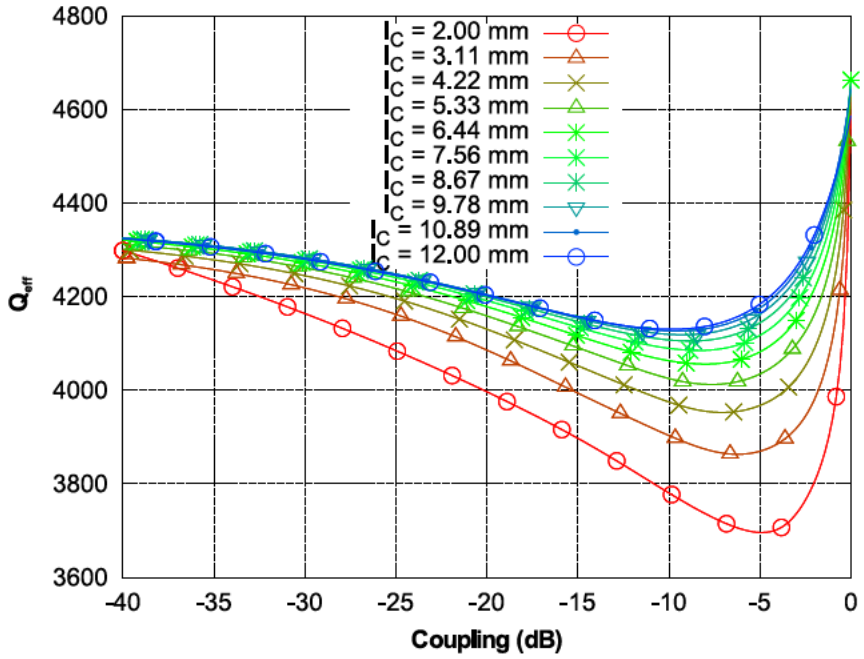

Figure 5.31: Effective Q-factor of a sinusoidal iris versus the coupling coefficient for different iris thicknesses.

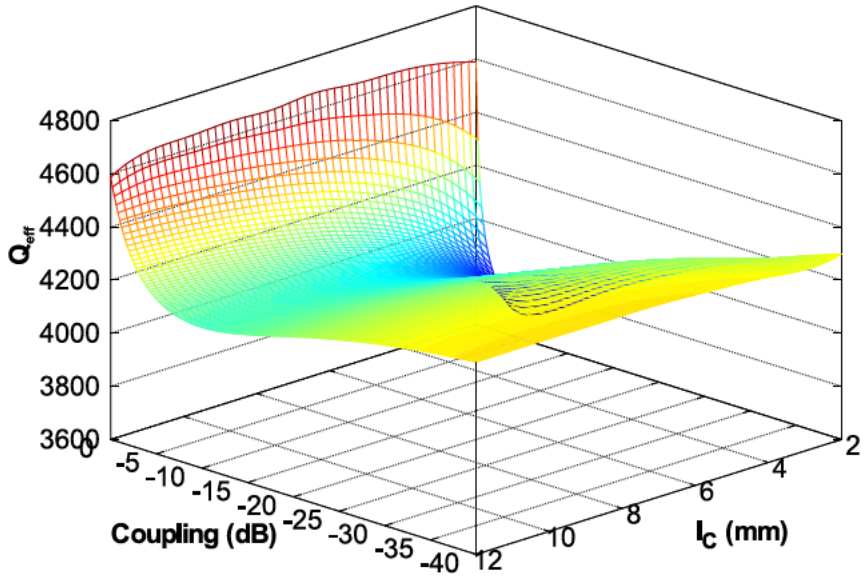

Figure 5.32: Effective Q-factor of a sinusoidal iris versus the coupling coefficient for different iris thicknesses.

5.4.2 Contribution of Each Coupling to Overall Filter Loss

In the previous section, the effective Q-factor improvement of different coupling geometries over a rectangular iris taken as baseline has been shown. However, the impact of these improvements in the final filter insertion loss varies depending on the position of the coupling in the filter. To show this, the equivalent circuits of filters of orders from 4 to 9 with specifications given in Table 5.1 and with rectangular irises have been designed. Iteratively, the rectangular irises have been substituted by rounded circular windows with the same effective Q improvement and their insertion loss global improvement has been recorded. The contribution of each coupling to the overall filter insertion loss improvement is presented in Figure 5.33 for filters of different orders. In all cases, the contribution to the overall improvement of the filter is much larger in the central couplings of the filter. This can be explained due to the larger stored energy in the central resonators of an in-line filter topology, as recognized in [Mendoza et al., 2012]. The contribution of each resonator to the total stored energy of the complete filter has also been calculated using the equivalent circuits, and it is presented in Figure 5.34. These results state that it is optimum to reduce losses in the irises lying in the central positions of the filter, rather than in the couplings located at the edges, if the improvement cannot be applied to all the couplings of a given structure due to other restrictions such as volume and mass.

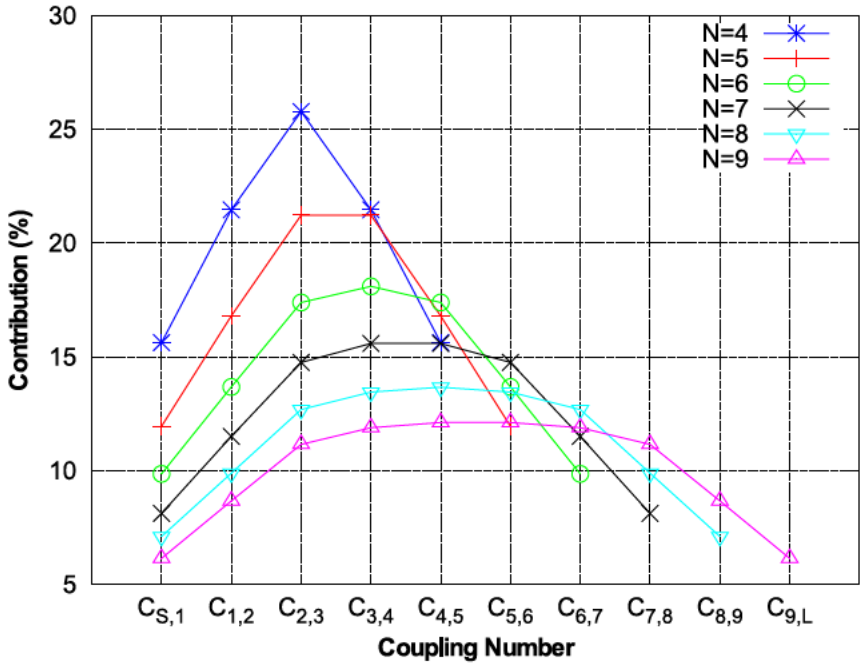

Figure 5.33: Contribution of each coupling to the overall filter insertion loss improvement at f_0 when all the couplings are enhanced for filters of order $N = 4$, $N = 5$, $N = 6$, $N = 7$, $N = 8$ and $N = 9$.

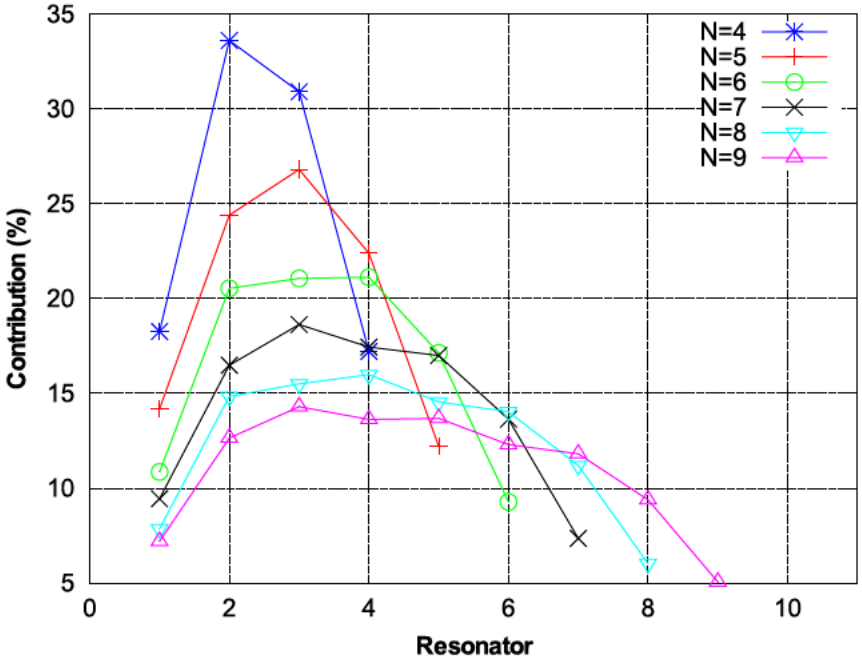

Figure 5.34: Contribution of each resonator to the overall filter stored energy at f_0 for filters of order $N = 4$, $N = 5$, $N = 6$, $N = 7$, $N = 8$ and $N = 9$.

5.4.3 Comparison Between All Coupling Geometries

Table 5.2, Table 5.3 and Table 5.4 collect the maximum effective Q-factors of the different geometries for all the three coupling values studied in this chapter. The improvements over the baseline rectangular geometry are also shown. It is interesting to observe that the maximum improvement in the external coupling is always smaller than the improvement obtained in the inter-resonator couplings. This can be explained with the aid of the fields in Figure 5.35. Note that the current densities are very strong in both sides of the inter-resonator couplings whereas the current density in the external coupling is much higher next to the cavity than to the input waveguide. Hence, the same modification in the geometry of all the couplings will result in a larger improvement in the inter-resonator couplings.

Table 5.2: $Q_{effS,1}$ summary

Geometry	Max Q_{eff}	Improvement (%)
Rectangular Iris (baseline)	3906.6	0
Rounded Rectangular Iris	4043.1	2.29
Sinusoidal Iris	4120.6	5.48
Parabolic Iris	4114.5	5.32
Elliptic Posts	3871.4	-0.9
Circular Posts	4063.2	4
Rounded Circular Window	4257.9	8.99
Sinusoidal-Circular Window	4290.4	9.82
Sinusoidal-Circular Window (with rounded cavities)	4598.1	17.7

Table 5.3: $Q_{eff1,2}$ summary

Geometry	Max Q_{eff}	Improvement (%)
Rectangular Iris (baseline)	3980.3	0
Rounded Rectangular Iris	4134.1	3.86
Sinusoidal Iris	4247.7	6.72
Parabolic Iris	4238.5	6.49
Elliptic Posts	4111	3.28
Circular Posts	4127.1	3.69
Rounded Circular Window	4405.1	10.67
Sinusoidal-Circular Window	4476.4	12.46
Sinusoidal-Circular Window (with rounded cavities)	4912.3	23.42

Table 5.4: $Q_{eff2,3}$ summary

Geometry	Max Q_{eff}	Improvement (%)
Rectangular Iris (baseline)	4018.6	0
Rounded Rectangular Iris	4159.3	3.50
Sinusoidal Iris	4270.5	6.27
Parabolic Iris	4261.5	6.04
Elliptic Posts	4147.1	3.20
Circular Posts	4142.9	3.09
Rounded Circular Window	4416.7	9.91
Sinusoidal-Circular Window	4493.4	11.81
Sinusoidal-Circular Window (with rounded cavities)	4946.7	23.10

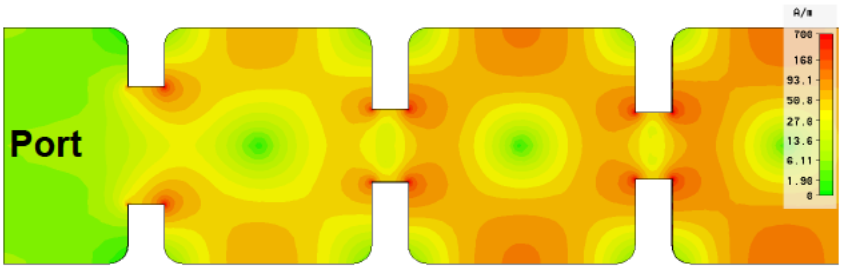

Figure 5.35: Current densities produced in the couplings of a five degree waveguide cavity filter.

It has been shown that the performance in terms of effective Q of the couplings of a filter can be improved by modifying one of their dimensions and adjusting the other to yield the same coupling coefficient. However, it is clear from previous subsections that the modification of the geometry of the coupling structure has a larger impact on Q_{eff}. Combining both techniques, improvements over 10% can be obtained if the geometry of the cavities remains the same. However, if the cavities

are also optimized, improvements of more than 20% with a little impact on spurious free range can be achieved.

Regarding the spurious free range, it has been shown that it decreases as the coupling structure extends in the direction of propagation, for all the presented geometries. Whereas the elliptic double posts is the less sensitive structure to this fact, the rectangular iris seems to be the most sensitive. Also, the drop in spurious free range at a certain coupling thickness increases as it does the coupling coefficient. In all cases, the spurious free range tends asymptotically to a value of 57% when the iris becomes very thin, which is the spurious free range of a closed unperturbed WR-75 cavity at $f_0 = 11$ GHz.

The performances of the coupling structures can also be evaluated as a trade off between effective Q-factor and spurious free range. One possibility is to define a global quality parameter as

$$C = \frac{Q_{\text{eff}}}{Q_{\text{effB}}} \frac{SFR}{SFR_B} \tag{5.18}$$

where Q_{effB} and SFR_B are the maximum effective Q-factor and maximum spurious free range of the baseline geometry (when $l_C = 2$ mm). Figure 5.36 shows the performances obtained for the different coupling structures investigated in this chapter and their geometries, for one of the studied inter-resonator coupling values ($k_{1,2}$). It can be observed that the parabolic iris, the sinusoidal iris and the rounded circular window are very similar in terms of the global quality parameter defined in (5.18), and are more optimum than the rectangular iris and the elliptic double posts. The sinusoidal-circular window is the best geometry in WR-75 rectangular waveguide obtained so far in terms of the previously defined global quality parameter. The sinusoidal-circular window with rounded cavities shows an improvement of almost 20% with respect to the traditional rectangular iris in WR-75.

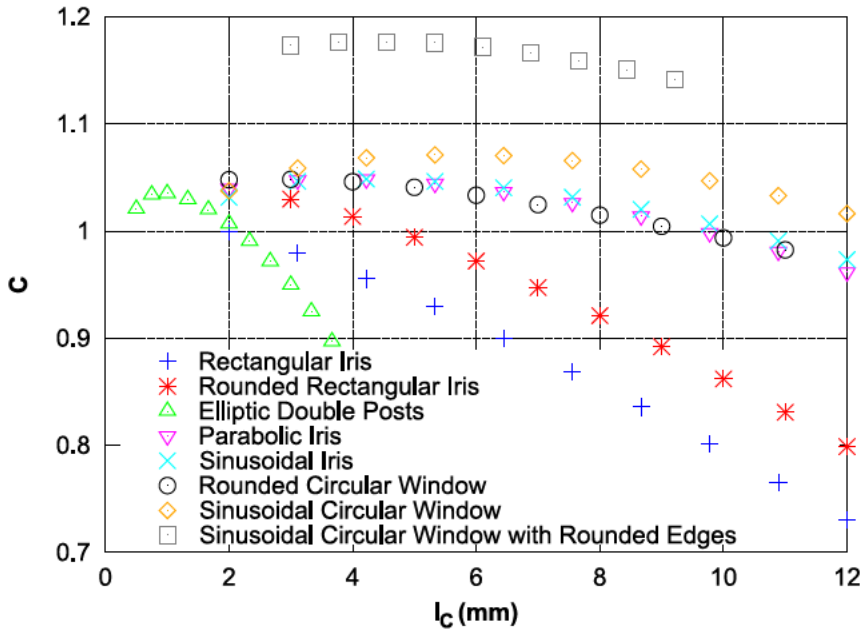

(a)

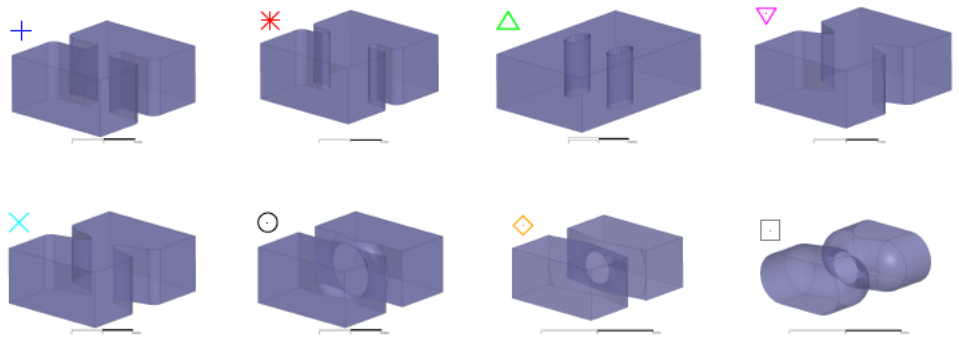

(b)

Figure 5.36: (a) Performance of several coupling structures defined as a relation of effective Q-factor and spurious free range and (b) their geometries.

5.5 Theory Validation

To validate the previous theory, a total of six waveguide filters with different coupling geometries but same specifications as listed in Table 5.1 have been designed employing the standard filter design method [Matthaei et al., 1980], [Levy, 1973], and manufactured.

The filters are divided in two different sets: the first set comprises two filters with different coupling geometries but same Q_{eff}, while the second set encompasses three filters with different coupling geometries and different Q_{eff} and one more filter with different coupling and cavity geometries and higher Q_{eff}.

Figure 5.37 shows the geometry of the filters in set 1. While the coupling structures of the filter in Figure 5.37(a) are made of rectangular irises, the coupling structures of the one in Figure 5.37(b) are made of elliptic double posts. The dimensions are given in Table 5.5. Note that both filters are designed in standard

WR-75 rectangular waveguide (variables a and b)

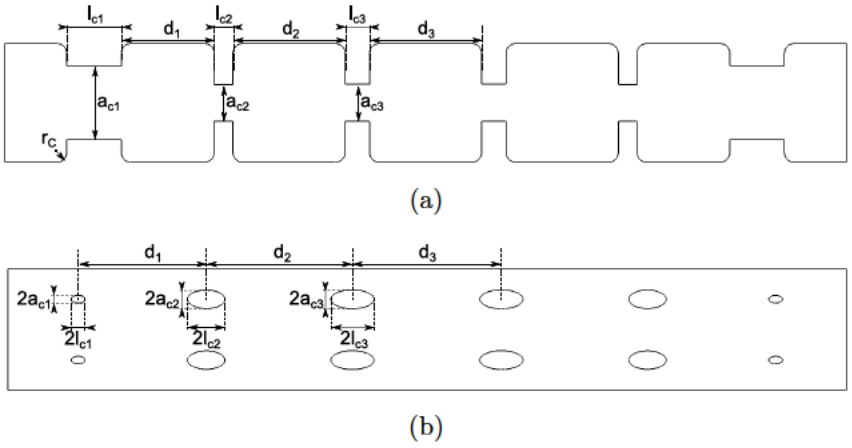

Figure 5.37: Designed filters from set 1 with different coupling geometries but same effective Q-factor: (a) rectangular irises filter and (b) elliptic double posts filter.

Table 5.5: Set 1: filter physical dimensions

Parameter	Filter(a) (mm)	Filter(b) (mm)
a	19.05	19.05
b	9.525	9.525
d_1	15.021	20.106
d_2	18.152	22.945
d_3	18.140	23.383
l_{C1}	8.805	1.077
l_{C2}	3.028	2.945
l_{C3}	3.940	3.402
a_{C1}	11.904	0.606
a_{C2}	5.934	1.440
a_{C3}	6.000	1.471
r_C	1.5	N/A

Figure 5.38(a) shows full wave simulations of the filters from the first set. As expected, the RF responses match each other and excellent agreement in $S_{2,1}$ at center frequency is obtained as shown in Figure 5.38. Table 5.6 shows the value of Q_{eff} chosen for the coupling structures of both filters and the final value of insertion loss. Both filters exhibit essentially the same insertion loss. This example demonstrates that irises exhibiting same effective Q lead to filters with same insertion losses.

Table 5.6: Set 1: Q_{eff} and IL

Filter	Q_{eff}	IL (dB)	Diff. (%)
Rectangular Irises	3950	0.7329	N/A
Elliptic Double Posts	3950	0.7304	0.34

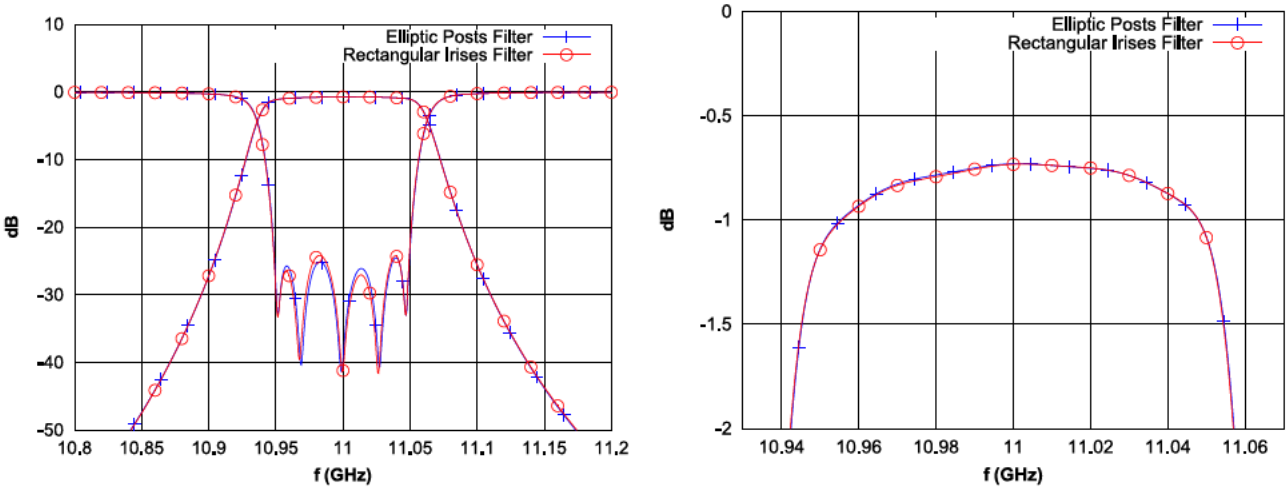

(a) (b)

Figure 5.38: (a) Simulated RF responses of the filters in set 1 using CST Microwave Studio and (b) $S_{2,1}$ detail.

Figure 5.39 shows the simulated out of band responses of the filters in set 1. The calculated spurious free range in the individual cavity-coupling structures of the filter is shown in Table 5.7 together with the spurious free range of the final designed filters. It can be noted that the spurious free range of the filters is a combination of the values obtained from the individual cavity-coupling structures, but it does not lay between them necessarily. However, it is interesting to observe that the spurious free range of the complete filters tends to the maximum values obtained in the individual cavity-coupling structures. In this case, the individual cavity-coupling structures of both filters have very similar maxima and, therefore both filters exhibit similar spurious free range values, with the spurious free range of the filter with rectangular irises being slightly larger than that of the filter with elliptic double posts.

Table 5.7: Set 1: spurious free range

Filter	$SFR_{0,1}$	$SFR_{1,2}$	$SFR_{2,3}$	SFR_{filter}
Rectangular Irises	41.239	55.727	55.594	53.934
Elliptic Double Posts	55.699	54.070	53.983	51.793

The geometries of the filters from set 2 are presented in Figure 5.40. In this case, four filters with different geometries and different Q_{eff} have been studied: one with rectangular shaped irises in WR-75 waveguide with a low Q_{eff} (Figure 5.40(a)), one with sinusoidal shaped irises in WR-75 waveguide with a larger Q_{eff} (Figure 5.40(b)), another one with circular shaped windows in WR-75 waveguide with high Q_{eff} (Figure 5.40(c)), and one with sinusoidal-circular windows as coupling structures and with rounded cavities which has the largest Q_{eff} (Figure 5.40(d)). The dimensions are given in Table 5.8. The waveguide dimensions are given by the variables a and b.

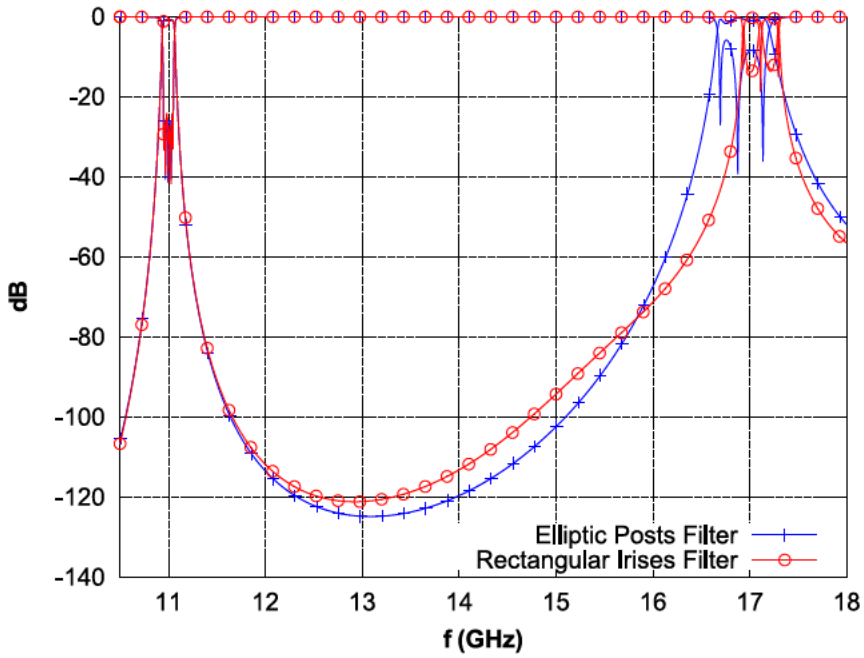

Figure 5.39: Simulated out of band responses of the filters in set 1 using CST Microwave Studio.

Table 5.8: Set 2: filter physical dimensions

Parameter	Filter(a) (mm)	Filter(b) (mm)	Filter(c) (mm)	Filter(d) (mm)
a	19.05	19.05	19.05	21.287
b	9.525	9.525	9.525	9.876
d_1	13.489	11.574	13.358	14.528
d_2	15.973	13.397	15.661	16.252
d_3	16.215	13.547	15.885	16.393
l_{C1}	10	9	8	6
l_{C2}	10	9	8	6
l_{C3}	10	9	8	6
a_{C1}	12.193	9.447	11.333	10.579
a_{C2}	9.274	5.648	8.135	6.313
a_{C3}	8.785	5.124	7.635	5.759
r_C	1.5	1.5	N/A	b/2-0.5
r_G	N/A	N/A	N/A	b/2

The RF responses from full-wave simulations of the filters in set 2 are shown in Figure 5.41(a) and Figure 5.41(b). It is important to notice the perfect match obtained between the return loss of all the four filters so insertion loss can be fairly compared. As predicted by Q_{eff}, the insertion loss of the rectangular shaped irises filter is the worst one, being the insertion loss of the sinusoidal-circular windows filter with rounded cavities the best one. The insertion loss of the filter with sinusoidal irises is slightly worse than the filter with circular windows, as predicted by the effective Q-factor. Table 5.9 shows the value of Q_{eff} of the coupling structures of the filters from set 2, the predicted improvement by Q_{eff}, the final value of insertion

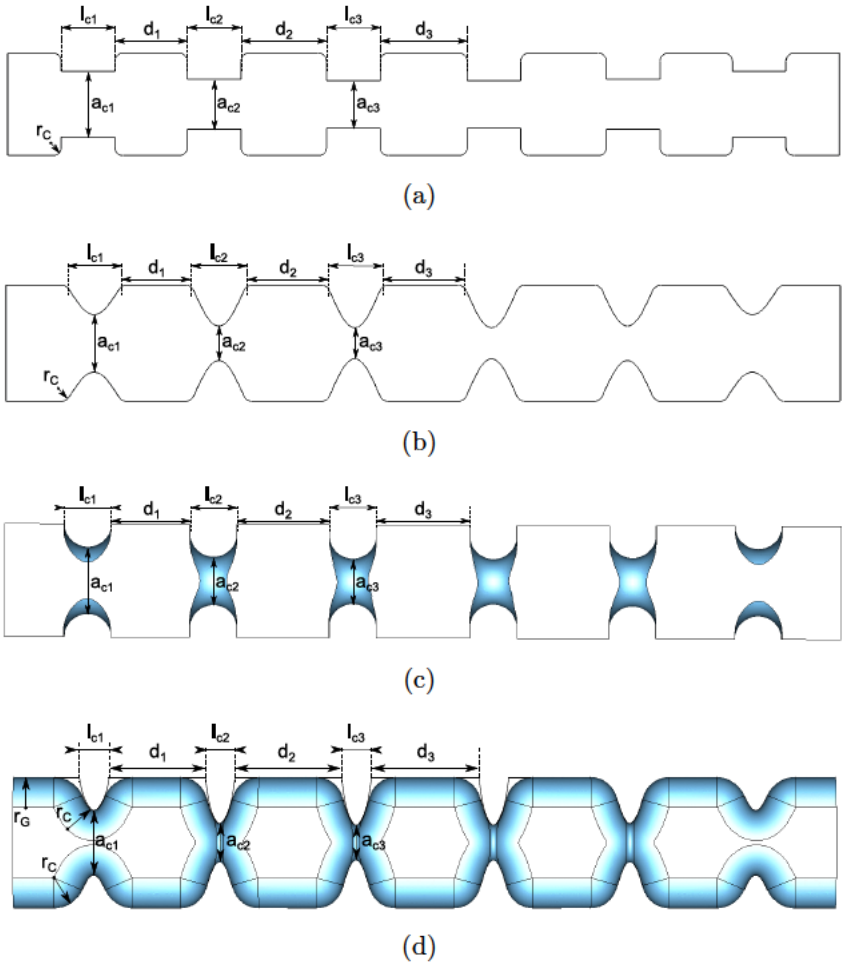

Figure 5.40: Designed filters from set 2 with different coupling geometries and different effective Q-factors: (a) rectangular irises filter, (b) sinusoidal irises filter, (c) circular windows filter, and (d) sinusoidal-circular windows filter with rounded cavities.

loss, and the final improvement obtained from the RF responses. It can be observed that the improvements obtained in the insertion losses of the filters are in agreement with the improvements predicted in Q_{eff} by the theory presented in this chapter.

Table 5.9: Set 2: Q_{eff} and IL

Filter	Q_{eff}	Impr. (%)	IL (dB)	Impr. (%)
Rectangular Irises	~3730	N/A	0.771	N/A
Sinusoidal Irises	~4250	13.9	0.676	12.3
Circular Windows	~4360	16.9	0.659	14.5
Sinusoidal-Circular Windows with Rounded Cavities	~4900	31.4	0.591	23.3

The out of band responses of the filters in set 2 are collected and shown in Figure 5.42. Table 5.10 shows the spurious free range obtained from the individual cavity-coupling structures and the values obtained from the final designed filters. It

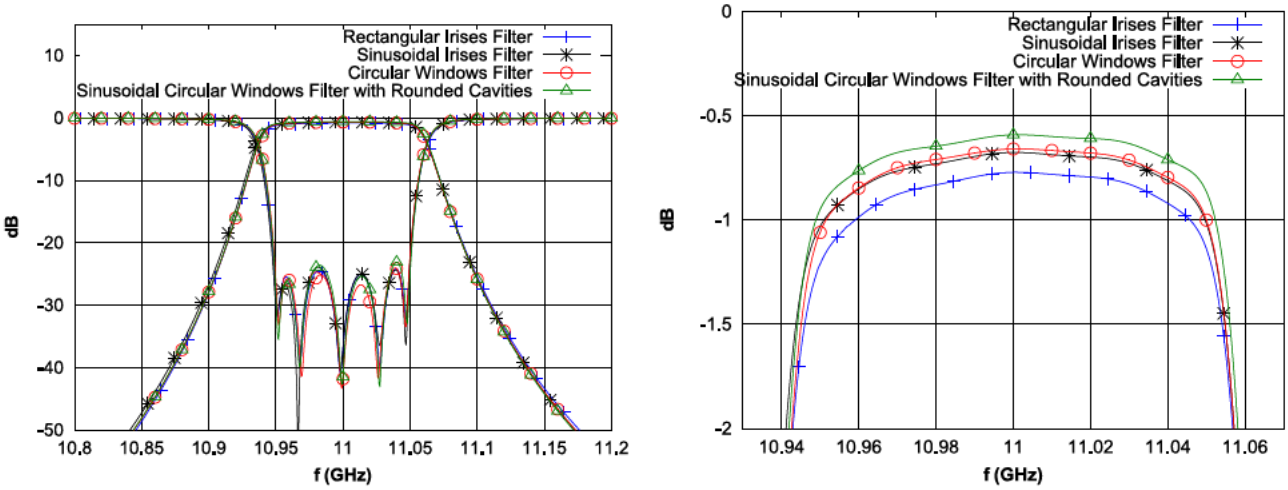

(a) (b)

Figure 5.41: (a) Simulated RF responses of the filters in set 2 using CST Microwave Studio and (b) $S_{2,1}$ detail.

can be observed that the filter with sinusoidal irises and the filter with sinusoidal-circular windows and rounded cavities exhibit essentially the same spurious free range in the individual cavity-coupling structures and thus, the spurious free range of the filters is almost identical. Also, the spurious free ranges of the individual cavity-coupling structures of the filter with rectangular irises are the lowest ones of all the filters considered in set 2 and hence the spurious free range of the complete filter is the lowest one, too. Finally, note that the spurious free range of both the individual cavity-coupling structures of the filter with circular windows and the complete filter lay in between the values obtained in the rest of the filters of set 2.

Table 5.10: Set 2: spurious free range

Filter	$SFR_{0,1}$	$SFR_{1,2}$	$SFR_{2,3}$	SFR_{filter}
Rectangular Irises	37.932	47.692	49.279	45.432
Sinusoidal Irises	51.473	53.618	54.131	52.339
Circular Windows	49.891	52.133	52.894	50.600
Sinusoidal-Circular Windows with Rounded Cavities	51.618	53.799	54.301	52.468

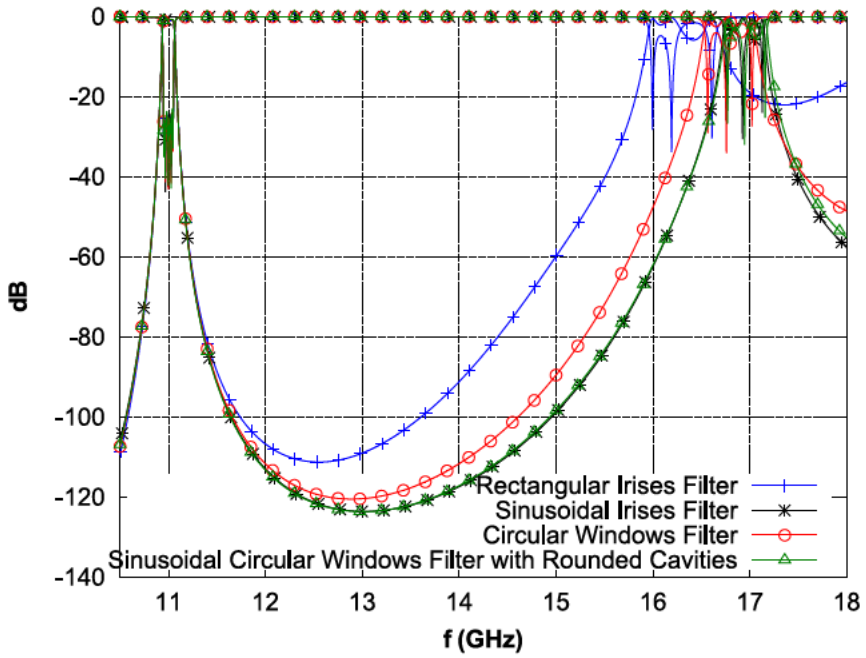

Figure 5.42: Simulated out of band responses of the filters in set 2 using CST Microwave Studio.

5.5.1 Application to filters in Chapter 2

In Chapter 2, two filters with different geometries but same electrical response were studied. On the one hand, a rectangular waveguide cavity filter with rectangular coupling structures was taken as baseline. On the other hand, a rounded waveguide cavity filter with parabolic irises was chosen to show conductor loss improvement due to shaped geometries.

In this section, the theory developed in this work is applied to these two filters when the aluminium alloy AlSi10Mg (Table 2.1) is used as conductor and the result is shown in Table 5.11.

Table 5.11: Calculated Q_{eff} from filters in Chapter 2 when AlSi10Mg is used as conductor

Filter	$Q_{\text{eff},01}$	Impr. (%)	$Q_{\text{eff},12}$	Impr. (%)	$Q_{\text{eff},23}$	Impr. (%)	IL (dB)	Impr. (%)
Baseline	∼3575	N/A	∼3633	N/A	∼3666	N/A	0.803	N/A
Shaped	∼4247	18.8	∼4548	25.19	∼4575	24.8	0.644*	19.8

*corrected value to match the same bandwidth of the baseline filter

Table 5.12: Spurious free range from filters in Chapter 2

Filter	$SFR_{0,1}$	$SFR_{1,2}$	$SFR_{2,3}$	SFR_{filter}
Baseline	53.745	55.700	56.064	54.636
Shaped	49.100	48.709	49.027	47.064

The improvement in effective Q-factor of the shaped geometry filter with respect to the baseline filter is around 19% for the external coupling and around 25% for the inter-resonator couplings. Due to the slight mismatch obtained in return loss in the shaped filter (see Figure 2.15 and Figure 2.16(b)), the insertion loss has been chosen when the transmission parameter is maximum, for both the baseline and the shaped filter. In that case, an improvement of around 20% is obtained for the shaped geometry filter.

The spurious free range of the individual cavity-coupling structures of both the baseline and the shaped filters is collected in Table 5.12, as well as the spurious free range obtained from the complete filters. As in previous cases, the spurious free range of the complete filters tend to the maximum value obtained in the individual cavity-coupling structures, being the one from the baseline filter larger than the one from the shaped filter, as predicted by the individual values. The results are in good agreement with the results reported in the previous chapter for these filters, thus contributing to the validation of the novel effective Q-factor derived in this work.

5.6 Conclusion

A novel effective quality factor (Q_{eff}) that includes losses due to waveguide resonators and coupling structures has been defined in this chapter. The novel Q-factor has been extracted from a lumped element version of an equivalent circuit that accurately represents losses in inter-resonator and external coupling structures, which was derived following the theory in Chapter 4. The new effective Q-factor can predict if a specific coupling structure will yield more or less losses than others in a final filter. This allows the optimization of individual coupling structures to obtain reduced losses. It also eliminates the need of running full-wave analysis of the complete filter, thus saving great amount of time if a geometry optimization is to be conducted. The spurious free range of the individual cavity-coupling structures of a filter has also been calculated and results show that it can be used to predict the spurious free range of a complete filter with good accuracy. To prove the theory, two sets of filters have been designed. The first set comprises two waveguide direct-coupled-cavity filters with the same specifications and same effective Q-factor in their coupling structures but with different coupling geometries. The second set encompasses four waveguide direct-coupled-cavity filters with different geometries and different effective Q-factors. Simulations show that the filters from set 1 with the same effective Q-factor yield almost identical insertion loss whereas the filter from set 2 with the largest Q_{eff} in all its coupling structures has lowest insertion loss, thus validating the novel effective Q-factor definition.

CHAPTER 6

DIMENSIONAL SYNTHESIS OF NARROW-BAND WAVEGUIDE DIRECT-COUPLED-CAVITY FILTERS WITH OPTIMIZED GEOMETRIES

This chapter is devoted to the dimensional process of shaped filters, whose resonators slopes are usually affected by the shaping process. It is true that the slope parameter is often referred to a resonator, instead of to a coupling structure. However, due to the impossibility of separating cavities and coupling structures in waveguide direct-coupled-cavity filters, the effects in slope parameters can either be produced by resonator shaping as well as by coupling shaping.

Following traditional techniques to find the physical dimensions of such filters lead to responses with wrong return loss levels and wrong filter bandwidths. The theory presented here allows to find the correct slope parameter for each resonator and adjust the design equations to find the final accurate dimensions of the filter.

Examples of shaped filters showing this problem are included in this chapter. These filters are designed using traditional dimensional techniques and the proposed modified technique and both simulated responses are compared to each other. The initial target filter response can be perfectly recovered using the new proposed technique with no need of lengthy full-wave optimizations.

6.1 Introduction

The use of waveguide direct-coupled-cavity filters is very popular in the space sector since they dissipate low power and can handle great amount of power. Every percentage of dissipated power can be converted into revenue gain due to the increased payload efficiency. To this aim, new techniques to reduce dissipation loss in microwave filters are searched. In [Flory and Taber, 1997], a new resonator based on Bragg reflectors that increases the unloaded Q-factor of that obtained with traditional rectangular waveguides is presented. Dielectric resonators [Cohn, 1968] are also used when high Q-factors are needed and when volume is a constrain. How-

ever, the main disadvantage of this kind of structures is that the center frequency variation over temperature is excessive for many applications, requiring temperature stabilization.

In the last years, techniques that are able to manufacture very complex shapes at no increased costs are arising [Crawford and Beaman, 1999] and have already been used for the fabrication of RF components [Gilmore and Booth, 2008]. With the maturing of these new fabrication techniques, a new approach can be thought for the loss reduction in waveguide filters: shaping resonator and coupling geometries. Filters with optimized geometries were manufactured using Selective Laser Melting (SLM) in [Lorente et al., 2009b] and proved to successfully reduce the overall filter dissipation losses.

However, the slope parameters of the resonators are modified by the shaping process, and the traditional dimensional techniques that use frequency independent impedance inverters [Cohn, 1957], are shown to introduce big errors during the final dimensional process of the filter. The importance for the correct modeling of the slope parameters of resonators, in order to obtain accurate dimensional synthesis, was already recognized in [Vanin et al., 2004]. In that work, a correction of the slope parameters of resonators due to the frequency dependence of the irises was introduced. The introduction of this correction in the slope parameters allowed to perform accurate dimensioning for very wide-band filters. In that work, the transmission parameters of a coupling structure were calculated using a full-wave simulation program and compared to those of frequency dependant impedance inverter. To do so, a coupling structure model was proposed and simulated in the full-wave program. However, it is not clear where the reference planes of the ports must be placed to extract the phase of the reflection scattering parameter that is later used to construct the transmission parameter matrix. Furthermore, the calculation of the slope parameters of the external coupling structures is based only in empirical results and no detailed analysis was performed.

In the above context, a novel technique that allows an accurate dimensional synthesis of narrow-band filters that use shaping techniques in cavities and coupling elements to optimize loss performance is presented in this chapter. First, it is shown that the shaping processes seriously affect the slope parameters of resonators. Therefore, the direct application of traditional dimensional techniques that use frequency independent impedance inverters leads to serious errors in the final filter response. The novel technique presented here allows to accurately compute the effect of shaping in the slope parameters of already dimensioned resonators, whose dimensions have been obtained with traditional dimensioning techniques that use frequency independent impedance inverters. Once the effect is extracted, a correction is introduced in the slope parameters of the isolated resonators. It is shown that when the appropriate corrections are introduced, the dimensional synthesis leads to very accurate dimensioning of the different parts of the filter, recovering an almost ideal response of the shaped filter structure. The objective of the technique derived is similar to the one presented in [Vanin et al., 2004]: to take into account the slope parameter distortion introduced by the coupling structures to improve the design process of the filter. However and in contrast to the previous work [Vanin et al., 2004], the analysis here is performed on both the inter-resonator as well as the external couplings, and the slope parameter correction is rigorously

derived and validated for both cases. Furthermore, the new technique is performed using coupling coefficients k and scattering parameters, which are more familiar concepts to the filter engineer than those of transmission parameters used in the previous work [Vanin et al., 2004].

To illustrate the application of the novel technique, two examples of shaped filters where the problem can be clearly observed are designed. In the first case, a narrow-band filter with 4.5% bandwidth has been chosen. In the second case, a filter with narrower bandwidth but with higher center frequency than the previous filter is used. Both filters have been designed following the traditional direct dimensional technique [Cohn, 1957], and then applying the corrections in the slope parameters of the resonators. Results indicate large errors in the final recovered bandwidth when the traditional direct dimensional technique is applied. This indicates errors in the final synthesized couplings of the filter. However, when corrections are applied to the slope parameters of the resonators, the recovered responses exhibit perfect characteristics as compared to the target specifications. A third filter with shaped cavities and coupling elements has also been designed and manufactured. Both the traditional and the novel techniques have been applied for the design, again confirming that target specifications can be perfectly recovered if the novel technique is used. Measured results show excellent agreement with simulation results. This shows the effectiveness of the technique presented, and its usefulness in the design of practical shaped filters, for optimized loss performance, with fixed target specifications.

6.2 Slope Parameter Modification

In this section the basic concepts and definitions behind the slope parameters of ideal resonators are reviewed. The slope parameter of a resonator [Matthaei et al., 1980] is related to its stored energy. For series type resonators, the reactance slope parameter (6.1) is used whereas the susceptance slope parameter (6.2) is used for parallel type resonators.

$$\chi = \frac{\omega_0}{2} \left. \frac{dX}{d\omega} \right|_{\omega 0} \tag{6.1}$$

$$b = \frac{\omega_0}{2} \left. \frac{dB}{d\omega} \right|_{\omega 0} \tag{6.2}$$

In the previous expressions, X is the reactance of the input impedance (Z_{in}) of a series resonator and B is the susceptance of the input admittance (Y_{in}) of a parallel resonator.

Figure 6.1(a) shows a waveguide cavity resonator with a rounded cross section. Its lossless equivalent circuit is presented in Figure 6.1(b) and Figure 6.1(c), when transmission line or lumped element resonators are used, respectively.

In Figure 6.1, Z_C is the characteristic impedance of the fundamental mode, β_C is its propagation constant, $Z_{\text{in,TL}}$ is the input impedance of the transmission line resonator, and $Z_{\text{in,LC}}$ is the input impedance of the lumped elements resonator.

Expressions for the reactance slope parameter of the transmission line resonator (6.5) as well as for the lumped elements resonator (6.6) can be obtained by combining their input impedances (6.3) and (6.4) into (6.1), respectively, as

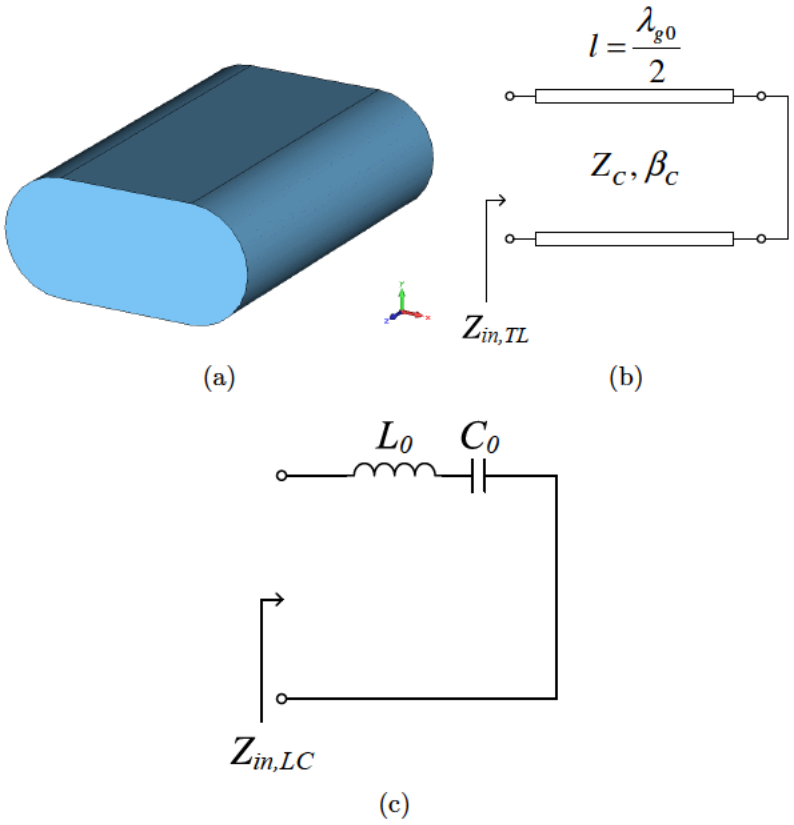

Figure 6.1: (a) Waveguide cavity, (b) its equivalent transmission line resonator, and (c) its equivalent lumped element resonator.

$$Z_{\text{in,TL}} = jZ_C \tan \beta l \tag{6.3}$$

$$Z_{\text{in,LC}} = j\left(\omega L_0 + \frac{1}{\omega C_0}\right) \tag{6.4}$$

$$\chi_0 = Z_C \frac{\pi}{2}\left(\frac{\lambda_{g0}}{\lambda_0}\right)^2 \tag{6.5}$$

$$\chi_0 = \omega_0 L_0 \tag{6.6}$$

where (χ_0) indicates the slope parameter of the isolated ideal resonator.

When a given resonator is connected to an external structure with a shaped coupling element, its slope parameter as computed with the previous expressions is strongly modified. In the next subsections a procedure to compute the effects of shaped coupling structures in the slope parameters of the resonators attached to them is presented. The analysis will be performed separately for both inter-resonator and external couplings.

6.2.1 Inter-Resonator Coupling

Consider the two waveguide resonators coupled through a geometrically optimized aperture (shaped coupling element) as shown in Figure 6.2.

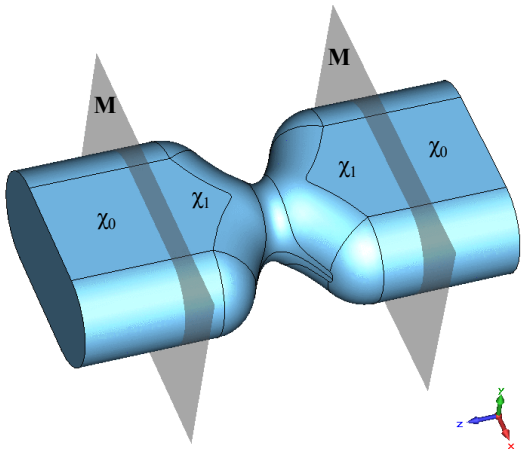

Figure 6.2: Waveguide cavities coupled through a shaped aperture.

With the aid of a full-wave simulation program and applying the even and odd mode theory already seen in Chapter 4, the dimensions of the above structure can be adjusted to give a coupling coefficient k_{C0} (4.8). If two ports are added at the terminal planes in the structure of Figure 6.2, the transmission parameter S_{21} for this coupling is obtained. The reactance slope parameter $\chi_{\text{eff},0}$ of the cavities in Figure 6.2 (cavities with perfect short at one end and a shaped coupling geometry at the other) can be obtained with the traditional theory [Matthaei et al., 1980] as

$$\chi_{\text{eff},0} = \frac{K}{k_{C0}} \tag{6.7}$$

where K is the value of the impedance inverter associated to the coupling and can be obtained from the previously calculated transmission parameter as

$$K = Z_C \left(\frac{1}{|S_{21}|} - \sqrt{\frac{1}{|S_{21}|^2} - 1} \right) \tag{6.8}$$

In the model of Figure 6.2, the same resonator cross section as that of the cavity in Figure 6.1(a) is used. However, the slope parameter ($\chi_{\text{eff},0}$) does not agree with the slope parameter of the isolated resonator (χ_0). This is due to the influence of the geometrically optimized coupling structure used in the model. The characteristic impedance of the line depends on the resonator cross section, which varies in the vicinity of the coupling in the model of Figure 6.2, thus yielding a slope parameter that is dependent on the direction of propagation. If Z_C is assumed constant and normalized to 1 Ω, an effective constant slope parameter can then be obtained, simplifying the problem.

The effective slope parameter can be taken as an average between the slope parameter of a constant cross section closed cavity (χ_0) and the slope parameter

of a cavity with identical coupling apertures at both ends (χ_1). To prove this, the equivalent circuit of the model in Figure 6.2 is shown in Figure 6.3.

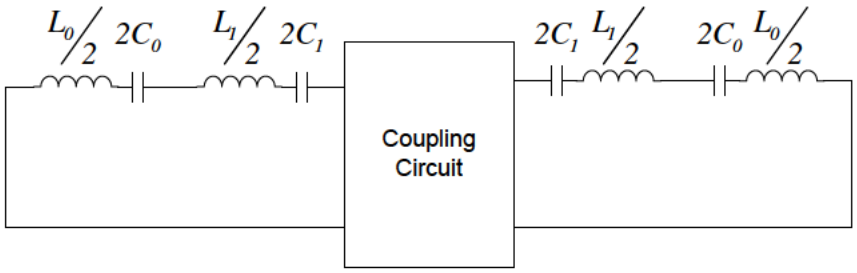

Figure 6.3: Equivalent circuit of the structure in Figure 6.2.

If we focus our attention on the structure in Figure 6.2, it is seen that, for example, each resonator can be viewed as formed by two half-resonators. The first half is formed by a closed unperturbed resonator of the type shown in Figure 6.1(a). The second half is a resonator perturbed by the shaped coupling window. In the equivalent circuit of Figure 6.3, the unperturbed resonator is denoted with the lumped elements (L_0, C_0), while the perturbed resonator is indicated with lumped elements (L_1, C_1). Hence, the slope parameter of the complete resonator in the previous circuit is obtained using the classical definition as

$$\chi_{\text{eff},0} = \omega_0 L_{\text{eff},0} = \omega_0 \frac{L_0 + L_1}{2} = \frac{\chi_0 + \chi_1}{2} \tag{6.9}$$

where $L_{\text{eff},0}$ is the equivalent inductance of two series inductances (L_0 and L_1). From the last expression we can conclude that the effective slope parameter of a complete resonator with a perfect short at one end and a geometry optimized coupling at the other end can be seen as the average of the slope parameters of a resonator with perfect shorts at both ends and a resonator with identical couplings at both ends.

A reduced model (see Figure 6.4) can be obtained if magnetic walls are placed at the M planes in the model of Figure 6.2. Its equivalent circuit can be seen in Figure 6.5.

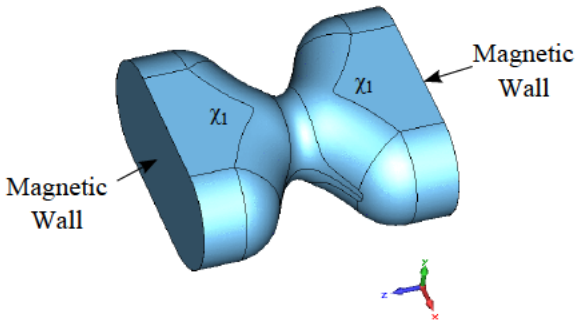

Figure 6.4: Halved waveguide cavities coupled through a shaped aperture.

The process to be followed for calculating the slope parameter (χ_1) of the resonators in the reduced model of Figure 6.4 is exactly the same as in the previous

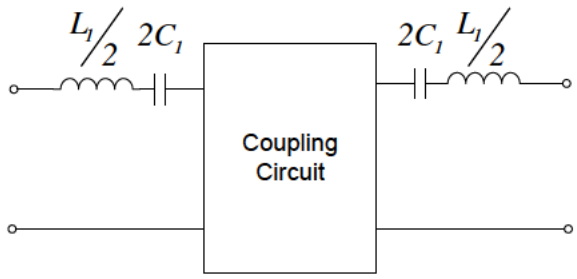

Figure 6.5: Equivalent circuit of the structure in Figure 6.4.

case. However, it is to note that the adjusted dimensions of the coupling structure to yield a given coupling coefficient k_C are different from the ones obtained if the complete model is used. This is because of the different slope parameter obtained. In the complete model (Figure 6.2) the slope parameter ($\chi_{\text{eff},0}$) can be seen as an average between the slope parameter of a closed unperturbed cavity (χ_0) and that of a cavity with identical couplings at both ends (χ_1). On the other hand, the slope parameter of the reduced model (Figure 6.4) is χ_1 directly. Therefore, the reduced model in Figure 6.4 can be used instead of the complete model in Figure 6.2 if χ_1 is searched.

The dimensions of the model with complete resonators and the model with halved resonators have been adjusted to give the same coupling coefficient k_{C0} as shown in Table 6.1. As the final dimensions of the coupling structure are different for the two models, the transmission parameter S_{21} obtained from full-wave simulation is also different. The effective reactance slope parameter ($\chi_{\text{eff},0}$) can be obtained for the model with complete resonators and the reactance slope parameter χ_1 can be derived using (6.9) and (χ_0). Note that the latter agrees very well with the slope parameter (χ_1) derived directly from the model with halved resonators.

Table 6.1: Coupling parameters for a center frequency $f_0 = 11$ GHz

Parameter	Full Resonator Model	Half Resonator Model
k_{C0}	0.008854	0.008854
$\lvert S_{21}\rvert$ in dB	-24.963	-24.819
χ_0	$3.136Z_C$	$3.136Z_C$
$\chi_{\text{eff},0}$	$3.192Z_C$	N/A
χ_1	$3.249Z_C$	$3.246Z_C$

6.2.2 External Coupling

Figure 6.6 shows a waveguide cavity coupled to the input feed line through a geometrically optimized coupling, whose dimensions are adjusted to give the desired external Q-factor $Q_{\text{ext}0}$ at the design center frequency f_0.

The transmission parameter S_{21} of the coupling structure can be obtained if a simulation with two ports is run. The reactance slope parameter ($\chi_{\text{eff},0}$) of the cavity in the model of Figure 6.6(cavity with perfect short at one end and a shaped

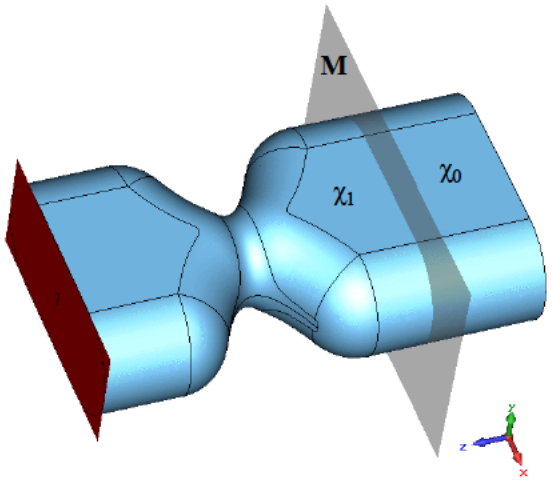

Figure 6.6: Waveguide cavity coupled to the input feed line.

coupling geometry at the other) can then be obtained using the traditional theory [Matthaei et al., 1980] as

$$\chi_{\text{eff},0} = K^2 Q_{\text{ext}0} \tag{6.10}$$

where K is the value of the impedance inverter associated to the input (output) coupling, and can be obtained using (6.8).

Again, the slope parameter of the cavity in Figure 6.6 ($\chi_{\text{eff},0}$) can be seen as an average between the slope parameter of a closed cavity (χ_0) and that of a perturbed cavity due to identical shaped coupling structures at both ends (χ_1). The equivalent circuit of the model in Figure 6.6 is presented in Figure 6.7.

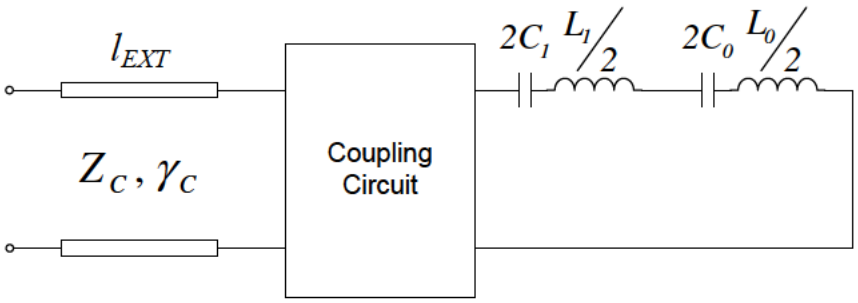

Figure 6.7: Equivalent circuit of the structure in Figure 6.6.

As in the inter-resonator case, the whole cavity in Figure 6.6 can be viewed as composed of two half-resonators. The first one corresponds to an unperturbed resonator of the type shown in Figure 6.1(a) with perfect shorts at both ends, while the second half resonator is perturbed by the same shaped coupling window at both ends. The unperturbed resonator is denoted in Figure 6.7 with lumped elements (L_0, C_0), and the perturbed one with elements $(L_1 C_1)$.

The slope parameter of the complete resonator in Figure 6.7 with a perfect short at one of its ends and a geometry optimized coupling at the other end is then obtained using the classical definition as

$$\chi_{\text{eff},0} = \omega_0 L_{\text{eff},0} = \omega_0 \frac{L_0 + L_1}{2} = \frac{\chi_0 + \chi_1}{2} \tag{6.11}$$

where $L_{\text{eff},0}$ is the equivalent inductance of two series inductances (L_0 and L_1). It can be observed that the effective slope parameter of the complete resonator shown in Figure 6.6 can be seen as the average of the slope parameters of the two resonators considered (one with perfect shorts at both ends and one with identical coupling structures at both ends).

6.3 Dimensional Synthesis

In this section we derive a new dimensional synthesis technique that takes into account the effects of shaped coupling elements in the slope parameters of the adjacent resonators. A flow-chart of the design technique, indicating all steps, is shown in Figure 6.8.

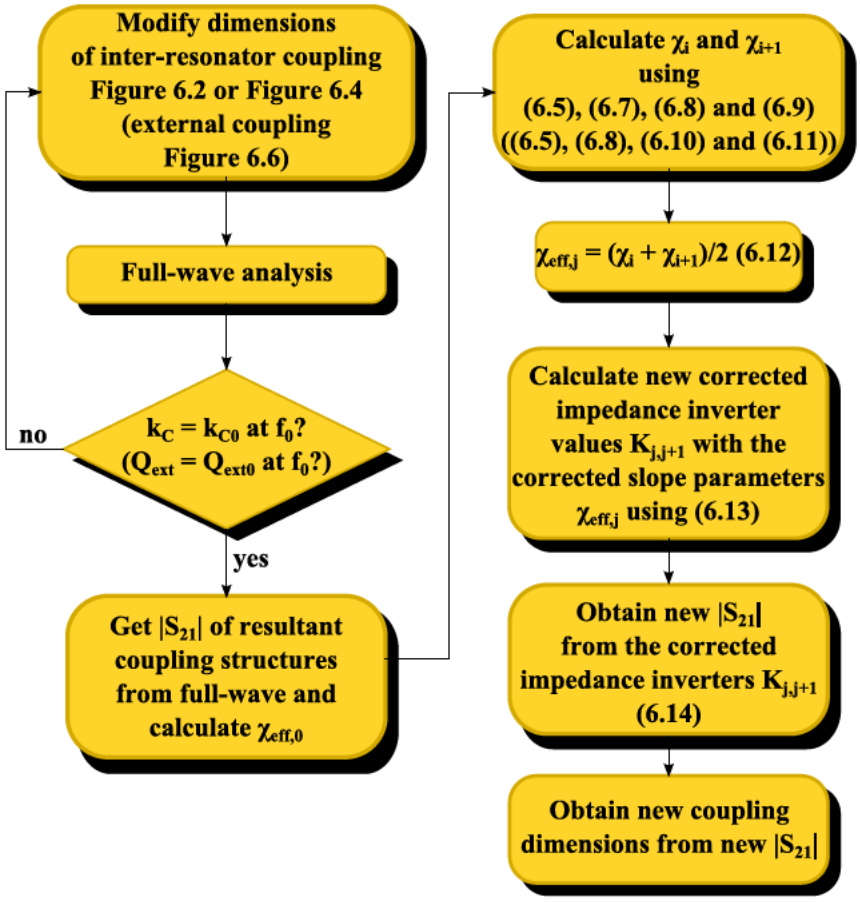

Figure 6.8: Flow chart of the novel dimensional synthesis.

The proposed new dimensional synthesis of the coupling structures of filters with optimized geometries is a two steps process. In the first step, the dimensions of the inter-resonator coupling (Fig. 6.2) as well as the dimensions of the external coupling (Fig. 6.6) are adjusted with the aid of a full-wave simulation program until the desired coupling coefficient ($k_C = k_{C0}$) or external Q-factor ($Q_{\text{ext}} = Q_{\text{ext0}}$) at the

design center frequency are obtained, respectively. Then, the transmission parameter (S_{21}) can be directly simulated from the previously adjusted structures and the slope parameter $\chi_{\text{eff},0}$ of a cavity with a perfect short at one end and a geometry optimized coupling at the other end (as the cavities shown in Figure 6.2 and in Figure 6.6) can be calculated using (6.7) and (6.8) in the case of an inter-resonator coupling and using (6.8) and (6.10) in the case of an external coupling. Then, the slope parameter of a resonator with identical coupling structures at both ends is calculated by isolating χ_1 in (6.9) or (6.11). If this is done for the different couplings of a filter, the slope parameters of cavities with different coupling geometries at each end $\chi_{\text{eff},j}$ can be computed as the average of the slope parameters of two different cavities with identical coupling geometries at both ends (χ_i and χ_{i+1}) as in (6.12).

$$\chi_{\text{eff},j} = \frac{\chi_i + \chi_{i+1}}{2} \tag{6.12}$$

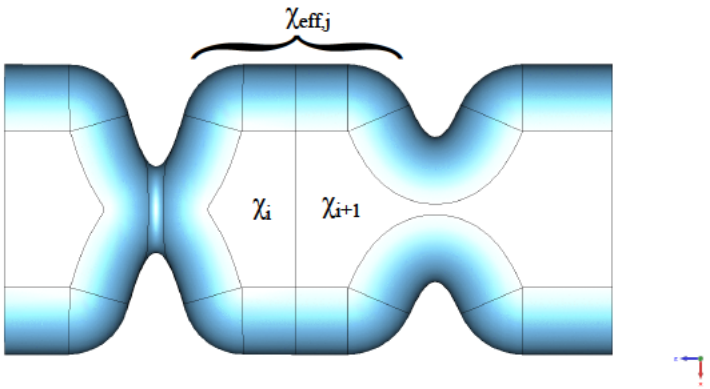

Figure 6.9: Effective resonator slope parameter in a filter with optimized geometries.

In the second step, the values of corrected impedance inverters are calculated using these new slope parameters ($\chi_{\text{eff},j}$) and the traditional filter theory [Matthaei et al., 1980] as

$$\begin{aligned} K_{01} &= M_{01}\sqrt{Z_C\ \chi_{\text{eff},1}\ w} \\ K_{j,j+1}|_{j=1,n-1} &= \sqrt{\chi_{\text{eff},j}\ \chi_{\text{eff},j+1}}\, w\, M_{j,j+1} \\ K_{n,n+1} &= M_{n,n+1}\sqrt{Z_C\ \chi_{\text{eff},n}\ w} \end{aligned} \tag{6.13}$$

In the last expression (6.13), $K_{j,j+1}$ is the value of the corrected impedance inverter, $M_{j,j+1}$ denotes de normalized coupling coefficient obtained from filter synthesis techniques, and w refers to the fractional bandwidth. From the corrected impedance inverter, the amplitude of the transmission parameter $S_{21,j,j+1}$ can be calculated as

$$\left|S_{21_{j,j+1}}\right| = \frac{2Z_C}{K_{j,j+1} + \dfrac{1}{K_{j,j+1}}Z_C^2} \tag{6.14}$$

where (Z_C) can again be normalized to one. In the last task of the procedure, the dimensions of the coupling structures are adjusted until the absolute values of the corrected transmission parameters ($\left|S_{21_{j,j+1}}\right|$) are obtained.

Figure 6.8 summarizes the process to be followed to find the correct coupling dimensions when shaped coupling geometries are used in the filter structure.

6.4 Examples and Validation

Two examples of filters with optimized geometries have been designed and simulated using the traditional filter theory and the novel approach discussed in this chapter, and the results are presented in this section. Figure 6.10(a) shows the first operation in the design of the geometrically optimized filter considered here. In this case, rectangular boxes are used as resonators and circular windows with a sinusoidal shape along its z-dimension are used as coupling apertures. Next, a fillet operation with a radii r_1 in the cavity edges and r_{Ci} in the different edges of the coupling structures has been applied to obtain the final shaped filter, as can be seen in Figure 6.10(b).

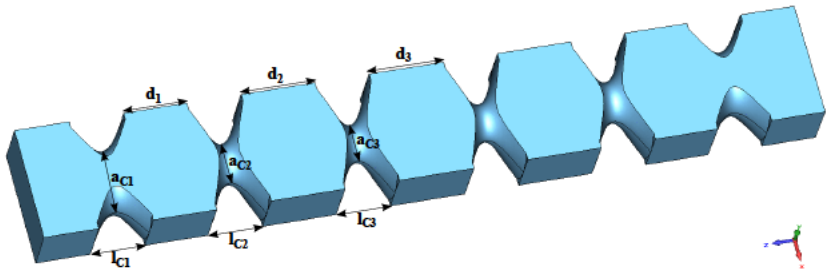

(a)

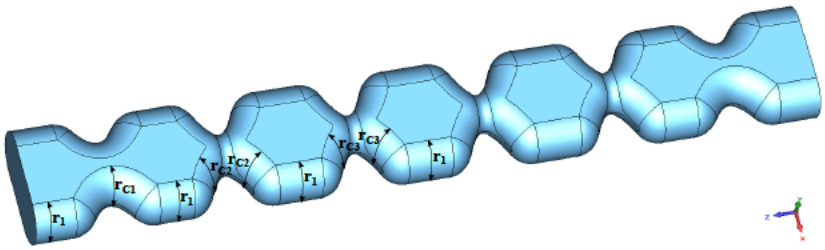

(b)

Figure 6.10: Filter geometry with shaped elements: (a) first design step and (b) second design step.

From the basic shaped geometry shown in Figure 6.10(b), we will consider the design of two different filters.

6.4.1 Example 1

A filter with geometry as in Figure 6.10(b) and with the specifications as in Table 6.2 has been designed following the standard filter theory and the novel approach presented in this chapter.

The K-inverter target values assuming a constant slope parameter $\chi_0 = 3.13558 Z_C$ (6.5) of a closed unperturbed resonator (Figure 6.1(a)) are shown in

Table 6.2: Example 1: filter specifications

Parameter	Value
Degree	5
f_0	11 GHz
BW	500 MHz
RL	25

Table 6.3 (traditional design technique).

Table 6.3: Example 1: K-inverter target values (traditional design)

$K_{0,1}$	$K_{1,2}$	$K_{2,3}$
$0.423Z_C$	$0.139Z_C$	$0.097Z_C$

However, as stated in the previous section, shaped geometry couplings modify the slope parameters χ_i of their adjacent cavities.

These can be obtained from $\chi_{\text{eff},0}$ and χ_0 as explained in Section 6.2.1 for the inter-resonator couplings and in Section 6.2.2 for the external couplings, and are shown in Table 6.4.

Table 6.4: Example 1: modified slope parameters of adjacent cavities to shaped couplings (χ_i)

-	Coupling 1	Coupling 2	Coupling 3
χ_0	$3.136Z_C$	$3.136Z_C$	$3.136Z_C$
$\chi_{\text{eff},0}$	$3.250Z_C$	$3.330Z_C$	$3.291Z_C$
χ_i	$3.365Z_C$	$3.524Z_C$	$3.447Z_C$

The values in Table 6.4 are now used to derive the effective slope parameters $\chi_{\text{eff},j}$ of the complete cavities in the filter as (6.12). Table 6.5 collects the calculated effective slope parameters of the cavities in the filter.

Table 6.5: Example 1: effective slope parameters of complete cavities with different coupling geometries at each end ($\chi_{eff,j}$)

$\chi_{\text{eff},1}$	$\chi_{\text{eff},2}$	$\chi_{\text{eff},3}$
$3.4444Z_C$	$3.4854Z_C$	$3.4474Z_C$

The final corrected K-inverter target values of the couplings in the filter are calculated using (6.13) and the computed effective slope parameters of cavities with different couplings at each end. Table 6.6 collects the K-inverter target values obtained with the traditional filter design and the corrected ones obtained with the novel design explained in this chapter. The deviation between the traditional values and the corrected ones is also shown. The strong deviation of more than 10% in some couplings clearly indicates that the traditional design process cannot successfully be applied to this kind of shaped filters.

Table 6.6: Example 1: K-inverter target values (traditional and novel design)

	Traditional Design	Novel Design	Deviation (%)
$K_{0,1}$	$0.423Z_C$	$0.443Z_C$	4.81
$K_{1,2}$	$0.139Z_C$	$0.153Z_C$	10.50
$K_{2,3}$	$0.097Z_C$	$0.108Z_C$	10.55

Table 6.7: Example 1: physical dimensions

Parameter	Value (mm)	
	Traditional Design	Novel Approach
a	21.287	21.287
b	9.876	9.876
d_1	8.363	8.082
d_2	11.157	10.895
d_3	11.617	11.382
a_{C1}	13.971	14.153
a_{C2}	10.747	10.989
a_{C3}	9.931	10.155
l_{C1}	10	10
l_{C2}	10	10
l_{C3}	10	10
r_1	$b/2$	$b/2$
r_{C1}	$b/2$	$b/2$
r_{C2}	$b/2$	$b/2$
r_{C3}	$b/2$	$b/2$

The resulting dimensions of both designs are collected in Table 6.7.

The simulated responses of the filter designed using both the standard and the novel approach are collected in Figure 6.11. The response of the circuit theory is also shown for comparison. The return loss level of the filter designed with the standard filter theory is around 25 dB. However, its synthesised bandwidth is 457.5 MHz. Note that the desired response is perfectly recovered with 500 MHz of bandwidth and similar behavior of return losses of 25 dB, if the novel approach is used instead.

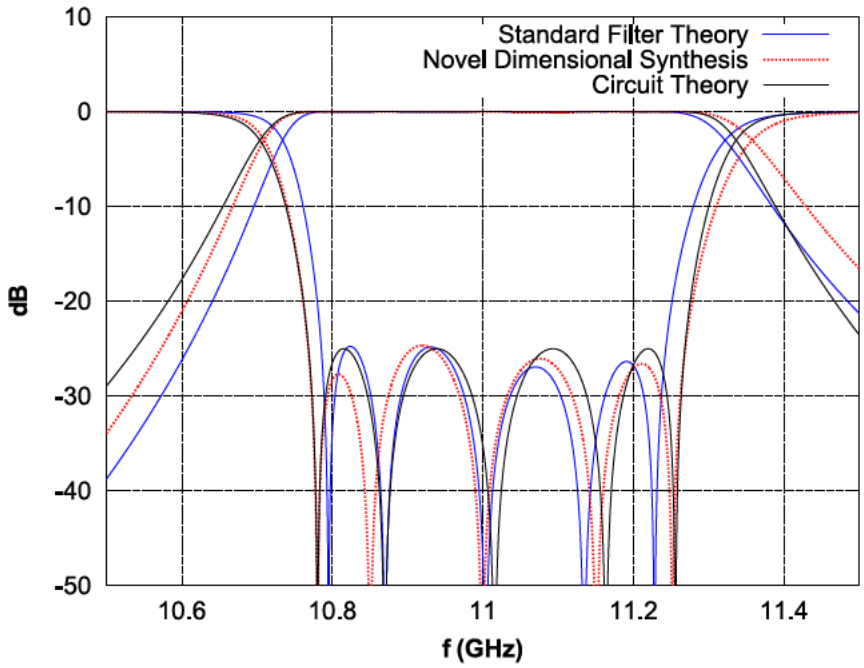

Figure 6.11: Full-wave RF response of the filter in example 1 designed following the traditional and the novel dimensional techniques.

6.4.2 Example 2

A smaller bandwidth than the one used in example 1 will translate in smaller coupling apertures and it will definitely reduce the impact of shaped coupling windows on the slope parameter of the cavities. In the next example, the filter fractional bandwidth is reduced to approximately 1.8%. However the center frequency has been shifted to the WR-75 upper frequency band-edge, which will make the cavities shorter and hence will increase the impact of shaped coupling windows on the slope parameter of the cavities. The filter specifications are collected in Table 6.8.

Table 6.8: Example 2: filter specifications

Parameter	Value
Degree	5
f_0	14 GHz
BW	250 MHz
RL	25

Table 6.9 shows the modified reactance slope parameters χ_i of the adjacent cavities to the shaped geometry couplings (cavities with the geometry optimized coupling at one end and a perfect short at the other end) and the computed effective reactance slope parameters $\chi_{\text{eff},j}$ of the cavities with different coupling geometries at each end, at the filter center frequency. The reactance slope parameter of a closed unperturbed cavity χ_0 is also shown. In Table 6.10 the final values of the K-inverters obtained with the traditional theory and the novel approach are presented and the deviation is calculated. Again, these strong deviations (in one case of more than

13%) suggest that the traditional theory must be corrected for shaped geometry filters.

Table 6.9: Example 2: modified slope parameters of adjacent cavities to shaped couplings (χ_i) and effective slope parameters of complete cavities with different coupling geometries at each end ($\chi_{eff,j}$)

Parameter	Value
χ_0	$2.270Z_C$
χ_1	$2.843Z_C$
χ_2	$2.499Z_C$
χ_3	$2.470Z_C$
$\chi_{\text{eff},1}$	$2.671Z_C$
$\chi_{\text{eff},2}$	$2.484Z_C$
$\chi_{\text{eff},3}$	$2.470Z_C$

Table 6.10: Example 2: K-inverter target values (traditional and novel design)

	Traditional Design	Novel Design	Deviation (%)
$K_{0,1}$	$0.226Z_C$	$0.245Z_C$	8.47
$K_{1,2}$	$0.039Z_C$	$0.045Z_C$	13.47
$K_{2,3}$	$0.028Z_C$	$0.030Z_C$	9.11

The dimensions of the designed filters using both the traditional and the novel techniques are collected in Table 6.11.

Table 6.11: Example 2: physical dimensions

Parameter	Value (mm)	
	Traditional Design	Novel Approach
a	21.287	21.287
b	9.876	9.876
d_1	6.921	6.741
d_2	8.513	8.418
d_3	8.660	8.593
a_{C1}	9.416	9.610
a_{C2}	6.252	6.435
a_{C3}	5.765	5.880
l_{C1}	8	8
l_{C2}	8	8
l_{C3}	8	8
r_1	$b/2$	$b/2$
r_{C1}	$b/2 - 0.5$	$b/2 - 0.5$
r_{C2}	$b/2 - 0.5$	$b/2 - 0.5$
r_{C3}	$b/2 - 0.5$	$b/2 - 0.5$

Figure 6.12 shows the full-wave response of the filter designed following both approaches and the response of the circuit theory for comparison. In this case the return loss level of the filter designed with the standard theory is around 22 dB and the bandwidth is reduced to 239 MHz, clearly indicating that the synthesized couplings are wrong. Again, when the novel approach is used, the response directly obtained from the synthesized dimensions exhibits exactly 250 MHz bandwidth, and the correct design value of return losses of 25 dB.

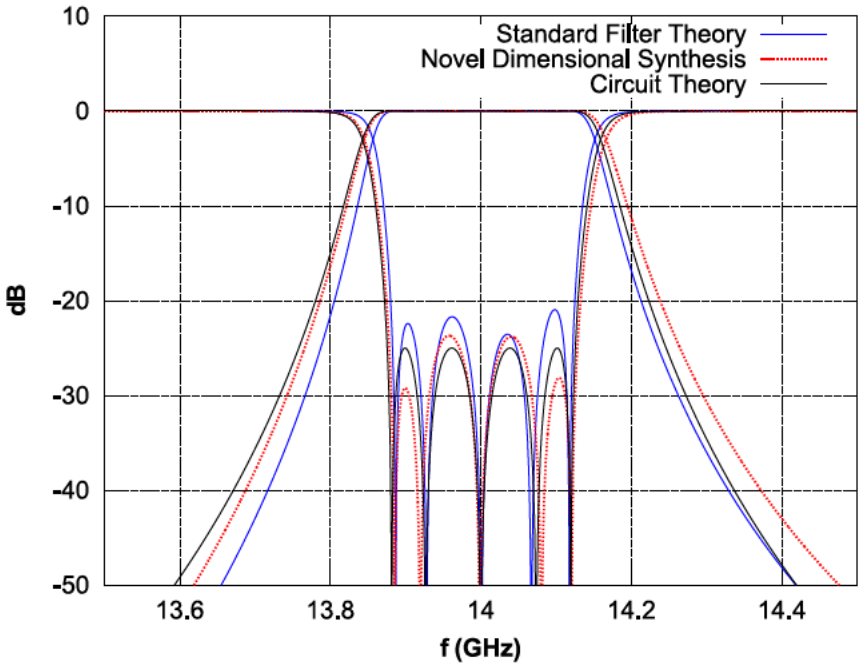

Figure 6.12: Full-wave RF response of the filter in example 2 designed following the traditional and the novel dimensional techniques.

These results demonstrate that the target specifications are exactly recovered when the new proposed technique is used, without extra optimization processes applied to the full filter structure.

6.5 Measurements

The manufacturing of shaped filters as the one shown in Figure 6.10(b) with standard machining methods is very complex and manufacturing tolerances would definitely force the use of tuning screws in the final manufactured filter. To prove the theory presented in this chapter, a less complex geometry than the ones shown in the previous section has been selected for manufacturing. Measurement results of a fifth degree waveguide cavity filter with internal geometry as in Figure 6.13 and with the specifications given in Table 6.12 are presented in this section.

The filter has also been designed following the standard filter theory and the novel approach presented in this chapter. The modified reactance slope parameters χ_i of the adjacent cavities to the shaped geometry couplings (cavities with the geometry optimized coupling at one end and a perfect short at the other end) are collected in Table 6.13 together with the effective reactance slope parameters $\chi_{\text{eff},j}$

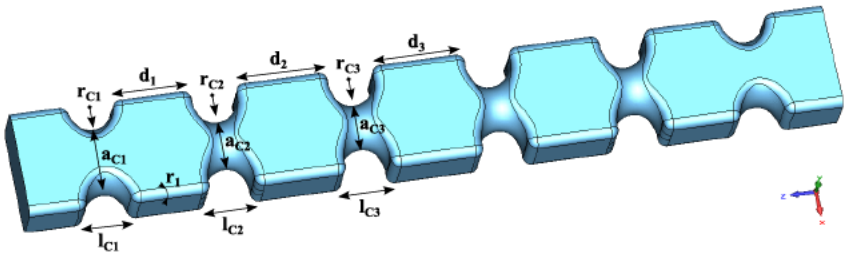

Figure 6.13: Internal filter geometry of the manufactured prototype.

Table 6.12: Manufactured prototype: filter specifications

Parameter	Value
Degree	5
f_0	11 GHz
BW	100 MHz
RL	25

of the different cavities of the filter (with different couplings at each end) and the reactance slope parameter of a closed unperturbed cavity. The final values of the K-inverters obtained with the traditional theory and the novel approach are presented in Table 6.14 and its deviation is shown.

Table 6.13: Manufactured prototype: modified slope parameters of adjacent cavities to shaped couplings (χ_i) and effective slope parameters of complete cavities with different coupling geometries at each end ($\chi_{eff,j}$)

Parameter	Value
χ_0	$3.291 Z_C$
χ_1	$3.494 Z_C$
χ_2	$3.356 Z_C$
χ_3	$3.340 Z_C$
$\chi_{eff,1}$	$3.425 Z_C$
$\chi_{eff,2}$	$3.348 Z_C$
$\chi_{eff,3}$	$3.340 Z_C$

Table 6.14: Manufactured prototype: K-inverter target values (traditional and novel design)

	Traditional Design	Novel Design	Deviation (%)
$K_{0,1}$	$0.194 Z_C$	$0.198 Z_C$	2.01
$K_{1,2}$	$0.029 Z_C$	$0.030 Z_C$	2.89
$K_{2,3}$	$0.020 Z_C$	$0.021 Z_C$	1.61

The resulting dimensions of both designs are collected in Table 6.15.

The full-wave response of the filter obtained with the traditional design process is compared against the one of the filter designed with the novel technique in Fig-

Table 6.15: Manufactured prototype: physical dimensions

Parameter	Value (mm)	
	Traditional Design	Novel Approach
a	19.05	19.05
b	9.525	9.525
d_1	13.614	13.558
d_2	15.932	15.902
d_3	16.154	16.135
a_{C1}	11.328	11.370
a_{C2}	8.148	8.189
a_{C3}	7.661	7.682
l_{C1}	8	8
l_{C2}	8	8
l_{C3}	8	8
r_1 (radius)	1.5	1.5
r_{C1} (radius)	$l_{C1}/2$	$l_{C1}/2$
r_{C2} (radius)	$l_{C2}/2$	$l_{C2}/2$
r_{C3} (radius)	$l_{C3}/2$	$l_{C3}/2$

ure 6.14. The response of the circuit theory is also shown for comparison. It can be noted that the bandwidth of the filter is perfectly recovered after using the novel design technique (98 MHz in the case of the traditional design and 100 MHz in the case of the novel design).

The filter designed with the novel technique has been manufactured and measured and the response is shown in Figure 6.15. The full-wave response including ohmic losses is also shown. Note that good agreement between simulation and measurement has been obtained (no tuning has been carried out in the manufactured filter). A slight frequency shift is present between full-wave simulation and measurements. However, this can be explained as the filter was designed assuming vacuum conditions but was measured at ambient conditions. Figure 6.16 plots the responses of the simulated and measured filters using a normalized frequency axis. It can be observed that exactly the target bandwidth of 100 MHz has been obtained in the measured prototype. A photo of the manufactured filter is also shown in Figure 6.17.

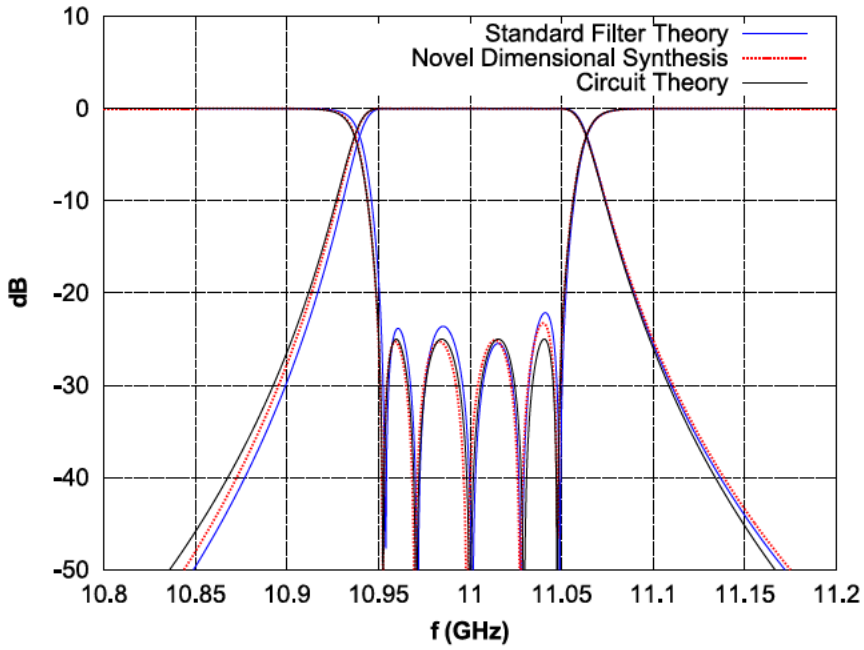

Figure 6.14: Full-wave RF response of the manufactured filter designed following the traditional and the novel dimensional techniques.

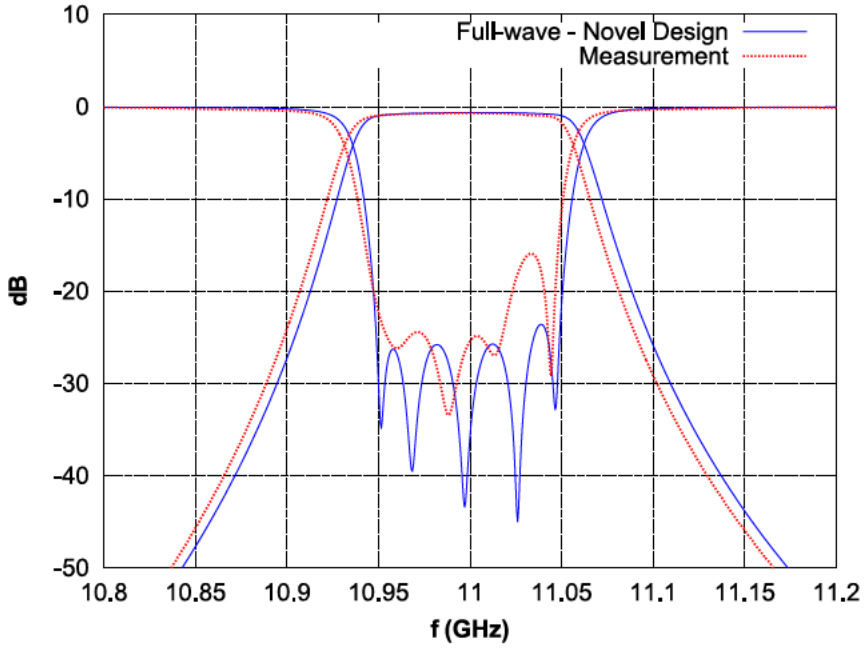

Figure 6.15: Measured and full-wave RF responses of the manufactured filter designed following the novel dimensional technique.

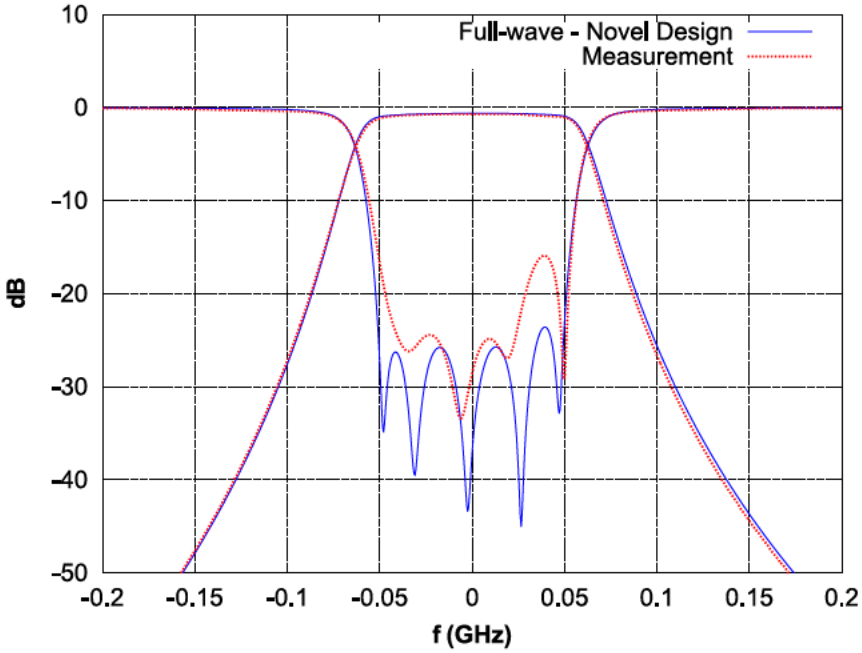

Figure 6.16: Measured and full-wave RF responses of the manufactured filter designed following the novel dimensional technique in a normalized frequency axis.

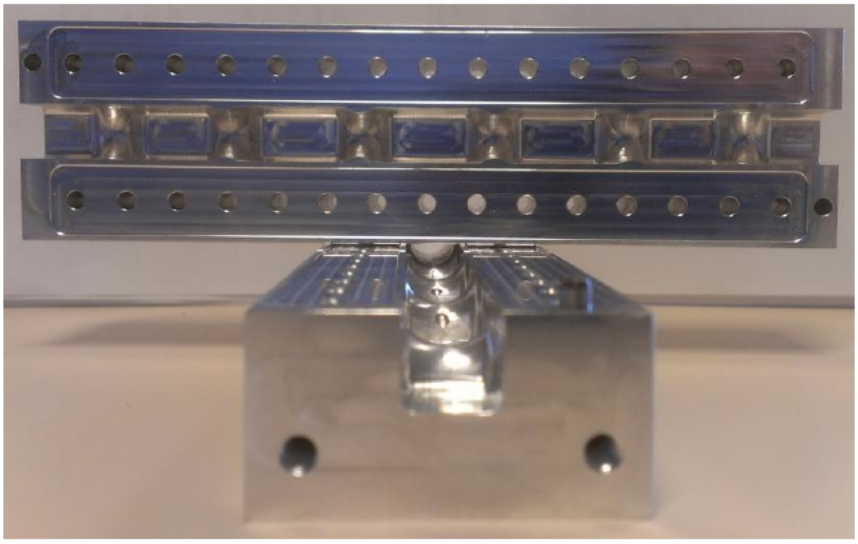

Figure 6.17: Manufactured prototype.

6.6 Conclusion

A novel approach for the dimensional synthesis of narrow-band filters with optimized geometries has been presented in this chapter. Shaping filter structures is an option when reduced insertion loss is desired. However, the characteristic impedance of the optimized resonators varies along their lengths, and so their slope parameters. Also, optimized coupling geometries affect the slope parameter of the resonators, resulting in deviated filter responses if the standard filter design theory that uses frequency independent impedance inverters is employed. The dimensional synthesis presented here corrects the deviations by introducing appropriate corrections in the slope parameters of the resonators. Two examples of narrow-band shaped filters are presented to demonstrate that the desired filter responses can be perfectly recovered if the novel approach is used, avoiding the use of lengthy full-wave optimizations on the complete structures. Also, a narrow-band waveguide cavity filter with shaped geometry has been manufactured and measured. No tuning process has been applied neither to the cavities nor to the couplings. Very good agreement with full-wave simulation is achieved.

CHAPTER 7

CONCLUSIONS AND FUTURE WORK

7.1 Conclusions

The work presented in this thesis has been thoroughly structured to achieve the final main goal: the search of techniques for the loss reduction in waveguide direct-coupled-cavity filters through geometry optimization. It is clear that to reach such an objective, the geometry of the resonators and the coupling structures must be modified in a way that the final insertion loss of the filter is successfully reduced. However, brute force optimization of a complete filter with complex geometries and with so many parameters such as cavity and coupling dimensions, roundings, chamfered edges, curvatures that follow mathematical functions, etc., that increase with the order of the filter, would be an extremely tedious task. To follow this direct path would most probably lead to a deep frustration and a quite large amount of lost time. The main goal is clear, but to succeed, the overall problem of the loss reduction in the final filter must be subdivided in smaller tasks or minor goals that will lead to reach the main concern once they are fulfilled.

One of the firsts questions that arise during this journey is whether the final geometry optimized filter would be manufacturable or, on the contrary, it would only remain inside one mind and computer with no possibility of bringing it to the real world (at least with today's technology). Chapter 3 is the answer to this first question: some previous results on the topic were taken and an assessment of a novel manufacturing technology called *Selective Laser Melting* which is able to build extremely complex geometries at no additional costs was carried out for its use in the fabrication of waveguide filters with optimized geometries. Several prototypes of two designs were fabricated: a baseline filter with traditional rectangular geometries and a novel shaped filter. These filters were successfully built with this modern technology in two different materials: an aluminium alloy (AlSi10Mg) that resulted to be very light but had an inherent surface roughness larger than desired, and titanium (grade II) which was heavier than the aluminium alloy but, on the contrary, the surface roughness was considerably smaller. In Chapter 3, the surface roughness of several samples (pieces of the designed filters) fabricated with the same technology was measured. In addition, an accuracy assessment on the mentioned samples was

performed, which helped to later calibrate the system for the manufacturing of the real filters. The physical dimensions of the samples were measured in all directions and the study revealed higher tolerances in those dimensions parallel to the growing direction. A clear tolerance value could not be determined, but values between 50 μm and 140 μm were measured and were highly dependant on the growing direction. However, the manufacturing of a waveguide filter is not only the fabrication process of the hardware itself, but also surface treatments must be performed to reach a quality part. A chemical polishing process was applied to two titanium filters (baseline Ti3 and shaped Ti4). The measured response of these filters showed a considerably reduced insertion loss compared to their response before the polishing process (around 40% smaller loss). They also showed a substantial increase in bandwidth and around 50 MHz down-shift in frequency. As expected, the chemical polishing not only reduced the surface roughness of the material, but also the internal dimensions of the filters, thus widening the bandwidth and down-shifting the center frequency. As a result of this, also insertion loss must improve. At the same time, a successful silver plating attempt was carried out on the shaped aluminium filter (Al2). The insertion loss of the filter reduced in around 65% due to the better conductivity of silver compared to aluminium. In this case, the bandwidth and center frequency of the filter barely changed. A surprising result obtained during this work is that the sensitivity of waveguide filters to manufacturing tolerances is reduced due to the shaped geometries. It was found that rounded geometries helped to the loss reduction in waveguide filters since they lead to a more evenly distribution of the surface currents that flow through the filter. These rounded geometries cause a softer transition between coupling structures and cavities and therefore, a deviation of the geometry in one direction causes a deviation in the other directions, too, which in turns, reduces the filter sensitivity.

At this point, the SLM technology was proved to be acceptable for the manufacturing of shaped waveguide filters and the door was open to a new concept of waveguide filter design. The next step was to find a structured and valid optimization method that could be applied to segmented parts of the filter, resulting in an effective insertion loss reduction once the parts were assembled. Hence, a precise equivalent circuit of the filter had to be developed, that completely characterized the losses due to resonators and coupling structures. The segmentation line was chosen to be the center of each analytical resonator (not physical), where the phase of the transmitted signal is known. In Chapter 4, the lossy equivalent circuit for inter-resonator couplings (for narrow-band filters) was obtained following a step-by-step procedure based on an even and odd analysis formalism. For the external coupling, the same lossy equivalent circuit was proposed and four different approaches for the calculation of the element values were analyzed. The idea was to equate the simulated input impedance of a proposed model (that included the external coupling under study) with the analytical input impedance of the proposed equivalent circuit at the center frequency of the filter and at a second frequency point. Using the real and imaginary parts of the impedances, a system of four equations with four unknowns could be formulated and solved. The second frequency point should be chosen near resonance, where the frequency dependence of the waveguide coupling model and the equivalent circuit are still similar. A lossy transmission line of half-wavelength length was used as equivalent circuit for the resonators. Finally, the

lossy equivalent circuit of the complete filter was the result of cascading the equivalent circuits of the individual coupling structures and resonators. The theory was successfully applied to two waveguide filters designs at different frequencies: a first order filter with only one cavity and external couplings and a fifth order filter with parabolic irises. The filter bandwidth, center frequency, and insertion loss of the filters were perfectly predicted using the developed new lossy equivalent circuit. The theory was also successfully applied to the response optimization of a wide range of filters avoiding the use of full-wave simulations of complete filter structures and to yield analyses of arbitrarily-shaped filters including losses in both resonators and coupling structures.

The lossy equivalent circuit was proved to accurately predict the insertion loss of a filter with no need of simulating the complete structure, but only the segmented parts. However, a suitable parameter must still be extracted from the equivalent circuit that could be used as goal function in the optimization of the different segmented parts of the filter. The parameter should be able to represent accurately the losses introduced by coupling structures, independently on their shapes and hence, an improvement at this level should yield a reduction in the final insertion loss of the filter. This was achieved by defining a novel effective quality factor for both the inter-resonator and external couplings that takes into account losses due to the coupling structures and the adjacent resonators, as presented in Chapter 5. The effective Q-factor of coupling structures with different geometries such as rectangular irises, sinusoidal irises, circular windows, circular windows with sinusoidal shape along the propagation direction, etc., was obtained and compared to each other. For the first time, a systematic study on the impact of the dimensions and geometry of the coupling structures on the losses of the filter was performed. The analysis showed that, in general, a thicker coupling structure yield to lower losses, but at the expense of enlarging the final filter (note that this was not the case for the rectangular iris structure). While thickening the coupling structure yielded improvements of 4% to 8%, switching between geometries could improve the effective Q-factor in more than 12%. The structure with the lower effective Q-factor resulted to be the traditional rectangular iris, whereas the best structure was the sinusoidal-circular window, with an improvement of around 12% over the rectangular iris, defined as baseline. Although the goal was not to find the optimum shape for direct-coupled-cavity filters, an improvement over the baseline design of 23% was achieved by rounding the edges of the resonators. In addition, the spurious free range of the segmented parts was also calculated and it was shown that thicker coupling structures yielded lower spurious free range values, for all the studied geometries. On the other hand, results showed that the degradation of the spurious free range with the thickness of the coupling aperture was very small for the sinusoidal-circular window structure with rectangular or rounded cavities. Therefore, this structure showed the best performance in terms of effective Q-factor and spurious free range. Also, shaping in coupling structures did not decrease the multipactor threshold as the shaping was applied far from where high E-fields concentrate.

As said before, the improvement of the effective Q-factor of the structures usually led to longer geometries. As volume is also of high concern, a study on the contribution of each coupling in a filter to the total loss was also carried out. As expected, couplings located at the center of the filter contributed to a higher extend

to the overall filter loss than external couplings. Hence, internal couplings must be first improved when other restrictions such as volume and mass also apply.

The theory was successfully proved to work by designing two different sets of filters: the first set comprised two filters with totally different coupling geometries but exactly the same effective Q-factor of the segmented parts whereas the second set was composed of filters with different coupling geometries and different effective Q-factors. The simulated results of the filters from the first set showed essentially the same in-band performance and same insertion loss. In the second set, the insertion loss of the final filters trended perfectly with what predicted by their effective Q-factors. Also, the spurious free range of the filters from both sets was in very good agreement with what observed in the individual segmented parts.

The design of geometry optimized filters, however, required a separate study and a new design procedure was proposed. The shaped coupling geometries were found to modify the slope parameters of the cavities on their sides, thus yielding to errors in the final designed filters, i.e. responses with different bandwidths and not perfectly matched return losses. Hence, a final lengthy full-wave optimization of the filter to perfectly meet the specifications was required. Chapter 6 proposes an iterative process for the design of filters with optimized geometries, that avoid costly full-wave optimizations. The process begins from an already dimensioned filter (for example using the traditional filter theory) and calculates how each coupling affects the resonator slope parameter. With this information, the effective slope parameter of the resonator corrected with the influence of its adjacent coupling structures can be calculated and used with the traditional filter theory to obtain the final corrected dimensions of the filter. At the end of the chapter, three filters designed following both the traditional and the novel approach were presented. Deviations of up to 10% could be corrected following the novel approach.

The proposed final goal of this thesis was then successfully achieved: techniques for the loss reduction on waveguide direct-coupled-cavity filters were proposed and verified. From this point on, new fields of application and ideas arise.

7.2 Future Work

The work presented in this thesis opens several future research topics, some of which are listed here:

- In Chapter 6, a novel dimensional process for shaped filters, whose resonators slopes are usually affected by the shaping process, was developed. However, the technique was solely applied on traditional dimensioning theories that use frequency independent impedance inverters. Further work may be conducted for the case of techniques that make use of frequency dependent impedance inverters.

  Also, the theory was validated with filters of different bandwidths (up to 5%), different frequencies and different geometries. In order to consolidate the theory, further examples of filters with different orders may be performed.

- Application of the proposed technique to optimize arbitrarily shaped geometries.

In this thesis, only geometries obtained from mathematical curves were studied. However, the application of the novel theory developed here to optimize arbitrarily shaped geometries is of great interest as they could yield to even larger improvements in the losses of a filter.

- Application of the proposed technique to wide-band filters.

  The work presented here uses a lossy equivalent version of the traditional narrow-band filter equivalent circuit to extract a parameter that is then used in the optimization process. Hence, this parameter cannot be used for the optimization of waveguide wide-band filters since they are not represented by the previous equivalent circuit. Although loss reduction is, in general, of higher concern in narrow-band filters, the proposed future research line could be of interest in cases where wide bandwidths and losses are relevant.

- Loss reduction in waveguide cavity filters with any topology.

  The technique presented in this thesis is only applied to direct-coupled-cavity filters. Since, in practice, also filters with general topologies are used, the application of the presented techniques for the loss reduction in these filters would be of extreme interest. The extraction of the lossy equivalent circuit must be modified to include cross couplings, and also the extraction of the goal parameter. However, the theoretical framework has already been developed in this work and could be used to this purpose.

- Search of techniques for the loss reduction in dielectric waveguide filters.

  Dielectric waveguide filters are becoming very popular since they can offer reduced volume, high Q-factor filters. In dielectric filters, ohmic losses due to material finite conductivity are present, but also of high concern is the loss produced inside the dielectric materials due to their inherent dissipation of electromagnetic energy. The theory presented in this thesis can serve as an idea and as an starting point to study the loss reduction in dielectric waveguide filters by shaping dielectric materials.

APPENDIX A
LIST OF PUBLICATIONS

A.1 Publications in International Journals

[Lorente et al., 2009a] **Lorente, J. A.**, Mendoza, M. M., and Ernst, C. (2009a). Single part microwave filters made from selective laser melting. *ESA Working Paper 2367*.

[Mendoza et al., 2012] Mendoza, M. M., Ernst, C., **Lorente, J. A.**, Alvarez Melcon, A., and Seyfert, F. (2012). On the relation between stored energy and fabrication tolerances in microwave filters. *IEEE Trans. Microw. Theory Techn.*, 60(7):2131–2141.

[Lorente et al., 2013] **Lorente, J. A.**, Ernst, C., and Alvarez Melcon, A. (2013). Rigorous derivation of lossy equivalent circuit for narrow-band waveguide direct-coupled-cavity filters. *IET Microwaves, Antennas & Propagation*, 7(4):251–258.

[Lorente et al., 2013 submitted] **Lorente, J. A.**, Ernst, C., and Alvarez Melcon, A. (2013 [submitted]). Dimensional synthesis of narrow-band waveguide direct-coupled-cavity filters with optimized geometries. *IET Microwaves, Antennas & Propagation*.

[Lorente et al., In Process] **Lorente, J. A.**, Ernst, C., and Alvarez Melcon, A. ([Under preparation]). Loss reduction in narrow-band waveguide direct-coupled-cavity filters by shaping coupling structures. To be submitted to *International Journal of Circuit Theory and Applications.*

A.2 Publications in International Conferences

[Lorente et al., 2009b] **Lorente, J. A.**, Mendoza, M. M., Petersson, A. Z., Pambaguian, L., Alvarez Melcon, A., and Ernst, C. (2009b). Single part microwave filters made from selective laser melting. In *39th European Microwave Conference (EuMC)*, pages 1421–1424.

[Lorente et al., 2010a] **Lorente, J. A.**, Mendoza, M. M., and Ernst, C. (2010a). Single part microwave filters made from selective laser melting. In *First Networking/Partnering Day in ESTEC, ESA, The Netherlands*.

[Mendoza Raya et al., 2011] Mendoza Raya, J. E., Quesada Pereira, F., Mendoza, M. M., **Lorente, J. A.**, Alvarez Melcon, A. A., Gimeno Martinez, B., and Boria Esbert, V. (2011). Multipactor analysis in dual-mode inductive cavity bandpass filters. In *International Workshop on Multipactor, Corona and Passive Intermodulation in Space RF Hardware*.

[Mendoza et al., 2011b] Mendoza, M. M., **Lorente, J. A.**, Alvarez Melcon, A., and Ernst, C. (2011b). Prediction of fabrication yield from low-pass prototype in a butterworth direct-coupled cavity filter. In *41st European Microwave Conference (EuMC)*, pages 736–739.

[Lorente et al., 2012] **Lorente, J. A.**, Ernst, C., and Alvarez Melcon, A. (2012). Accurate derivation of lossy equivalent circuit of waveguide external coupling. In *International Workshop on Microwave Filters, Toulousse (France)*.

A.3 Publications in Spanish National Journals

[Lorente et al., 2010b] **Lorente, J. A.**, Mendoza, M. M., Gomez Diaz, J. S., Vigueras, M. G., Shahvarpour, A., Martinez Ros, A., Jimenez Nogales, M., Guzman Quiros, R., and Alvarez Melcon, A. (2010b). Filtros de microondas de una sola pieza realizados mediante fundido selectivo por láser. *Revista III Jornadas Introducción a la Investigación UPCT*. Ed. Aglaya, ISSN 1888-8356, Deposito Legal: Mu-1618-2008.

[Gomez Diaz et al., 2010] Gomez Diaz, J. S., Vigueras, M. G., Shahvarpour, A., Mendoza, M. M., **Lorente, J. A.**, Martinez Ros, A., Jimenez Nogales, M., Guzman Quiros, R., and Alvarez Melcon, A. (2010). Antena leaky-wave en guía-onda basada en metamateriales: Método de análisis y diseño y validación experimental. *Revista III Jornadas Introducción a la Investigación UPCT*. Ed. Aglaya, ISSN 1888-8356, Depósito Legal: Mu-1618-2008.

[Gomez Diaz et al., 2011] Gomez Diaz, J. S., Mendoza, M. M., **Lorente, J. A.**, and Alvarez Melcon, A. (2011). Nueva condición circuital para el diseño de antenas CRLH LW que presenten una tasa de radiación constante en todo el espacio. *Revista IV Jornadas Introducción a la Investigación UPCT*. Ed. Aglaya, ISSN 1888-8356, Depósito Legal: Mu-1618-2008.

[Mendoza et al., 2011a] Mendoza, M. M., Gomez Diaz, J. S., **Lorente, J. A.**, and Alvarez Melcon, A. (2011a). Predicción de la sensibilidad ante tolerancias de fabricación en un filtro guía-onda butterworth. *Revista IV Jornadas Introducción a la Investigación UPCT*. Ed. Aglaya, ISSN 1888-8356, Depósito Legal: Mu-1618-2008.

A.4 Publications in Spanish National Conferences

[Mendoza et al., 2011c] Mendoza, M. M., **Lorente, J. A.**, Gomez Diaz, J. S., Rebenaque, D. C., Alvarez Melcon, A. A., and Ernst, C. (2011c). Predicción de la sensibilidad ante tolerancias de fabricación en un filtro guía onda butterworth. In *XXVI Simposium Nacional de la Unión Científica Internacional de Radio URSI*.

[Mendoza Raya et al., 2012] Mendoza Raya, J. E., **Lorente, J. A.**, Mendoza, M. M., Quesada Pereira, F., Alvarez Melcon, A., and Guglielmi, M. (2012). Control de la posición de los ceros de transmisión en filtros modo-dual guíaonda inductivos. In *XXVII Simposium Nacional de la Unión Científica Internacional de Radio URSI*.

[Perez Escudero et al., 2013] Perez Escudero, J. M., Alvarez Melcon, A., **Lorente, J. A.**, and Guglielmi, M. (2013). Técnica para la reducción de espureos basada en el control del espesor de las ventanas de acoplo. In *XXVIII Simposium Nacional de la Unión Científica Internacional de Radio URSI*.

APPENDIX B

MEAN AND STANDARD DEVIATION OF SAMPLES A AND B

In this appendix, the calculation of the mean and the standard deviations from the physical measurements of sample A and sample B from Chapter 2 is given in detail. For each xyz-direction, the absolute value of the difference between the different physical dimensions measured in the actual xyz-direction and their nominal values are used in the calculation of the mean deviation and the standard deviation. The results for sample A are given in (B.1)-(B.6). Equations (B.7)-(B.12) calculate the mean deviation as well as the standard deviation in the different dimensions of sample B.

$$\begin{aligned}\mathrm{MD}_{X,A} &= \frac{1}{8}\left(|x_{15}-d|+|x_{16}-d|+|x_{17}-d|+|x_{18}-e|+|x_{19}-e|+|x_{20}-e|+|x_{25}-f|+|x_{26}-f|\right)= \\ &= \frac{1}{8}(|5.73-5.756|+|5.72-5.756|+|5.74-5.756|+|7.51-7.583|+|7.49-7.583|+ \\ &+|7.51-7.583|+|0.99-1|+|0.95-1|) = 0.0471 \text{ mm}\end{aligned} \tag{B.1}$$

$$\begin{aligned}\mathrm{MD}_{Y,A} &= \frac{1}{9}\left(|x_{1}-a|+|x_{2}-a|+|x_{3}-a|+|x_{4}-a|+|x_{5}-a|+|x_{21}-f|+|x_{22}-f|+|x_{23}-f|+|x_{24}-f|\right)= \\ &= \frac{1}{9}(|11.66-11.525|+|11.65-11.525|+|11.56-11.525|+|11.50-11.525|+ \\ &+|11.53-11.525|+|1.01-1|+|1.11-1|+|1.08-1|+|1.01-1|) = 0.0594 \text{ mm}\end{aligned} \tag{B.2}$$

$$\begin{aligned}\mathrm{MD}_{Z,A} &= \frac{1}{9}\left(|x_{6}-b|+|x_{7}-b|+|x_{8}-b|+|x_{9}-b|+|x_{10}-b|+|x_{11}-b|+|x_{12}-c|+|x_{13}-c|+|x_{14}-c|\right)= \\ &= \frac{1}{9}(|3.18-3|+|2.97-3|+|3.04-3|+|3.17-3|+|3.16-3|+|3.18-3|+|16.56-16.727|+ \\ &+|16.55-16.727|+|16.60-16.727|) = 0.1368 \text{ mm}\end{aligned} \tag{B.3}$$

$$\begin{aligned}\sigma_{X,A} &= \sqrt{\frac{1}{8}\begin{pmatrix}(x_{15}-d)^2+(x_{16}-d)^2+(x_{17}-d)^2+(x_{18}-e)^2+ \\ +(x_{19}-e)^2+(x_{20}-e)^2+(x_{25}-f)^2+(x_{26}-f)^2\end{pmatrix}}= \\ &= \sqrt{\frac{1}{8}\begin{pmatrix}(5.73-5.756)^2+(5.72-5.756)^2+(5.74-5.756)^2+(7.51-7.583)^2+ \\ +(7.49-7.583)^2+(7.51-7.583)^2+(0.99-1)^2+(0.95-1)^2\end{pmatrix}} = 0.0549 \text{ mm}\end{aligned} \tag{B.4}$$

$$\sigma_{Y,A} = \sqrt{\frac{1}{9}\left(\begin{array}{r}(x_1-a)^2+(x_2-a)^2+(x_3-a)^2+(x_4-a)^2+(x_5-a)^2+\\ +(x_{21}-f)^2+(x_{22}-f)^2+(x_{23}-f)^2+(x_{24}-f)^2\end{array}\right)} = \tag{B.5}$$
$$= \sqrt{\frac{1}{9}\left(\begin{array}{r}(11.66-11.525)^2+(11.65-11.525)^2+(11.56-11.525)^2+(11.50-11.525)^2+\\ +(11.53-11.525)^2+(1.01-1)^2+(1.11-1)^2+(1.08-1)^2+(1.01-1)^2\end{array}\right)} = 0.0778 \text{ mm}$$

$$\sigma_{Z,A} = \sqrt{\frac{1}{9}\left(\begin{array}{r}(x_6-b)^2+(x_7-b)^2+(x_8-b)^2+(x_9-b)^2+(x_{10}-b)^2+(x_{11}-b)^2+\\ +(x_{12}-c)^2+(x_{13}-c)^2+(x_{14}-c)^2\end{array}\right)} = \tag{B.6}$$
$$= \sqrt{\frac{1}{9}\left(\begin{array}{r}(3.18-3)^2+(2.97-3)^2+(3.04-3)^2+(3.17-3)^2+(3.16-3)^2+\\ +(3.18-3)^2+(16.56-16.727)^2+(16.55-16.727)^2+(16.60-16.727)^2\end{array}\right)} = 0.1480 \text{ mm}$$

$$\text{MD}_{X,B} = \frac{1}{8}\left(|x_{15}-d|+|x_{16}-d|+|x_{17}-d|+|x_{18}-e|+|x_{19}-e|+|x_{20}-e|+|x_{25}-f|+|x_{26}-f|\right) = \tag{B.7}$$
$$= \frac{1}{8}(|5.78-5.756|+|5.72-5.756|+|5.70-5.756|+|7.48-7.583|+|7.50-7.583|+$$
$$+|7.47-7.583|+|1.01-1|+|0.94-1|) = 0.0606 \text{ mm}$$

$$\text{MD}_{Y,B} = \frac{1}{9}\left(|x_1-a|+|x_2-a|+|x_3-a|+|x_4-a|+|x_5-a|+|x_{21}-f|+|x_{22}-f|+|x_{23}-f|+|x_{24}-f|\right) = \tag{B.8}$$
$$= \frac{1}{9}(|11.64-11.525|+|11.70-11.525|+|11.68-11.525|+|11.61-11.525|+$$
$$+|11.63-11.525|+|1.20-1|+|1.04-1|+|1.00-1|+|1.16-1|) = 0.1150 \text{ mm}$$

$$\begin{aligned}\mathrm{MD}_{Z,B} &= \frac{1}{9}\left(|x_6-b|+|x_7-b|+|x_8-b|+|x_9-b|+|x_{10}-b|+|x_{11}-b|+|x_{12}-c|+|x_{13}-c|+|x_{14}-c|\right)= \\ &= \frac{1}{9}(|3.04-3|+|3.05-3|+|3.17-3|+|3.12-3|+|3.09-3|+|3.09-3|+|16.61-16.727|+ \\ &+|16.64-16.727|+|16.57-16.727|) = 0.1023 \text{ mm}\end{aligned} \tag{B.9}$$

$$\begin{aligned}\sigma_{X,B} &= \sqrt{\frac{1}{8}\begin{pmatrix}(x_{15}-d)^2+(x_{16}-d)^2+(x_{17}-d)^2+(x_{18}-e)^2+\\ +(x_{19}-e)^2+(x_{20}-e)^2+(x_{25}-f)^2+(x_{26}-f)^2\end{pmatrix}}= \\ &= \sqrt{\frac{1}{8}\begin{pmatrix}(5.78-5.756)^2+(5.72-5.756)^2+(5.70-5.756)^2+(7.48-7.583)^2+\\ +(7.50-7.583)^2+(7.47-7.583)^2+(1.01-1)^2+(0.94-1)^2\end{pmatrix}} = 0.0698 \text{ mm}\end{aligned} \tag{B.10}$$

$$\begin{aligned}\sigma_{Y,B} &= \sqrt{\frac{1}{9}\begin{pmatrix}(x_1-a)^2+(x_2-a)^2+(x_3-a)^2+(x_4-a)^2+(x_5-a)^2+\\ +(x_{21}-f)^2+(x_{22}-f)^2+(x_{23}-f)^2+(x_{24}-f)^2\end{pmatrix}}= \\ &= \sqrt{\frac{1}{9}\begin{pmatrix}(11.64-11.525)^2+(11.70-11.525)^2+(11.68-11.525)^2+(11.61-11.525)^2+\\ +(11.63-11.525)^2+(1.20-1)^2+(1.04-1)^2+(1.00-1)^2+(1.16-1)^2\end{pmatrix}} = 0.1305 \text{ mm}\end{aligned} \tag{B.11}$$

$$\begin{aligned}\sigma_{Z,B} &= \sqrt{\frac{1}{9}\begin{pmatrix}(x_6-b)^2+(x_7-b)^2+(x_8-b)^2+(x_9-b)^2+(x_{10}-b)^2+(x_{11}-b)^2+\\ +(x_{12}-c)^2+(x_{13}-c)^2+(x_{14}-c)^2\end{pmatrix}}= \\ &= \sqrt{\frac{1}{9}\begin{pmatrix}(3.04-3)^2+(3.05-3)^2+(3.17-3)^2+(3.12-3)^2+(3.09-3)^2+\\ +(3.09-3)^2+(16.61-16.727)^2+(16.64-16.727)^2+(16.57-16.727)^2\end{pmatrix}} = 0.1103 \text{ mm}\end{aligned} \tag{B.12}$$

APPENDIX C
MATCHED CIRCUIT RESPONSES

In this appendix, the matched RF responses of all the simulations and measurements shown in Chapter 2 are collected. Two techniques have been used for the fitting of the curves: a manual tuning of an equivalent lumped element circuit and the modified cauchy method. The original response is always shown for comparison.

C.1 Manual Circuit Matching

The matched responses of the simulations with and without considering surface roughness are listed in section C.1.1. Section C.1.2 collects the matched responses of the measured filters as received (before plating, tuning or polishing). Next, the matched responses of the surface treated filters can be seen in section C.1.3. Finally, section C.1.4 collects all the matched responses of the tuned filters.

C.1.1 Simulations

Flat Surface

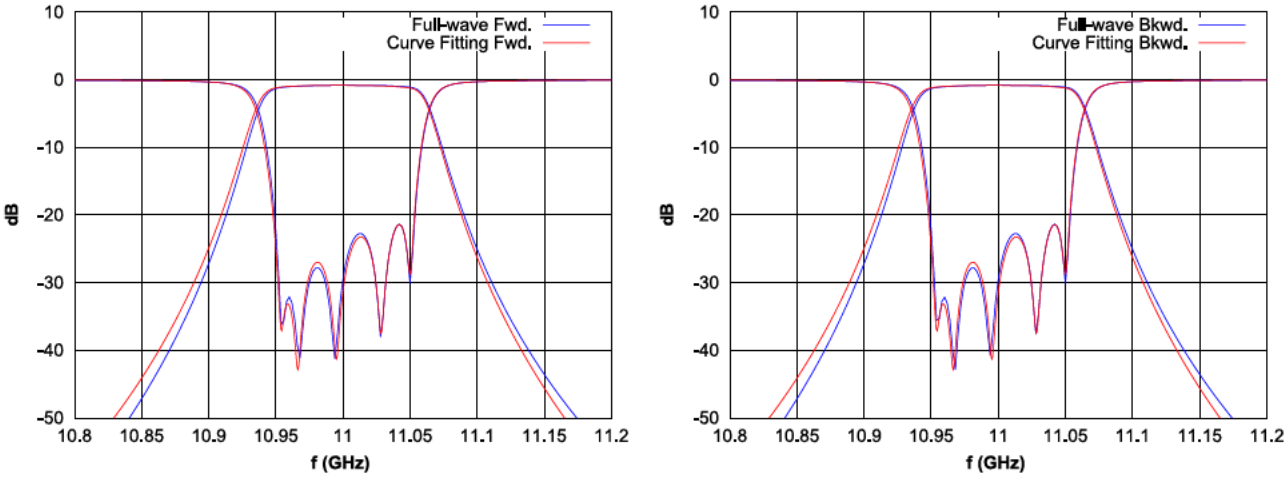

(a) (b)

Figure C.1: Matched RF response of the full-wave aluminium alloy (AlSi10Mg) baseline filter: (a) forward response, and b) backward response.

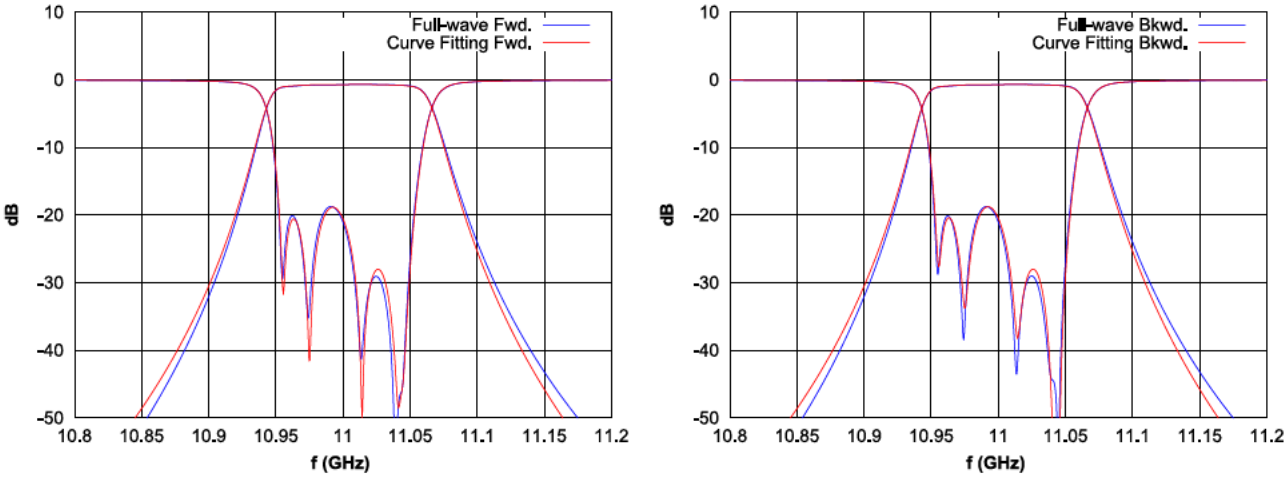

(a) (b)

Figure C.2: Matched RF response of the full-wave aluminium alloy (AlSi10Mg) shaped filter: (a) forward response, and b) backward response.

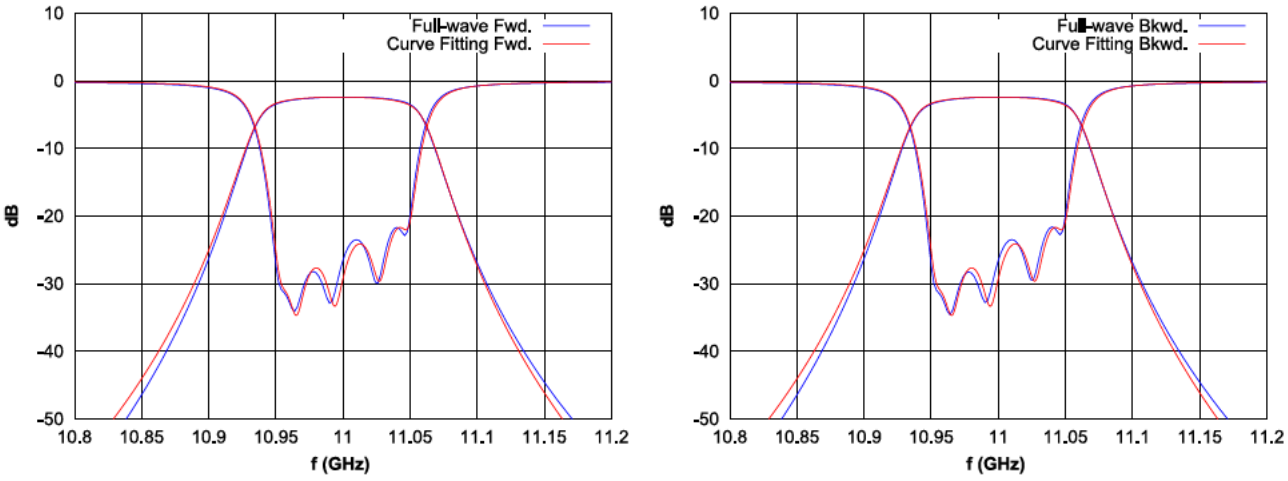

(a) (b)

Figure C.3: Matched RF response of the full-wave titanium (grade II) baseline filter: (a) forward response, and b) backward response.

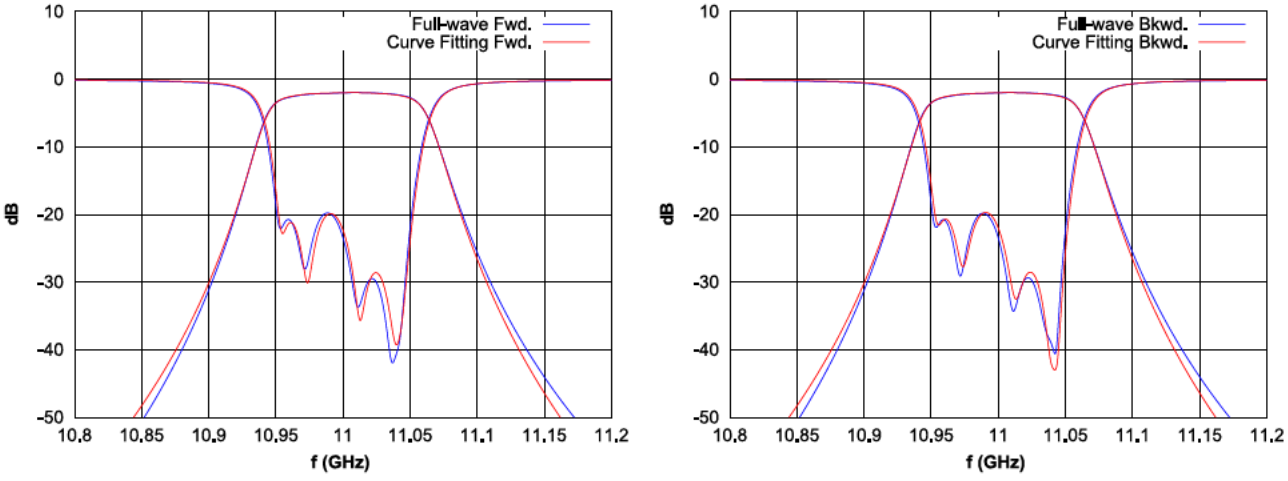

(a) (b)

Figure C.4: Matched RF response of the full-wave titanium (grade II) shaped filter: (a) forward response, and b) backward response.

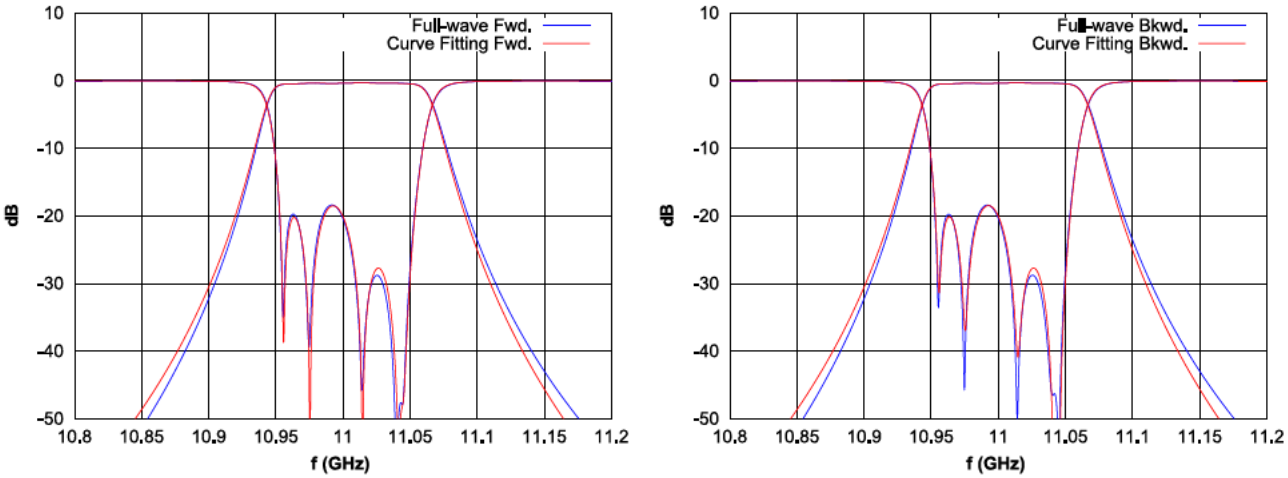

(a) (b)

Figure C.5: Matched RF response of the full-wave silver shaped filter: (a) forward response, and b) backward response.

Surface Roughness as in Table 3.6

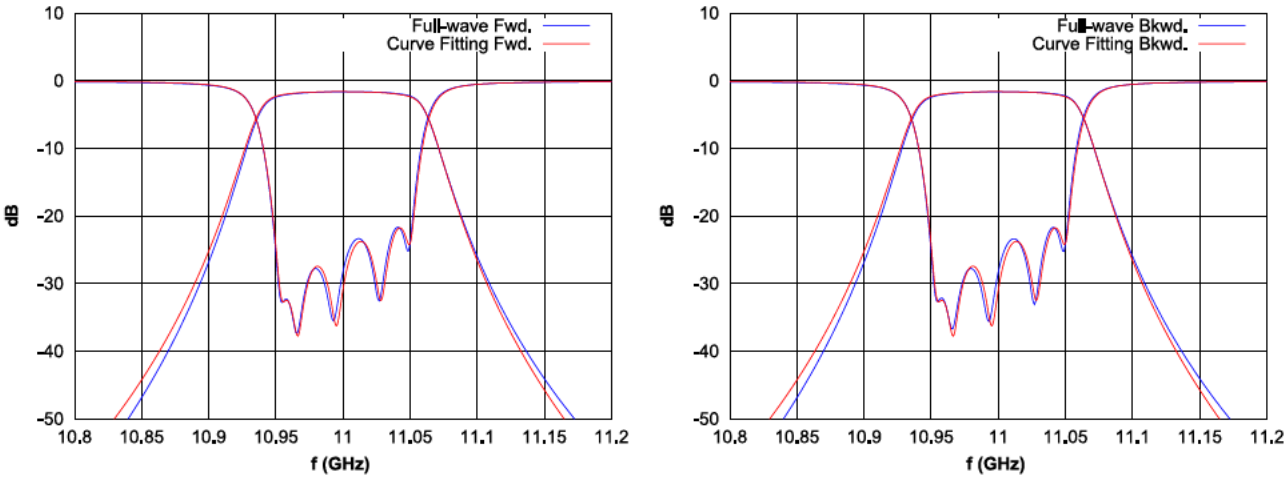

(a) (b)

Figure C.6: Matched RF response of the full-wave aluminium alloy (AlSi10Mg) baseline filter including surface roughness effects: (a) forward response, and b) backward response.

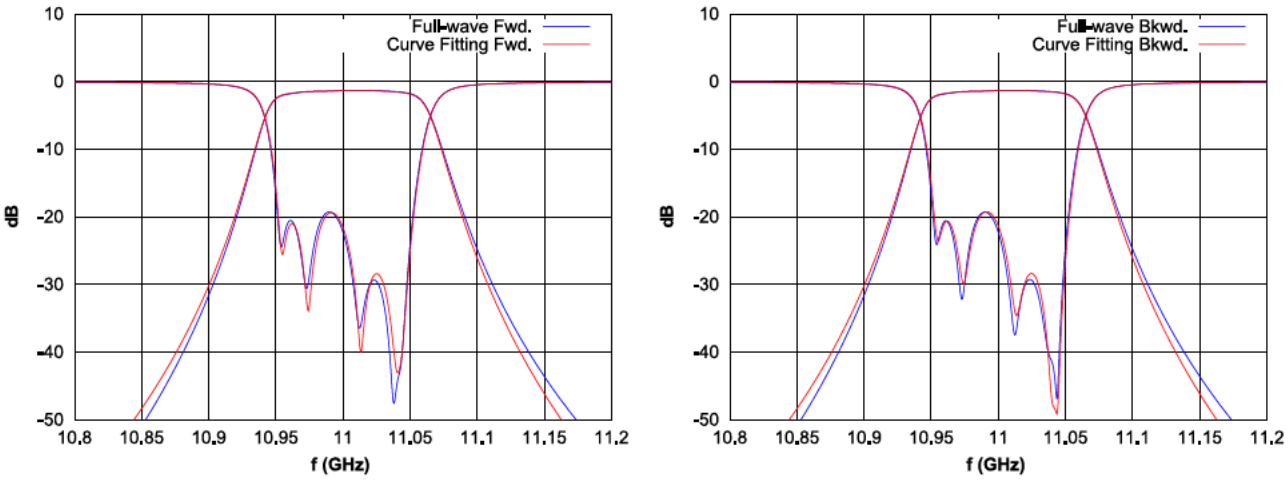

(a) (b)

Figure C.7: Matched RF response of the full-wave aluminium alloy (AlSi10Mg) shaped filter including surface roughness effects: (a) forward response, and b) backward response.

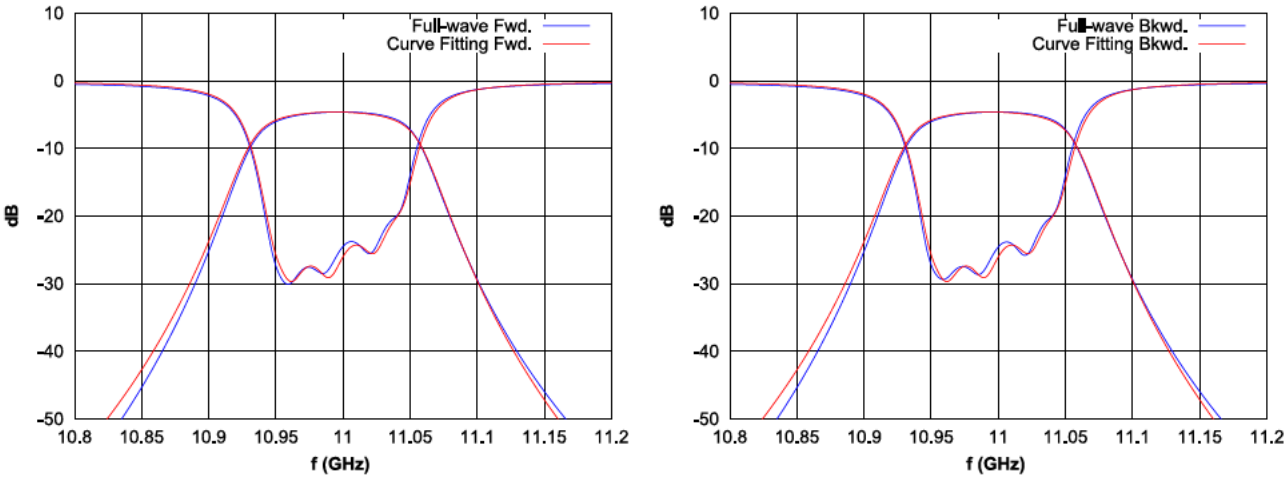

(a) (b)

Figure C.8: Matched RF response of the full-wave titanium (grade II) baseline filter including surface roughness effects: (a) forward response, and b) backward response.

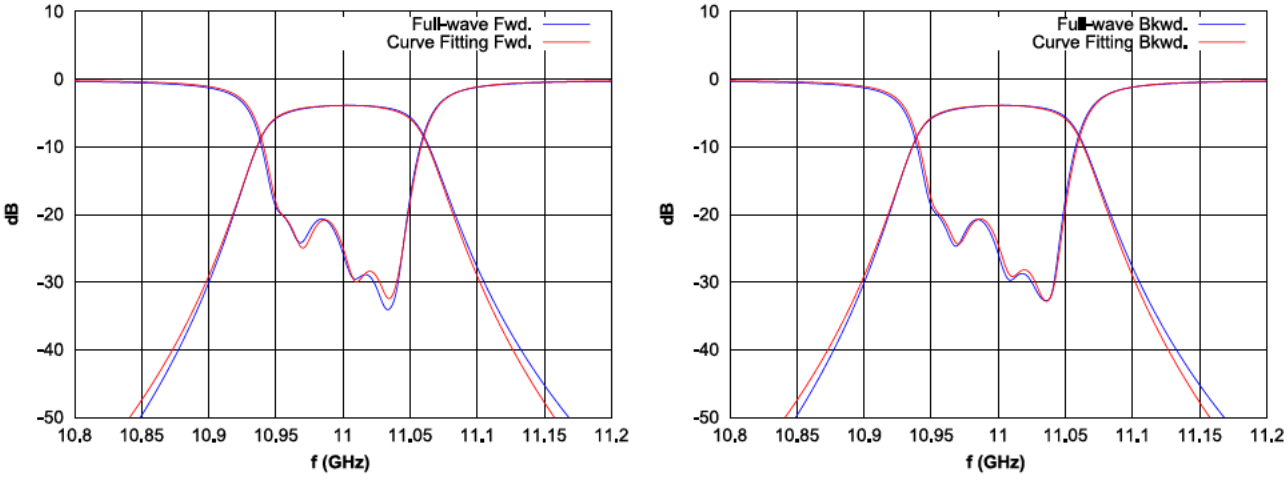

(a) (b)

Figure C.9: Matched RF response of the full-wave titanium (grade II) shaped filter including surface roughness effects: (a) forward response, and b) backward response.

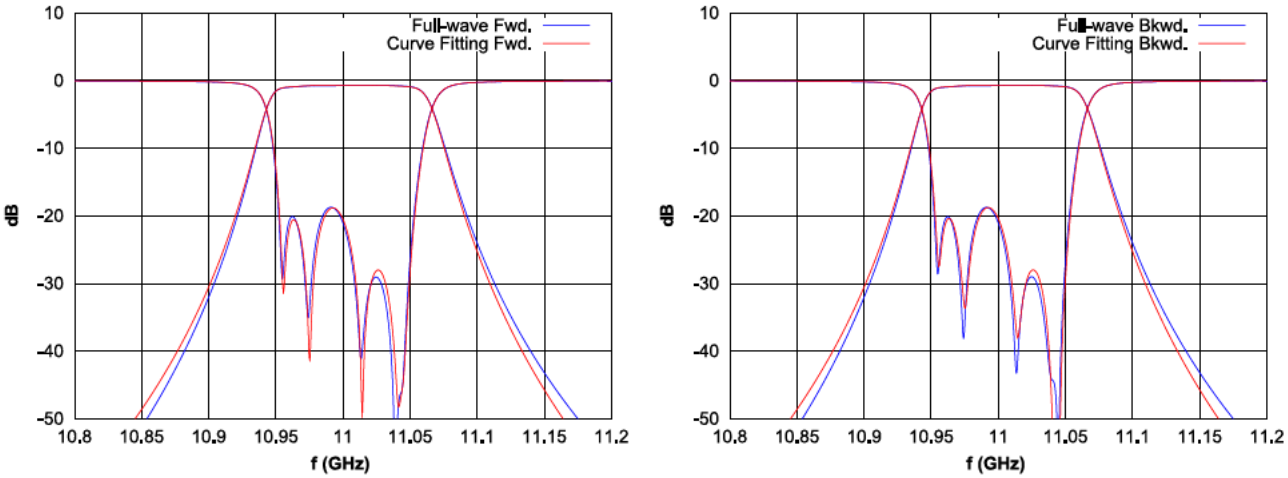

(a) (b)

Figure C.10: Matched RF response of the full-wave silver shaped filter including surface roughness effects: (a) forward response, and b) backward response.

C.1.2 Unmodified Filters

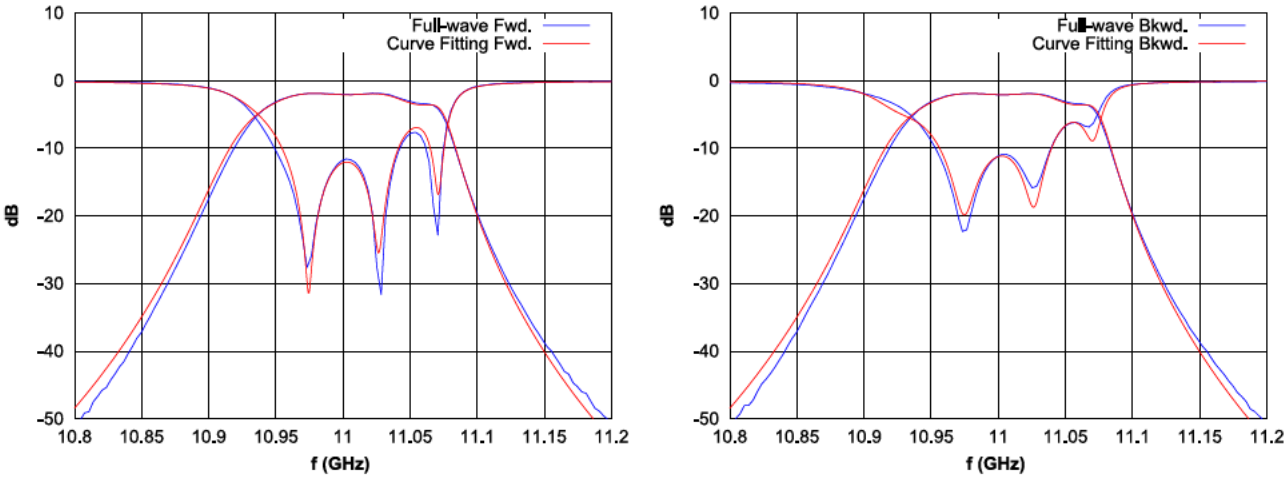

(a) (b)

Figure C.11: Matched RF response of the measured Al1 baseline filter as received: (a) forward response, and b) backward response.

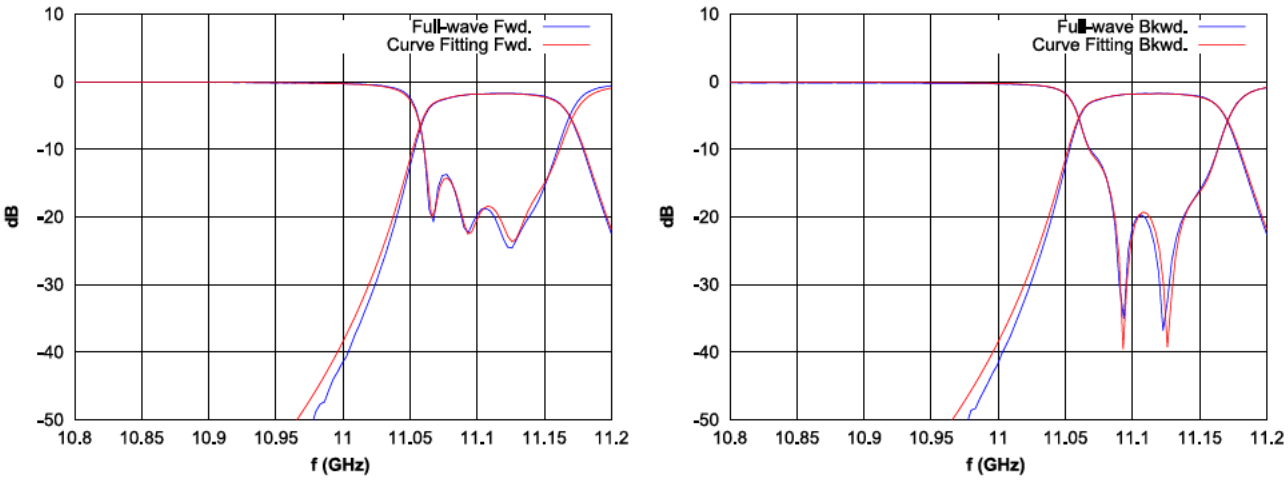

(a) (b)

Figure C.12: Matched RF response of the measured Al2 shaped filter as received: (a) forward response, and b) backward response.

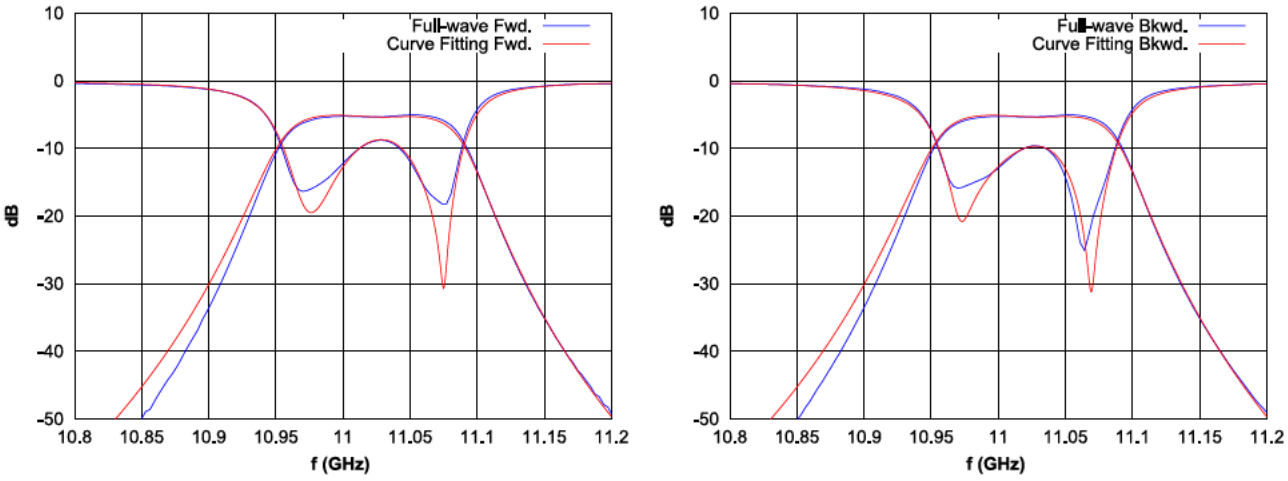

(a) (b)

Figure C.13: Matched RF response of the measured Ti1 baseline filter as received: (a) forward response, and b) backward response.

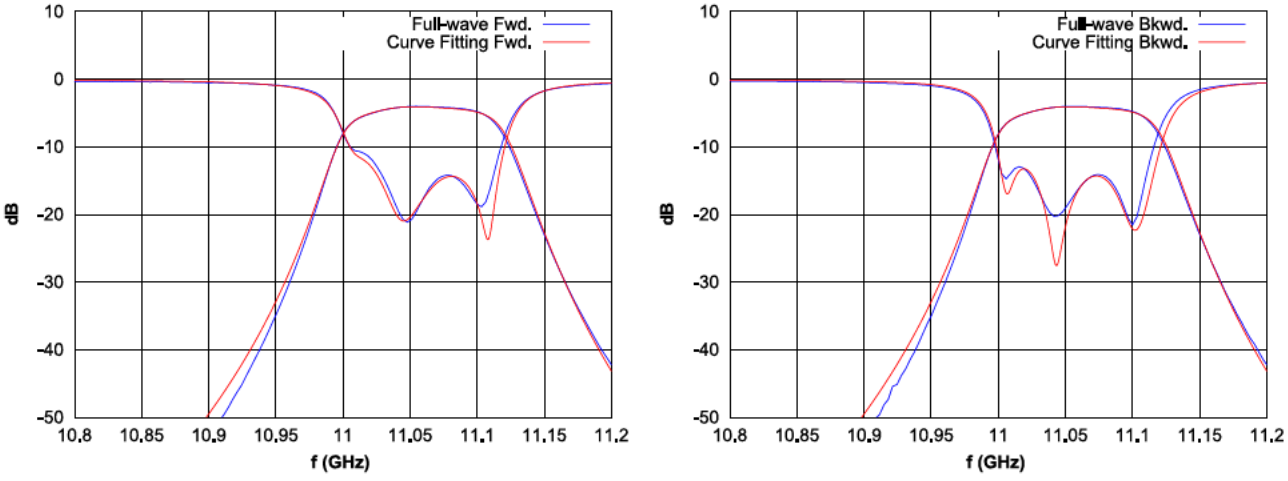

(a) (b)

Figure C.14: Matched RF response of the measured Ti2 shaped filter as received: (a) forward response, and b) backward response.

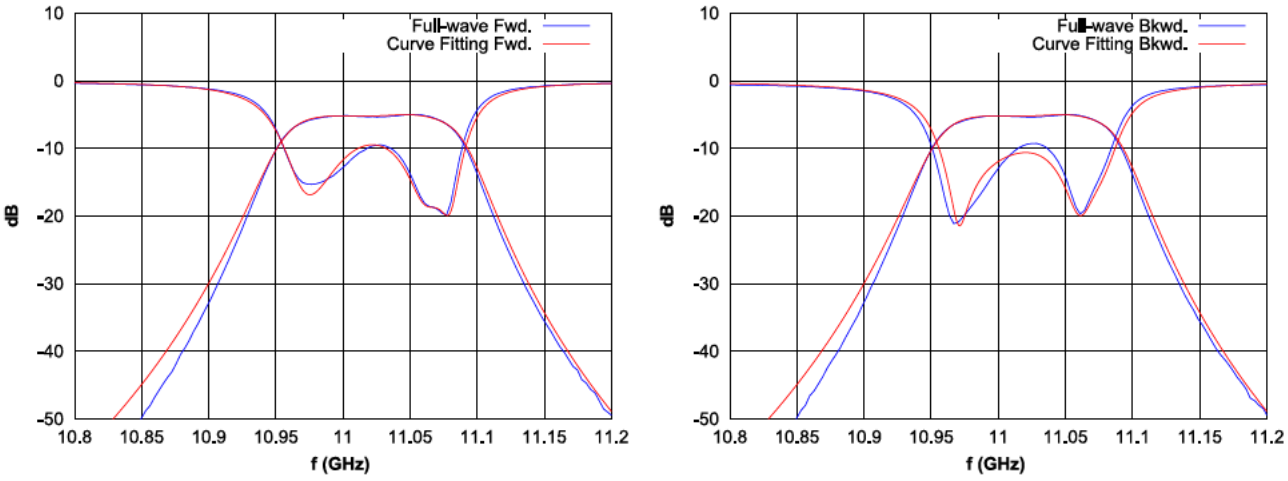

(a) (b)

Figure C.15: Matched RF response of the measured Ti3 baseline filter as received: (a) forward response, and b) backward response.

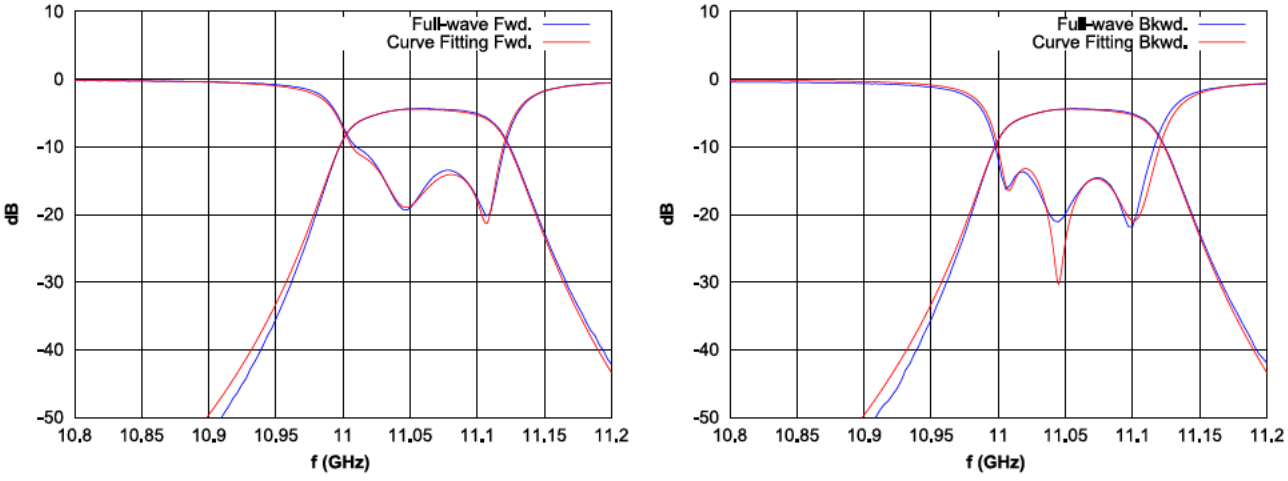

(a) (b)

Figure C.16: Matched RF response of the measured Ti4 shaped filter as received: (a) forward response, and b) backward response.

C.1.3 Surface-Treated Filters

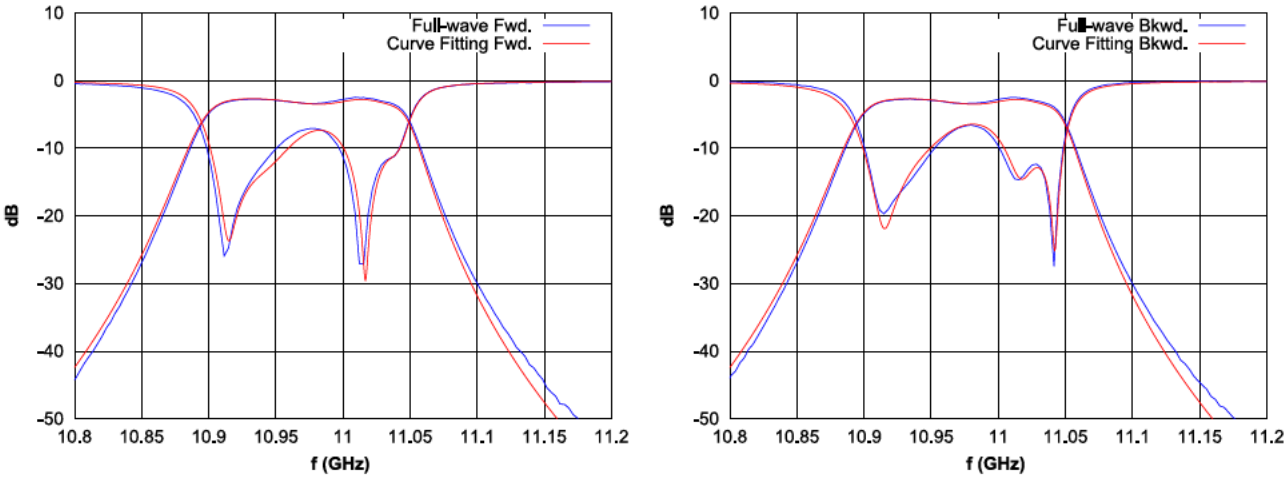

(a) (b)

Figure C.17: Matched RF response of the measured Ti3 baseline filter after a chemical polish process: (a) forward response, and b) backward response.

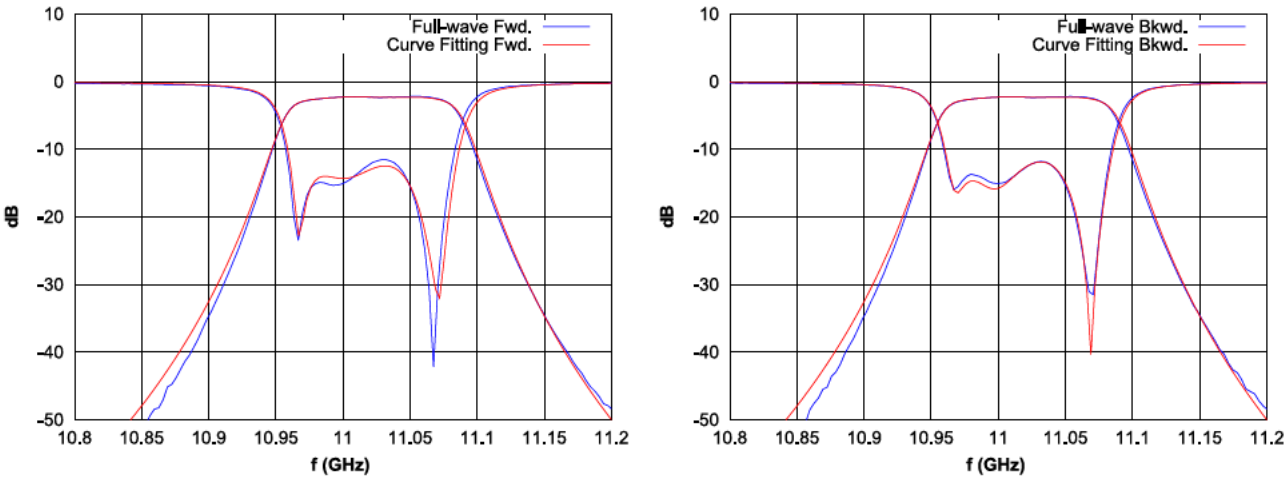

(a) (b)

Figure C.18: Matched RF response of the measured Ti4 shaped filter after a chemical polish process: (a) forward response, and b) backward response.

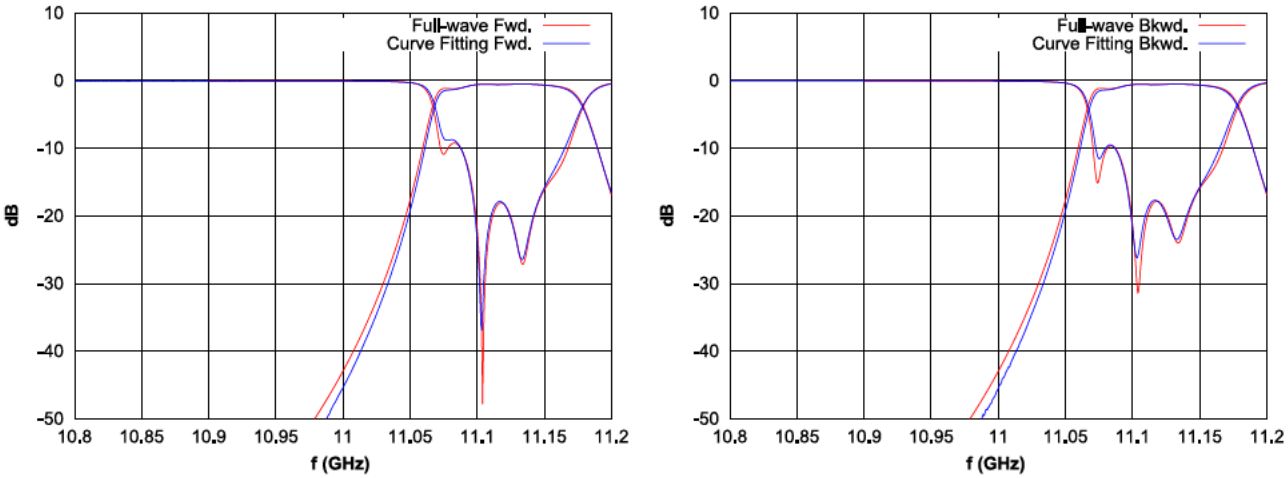

(a) (b)

Figure C.19: Matched RF response of the measured Al2 shaped filter after a silver plating process: (a) forward response, and b) backward response.

C.1.4 Tuned Filters

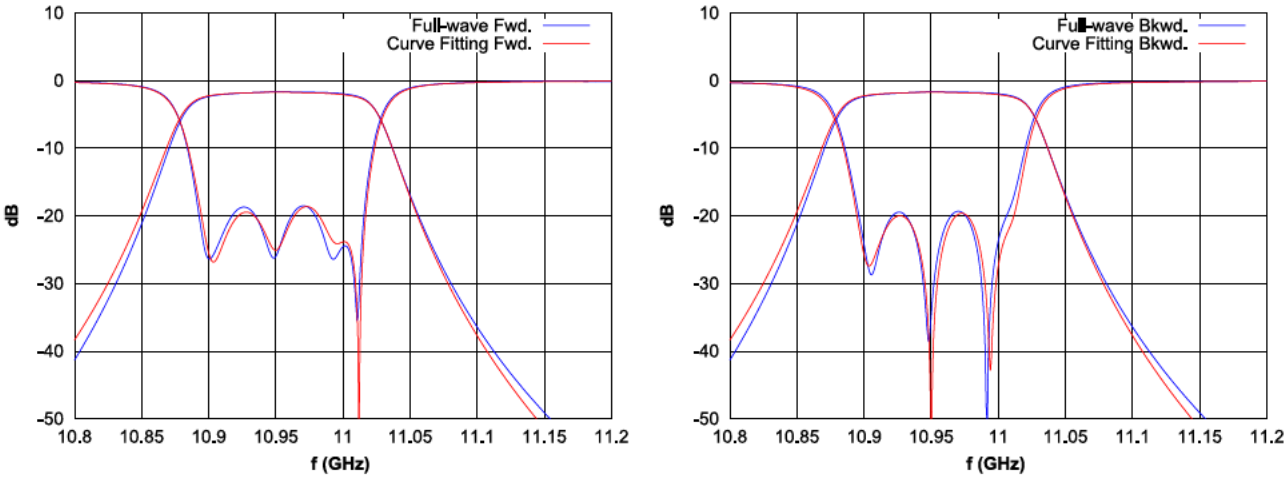

(a) (b)

Figure C.20: Matched RF response of the measured Al1 baseline filter after minimal tuning of the resonators: (a) forward response, and b) backward response.

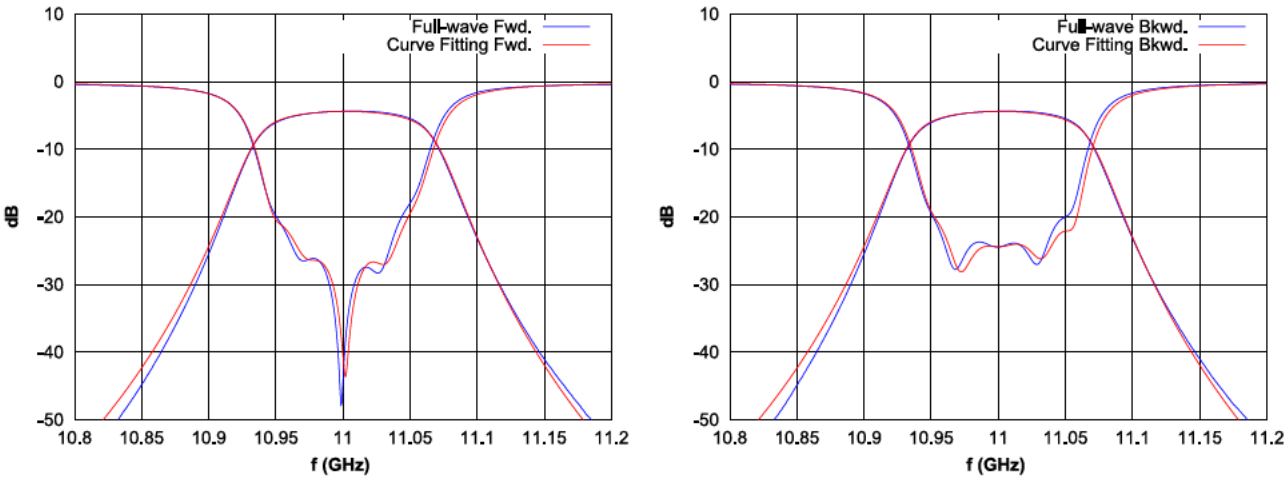

(a) (b)

Figure C.21: Matched RF response of the measured Ti1 baseline filter after minimal tuning of the resonators: (a) forward response, and b) backward response.

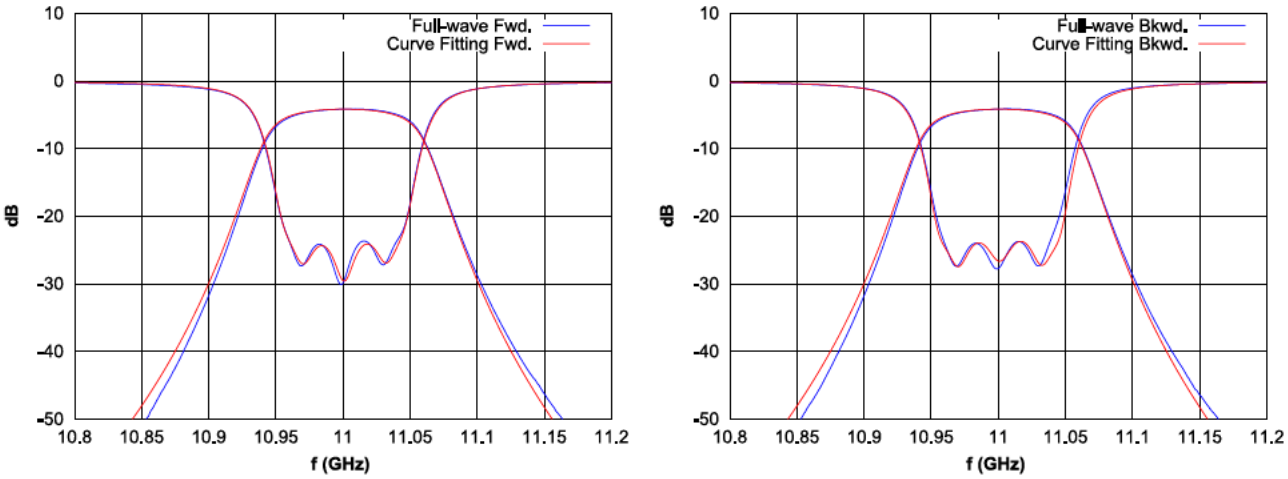

(a) (b)

Figure C.22: Matched RF response of the measured Ti2 shaped filter after minimal tuning of the resonators: (a) forward response, and b) backward response.

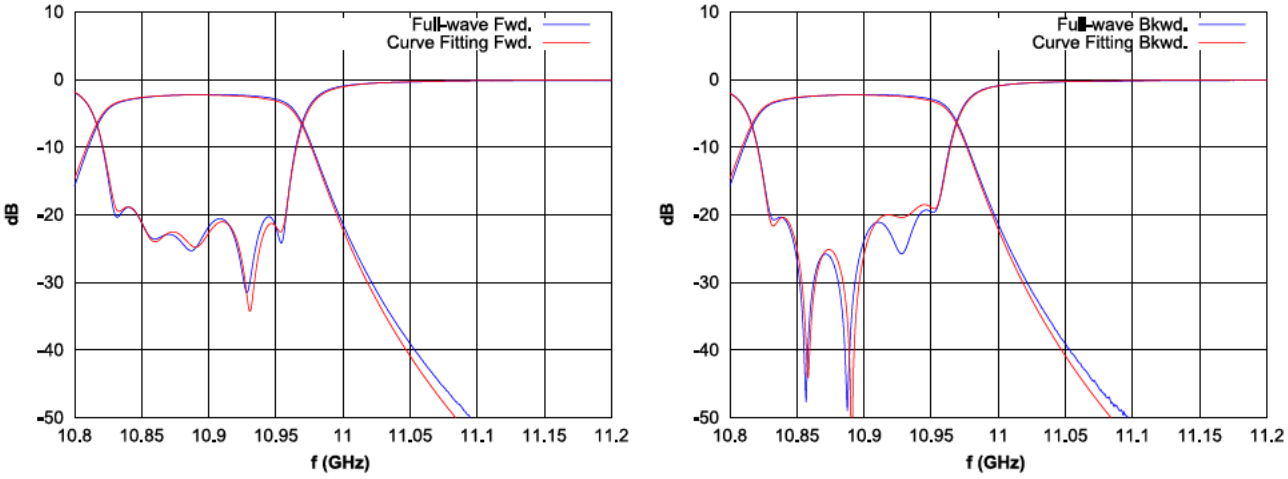

(a) (b)

Figure C.23: Matched RF response of the measured Ti3 baseline filter after a chemical polish process and minimal tuning of the resonators: (a) forward response, and b) backward response.

C.2 Modified Cauchy Method

From Figure C.24 to Figure C.33, the responses obtained from the extracted polynomial models using the modified Cauchy Method are compared to those obtained by measurements. Very good agreement can be observed between both curves.

C.2.1 Unmodified Filters

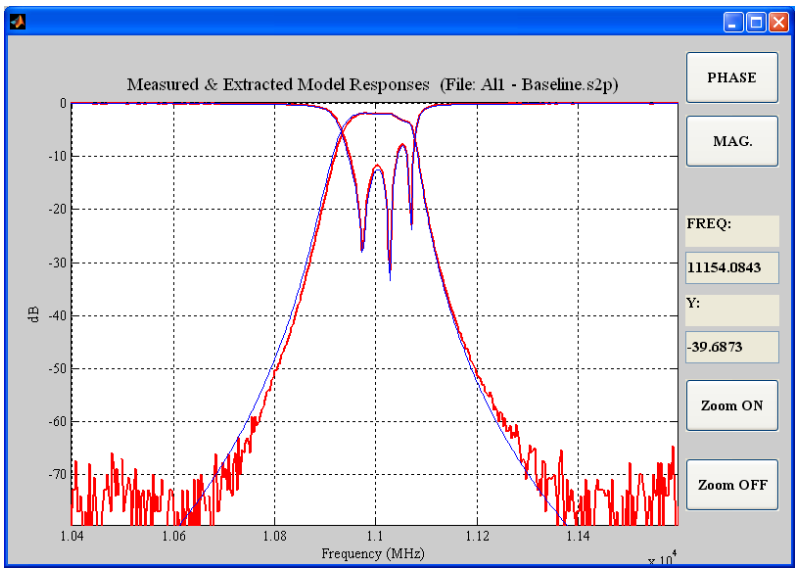

Figure C.24: Matched RF response of the measured Al1 baseline filter as received.

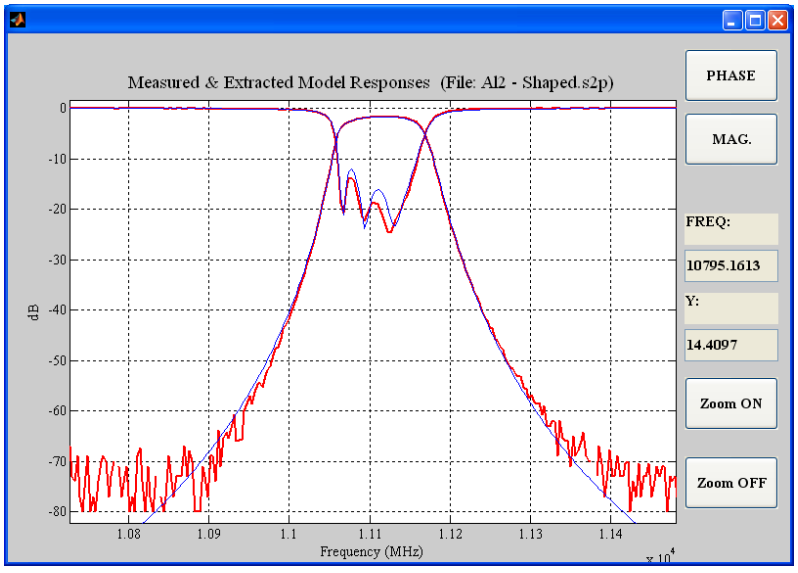

Figure C.25: Matched RF response of the measured Al2 shaped filter as received.

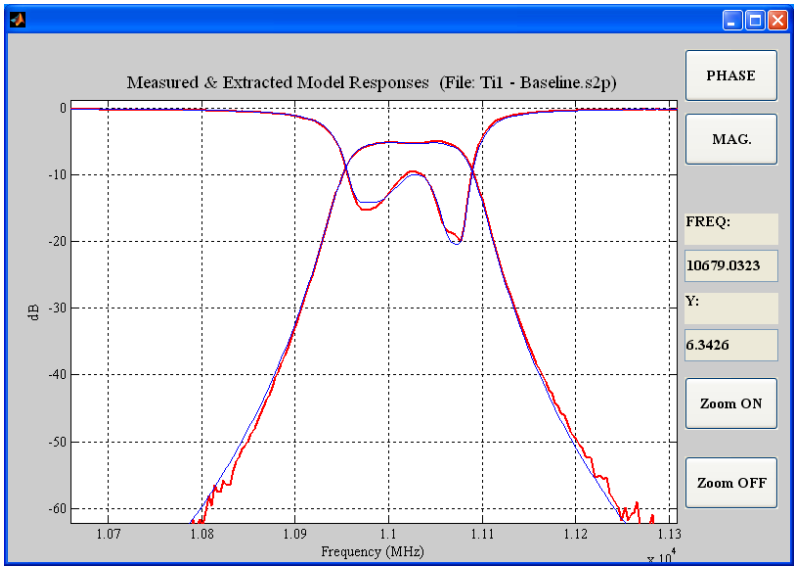

Figure C.26: Matched RF response of the measured Ti1 baseline filter as received.

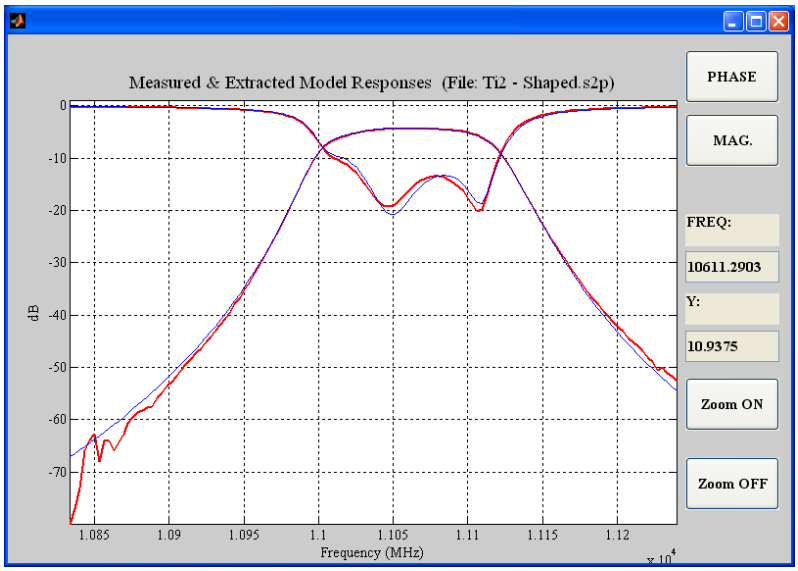

Figure C.27: Matched RF response of the measured Ti2 shaped filter as received.

C.2.2 Surface-Treated Filters

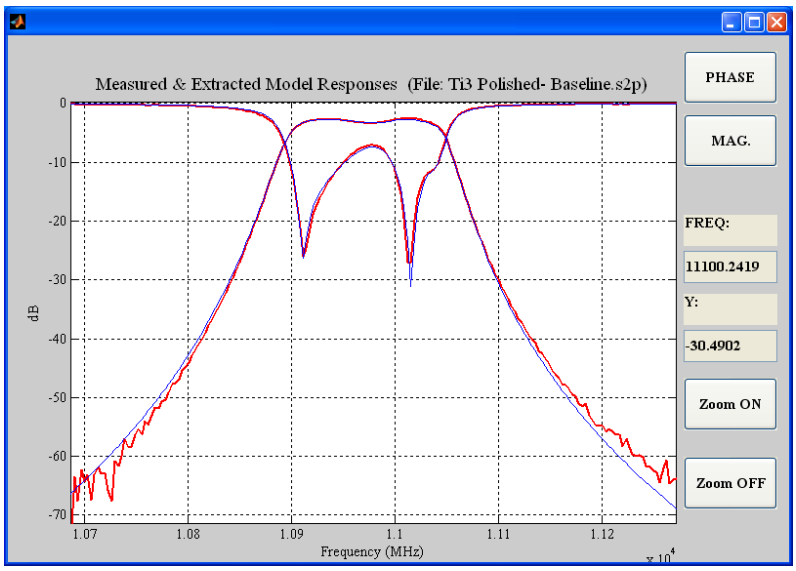

Figure C.28: Matched RF response of the measured Ti3 baseline filter after a chemical polish process.

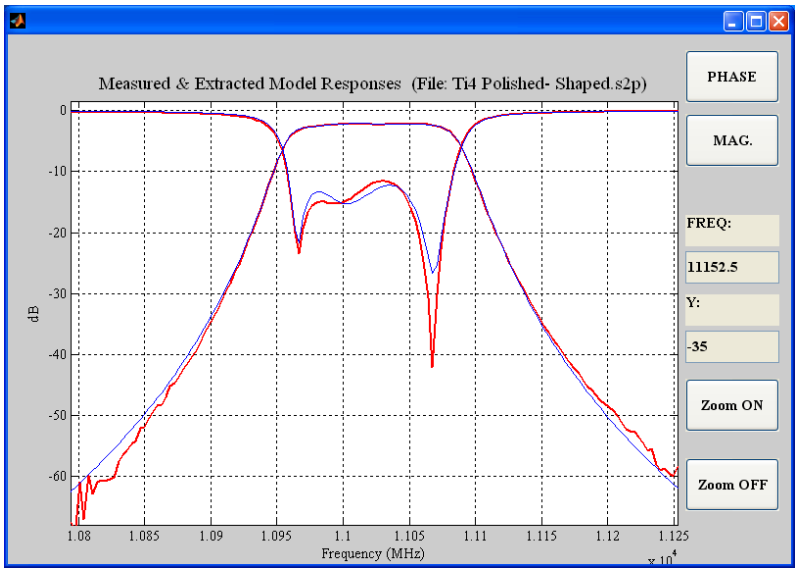

Figure C.29: Matched RF response of the measured Ti4 shaped filter after a chemical polish process.

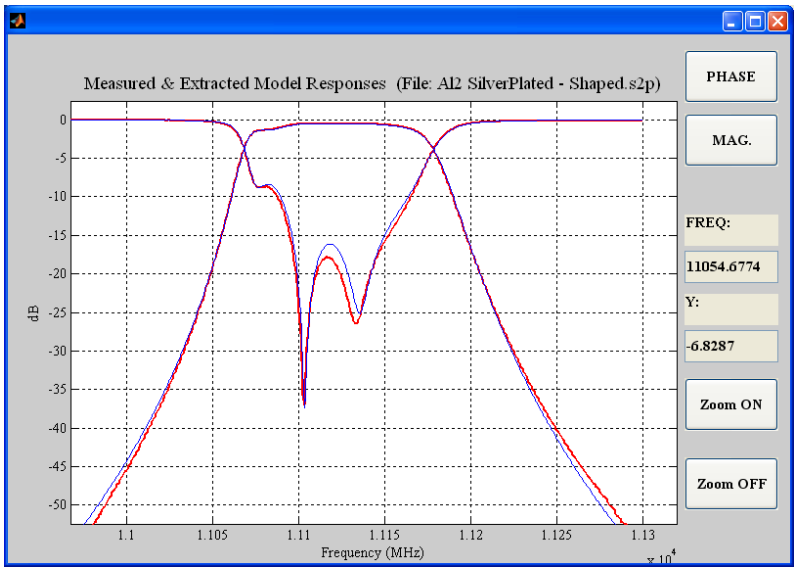

Figure C.30: Matched RF response of the measured Al2 shaped filter after a silver plating process.

C.2.3 Tuned Filters

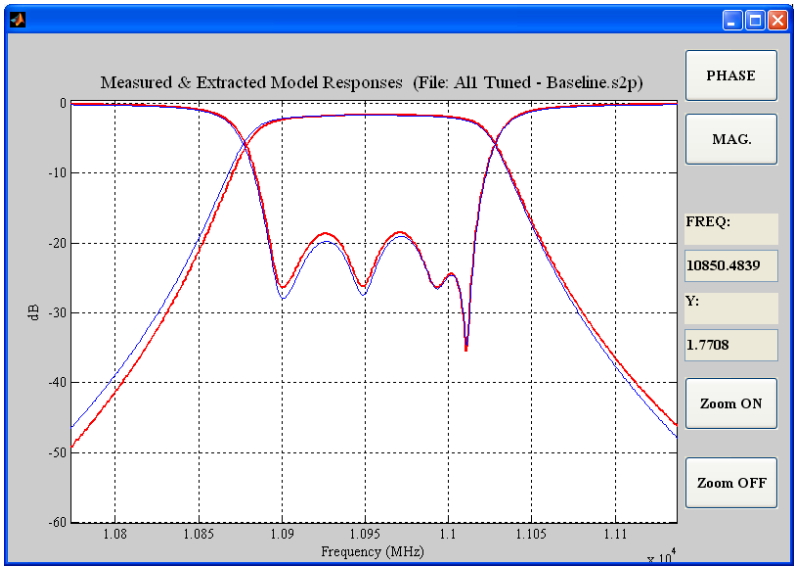

Figure C.31: Matched RF response of the measured Al1 baseline filter after minimal tuning of the resonators.

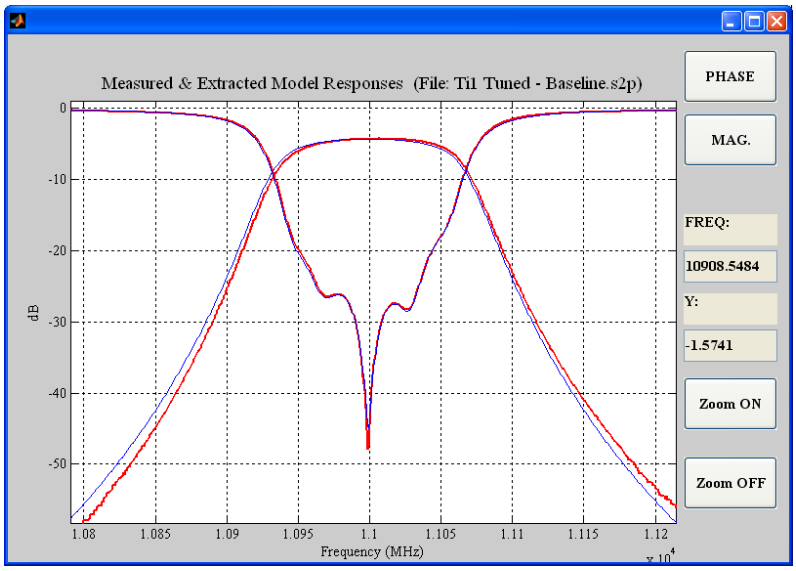

Figure C.32: Matched RF response of the measured Ti1 baseline filter after minimal tuning of the resonators.

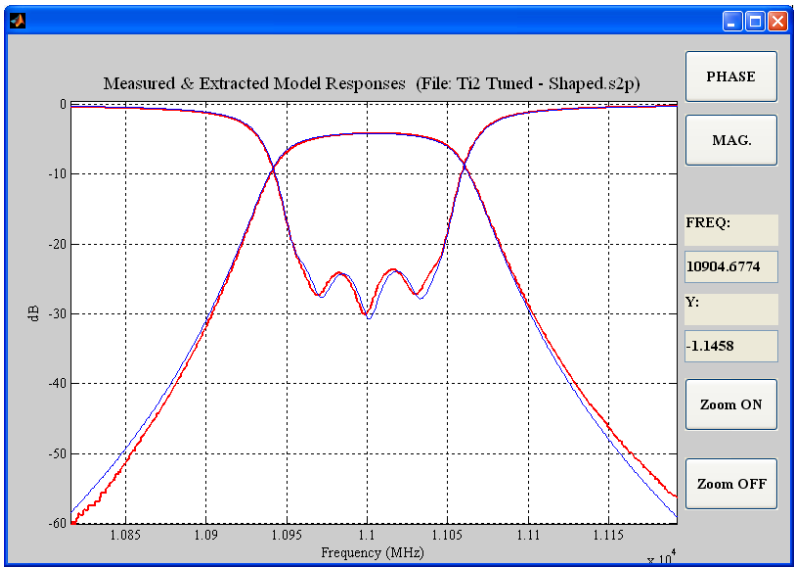

Figure C.33: Matched RF response of the measured Ti2 shaped filter after minimal tuning of the resonators.

APPENDIX D

HALVED RESONATORS MODEL - PROVE

Consider the odd mode equivalent circuit (Figure D.1) of the model in Figure 4.5(a), where $X_S = \omega L_S$ for inductive couplings. The resonant condition of this circuit is given by (D.1).

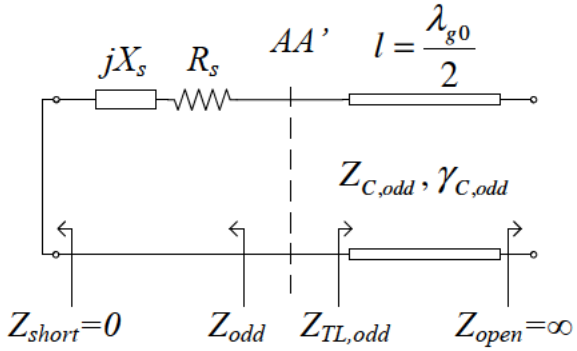

Figure D.1: Odd mode equivalent circuit of the model in Figure 4.5(b).

$$\Im\left(z_{TL,odd,full}\right)\big|_{\omega_{odd,full}} + \omega_{odd,full} L_S = 0 \tag{D.1}$$

Now, consider the odd mode equivalent circuit of the model in Figure 4.9(a). The resonator has been split in two symmetric halves and only one has been taken. In this case, the resonant condition is given by (D.2).

$$\Im\left(z_{TL,odd,half}\right)\big|_{\omega_{odd,half}} + \omega_{odd,half} L_S = 0 \tag{D.2}$$

Combining (D.1) and (D.2), the following relation between both circuits can be established:

$$\omega_{odd,half} = \omega_{odd,full} \frac{\Im\left(z_{TL,odd,half}\right)}{\Im\left(z_{TL,odd,full}\right)} \tag{D.3}$$

Equation (D.3) is a transcendental equation since $\omega_{odd,half}$ is needed to calculate $z_{TL,odd,half}$ and vice versa. Hence it has to be solved numerically.

Similarly, the even mode equivalent circuits in Figure D.2 and Figure 4.12 correspond to the even models in Figure 4.5(a) and Figure 4.9(a), respectively. Their resonant condition is found to be as (D.4) and (D.5), respectively, where $X_S = \omega L_S$ and $X_P = \omega L_P$ can be selected for inductive couplings.

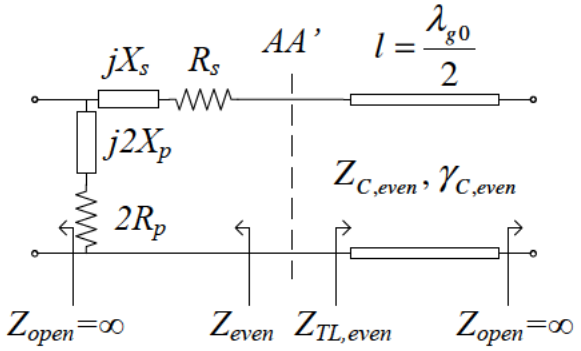

Figure D.2: Even mode equivalent circuit of the model in Figure 4.5(b).

$$\Im\left(z_{TL,even,full}\right)\big|_{\omega_{even,full}} + \omega_{even,full}\left(L_S + 2L_P\right) = 0 \tag{D.4}$$

$$\Im\left(z_{TL,even,half}\right)\big|_{\omega_{even,half}} + \omega_{even,half}\left(L_S + 2L_P\right) = 0 \tag{D.5}$$

Combining (D.4) and (D.5), the following relation between both circuits can be established:

$$\omega_{even,half} = \omega_{odd,full}\frac{\Im\left(z_{TL,even,half}\right)}{\Im\left(z_{TL,even,full}\right)} \tag{D.6}$$

which again has to be solved numerically since it is a transcendental equation. To validate the above equations, two full-wave simulations have been run. The first model is composed of two complete cavities coupled through a waveguide iris (as shown in Figure 4.5(a)), while the second one consists of two halved cavities coupled together with the same waveguide iris (Figure 4.9(a)). Both designs are characterized by the same coupling coefficient at the same centre frequency. Table D.1 collects the simulated even and odd frequencies of the above mentioned two models and the theoretical values derived using (D.3) and (D.6), for the case of the half resonator structure. The centre frequency and the coupling coefficient calculated with (4.31) and (4.32) are also shown.

Table D.1: Full cavity and half cavity design parameters

Parameter	Full cavity design (full-wave)	Half cavity design (full-wave)	Half cavity design (theory)
f_{odd}	11.0357	11.0732	11.0734
f_{even}	10.9622	10.9270	10.9266
f_0	10.9988	10.9994	10.9993
$k_{i,j}$	0.006679	0.006645	0.006672

An excellent agreement of less than 0.5% between the calculated parameters for the half cavity design and its simulation can be observed. Thus, the initial assumption where the transmission line resonator is divided in half due to the use of magnetic walls is proved (Figure 4.9(a)).

APPENDIX E

HIGH POWER HANDLING IN GEOMETRY OPTIMIZED FILTERS

E.1 Introduction

In this appendix a high power handling evaluation on filters with rectangular and shaped irises is presented. To achieve this, two commercial packages are used: *CST Particle Studio 2010* and *Fest3D V6.6.1*. The aim is to compare the minimum multipactor breakdown threshold obtained in waveguide filters with optimized coupling geometries against the one obtained in filters having traditional rectangular shapes. A second goal is to get insight from both commercial softwares and to understand how the simulated multipactor breakdown values compare with the predicted values from parallel plate theory. Furthermore, goal is to understand how the initial configuration on the simulation software packages can affect the multipactor breakdown prediction in waveguide structures. To achieve all the aforementioned goals, three waveguide cavity filters have been designed and simulated for multipactor: one filter with rectangular cavities and rectangular irises and reduced height of 1 mm, one filter with rectangular cavities and rectangular irises and reduced height of 5 mm, and another filter with rectangular cavities and parabolic shaped irises and reduced height of 5 mm.

As a worst-case scenario, the parallel plate approximation is used for all the three samples and the results are compared against those obtained in simulations. When this approximation is used, information about the fields in the structures is required. Thus, the peak E field at frequencies within the passband and band edges is calculated in all the cavities of the proposed filters. The maximum peak E field, its location, and its frequency are then obtained, and the voltage along the gap where the maximum peak E field is located is derived. Finally, the breakdown voltage can be calculated either by using the *ECSS Multipactor Tool Version 1.1* from the European Space Agency or by solving some simple equations.

E.2 Sample 1: 1 mm GAP 5th Degree Direct-Coupled-Cavity Band-Pass Filter with Rectangular Cavities and Rectangular Irises

The internal shape of sample 1 can be seen in Figure E.1. The filter has been designed to satisfy the specifications shown in Table E.1.

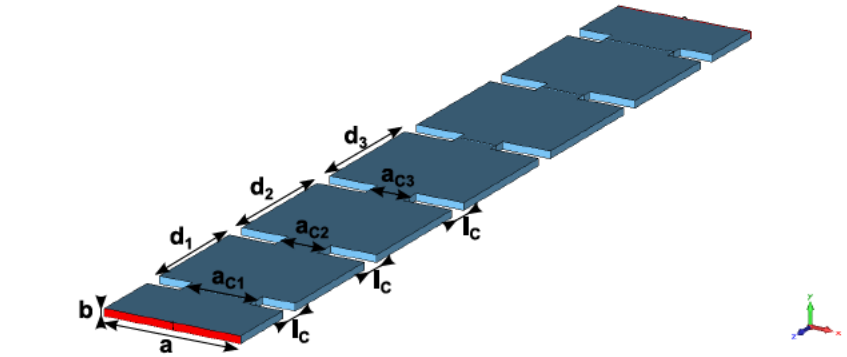

Figure E.1: Sample 1: internal shape.

Table E.1: Sample 1: design specifications

Parameter	Value
Type	Chebyshev
Degree	5
Center frequency	11 GHz
Filter ripple bandwidth	100 MHz
Return loss	30
Material conductivity	PEC

The physical dimensions are collected in Table E.2 and the simulated RF response can be seen in Figure E.2. As can be noted, the simulation matches the specifications in Table E.1.

Table E.2: Sample 1: physical dimensions in mm

Parameter	Value
a	19.05
b	1
l_C	3
a_{C1}	9.764
a_{C2}	6.051
a_{C3}	5.486
d_1	16.544
d_2	18.238
d_3	18.378

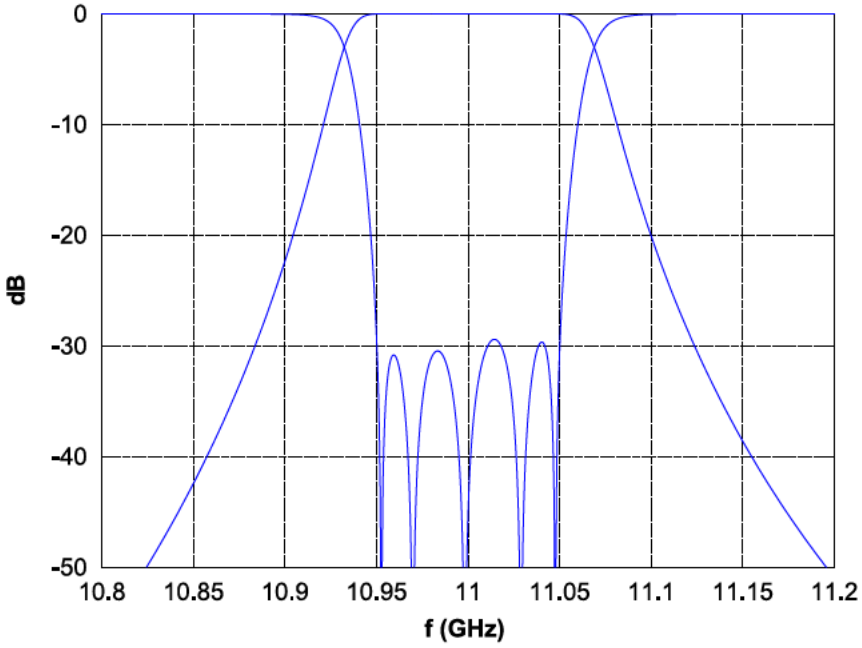

Figure E.2: Sample 1: simulalted RF response.

E.2.1 Parallel Plate Prediction

Figure E.3 depicts the peak E field calculated along the passband in the five cavities of the filter. It can be noted that the maximum value is given in cavity two at the lower edge of the passband ($E_{\max} = 86659$ V_p at $f_m = 10.938$ GHz). Thus, the second cavity of the filter is then chosen to carry out a multipactor analysis at the aforementioned frequency where the peak E field is maximum.

Khan [Khan, 1997] already proved that the peak E field strength oscillates around the center position in the cavity with changing frequencies. Moreover, Ernst [Ernst and Postoyalko, 2003] computed the deviation of the maximum field strength from the center position in the cavities of some filters with different bandwidths. It is seen that the maximum field strength remains almost in the center for a narrow-band filter. Therefore, the center point of the cavities will be taken as the gap where the multipactor analysis will be carried out.

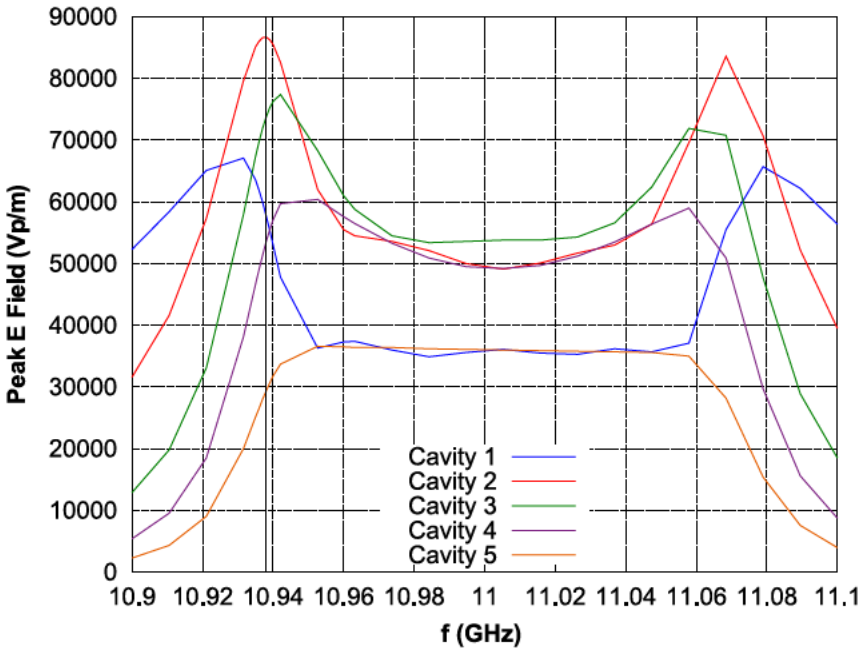

Figure E.3: Sample 1: peak E field along the passband in the five cavities of the filter.

The maximum peak voltage that will occur in sample 1 for an input power of $P_{IN} = 1$ W_p can be calculated as

$$V_m = \int_y E(f = f_m) \cdot dy = 86.64 V_p \tag{E.1}$$

where the path of integration along the 'y' coordinate is situated in the center position of the second cavity, as commented previously.

The voltage threshold of the filter can be computed by configuring the *ECSS Multipactor Tool Version 1.1* as a single carrier problem at f_m with a gap of 1 mm and for a type 1 component with silver surface (Figure E.4). The voltage threshold is given in (E.2).

$$V_{TH} = 685.14 V_p \tag{E.2}$$

Finally, the power threshold (P_{TH}) can be obtained either by means of (E.3) or by using the Multipactor Tool.

$$P_{TH} = P_{IN} \frac{V_{TH}^2}{V_m^2} = 62.54 W_p \tag{E.3}$$

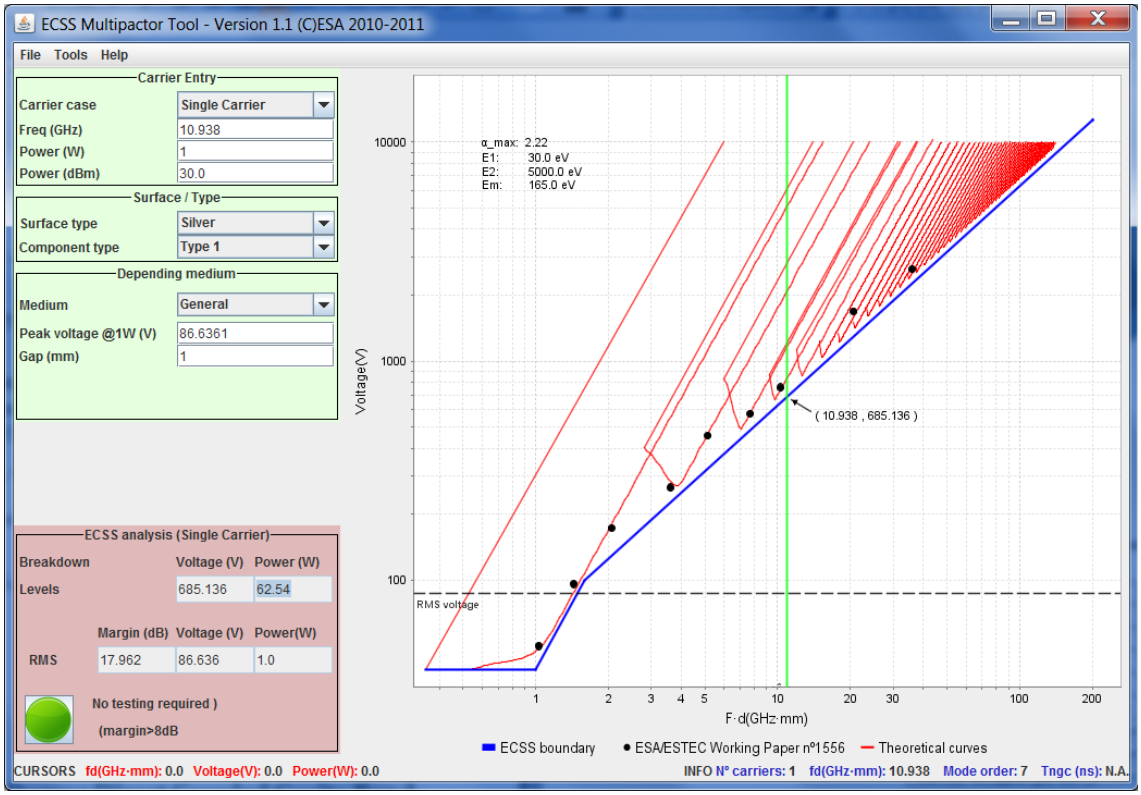

Figure E.4: ECSS Multipactor Tool Version 1.1 showing input parameters and predicted threshold.

E.2.2 CST PS Prediction

The following steps have been followed to predict the multipactor threshold using CST Studio:

- Calculate E and H fields of the structure under study, which are normalized to an input power of 1 W, at the frequency of interest with CST MWS and export them to an ASCII file.
- Change the problem type to Particle/PIC (CST PS).
- Change the conducting material to one with enabled secondary electrons emission or define particle emission properties in the current material.
- Add a particle source where the multipactor effect is to be studied.
- Import the E and H fields previously calculated in CST MWS and multiply them by a factor of $\sqrt{P_{TH}}$, where the variable P_{TH} stands for power threshold. A sweep will be set up in this variable, and the fields will be scaled by the $\sqrt{P_{TH}}$ factor.
- Run the parameter sweep in the PIC solver with no field excitations except for the external imported ones.

In CST PS, there is no need to recalculate the E and H fields of the complete structure as they have already been exported to an ASCII file from CST MWS. Thus, just the second cavity and half of the first and third cavities (Figure E.5) are studied in CST PS. In this way, the total volume to mesh is reduced and the mesh density can be improved for the same simulation time. Note that only the fields corresponding to this volume must be exported in CST MWS. No mesh convergence study has been performed for this sample.

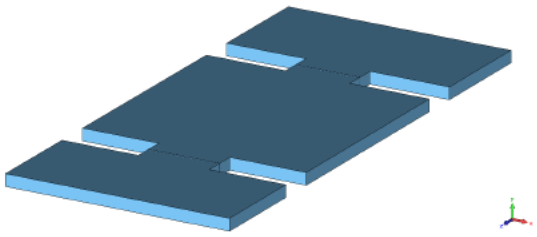

Figure E.5: Sample 1: selected geometry where multipactor has been analyzed using CST Studio.

Finally, configuring CST PS with the parameters shown in Table E.3 and setting up the simulation time to 20 ns, the graph particle population versus time is obtained for the different values of the power variable, Figure E.6. The electron source have been assigned to the top-wall of the cavity.

Table E.3: Sample 1: input parameters for the CST PS Solver

Parameter	Value
Total Simulation Time	44h 22min 43sec
Mesh Cells	181566
Initial Number of Electron Sources	213
PIC Emission Model	Gauss
Kinetic Type	Energy
Kinetic Value	10eV
Kinetic Spread	0%
Angular Spread	0°
Charge	$213 \times 1.6 \cdot 10^{-19} C$
Bunches	1
Sigma	0.2 ns
Cutoff Length	0.2 ns
Offset	0.2 ns
Bunches Distance	0
Frequency	10.938 GHz
Material	SEE - Silver

The linear part of the graph is due to CST PS injecting electrons every time step from 0 ns to 0.4 ns. These values can be controlled with the 'Charge', 'Bunches', 'Sigma', 'Cutoff Length', 'Offset' and 'Bunches Distance' parameters from Table E.3.

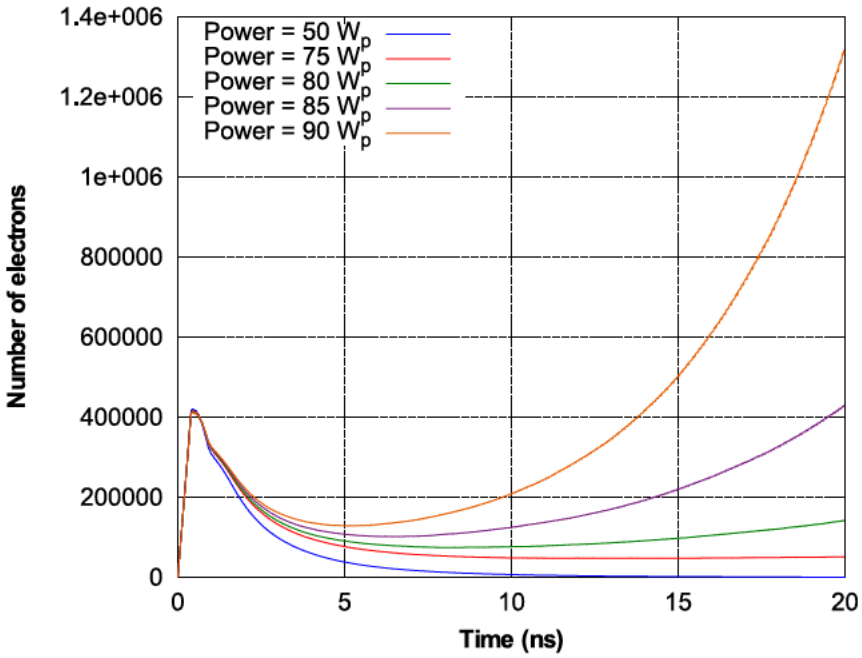

Figure E.6: Sample 1: particle population versus time for different power values.

Note that multipactor effect occurs when an avalanche of emitted electrons is produced, meaning an exponential growth of particles inside the waveguide structure. In this case, the multipactor power threshold predicted by CST PS lies within the range of $P_{TH} = 75W_p$ to $P_{TH} = 85W_p$.

E.2.3 Fest3D Prediction

The same structure has been simulated in Fest3D. The input parameter configuration can be seen in Figure E.7.

The search for the multipactor threshold in Fest3D is totally automated. The initial power and the maximum power where the analysis will be carried out have to be given as input data for the simulation. No field simulations are required since Fest3D computes them automatically when running a multipactor simulation.

For sample 1, the multipactor simulation in Fest3D took about three minutes and the predicted power threshold was $P_{TH} = 50.63W_p$.

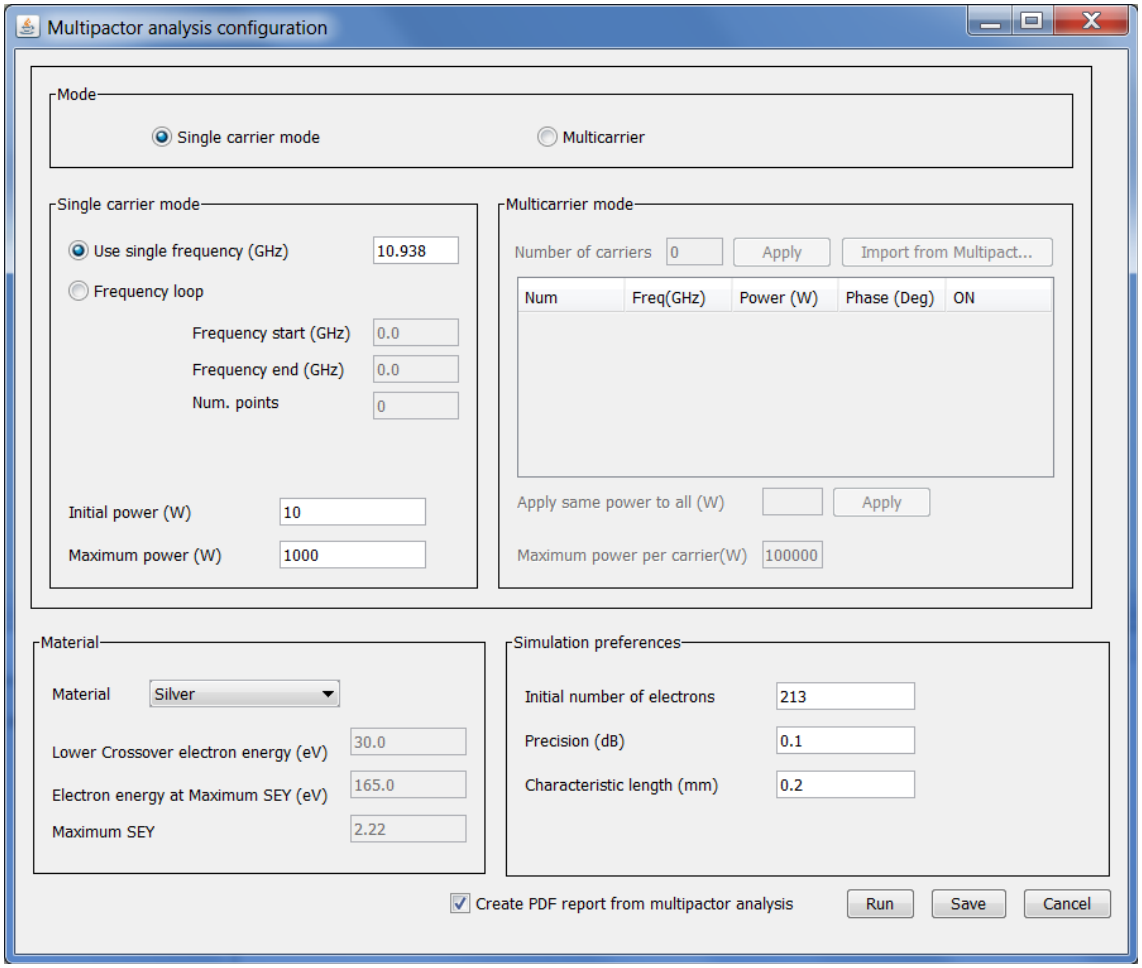

Figure E.7: Sample 1: input parameters for the Fest3D multipactor analysis.

E.3 Sample 2: 5 mm GAP 5th Degree Direct-Coupled-Cavity Band-Pass Filter with Rectangular Cavities and Rectangular Irises

Figure E.8 shows the internal geometry of sample 2. The filter has been designed to comply with the same specifications as sample 1 (see Table E.1).

The physical dimensions of sample 2 can be seen in Table E.4 and its simulated RF response in Figure E.9. Note that the only difference with sample 1 is the height of the filter.

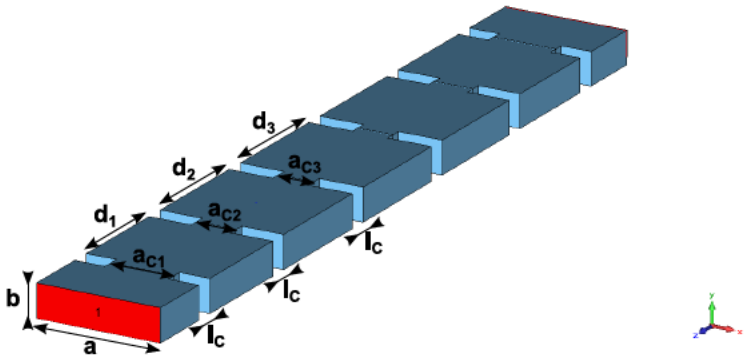

Figure E.8: Sample 2: internal shape.

Table E.4: Sample 2: physical dimensions in mm

Parameter	Value
a	19.05
b	1
l_C	3
a_{C1}	9.764
a_{C2}	6.051
a_{C3}	5.486
d_1	16.544
d_2	18.238
d_3	18.378

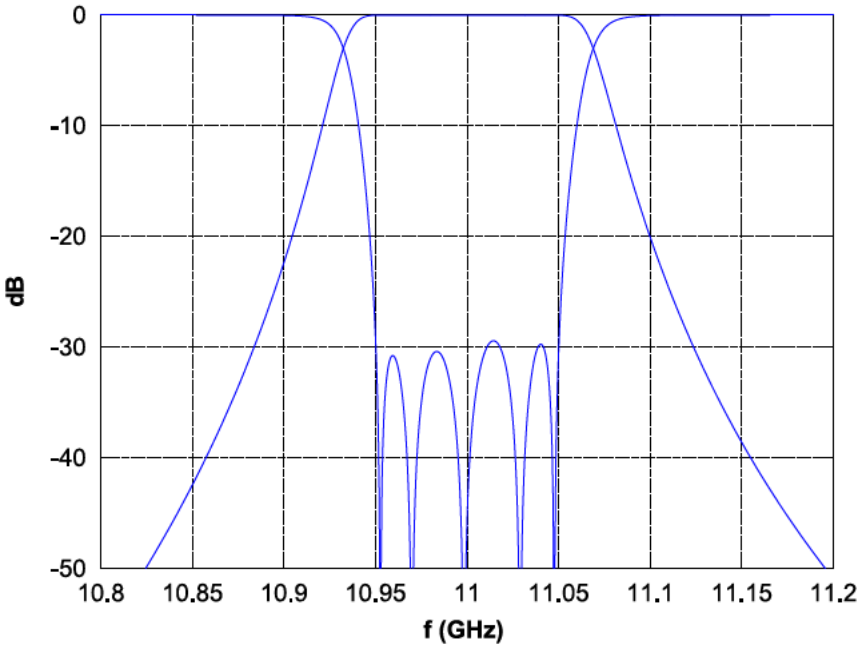

Figure E.9: Sample 2: simulalted RF response.

E.3.1 Parallel Plate Prediction

Figure E.10 depicts the peak E field calculated along the passband in the five cavities of the filter. Again, cavity two shows the maximum value at the lower edge of the passband ($f_m = 10.938$ GHz) and therefore, the second cavity of the filter is again chosen to carry out a multipactor analysis at the aforementioned frequency where the peak E field is maximum.

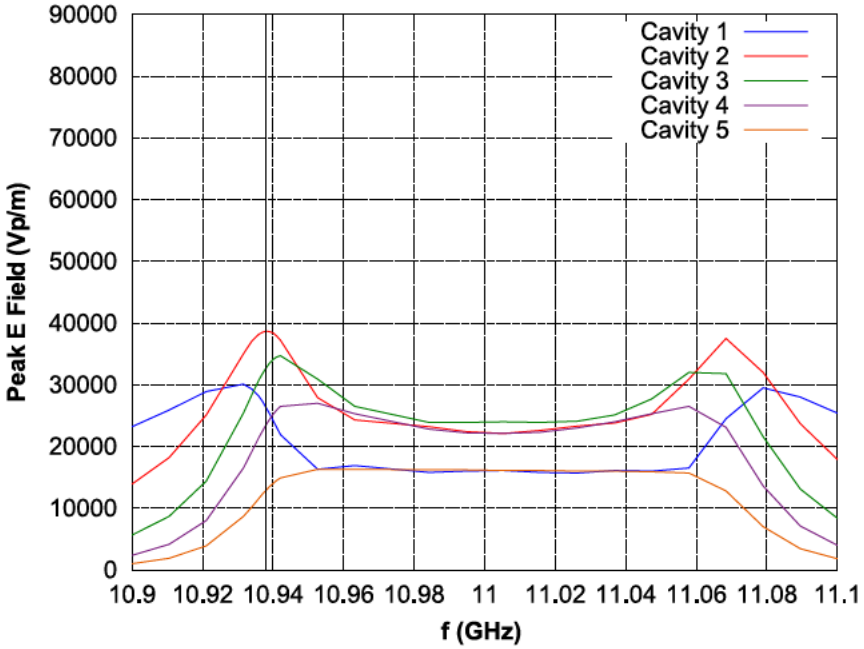

Figure E.10: Sample 2: peak E field along the passband in the five cavities of the filter.

The voltage in the center point of the second cavity at f_m can be calculated as (for an input power of $P_{IN} = 1$ W$_p$)

$$V_m = \int_y E(f = f_m) \cdot dy = 193.352 V_p \tag{E.4}$$

Configuring the Multipactor Tool as a single carrier problem at f_m with a gap of 5 mm and for a type 1 component with silver surface, the voltage threshold for the second design can be computed, (E.5).

$$V_{TH} = 3436.627 V_p \tag{E.5}$$

Finally, the power threshold (P_{TH}) can be obtained as

$$P_{TH} = P_{IN} \frac{V_{TH}^2}{V_m^2} = 315.913 W_p \tag{E.6}$$

E.3.2 CST PS Prediction

The selected structure from sample 2 where the multipactor analysis is to be carried out in CST PS can be seen in Figure E.11. Again, the second cavity of the filter

with half cavities on its sides is chosen since the maximum peak E field is produced at the center of this cavity.

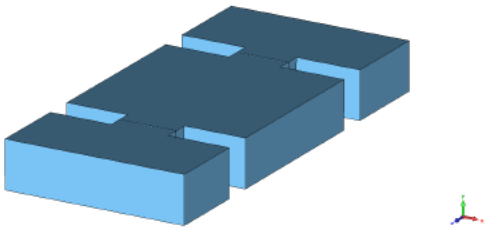

Figure E.11: Sample 2: selected geometry where multipactor has been analyzed using CST Studio.

Table E.5 collects the parameters to be configured for the multipactor simulation in CST PS.

Table E.5: Sample 2: input parameters for the CST PS solver

Parameter	Value
Total Simulation Time	62h 25min 20sec
Mesh Cells	119286
Initial Number of Electron Sources	213
PIC Emission Model	Gauss
Kinetic Type	Energy
Kinetic Value	10eV
Kinetic Spread	0%
Angular Spread	0°
Charge	$213 \times 1.6 \cdot 10^{-19} C$
Bunches	1
Sigma	0.2 ns
Cutoff Length	0.2 ns
Offset	0.2 ns
Bunches Distance	0
Frequency	10.938 GHz
Material	SEE - Silver

The results of running the power sweep on this structure can be seen in Figure E.12. In this sample, the multipactor breakdown predicted by CST PS was found to be larger than $P_{TH} = 800$ W_p but lower than $P_{TH} = 1600$ W_p.

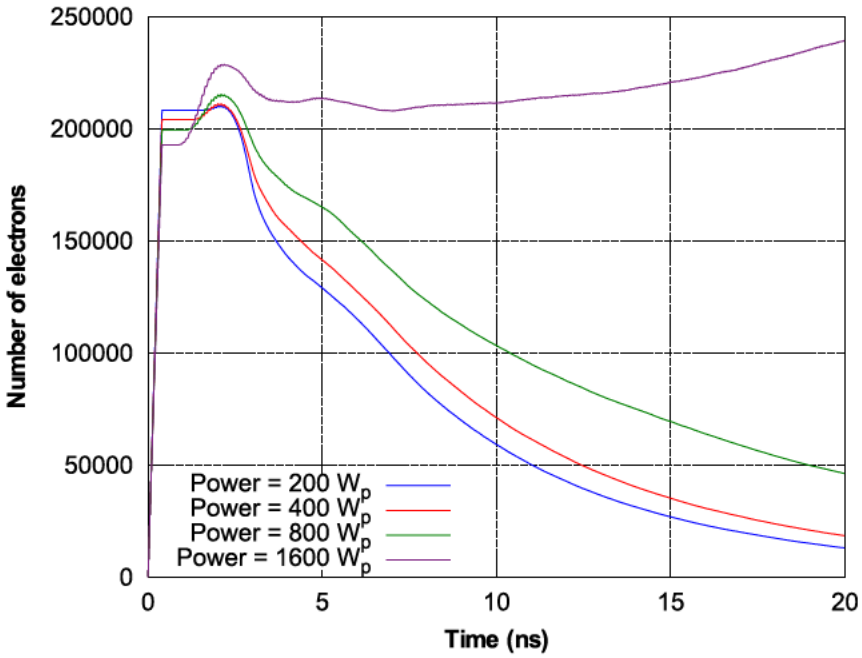

Figure E.12: Sample 2: particle population versus time for different power values.

Impact of the Initial Number of Electron Sources and Initial Energy on Multipactor Prediction

To understand how the initial number of electron sources (N_e) and initial energy (E) parameters of CST PS affect multipactor prediction in waveguide structures, a parameter sweep using these variables has been run. The parameter sweep plan is shown in Table E.6.

Table E.6: Sample 2: parameter sweep table for initial number of electron sources and initial energy study

Color	Density	N_e	E (Kinetic Value)
Blue	0.2	61	
Red	0.1675	82	
Green	0.135	108	Sweep from 1eV to 9eV
Purple	0.1025	213	
Orange	0.07	403	

The initial number of electrons cannot be directly swept in CST PS. A parameter called 'Density' which is inversely proportional to the initial number of electrons sources and can be found through the 'History List' in CST PS is modified instead. The values of the remaining parameters are collected in Table E.7.

From Figure E.13, the impact of the initial number of electrons and initial energy on multipactor prediction can be extracted. Note that the absolute value of electrons varies remarkably with these two parameters (the larger the initial number of electrons and the initial energy, the more secondary electrons are emitted, as expected) whereas the slope of the graphs remains almost identical one to another. Since the more electrons in the volume translates into larger simulation time and

Table E.7: Sample 2: input parameters for the CST PS solver

Parameter	Value
Total Simulation Time	48h 35min 30sec
Mesh Cells	119286
PIC Emission Model	Gauss
Kinetic Type	Energy
Kinetic Spread	0%
Angular Spread	0°
Charge	$213 \times 1.6 \cdot 10^{-19} C$
Bunches	1
Sigma	0.2 ns
Cutoff Length	0.2 ns
Offset	0.2 ns
Bunches Distance	0
Frequency	10.937 GHz
Material	SEE - Silver
P_{TH}	1600 W_p

these graphs do not vary their slope with N_e and E, it can be concluded that these two parameters must be left as low as possible. On the other hand, it is necessary to make sure that enough electron sources are placed where the maximum field occurs, otherwise the electron avalanche prediction can yield to non accurate and non realistic results.

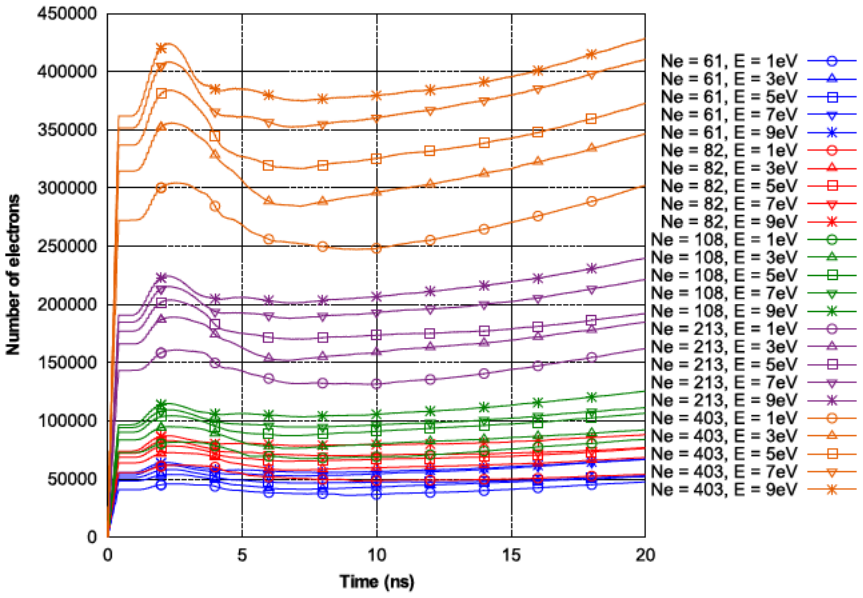

Figure E.13: Sample 2: particle population versus time for $P_{TH} = 1600\ W_p$ and for a different initial number of electrons and energies.

Impact of Mesh Density on Multipactor Prediction

A mesh convergence study has also been performed for this structure. The mesh of the design has been swept according to the values shown in Table E.8. The set up of the simulation parameters is collected in Table E.9.

Table E.8: Sample 2: parameter sweep table for the mesh density study

Lines per Wavelength	Mesh Cells	Simulation Time
20	220110	11h 30min 34sec
25	271950	20h 47min 49sec
30	428968	36h 35min 10sec
	TOTAL	68h 53min 33sec

Table E.9: Sample 2: input parameters for the CST PS solver

Parameter	Value
Initial Number of Electron Sources	403
PIC Emission Model	Gauss
Kinetic Type	Energy
Kinetic Value	10eV
Kinetic Spread	0%
Angular Spread	0°
Charge	$213 \times 1.6 \cdot 10^{-19} C$
Bunches	1
Sigma	0.2 ns
Cutoff Length	0.2 ns
Offset	0.2 ns
Bunches Distance	0
Frequency	10.938 GHz
Material	SEE - Silver

Figure E.14 shows the result of the mesh study. It is interesting to note how the slope of the particle growth varies with the quality of the mesh. This is extremely important since the multipactor phenomena could not be detected if the quality of the mesh is too low. Therefore, a mesh convergence study is needed to assure accuracy in multipactor prediction using CST PS. However, simulation time can be extremely large and it increases exponentially with the number of meshcells. Therefore, a trade-off between mesh density and simulation accuracy must be found.

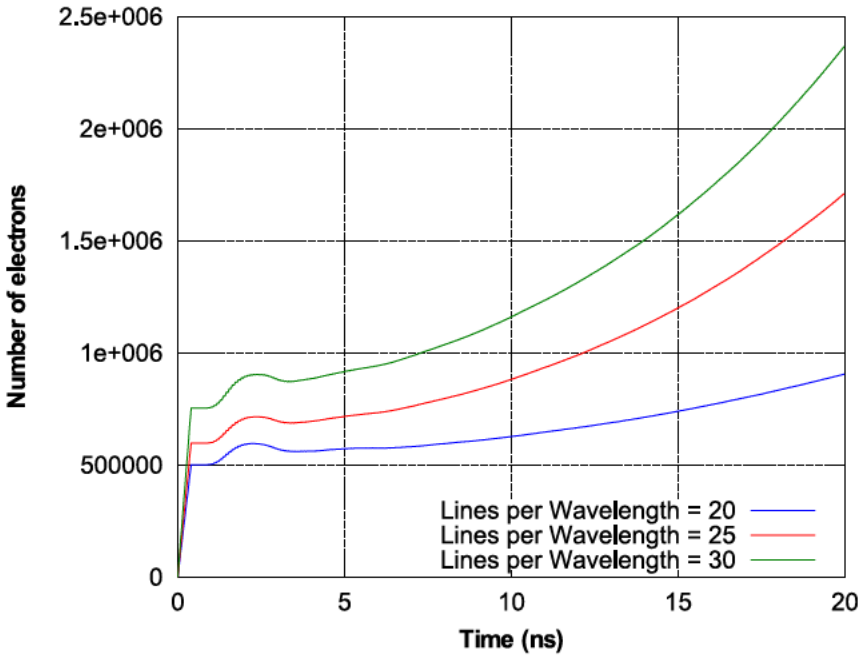

Figure E.14: Sample 2: particle population versus time for different mesh densities and $P_{TH} = 1600\ W_p$.

E.3.3 FEST3D Prediction

The input parameter configuration for the multipactor analysis in Fest3D of sample 2 is shown in Figure E.15.

In this case, the multipactor simulation in Fest3D takes around five minutes and the predicted power threshold is $P_{TH} = 575\ \mathrm{W_p}$.

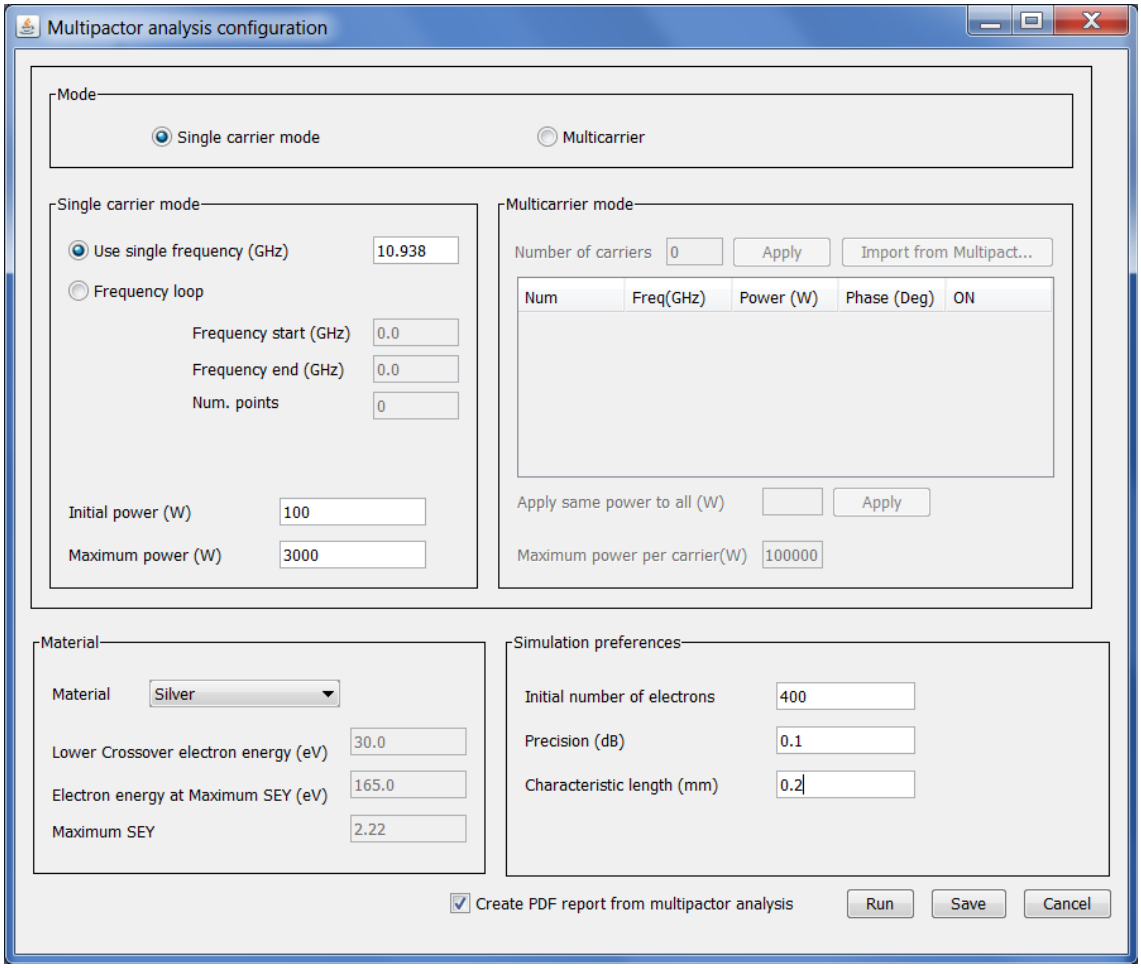

Figure E.15: Sample 2: input parameters for the Fest3D multipactor analysis.

Impact of the Initial Number of Electron and Mesh Density on Multipactor Prediction

As in CST PS, a study to understand how the initial number of electrons (N_e) and mesh density (*Characteristic length*) affect the multipactor breakdown prediction in Fest3D has been carried out. To check the consistency of the software, two rounds of simulations have been performed. Table E.10, Table E.11 and Table E.12 show the results of this investigation. The initial number of electrons has been swept from 10 to 400 for three different mesh densities. The rest of the parameters are configured as in Figure E.15.

Unlike in CST PS, the number of initial electrons for the multipactor simulation in Fest3D must be as high as possible (Figure E.16). Fest3D automatically sets the particle source in the cavity under study and on the adjacent cavities. Thus, it is not possible to manually reduce it to where the peak E field is known to be the maximum. The initial number of electrons must be carefully selected to make sure enough electrons are in this region. As can be seen in Figure E.16, the discrepancy between both rounds for a very low number of initial electrons is significant. On the other hand, when the initial number of electrons is large enough and the characteristic length of the mesh is reduced, different multipactor calculations runs converge to

Table E.10: Sample 2: Fest3D multipactor breakdown results in W_p for $N_e = 10$ to 400 and 1 mm characteristic length

	Sim.1	Sim. 2
N_e	P_{TH}	P_{TH}
10	2400	2475
20	787.5	2562.5
50	737.5	762.5
100	637.5	587.5
150	587.5	650
200	662.5	637.5
400	625	537.5

Table E.11: Sample 2: Fest3D multipactor breakdown results in W_p for $N_e = 10$ to 400 and 0.5 mm characteristic length

	Sim.1	Sim. 2
N_e	P_{TH}	P_{TH}
10	1993.75	1950
20	1200	493.75
50	875	1300
100	675	675
150	662.5	800
200	612.5	800
400	587.5	625

Table E.12: Sample 2: Fest3D multipactor breakdown results in W_p for $N_e = 10$ to 400 and 0.2 mm characteristic length

	Sim.1	Sim. 2
N_e	P_{TH}	P_{TH}
10	No multipactor	No multipactor
20	862.5	No multipactor
50	700	712.5
100	800	587.5
150	550	637.5
200	587.5	575
400	575	600

essentially the same multipactor threshold value.

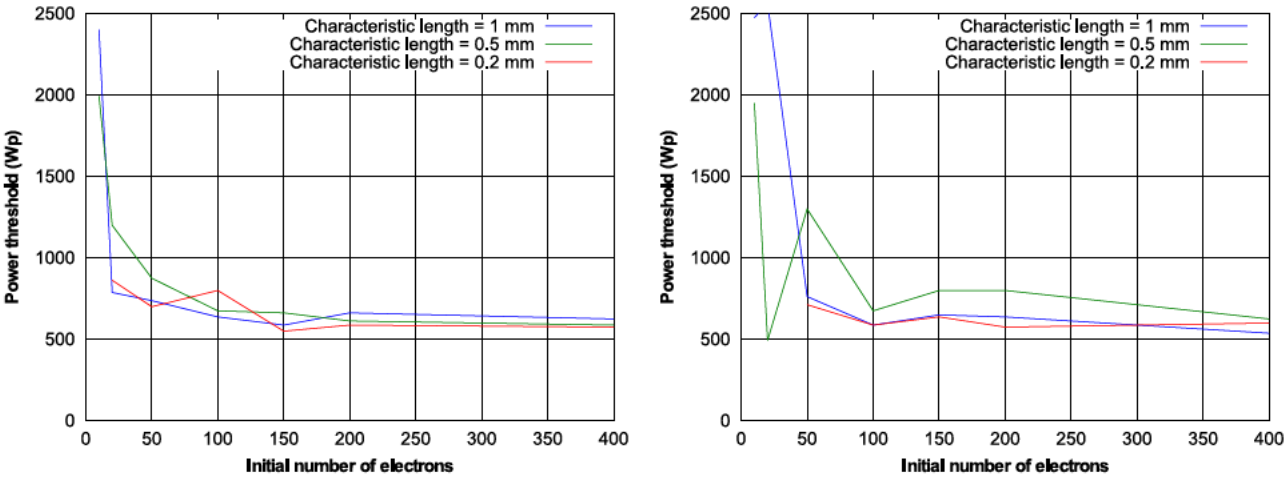

Figure E.16: Sample 2: power threshold versus initial number of electrons in Fest3D: (a) simulation 1 and (b) simulation 2.

E.4 Sample 3: 5 mm GAP 5th Degree Direct Coupled Cavity Band-Pass Filter with Rectangular Cavities and Parabolic Irises

A multipactor analysis has been carried out on a waveguide filter with rectangular cavities and shaped parabolic irises (Figure E.17). The filter has the same electrical response (Figure E.18) and physical height as the filter from sample 2 (taken as baseline). The aim is to compare the multipactor threshold obtained for both the baseline filter and the shaped one and to find out the impact of shaping the coupling structures on the power handling of waveguide filters. To that end, the multipactor threshold is calculated using first the parallel plate theory approximation and then using CST PS. However, Fest3D is not able to model this structure with parabolic shaped irises and a high power analysis is not possible using this software.

The physical dimensions of sample 3 are collected in Table E.13.

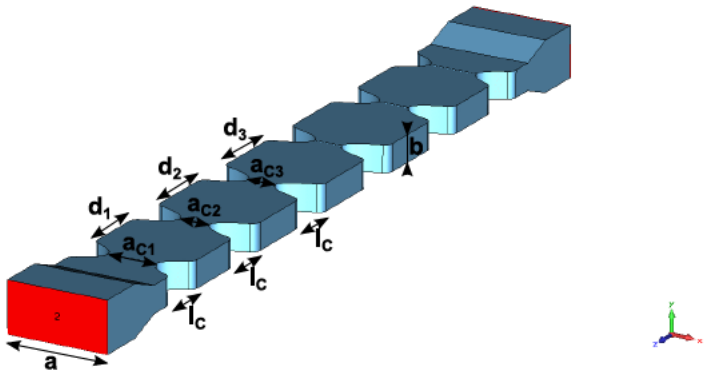

Figure E.17: Sample 3: internal shape.

Table E.13: Sample 3: physical dimensions in mm

Parameter	Value
a	19.05
b	5
l_C	8
a_{C1}	9.161
a_{C2}	5.668
a_{C3}	5.080
d_1	12.568
d_2	14.125
d_3	14.2917
r_C	1.5

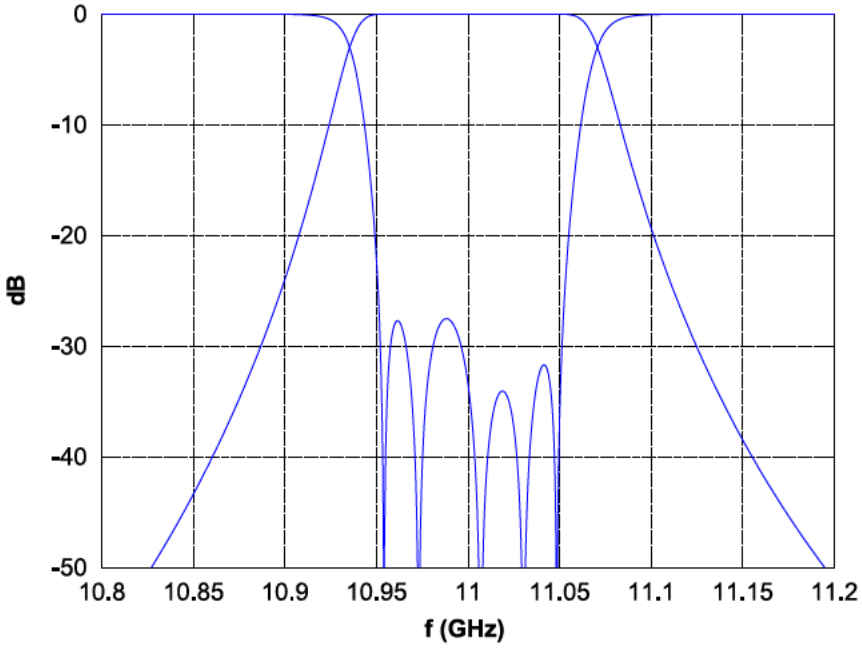

Figure E.18: Sample 3: simulalted RF response.

E.4.1 Parallel Plate Prediction

Figure E.19 shows the peak E field in all the cavities of sample 3 along the pass band.

The maximum peak E field is given in the second cavity at $f_m = 10.938$ GHz. The maximum peak voltage in the center of the second cavity at f_m can be calculated as (for an input power of $P_{IN} = 1$ W_p)

$$V_m = \int_y E(f = f_m) \cdot dy = 193.416 V_p \tag{E.7}$$

Configuring the Multipactor Tool as a single carrier problem at f_m with a gap of 5 mm and for a type 1 component with silver surface, the voltage threshold for the second design can be computed as

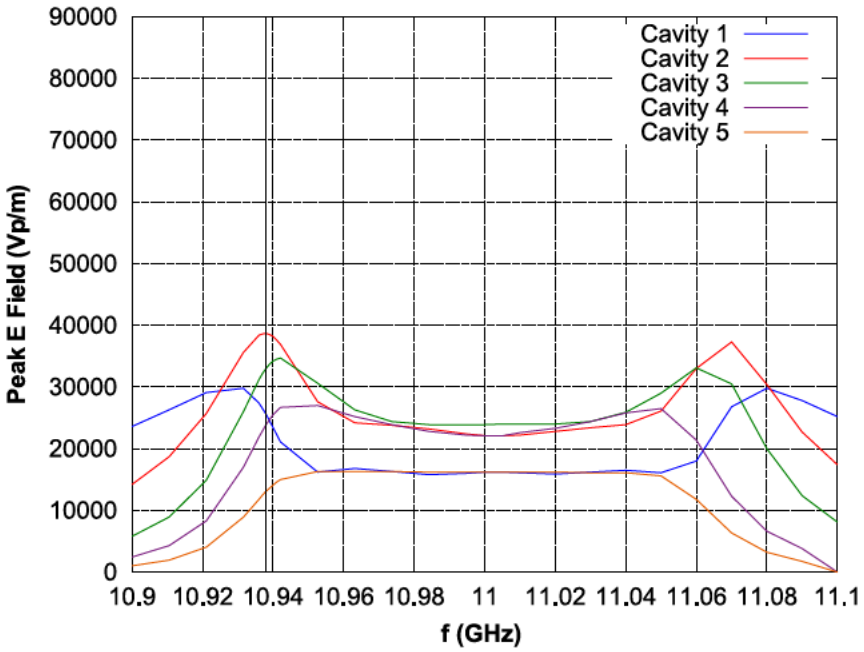

Figure E.19: Sample 3: peak E field along the passband in the five cavities of the filter.

$$V_{TH} = 3436.627 V_p \tag{E.8}$$

and the power threshold is

$$P_{TH} = P_{IN} \frac{V_{TH}^2}{V_m^2} = 315.704 W_p \tag{E.9}$$

It can be observed that the minimum multipactor threshold calculated using the parallel plate theory approximation gives essentially the same value as the one obtained in sample 2 with the baseline geometry (rectangular cavities and rectangular irises).

E.4.2 CST PS Prediction

Figure E.20 shows the selected structure from sample 3 where the multipactor analysis is to be carried out using CST PS. As previously, the second cavity of the filter with the half of the first and third cavities on its sides is chosen because the maximum peak E field is produced at the center of this cavity.

The parameters for the simulation are collected in Table E.14 and the results of the power sweep can be seen in Figure E.21.

The multipactor threshold predicted by CST PS in a filter with rectangular cavities and parabolic shaped irises is in the range from $P_{TH} = 1000$ W_p to $P_{TH} = 2000$ W_p. As well as the parallel plate theory, the multipactor breakdown predicted by CST PS for a filter with shaped irises is similar to the one obtained in the baseline geometry (sample 2). It can then be concluded that the shaping process does not essentially affect the multipactor risk in this kind of filters.

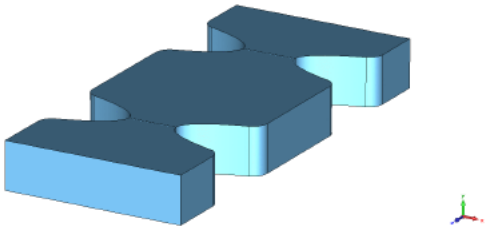

Figure E.20: Sample 3: selected geometry where multipactor has been studied.

Table E.14: Sample 3: input parameters for the CST PS solver

Parameter	Value
Total Simulation Time	22h 43min 23sec
Mesh Cells	267786
Initial Number of Electron Sources	288
PIC Emission Model	Gauss
Kinetic Type	Energy
Kinetic Value	10eV
Kinetic Spread	0%
Angular Spread	0°
Charge	$288 \times 1.6 \cdot 10^{-19} C$
Bunches	1
Sigma	0.2 ns
Cutoff Length	0.2 ns
Offset	0.2 ns
Bunches Distance	0
Frequency	10.938 GHz
Material	SEE - Silver

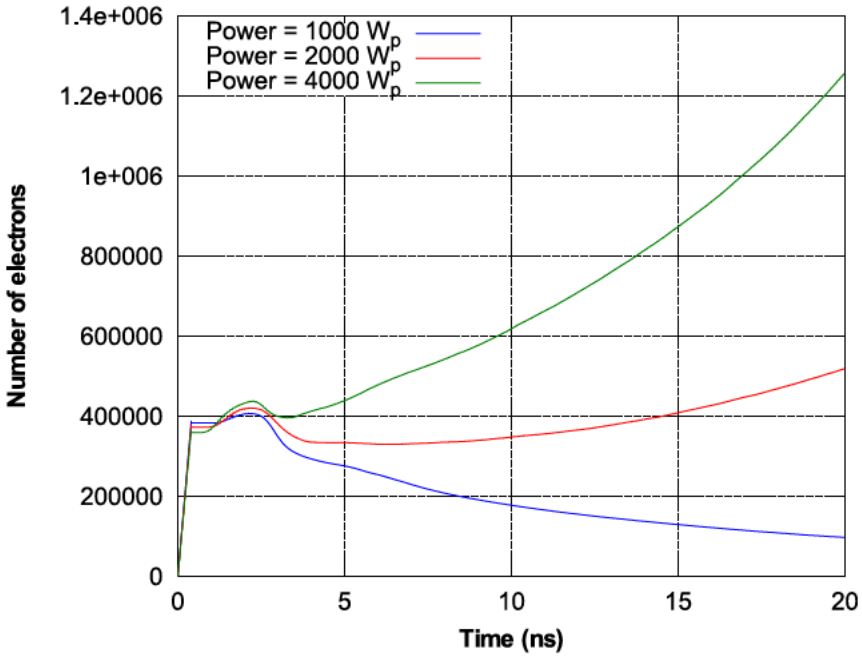

Figure E.21: Sample 3: particle population versus time for different power values.

E.5 Summary

Table E.15 collects the multipactor breakdown values predicted by the different approaches for the three samples investigated in this appendix.

Table E.15: Multipactor breakdown summary in W_p

	Parallel Plate	CST PS 2010	FEST3D
Sample 1 (1 mm gap)	62.54	75 - 80	50.625
Sample 2 (5 mm gap)	315.913	800 - 1600	575
Sample 3 (5 mm gap)	315.704	1000 -2000	N/A

In general, the breakdown prediction by the parallel plate theory applied to these examples should give conservative results, as can be observed in sample 2 and sample 3. This is not the case for sample 1, as the threshold obtained applying parallel plate theory is larger than that obtained using FEST3D. This can be explained by approximations in the parallel plate theory and inaccuracies in both softwares due to mesh quality. On the other hand, note that due to the large width to height ratio (a/b) in sample 1, its electrical behaviour approaches that of a parallel plate structure, thus the deviation between parallel plate and software prediction reduces.

The multipactor threshold predicted by CST PS for sample 2 and sample 3 are larger than those obtained by using the parallel plate approximation and FEST3D. As said previously, the parallel plate theory is more conservative and predicts lower thresholds for these two samples in comparison with CST PS and FEST3D. This is explained by the width to height ratio of these structures, which reduces considerably as they are five times higher than sample 1 whilst keeping the same width, which in turns reduces the similitude with the parallel plate scenario. Comparison between multipactor thresholds in samples 2 and 3 reveals that the shaping process of coupling structures and cavities does not have an important impact on RF breakdown risk. This can be explained by the fact that highest E fields are encountered around the central area of resonators, and these regions are hardly affected by the shaping process.

E.6 Conclusion

A multipactor breakdown analysis has been carried out for three waveguide structures. The main aim was to find out how shaped coupling structures in waveguide filters affect the multipactor threshold level. A second goal was to get insight from commercial softwares for the breakdown prediction and to understand how the simulated values compare with the predicted values from parallel plate theory. The multipactor analysis has been carried out following three approaches, although the use of all of them in all the samples was not possible. A comparison of the predicted values for the different samples can be seen in Table E.15.

- Sample 1 is the simplest structure and its geometry is very close to the parallel plate case. The predicted values from parallel plate, CST PS and FEST3D agree well.

- Sample 2 is the same structure as sample 1 but with a larger waveguide height. Thus, it is not as close as sample 1 to the parallel plate model. The predicted breakdown from the parallel plate theory is lower than those predicted by CST PS and FEST3D, and can be taken as a worst case value. In addition, the two softwares used here predict different threshold values for the same sample, giving CST PS the largest value. On the other hand, it was observed during the mesh convergence study that the use of higher quality meshes tends to increase the slope of the number of electrons inside the structure over time, which mean that a lower power must be used in the simulation to reach the multipactor threshold. Therefore, increasing the mesh quality in CST PS leads to a reduction in the difference in breakdown prediction between both softwares.

- Sample 3 is a filter with the same configuration and electrical response as sample 2, with also rectangular inline cavities and the same overall height, but with parabolic shaped irises instead of rectangular geometries. However, the shaping applied on the irises is far from where multipactor is expected to occur and so the multipactor results predicted by parallel plate theory and CST PS are almost identical to those obtained for sample 2. In this study, similar mesh quality was used in the analyses of sample 2 and sample 3, so a fair comparison could be done. It is concluded then that the shaping process applied to the coupling structures of waveguide direct-coupled-cavity filters has little or no impact in the multipactor threshold.

To understand how the initial number of electrons, the initial energy of the electrons and the mesh refinement affect on multipactor prediction, a sweep over these variables has been carried out in CST PS and Fest3D.

- It is interesting to observe that for CST PS the number of electrons and initial energy does not affect the slope of the particle versus time graphs (and thus multipactor prediction) as long as the particle source is carefully placed in the critical area. Therefore, these two parameters must be left as low as possible to reduce simulation time.

- In Fest3D, a direct control over the position of the particle source is not available since it is placed automatically. It is found that the discrepancy between results of different simulation rounds decreases as the number of electrons increases. Therefore, the initial number of electrons in Fest3D must be carefully selected. Moreover, simulations using different meshes studied in this work did not reveal any large threshold variations.

E.7 Drawbacks

Some problems were found during this study:

- The multipactor breakdown prediction in CST PS leads to very long simulation time as mesh refinement and power sweep must be carried out. Simulation times of one day to two days or even more could be necessary depending on the size and complexity of the geometry to be analyzed.
- More accurate results could have been obtained if the simulated time was increased, although that would have led to extremely long simulation times.
- Multipactor predictions in sample 1, sample 2 and sample 3 were run before studying the effect of varying the initial number of electrons and energy in CST PS. Thus, more accurate CST predictions could be obtained if the new knowledge is applied to sample 1, sample 2 and sample 3.

BIBLIOGRAPHY

[Amari, 2000] Amari, S. (2000). Sensitivity analysis of coupled resonator filters. *IEEE Trans. Circuits Syst. II, Analog Digit. Signal Process.*, 47(10):1017–1022.

[Cameron et al., 2007] Cameron, R. J., Mansour, R., and Kudsia, C. M. (2007). *Microwave Filters for Communication Systems: Fundamentals, Design and Applications*. John Wiley & Sons, Inc.

[Canos et al., 2003] Canos, A. J., Catala-Civera, J. M., Penaranda-Foix, F. L., Monzo-Cabrera, J., and De los Reyes, E. (2003). A new empirical method for extracting unloaded resonant frequencies from microwave resonant cavities. In *IEEE MTT-S Int. Microw. Symp. Dig.*, volume 3, pages 1823–1825.

[Chua and Mirshekar-Syahkal, 2003] Chua, L. H. and Mirshekar-Syahkal, D. (2003). Accurate and direct characterization of high-q microwave resonators using one-port measurement. *IEEE Trans. Microw. Theory Techn.*, 51(3):978–985.

[Cohn, 1968] Cohn, S. (1968). Microwave bandpass filters containing high-q dielectric resonators. *IEEE Trans. Microw. Theory Techn.*, 16(4):218–227.

[Cohn, 1957] Cohn, S. B. (1957). Direct-coupled-resonator filters. *Proc. IRE*, 45(2):187–196.

[Cohn, 1959] Cohn, S. B. (1959). Dissipation loss in multiple-coupled-resonator filters. *Proc. IRE*, 47(8):1342–1348.

[Collin, 2001] Collin, R. (2001). *Foundations for Microwave Engineering*. McGraw Hill, New York.

[Crawford and Beaman, 1999] Crawford, R. H. and Beaman, J. J. (1999). Solid freeform fabrication. *IEEE Spectr.*, 36(2):34–43.

[Deslandes and Boone, 2008] Deslandes, D. and Boone, F. (2008). General formulation for modeling bandpass filters with finite quality factors and resistive couplings. In *European Microw. Conf. EuMC*, pages 1042–1045.

[Ecclestone et al., 2007] Ecclestone, T. J., Booth, P., and Dawkins, A. (2007). Process selection for future single-feed-per beam feed chain components. In *29th ESA Antenna Workshop*.

[Ernst and Postoyalko, 2003] Ernst, C. and Postoyalko, V. (2003). Prediction of peak internal fields in direct-coupled-cavity filters. *IEEE Trans. Microw. Theory Techn.*, 51(1):64–73.

[Ernyei, 1983] Ernyei, H. (1983). Mechanical bandpass filter design with lumped element prototypes. *IEEE Trans. Circuits Syst.*, 30(2):89–107.

[Fletcher, 1972] Fletcher, R. (1972). *Fortran Subroutine for Minimization by Quasi-Newton Methods*. AERE, Harwell, England.

[Flory and Taber, 1997] Flory, C. and Taber, R. (1997). High performance distributed bragg reflector microwave resonator. *IEEE Trans. Ultrason., Ferroelectr., Freq. Control*, 44(2):486–495.

[Folgero and Kocbach, 2003] Folgero, K. and Kocbach, J. (2003). Yield-driven design of direct-coupled waveguide filters with minimum use of full wave em solvers. In *European Microw. Conf. EuMC*, pages 1365–1368.

[Gilmore and Booth, 2008] Gilmore, J. and Booth, P. (2008). Manufacturing of RF components using direct metal laser sintering. In *30th ESA Antenna Workshop*.

[Hong and Lancaster, 2001] Hong, J.-S. and Lancaster, M. J. (2001). *Microstrip Filters for RF/Microwave Applications*. John Wiley & Sons, Inc.

[Hunter, 2001] Hunter, I. (2001). *Theory and Design of Microwave Filters*. The Institution of Electrical Engineers, London.

[Hunter et al., 2002] Hunter, I. C., Billonet, L., Jarry, B., and Guillon, P. (2002). Microwave filters-applications and technology. *IEEE Trans. Microw. Theory Techn.*, 50(3):794–805.

[Kahrizi et al., 2002] Kahrizi, M., Safavi-Naeini, S., Chaudhuri, S., and Sabry, R. (2002). Computer diagnosis and tuning of rf and microwave filters using model-based parameter estimation. *IEEE Trans. Circuits Syst. I, Fundam. Theory Appl.*, 49(9):1263–1270.

[Khan, 1997] Khan, N. G. (1997). *High power microwave filters*. PhD thesis, Electronic and Electrical Engineers, University of Leeds.

[Lee and Tsai, 2008] Lee, H.-M. and Tsai, C.-M. (2008). A parameter extraction method for microwave direct-coupled-resonator filters with the consideration of component losses. In *IEEE MTT-S Int. Microw. Symp. Dig.*, pages 1083–1086.

[Levy, 1973] Levy, R. (1973). A generalized design technique for practical distributed reciprocal ladder networks. *IEEE Trans. Microw. Theory Techn.*, 21(8):519–526.

[Lorente et al., 2012] Lorente, J. A., Ernst, C., and Alvarez Melcon, A. (2012). Accurate derivation of lossy equivalent circuit of waveguide external coupling. In *International Workshop on Microwave Filters, Toulousse (France)*.

[Lorente et al., 2013] Lorente, J. A., Ernst, C., and Alvarez Melcon, A. (2013). Rigorous derivation of lossy equivalent circuit for narrowband waveguide direct-coupled-cavity filters. *IET Microwaves, Antennas & Propagation*, 7(4):251–258.

[Lorente et al., 2013 submitted] Lorente, J. A., Ernst, C., and Alvarez Melcon, A. (2013 [submitted]). Dimensional synthesis of narrow-band waveguide direct-coupled-cavity filters with optimized geometries. *IET Microwaves, Antennas & Propagation*.

[Lorente et al., In Process] Lorente, J. A., Ernst, C., and Alvarez Melcon, A. ([In Process]). Loss reduction in narrow-band waveguide direct-coupled-cavity filters by shaping coupling structures.

[Lorente et al., 2009a] Lorente, J. A., Mendoza, M. M., and Ernst, C. (2009a). Single part microwave filters made from selective laser melting. *ESA Working Paper 2367*.

[Lorente et al., 2010] Lorente, J. A., Mendoza, M. M., and Ernst, C. (2010). Single part microwave filters made from selective laser melting. In *First Networking/Partnering Day in ESTEC, ESA, The Netherlands*.

[Lorente et al., 2009b] Lorente, J. A., Mendoza, M. M., Petersson, A. Z., Pambaguian, L., Alvarez Melcon, A., and Ernst, C. (2009b). Single part microwave filters made from selective laser melting. In *39th European Microwave Conference (EuMC)*, pages 1421–1424.

[Macchiarella, 2010] Macchiarella, G. (2010). Extraction of unloaded q and coupling matrix from measurements on filters with large losses. *IEEE Microw. Wireless Compon. Lett.*, 20(6):307–309.

[Macchiarella and Traina, 2006] Macchiarella, G. and Traina, D. (2006). A formulation of the cauchy method suitable for the synthesis of lossless circuit models of microwave filters from lossy measurements. *IEEE Microw. Wireless Compon. Lett.*, 16(5):243–245.

[Marcuvitz, 1951] Marcuvitz, N. (1951). *Waveguide Handbook*. McGraw Hill, New York.

[Matthaei et al., 1980] Matthaei, G., Young, L., and Jones, E. (1980). *Microwave Filters, Impedance Matching Networks, and Coupling Structures*. Artech House.

[Mendoza et al., 2012] Mendoza, M. M., Ernst, C., Lorente, J. A., Alvarez Melcon, A., and Seyfert, F. (2012). On the relation between stored energy and fabrication tolerances in microwave filters. *IEEE Trans. Microw. Theory Techn.*, 60(7):2131–2141.

[Miraftab and Yu, 2009] Miraftab, V. and Yu, M. (2009). Advanced coupling matrix and admittance function synthesis techniques for dissipative microwave filters. *IEEE Trans. Microw. Theory Techn.*, 57(10):2429–2438.

[NASA, 2013] NASA (2013). National space science data center master catalog.

[Pozar, 1998] Pozar, D. (1998). *Microwave Engineering, 2nd Edition*. Wiley, New York.

[Rizzi, 1988] Rizzi, P. (1988). *Microwave Engineering: Passive Circuits*. Prentice-Hall International editions. Prentice Hall.

[Sengul, 2009] Sengul, M. (2009). Construction of lossless ladder networks with simple lumped elements connected via commensurate transmission lines. *IEEE Trans. Circuits Syst. II, Exp. Briefs*, 56(1):1–5.

[Sun and Chao, 1995] Sun, E.-Y. and Chao, S.-H. (1995). Unloaded Q measurement-the critical points method. *IEEE Trans. Microw. Theory Techn.*, 43(8):1983–1986.

[Suzuki and Hosono, 1983] Suzuki, M. and Hosono, T. (1983). Optimum sectional shape of dominant mode waveguide. *IEEE Trans. Microw. Theory Techn.*, 31(10):836–841.

[Tavares, 2009] Tavares, A. (2009). Testing filters constructed by the direct metal laser-sintering (dlms) technology - roughness measurements. Technical report, ESA/ESTEC.

[Terman, 1943] Terman, F. E. (1943). *Radio Engineers' Handbook*. McGraw-Hill, New York and London, 1 edition.

[Thal, 1982] Thal, H. L. (1982). Microwave filter loss mechanisms and effects. *IEEE Trans. Microw. Theory Techn.*, 30(9):1330–1334.

[Traina et al., 2007] Traina, D., Macchiarella, G., and Sarkar, T. K. (2007). New general formulation of the cauchy method for the accurate model extraction of higher order microwave systems. *Microwave and Optical Technology Letters*, 49(8):1957–1961.

[Vanin et al., 2004] Vanin, F. M., Schmitt, D., and Levy, R. (2004). Dimensional synthesis for wide-band waveguide filters and diplexers. *IEEE Trans. Microw. Theory Techn.*, 52(11):2488–2495.

[Yu, 2007] Yu, M. (2007). Power-handling capability for rf filters. *IEEE Microw. Mag.*, 8(5):88–97.

[Zafra, 2007] Zafra, A. (2007). Advanced geometries for Q improvement in waveguide filter design. Technical report, UPV.

[Zafra and Ernst, 2006] Zafra, A. and Ernst, C. (2006). Advanced shaping of coupling structures for waveguide filters to reduce losses. In *Int. Workshop on Microwave Filters*.

[Zaki and Chen, 1987] Zaki, K. A. and Chen, C. (1987). Coupling of non-axially symmetric hybrid modes in dielectric resonators. *IEEE Trans. Microw. Theory Techn.*, 35(12):1136–1142.

[Zverev, 1967] Zverev, A. (1967). *Handbook of FILTER SYNTHESIS*. Wiley, New York.